STATUS OF THESIS

Title of thesis	INFLUENCE OF PORE GEOMETRY, PRESSURE AND PARTIAL WATER SATURATION TO ELECTRICAL PROPERTIES OF RESERVOIR ROCK: MODEL AND LABORATORY INVESTIGATION

I   HILFAN KHAIRY

hereby allow my thesis to be placed at the Information Resource Center (IRC) of Universiti Teknologi PETRONAS (UTP) with following:

1. The thesis becomes the property of UTP.

2. The IRC of UTP may make copies of the thesis for academic purposes only.

3. This thesis is classified as

☐   Confidential

☑   Non-confidential

If this thesis is confidential, please state the reason:
_____
_____

The contents of the thesis will remain confidential for _____ years.

Remarks on disclosure:
_____
_____

Endorsed by

_____   _____
Signature of Author   Signature of Supervisor
Hilfan Khairy   A.P. Dr. Zuhar Zahir Tn. Harith

Permanent address:
Jln. Purnawirawan 7 No.16
Gn. Terang, Bandar Lampung,
Indonesia.

Date : _____   Date: _____

UNIVERSITI TEKNOLOGI PETRONAS

INFLUENCE OF PORE GEOMETRY, PRESSURE AND PARTIAL WATER
SATURATION TO ELECTRICAL PROPERTIES OF RESERVOIR ROCK:
MODEL AND LABORATORY INVESTIGATION

by

HILFAN KHAIRY

The undersigned certify that they have read, and recommend to the Postgraduate
Studies Program for acceptance this thesis for the fulfillment of the requirements for
the degree stated.

Signature   :

Main Supervisor   :   Assoc. Prof. Dr. Zuhar Zahir Tn. Harith

Signature   :

Head of Department :   Assoc. Prof. Ir. Abdul Aziz bin Omar

Date   : _____

INFLUENCE OF PORE GEOMETRY, PRESSURE AND PARTIAL WATER
SATURATION TO ELECTRICAL PROPERTIES OF RESERVOIR ROCK:
MODEL AND LABORATORY INVESTIGATION

by

HILFAN KHAIRY

A Thesis

Submitted to Postgraduate Studies Program

as a Requirement for the Degree of

DOCTOR OF PHILOSOPHY

GEOSCIENCES AND PETROLEUM ENGINEERING

UNIVERSITI TEKNOLOGI PETRONAS

BANDAR SERI ISKANDAR,

PERAK

JANUARY 2011

DECLARATION OF THESIS

Title of thesis

INFLUENCE OF PORE GEOMETRY, PRESSURE AND PARTIAL WATER SATURATION TO ELECTRICAL PROPERTIES OF RESERVOIR ROCK: MODEL AND LABORATORY INVESTIGATION

I   HILFAN KHAIRY

hereby declare that the thesis is based on my original work except for quotations and citations which have been duly acknowledged. I also declare it has not been previously or concurrently submitted for any other degree at UTP or other institutions.

Witnessed by

_____   _____
Signature of Author   Signature of Supervisor
Hilfan Khairy   A.P. Dr. Zuhar Zahir Tn. Harith

Permanent address:
Jln. Purnawirawan 7 No.16
Gn. Terang, Bandar Lampung,
Indonesia.

Date: _____   Date: _____

DEDICATION

For my beloved wife Mindrawaty and
my daughter Muthia and Mufida

Orang berilmu dan beradab tidak akan diam di kampung halaman
Tinggalkan negerimu dan merantaulah ke negeri orang
Merantaulah, kau akan dapatkan pengganti dari kerabat dan kawan
Berlelah-lelahlah, manisnya hidup terasa setelah lelah berjuang.

Aku melihat air menjadi rusak karena diam tertahan
Jika mengalir menjadi jernih, jika tidak, kan keruh dan menggenang

Singa jika tidak tinggalkan sarang tak akan dapat mangsa
Anak panah jika tidak tinggalkan busur tak akan kena sasaran

Jika matahari di orbitnya tidak bergerak dan terus diam
Tentu manusia bosan padanya dan enggan memandang

Bijih emas bagaikan tanah biasa sebelum digali dari tambang
Kayu gaharu tak ubahnya seperti kayu biasa jika di dalam hutan

Imam Syafii

ACKNOWLEDGMENTS

ABSTRACT

Pressure and saturation are of two important parameters to be considered to evaluate the electrical properties of reservoir rock. As confining pressure can cause pore space of the rock to collapse and rock properties to change, it is necessary to examine in details how much the pressure and saturation changes affect the electrical properties. Investigations of electrical properties of sandstones and carbonates are the main focus in this work. The effects of pore geometries, confining pressure, and partial water saturation on electrical properties are investigated. The new electrical dispersion models from 0.1 Hz until 0.2 MHz for shaly sandstone are also developed.

Petrographic image analysis is carried out to asses pore geometry of the media. Circularity, pore aspect ratio, pore size distribution and pore angle distribution are calculated to evaluate their effect on electrical dispersion. Confining pressure and water saturation observation are then evaluated to obtain their impact on pore structure and complex resistivity.

The result of this work shows that surface conductivity plays as a dominant factor particularly in shaly media and it is indicated by electrical resistivity dispersion in low water saturation. When evaluating surface conductivity, the pore geometry has to be considered because large structure is easier to saturate rather than small structure. Moreover, the high water salinity can significantly reduce diffusive layer thickness and if the pore radii are very small, the diffusive layer thickness will touch each other and block the anion movement.

In addition to these results, it is found that pore radius distribution provides more contribution to the electrical resistivity dispersion and becomes a basis to extract porosity from resistivity. Confining pressure only contributes small changes in pore geometry of media and the use of imaginary resistivity gives a better detection on it. Modified D-model and Archie's model are developed to calculate the dielectric

permittivity and effective conductivity in high water salinity saturated-rock as a function of water saturation degree.

ABSTRAK

Tekanan dan penepuan adalah dua parameter penting yang perlu diambil kira dalam menilai sifat-sifat kelektrikan sesebuah reservoir. Dengan keupayaan tekanan keliling untuk mengurangkan ruang liang batuan, kajian secara terperinci mengenai bagaimana kesan tekanan dan penepuan berubah-ubah secara kuantitif terhadap sifat elektrik batuan amatlah diperlukan. Kajian mengenai sifat elektrik bagi batuan pasir dan karbonat adalah fokus utama di dalam tesis ini. Kesan liang geometri, tekanan keliling dan penepuan air separa terhadap sifat keelektrikan batuan telah dijalankan. Model penyerakan elektrik baru dengan frekuensi di antara 0.1 Hz sehingga 0.2 MHz untuk batuan "shaly sandstone" telah dibuat.

Analisis imej petrografi telah dilakukan bagi menaksirkan liang geometri media. Tahap kebundaran zarah batuan, nisbah aspek liang, taburan saiz bagi liang dan taburan sudut liang telah dikenal pasti untuk menilai kesan faktor-faktor tersebut terhadap penyerakan elektrik dalam media. Tekanan keliling dan pemerhatian terhadap penepuan air kemudiannya dinilai bagi mengenal pasti impaknya terhadap struktur liang dan resistiviti rencam. Hasil akhir bagi kajian ini mendapati bahawa konduktiviti permukaan memainkan peranan penting terutama sekali terhadap media berlempung dan ini dibuktikan melalui penyerakan resistiviti elektrik pada ketepuan air rendah. Dalam menilai konduktiviti permukaan, liang geometri harus dititikberatkan kerana struktur yang besar lebih mudah ditepukan dengan air berbanding struktur kecil. Tambahan pula, tahap kemasinan air yang tinggi mampu mengurangkan ketebalan lapisan resapan dan jika jejari liang adalah kecil, ketebalan lapisan resapan tersebut akan bersentuh antara satu sama lain dan menghalang pergerakan anion.

Selain daripada itu, kajian ini juga mendapati taburan jejari liang banyak memberikan kesan terhadap dispersi resistiviti elektrik dan menjadi asas bagi mengekstrak porositi daripada resistiviti. Tekanan keliling hanya mempengaruhi

perubahan kecil di dalam liang geometri bagi media dan ia dikesan dengan menggunakan resistiviti bayangan. Model-D dan Model Archie yang diubahsuai telah diusulkan bagi tujuan mengira ketelusan dialektrik dan konduktiviti efektif di dalam batuan yang mempunyai kemasinan tinggi terhadap fungsi darjah penepuan air secara matematik.

TABLE OF CONTENTS

LIST OF TABLES

LIST OF FIGURES

CHAPTER 1

INTRODUCTION

1.1 Introduction

The knowledge of water saturation and its distribution is very important in hydrocarbon recovery assessment. The how and when reservoir monitoring is conducted requires some deep investigations on the physical properties that much govern or change during production. If the changes are large enough, the time-lapse reservoir monitoring can be employed to map fluid distribution, pressure, temperature and fluid front. One of the physical properties that may show significant changes during production is its electrical properties. However, the variation of pore geometries and pore throats as well as inhomogeneous distribution of microporosity may cause the water not to displace oil uniformly throughout the rock. Thus, the distribution of water before and after being produced may be quite different. For this reason, saturated and unsaturated fluid mechanism as well as pressure and pore geometry are the physical basis to understand the electrical responses of reservoir rock when recovery is addressed.

It has been more than a past decade that the application of electrical survey can be applied to investigate water fluid distribution in hydro-geophysics purposes. Recently, this method has the potential application to discriminate water-saturated reservoir and hydrocarbon-saturated reservoir because they have low resistivity and high resistivity contrast respectively. Thus, ones could produce the resistivity map between the swept and un-swept area when the oil is replaced by brine water during water flooding.

Since electrical properties of rock are considered highly sensitive to the fluid types and to saturation, these parameters can be exploited by using electromagnetic (EM) or

surface resistivity where the response is a function of bulk electrical resistivity. In term of cost, the EM technology would provide lower cost compared to time-lapse seismic monitoring.

To study the electrical properties feasibility for reservoir monitoring, it is required to investigate its effect with water saturation degree changes, confining pressure and pore geometry. This thesis presents the model and laboratory investigations of electrical properties of reservoir rock as an impact of water saturation degree, confining pressure and pore geometry. The main goals of this thesis are to characterize those effects on siliciclastic and carbonate rock and to develop a new electrical dispersion model in high water salinity dependent on water saturation.

1. 2 Research Background

Electrical properties especially resistivity and dielectric permittivity are two important parameters in geophysical exploration as well as in environmental geophysics studies. They are used as a main parameter to determine water saturation in wireline logging. Dielectric permittivity, conductivity or resistivity, are generally a wide range function of fluid content, porosity, degree of saturation, pore geometry and mineral content.

Dependency of resistivity, or reciprocal of conductivity, and dielectric permittivity to the water saturation can be evaluated in Archie's model [1] and some dielectric empirical relationships [2]. The Archie's law describes electrical behavior in sedimentary rock as a function of water saturation, porosity and fluid resistivity. To correlate resistivity with dielectric permittivity, the analytical evaluation of Maxwell equations is required [3, 4].

The specific characteristics of dielectric permittivity and resistivity have to be investigated for formation evaluation [5, 6], steam-flood effect [7], reservoir monitoring [8], reserve estimation by combining elastic and resistivity properties [9], CO_2 sequestration monitoring [10] and gas-hydrate concentration estimation [11]. Those are mostly implemented in sedimentary rock.

Rock matrix of sandstone or limestone usually has relative dielectric permittivity constant around 6-8 [12], whereas freshwater has around 80. However, when the rock

matrix is saturated by water, the dielectric exponentially increases to 10^6 at low frequency. This huge anomaly is very interesting to be studied because the phenomenon has a direct correlation with specific surface area, water saturation and permeability parameter [2]. In 1991, Ruffet et.al [13] study the pore geometry effect through complex conductivity and its relationship with nature of fractal. They find that specific surface area to pore volume ratio clearly correlate to fractal dimension of Le Mehaute and Crepy (MC) and Po Zen Wong (PZW) model. According to Krohn [14], the fractal character is a result of diagenesis.

Electrical double layer (EDL) is formed when there is a contact between pore water and solid grain. The presence of EDL may contribute to electrical properties of rock, depending on pore fluid, pore geometry and degree of saturation. The high water salinity is mainly influenced by a bulk volume of conduction process while low salinity is influenced by interlayer or fluid-grain surface conductivity [4, 13, 15, 16]. Estimation of water saturation in clean sandstone is usually compensated by using Archie's model. However, employing the Archie's law on the shaly sandstone is inappropriate as the law does not take into account surface conductivity effect on the clay mineral.

Since the carbonate rock is more heterogeneous and has very complicated structure, more emphasis should be considered in relating its electrical behavior to its rock properties. It is known that pore type of carbonate rock can be classified into a wide range of pore types based on petrographic image analysis such as vuggy, intercrystalline macroporosity, intercrystalline microporosity, macromouldic and intraparticle. These are obviously different from siliciclastic, where it has relatively similar pore type. The question now is that what the effect of pore geometry, pressure and saturation series is on electrical properties? Surely, the interrelationship among electrical properties, pore structure and geometry, pressure, saturation, wettability, fluid and reservoir properties is the key to accomplish a full understanding and to employ it as a tool for reservoir monitoring.

For more than 15 years the research on electrical properties of rock has been increased particularly on effect saturation, pore structure, wettability, shale content, modeling and dispersion. Siliciclastic rock again the object of most of the studies.

Lima and Sharma [17, 18] study the grain conductivity by considering self-similar mixtures of conductive grain. Later, they generalize the result to evaluate Maxwell-Wagner theory for membrane polarization in shaly sandstones. There are two possibilities of polarization mechanism occurrences that bound layer and diffusive layer polarization.

Knight and Ana [19] and Nguyen et.al [20] investigate a correlation of complex dielectric to water saturation and wettability. The dependency of complex dielectric to water saturation is highly significant as shown in direct measurement or in Bruggeman-Hanai-Sen (BHS) and complex refracted index method (CRIM). The real part of dielectric of oil-wet is lower than water-wet for low water saturation.

Suman and Knight [21] examine the presence of thin film during saturation either in water-wet or oil-wet system. Their result show that the saturation exponent n of Archie's model might differ for those systems. For water-wet system the exponent n is significantly lower compared to oil-wet system and gave various results in both drainage and imbibitions. This is attributed to the electrical continuity provided by this thin film as the effect of pore structure is founded very critical in determining resistivity of the samples. The pore microstructure might dictate the path of electric currents. An observation again through Archie's exponent n variation with pore size distribution yielded the magnitude of n and hysteresis is reduced substantially in water-wet than in oil-wet system when the size of neighboring pores of the network are correlated positively.

Revil and Glover [16] present surface conductivity model based on a description of surface chemical reactions and electrical diffuse layer processes. They consider an amphoteric mineral surface and derive the fractional occupancies of positive, negative, and neutral sites on the surface, and the fractional ionic diffuse layer densities, as a function of the salinity and the pH. The result is electrical surface conduction and is found to be dependent on the electrolyte concentration and pH.

Nguyen et.al [22] works on dielectric hysteresis. At the same water saturation, either drainage or imbibitions phase might have different complex dielectric permittivity and electric conductivity. The permittivity of imbibitions phase is lower than that of drainage especially when saturation water is less than 0.6.

4

The influence of grains shape, pore and oil droplet disperse in a dispersion model of carbonate rock is investigated by Seleznev [23]. He establishes the new model that incorporated the rock microstructures. The flatter grain component is believed to cause higher dielectric dispersion and lower effective mixture conductivity.

Szerbiak et.al [24] observes both petrophysical and electrical data of Ferron sandstone such as porosity, permeability, water content and complex dielectric permittivity on GPR's frequency about 75 MHz. Their observation result is that either an electrical conductivity or a dielectric constant has correlation with the volumetric water content. In the case of oven-dried samples, electrical conductivity is poorly estimated due to the significantly reduced mobility of ion.

Endres and Bertrand [25] develop a dielectric model by using differential effective medium (DEMA) and apply the result for clean sandstone and carbonate which is divided into three relative size scale categories: microscopic porosity, mesoscopic porosity and macroscopic porosity. The conclusion is that size scale of pores existing in the model contributed significantly to dielectric permittivity and porosity.

An observation is accomplished by Sengwa and Soni [26] for 17 different grades of dry and water-saturated limestone samples in frequency range of 100 Hz to 100 KHz. The analysis is focused on factors such as chemical composition, bulk density and porosity that much governed their dielectric parameter. At low frequency, chemical composition and bulk density are the major factors governing the dielectric constant. For water saturated samples, dielectric is also sensitive to porosity and grain size.

Toumelin and Verdin [27] develop a new approach in modeling the effect of pore connectivity and geometry of wide band electromagnetic dispersion from kilohertz to gigahertz frequency. The model is addressed to improve effective medium theory which does not consider pore connectivity. Meanwhile Rey and Jongmans [28] study the particle shape and orientation effect on resistivity. They find that the aligned elongated resistive particle such as pebbles embedded in conductive might induce anisotropy. A more recent work is presented by Abousrafa et.al [29] for pore geometry model of porous media in fully brine water saturated. They claim only

cementation factor has to be dependency with pore void radii and pore throat radii. Porosity and resistivity are strongly affected by pore void radii and pore throat radii respectively.

Most of the previous work is in low salinity water, GPR frequency and in clean sand media. Whereas, when dealing with high water salinity the effect of saturation degree should be taken into account, especially in shaly sand media. Furthermore, surface conductivity, pore geometry and electrical dispersion need to be studied more detail as it may correlate to porosity. To complete on previous studies, this research underlines four points to be evaluated in their relationship to electrical properties; they are: water saturation degree, confining pressure, pore geometry and surface conductivity. Medium of the study is sedimentary rock comprising of sandstone and carbonate.

1.3 Problem Statement

The presence of clay minerals throughout the rock either dispersed or coated may cause membrane polarization. This occurs when clay surface partially blocks ionic solution. Negative charges on clay minerals tend to capture the electrolyte cations and move to anions in the other ways.

Generally, electrical properties of the rock are divided into two folds either as a response of volumetric or as grain-fluid interfacing. Most of the conductivity models are established based on parallel conductor systems that are *electrolytic* and *clay* component. Archie's relationship is established based on electrolytic part. Whereas, clay component can be evaluated either by considering various clay types, clay distribution or may be evaluated by understanding physical and chemical phenomena at the border of grain and fluid. The simplest model to calculate effective conductivity/permittivity is based on clay distribution through mixing composite model. This is developed by assuming quasi-static approximation where the electromagnetic wavelength is much larger than the characteristic size of rock constituents, pores and grains. Thus, to accommodate the surface conductivity, the effective conductivity model must be developed.

An accurate estimation of water distribution or saturation needs a proper petrophysics model. Archie's model is the most popular formula to extract water saturation. This model is developed in water-saturated clean sandstone. The application of this model is usually used for siliciclastic reservoir with the porosity in the range of $0.05 < \phi < 0.4$ [30]. Applying the Archie's model in carbonate and shaly sandstone rock may result in an inaccurate saturation value. The wettability, complexity and heterogeneity of the carbonate rock in the same rock bodies or sample are believed to be the main causes. Thus, Archie's cementation and saturation factor representing tortuosity and fluid distribution respectively are found to have a great variation. Meanwhile in shaly sandstone, the problem may exist because of the effect of electrical double layer on the surface of solid grain.

 Electrical double layer (EDL) contributes more dominant in low water salinity and turn into volumetric conductivity in high water salinity [4, 13, 15, 16]. However, a preliminary study by Khairy H, et.al [31] indicates that even in high water salinity, EDL still dominantly contributes in low water saturation degree. This phenomenon is due to the more saline water will lead to the decreasing in the thickness of double layer. Therefore, conductivity of the rock in this case should be considered incorporating both of the volumetric and surface conductivity simultaneously as water saturation is increased. The new proposed model must take into account of saturation factor and surface conductivity.

The effect of EDL on electrical properties of rock also depends on the ratio of interface surface thickness to the pore radius [4]. If the pore radii are small, the double layer can touch each other and may prevent the motion of anion. While when pore radii are large, the ion motion is undisturbed. What is the effect of pore geometry on electrical properties? Is there any contribution of confining pressure to geometry changes? And how does the pressure influence electrical properties? Those should be answered to exploit electrical properties for reservoir evaluation.

In summary, this thesis will investigate the interrelationship of dielectric permittivity and conductivity to confining pressure, water saturation and pore geometry. It will exploit some existing mixing laws and develop a new electrical model based on the effective medium approximation.

1.4 Objectives

Having identified problems that have been discussed, the objectives of this thesis are set up as follows:

1. To investigate pore geometry interrelationship to resistivity dispersion in low to medium frequency range (0.01 Hz– 0.2 MHz).

2. To investigate the effects of pore radius distribution, pressure and saturation on electrical resistivity.

3. To develop a new dispersion model that incorporates electrical double layer for shaly material in high water salinity.

4. To verify the dielectric and conductivity model by optimization process using hybrid inversion and singular value decomposition.

1.5 Contributions

In accordance with the objectives mentioned above, here are the main contributions of this thesis to enrich the development of knowledge:

1. As Archie's law does not always work in shaly sandstone due to electrical double layer effect, therefore the conductivity model obtained in this project can be used to predict saturation.

2. The laboratory investigation of dielectric and conductivity of reservoir rock performed under high pressure may provide a more reliable subsurface model.

3. As we demonstrate, there will be certain criteria of reservoir rock which may give great effect to electrical properties in term of pore geometry, pore distribution, pressure and saturation.

4. Investigation on pore shape, pore type and pore distribution may help us to extract porosity and permeability information from electrical data. The extracting porosity from electrical dispersion gives an alternative tool for reservoir characterization.

5. Potential application of complex resistivity for water flooding monitoring is an alternatively newer, cheaper and easier method to exploit EM survey for time lapse monitoring.

1.6 Methodology

To investigate pore geometry effect to electrical properties, few samples are selected which represent various pore size distributions. There are nine samples studied consisting of five samples of sandstone and four samples of carbonate rock. The samples have different porosity ranging from 12.54 % to 31.94% and permeability ranging from 17.5 mD to 5091 mD. In this work, most of carbonate rocks have extremely larger pore size compared to sandstone.

The first step is to shape sedimentary core samples that fit with core- holder. Basic petrophysics measurement of porosity and permeability is then measured. After core cleaning to remove salt and oil within the rock is conducted, those samples are re-measured of their porosity and permeability. To test the samples whether can retain with overburden pressure, the cores are tested by analyzing their sonic velocity whilst

the confining pressure is increased and decreased from 0 until 3000 psi and in some samples until 5000 psi. The P-wave and both Sv and Sh waves are recorded in order to determine the impact of the stress.

To quantify pore space and its geometry, petrographic image analysis is conducted. The thin sections are produced and the images are classified into solid matrix and pore space. Description of solid matrix includes the identification of texture, mineralogy and diagenesis. Petrographic analyses starts from rock coring, cutting, grinding and preparing thin sections with thickness of 0.03 mm. The samples are then impregnated with blue dyed epoxy, and stained with alizarin red and potassium ferricyanide. The result of this step includes parameter that quantitatively describes pore space and its shape such as pore radius distribution, aspect ratio, pore angle, circularity and gamma. This result acts as a basis to correlate electrical dispersion with geometry of the pore.

The electrical properties evaluation which depends on pore geometry, pressure and saturation are the main focus of this third step. Dynamic of the pore fluid is simulated by considering water drainage and imbibitions. The complexities of pore geometry, in this case are pore radius distribution, to study their impact on electrical double layer or dispersion. The measurement workflow is started from sample preparation, measurement procedure, data acquisition and editing. The resistivity measurements are conducted on both two electrodes and four electrodes mode.

Electrical resistivity dispersion indicates an electrical double layer that occurs on the interface of solid grain to water fluid. This type of electricity phenomenon, in high water salinity, contributes more in initial low water saturation and vanishes when volumetric conductivity is introduced. The modified dispersion model is proposed based on D-model of Lima-Sharma's. This model assumes clay particle is dispersed around the solid grain. It utilizes the Wagner's model to extend the model into shaly material. To obtain the best fitting model parameter with experimental data, curve fitting optimization is developed by using hybrid inversion combined with singular value decomposition (SVD) technique. General flowchart of the research is depicted in Figure 1.1.
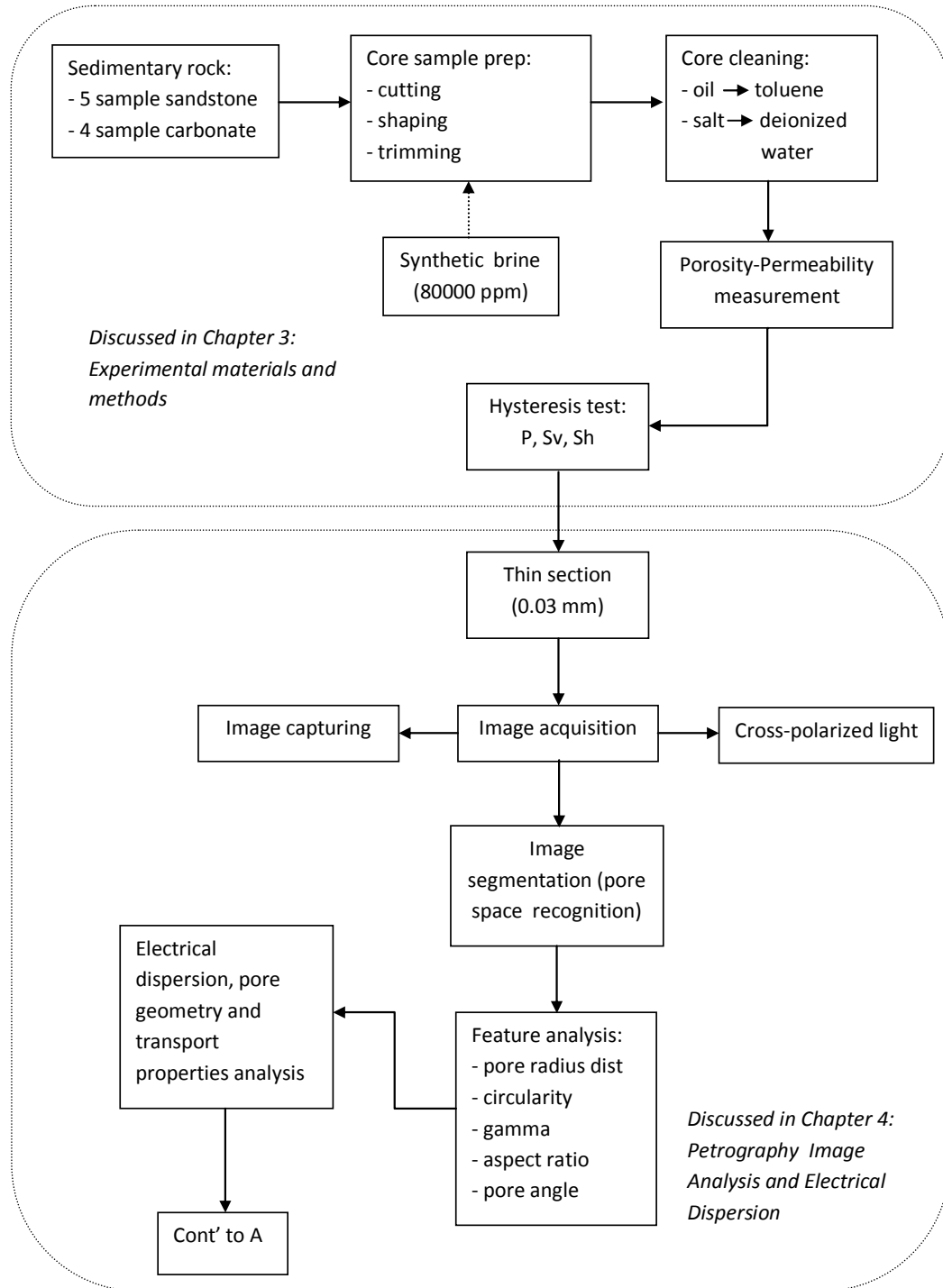
Figure 1.1 General flowchart of the research work.
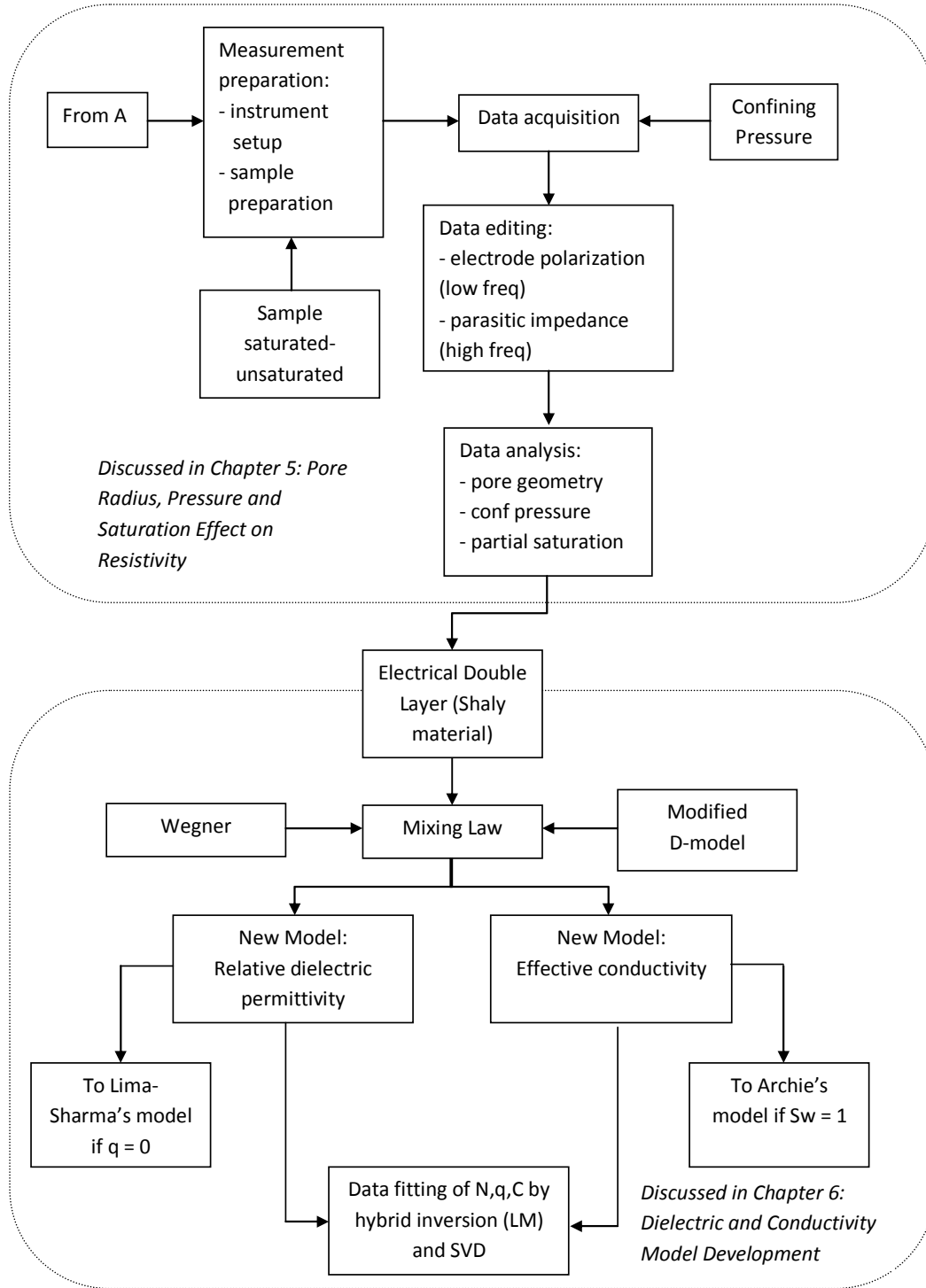
Figure 1.1 General flowchart of the research work (continuation).

1.7 Scope of Study

The scope of the research includes:

1. Petrographic study to describe rock forming mineral, texture and diagenesis.
2. Pore image quantification to obtain pore features such as pore radius distribution, pore aspect ratio, gamma, circularity and pore angle.
3. Scanning electron microscope analysis of the rock.
4. Complex resistivity measurement in range of frequency from 0.01 Hz to 0.2 MHz.
5. The exposure of confining pressure variation to the sample of 1000–3000 psi.
6. Partial water saturation with high water salinity of about 80,000 ppm.
7. The use of sandstone and carbonate as the reservoir rock.
8. Inversion method by using Lavenberg-Marquardt and singular value decomposition.

1.8 Thesis Outline

It begins with Chapter 1, introducing the research background, problem statement, objectives and contribution, and methodology of this research.

Chapter 2 covers brief review of siliciclastic and carbonate reservoir rock. The pore types and process of hydrocarbon lifting are included to give the basic understanding of hydrocarbon exploitation. Detail literature reviews in the area close to the current research are given in this chapter.

Chapter 3 consists of detail description of experimental procedures, apparatus and materials.

Chapter 4 provides the procedure of image analysis and scanning electron microscope (SEM). On each sample, its thin section is observed, and its pore type, geometry and distribution are analyzed. The pore geometry is identified by using optical microscope. The relationship among pore geometry, rock texture, and transport properties with resistivity dispersion is also presented.

Chapter 5 presents the measurement of workflow, data editing and experimental result for two types of reservoir rock, i.e. sandstone and carbonate rock. The discussion of resistivity is divided into two criteria, firstly to evaluate the effect of pore radius distribution and secondly to observe the effect of pressure and saturation.

Chapter 6 focuses on the electrical double layer phenomena and the evaluation on the existing model of electrical properties of rock. This chapter also proposes new dielectric permittivity dispersion and conductivity model and computational fitting technique to achieve best fit with experimental data.

Chapter 7 describes the general discussion and conclusion from previous chapters including statement, consideration and contribution in geophysical exploration.

CHAPTER 2

RESERVOIR ROCK AND ELECTRICAL EVALUATION

2.1 Reservoir Rock

Oil and gas is formed from the deposition of organism millions years ago. The deposition underwent compaction process, which transformed protein in organism to kerogen that under certain condition of pressure and temperature creates oil and gas. Since the density of hydrocarbon is lighter than water in the porous media, it prefers to migrate upwards until trapped by impermeable rock. This impermeable rock is known as "seal rock", whereas the porous media capable of storing hydrocarbon is known as "reservoir rock".

There are three most frequently encountered rocks in oil fields: shales, sandstones and carbonates. The last two are the most rock. Sandstone is the most frequently found in sedimentary rock, accounting approximately 20 percents of the entire group [32]. Hitherto, oil exploration still focuses in this type of rock even though carbonate rock gives the most significant incentive in storing hydrocarbon. More than 60 percents of the world's oil and 40 percents of the gas are held in carbonates [33].

Sandstones are all those medium-grained sedimentary rocks that comprised of more than 50 percents sand-size grains [32]. When the coarse-grained fractions are increased, they are called pebbly sandstones and then sandy conglomerates. Meanwhile if the fine-grained fractions increase, they turn into muddy sandstones and then sandy mudstones.

The structures of sandstones reflect their depositional process as well as environmental and post-depositional modification. Sandstones can be found in nearly all environments from the most proximal alluvial fan to the deepest marine basin

plain. Their texture is varied from very fine to very coarse grained, between 0.063 and 2.0 mm. The sorting can be varied from very poorly to very well sorting. The mature sandstones tend to have well rounded grains and very low matrix content. On the other hand it occurs in immature sandstones. The textural maturity of sandstones measures qualitatively the history of the duration and energy-level of its transport-deposition. The main compositions of sandstones are quartz, feldspar and rock fragment. Other components can include micas, clay minerals and biogenic fragments.

Porous rock media refer to the pore space among the solid grains inside the rock as illustrated in Figure 2.1, and the capacity of the rock to store pore fluids depends on it. There are three properties related to the pore space [4], they are:

1. Porosity: The fraction of pore space volume to bulk volume.

2. Specific surface area: The surface area of the pore related to the pore volume.

3. Permeability: The ability of the pore fluid to flow.

Theoretically, the smaller grain size leads in the porosity of the rock. On the other hand, highly sorted rock will have higher porosity. When considering grain shape, the porosity has tendency to increase from spherical to well-rounded grains.
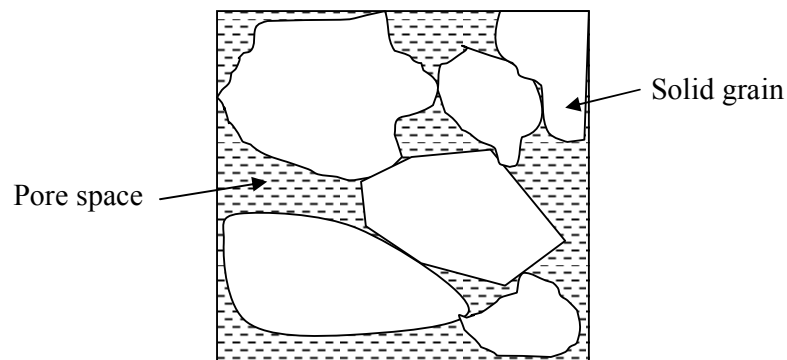
Figure 2.1 Illustration of grains and the pore spaces inside the rock.

In term of process, the porosity of rock is separated in two groups, either as primary porosity or as secondary porosity. The primary porosity refers to the genesis of the rock such as clastic sedimentation and organogenesis. Whereas, secondary

porosity is refer to the history of the rock such as tectonic and chemical processes and dissolution. Based on petrographic fabric, the porosity of rock are divided into several types as shown in Figure 2.2 [34], they are:

1. Interparticle porosity: The pore space between grains or particle.

2. Intraparticle porosity: The pore within skeletal of material.

3. Fracture porosity: The pore caused mainly by tectonic or mechanical compaction.

4. Vugular porosity: The pore spaced produced by the dissolution of grains.
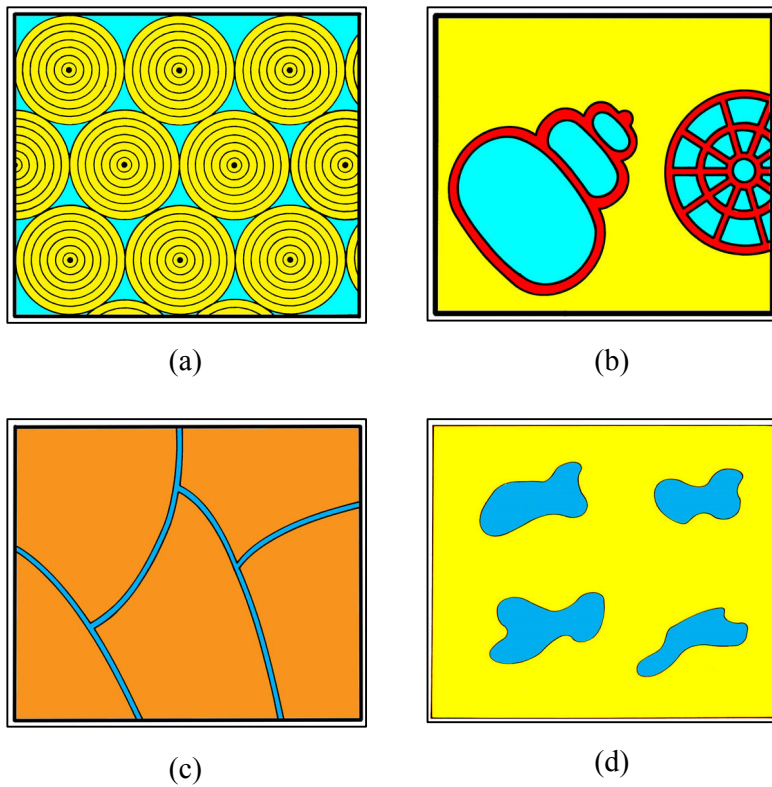
Figure 2.2 Illustration of rock porosity types: (a) interparticle, (b) intraparticle, (c) fracture porosity and (d) vugular porosity [35].

2.2 Hydrocarbon Lifting

Hydrocarbon normally formed, migrated, accumulated and trapped in the reservoir rock. There are two types of traps when hydrocarbon migrates upwards either in stratigraphic or in structural trap as depicted in Figure 2.3.

(a) Structural trap - Anticline type

(b) Structural trap – Fault type

(c) Stratigraphic trap – Truncated type

(d) Stratigraphic trap – Pinchout type
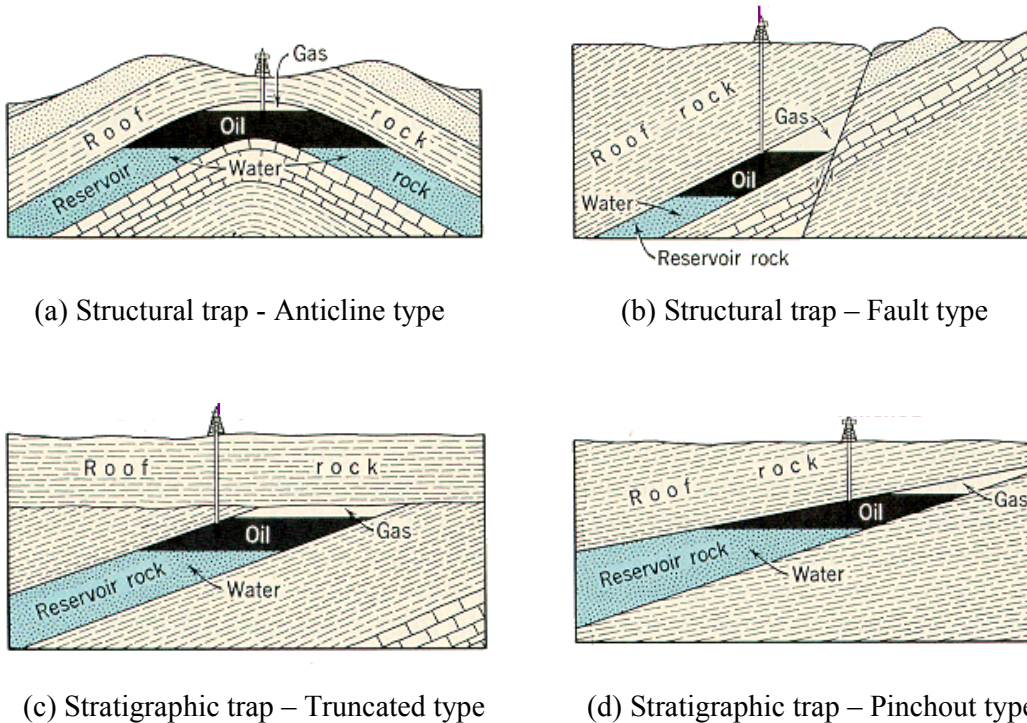
Figure 2.3 Typical of hydrocarbon trapping [36].

Once the oil accumulation has been identified, the drilling program is then executed. The drilling penetrates multiple formation layers until enters the reservoir rock. When the rotating bit drills, the drilling fluid carries out the cutting for disposal. To avoid overpressure, the drilling fluid pressure is kept more than the formation fluid pressure. As the mudcake thickens, the portion of drilling fluid to formation reduces because of filtration process. Three zones are created once the invasion has taken place: flushed zone, transition zone and undisturbed zone. In the flush zone, the fluid filtrates displace the formation water and the moveable fraction of hydrocarbons. The mixture of the filtrate fluid, hydrocarbon and formation water occurs in the transition zone.

The area which is not affected by the invasion is named as undisturbed zone. Diagram of invasion processes with their petrophysical parameter is depicted in Figure 2.4.
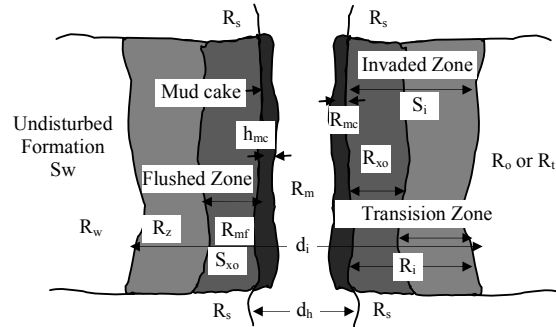
Figure 2.4 Diagram of invasion process.

The invasion on drilling fluid will affect the change of water resistivity from original formation water resistivity (Rw) to resistivity of mud filtrate (Rmf). The result of this invasion will create highly resistivity annulus surrounding the boreholes. This occurs because the mud filtrate resistivity is significantly lower than formation water. In a simple case of clean sand or clay-free formation, the conductivity only reflects the salinity of formation water.

The earlier model usually used for water saturation prediction for more than half century ago is Archie's formula [1]. This model is developed based on clay-free content. Since the rock matrix and hydrocarbon are nonconductive thus the flowing of the current through the medium only depends on pore-water saturation. If the hydrocarbon saturation of the formation increases, the resistivity of formation also increases. Similarly, as the pore-water fluid salinity decreases the rock resistivity, the formation resistivity increases. The Archie's formula can be written as:

$$R_t = \frac{aRw}{\phi^m S_w^n}$$

where:

Sw = water saturation ϕ= porosity
a= tortuosity factor
m= cementation factor
n= saturation exponent
R_w= formation factor resistivity
R_t= true formation resistivity

19

Cementation factor is a function of pore shape and its distribution can vary dependently on the rock texture. The cementation factor commonly takes value of more than 1 to around 5. A new interpretation of cementation factor has been proposed by Glover [37]. He interpreted the cementation factor as the rate of change of the ore connectedness.

2.3 Monitoring the Effect of Hydrocarbon Lifting

Evaluation of hydrocarbon distribution and saturation is usually proposed in order to improve hydrocarbon reserve and recovery. These can be increased by bypassing and un-drained oil and gas and by optimizing infill well location and flood patterns.

The latest technology used to evaluate the fluid distribution is by using 4D seismic survey. The 4D seismic is repetitive survey of 3D seismic in certain period of time, also called as time-lapse seismic monitoring. 4D seismic works based on the differences of seismic impedance magnitude before and after hydrocarbon was lifted. The sensitivity of its changes depends on the fluid types, saturation and pressure changes. Once their discrepancy formed during hydrocarbon production it will give some impact to the velocity of reservoir rock. Thus, the acoustic impedance will change in response to the alteration.

Another promising result in monitoring reservoir fluid movement developed recently is by calculating the electrical properties because there are much more influenced by the fluid properties rather than rock media. The capability of electrical resistivity extracted from electromagnetic survey to monitor water fluid movement is successfully studied by Zack et.al [38]. However, more studies are needed in the future regarding the effect of fluid properties, micro and macro structure of the rock and their relationship to the electrical properties.

2.4 Previous Work in Electrical Properties of Rock

2.4.1 Dielectric Properties

Knight and Nur [2] measure dielectric permittivity of sandstone at frequency range of 60 kHz until 4 MHz by using a two-electrode technique. The response of volumetric and electrode polarization is separated by plotting real and imaginary resistivity in Argand plot. The data below characteristic frequency are considered as noise coming from electrode polarization. They evaluate frequency and water saturation dependency to dielectric permittivity. Room pressure and temperature condition is used in this experiment and the water supplied for the experiment is fresh water. The specific surface area and surface area to volume ratio are two parameters calculated in this study. Result shows that dielectric permittivity has a power-law dependency upon frequency in all saturation degree for sandstone sample. The power-law constant increases linearly with saturation until certain threshold point and decreases with saturation beyond it. Later, Knight and Abad [19] investigate the effect of large deviation of dielectric permittivity at low saturation. They find that this deviation correlates with chemical state of the rock surface or rock to water interaction.

In 1994, Garrouch and Sharma [39] study the effect of salinity, stress, clay content and wettability on dielectric permittivity from 10 Hz to 10 MHz for sandstone samples. The measurement is conducted using both two- and four-electrode techniques. The influence of clay content can be observed through cation exchange capacity, or CEC parameter. Dielectric permittivity has adequate correlation to this CEC parameter. Permeability and porosity show a correlation to lower critical frequency or characteristic frequency. However, the increase of pressure mostly undisturbed the pore volume because the dielectric constant slightly decrease when it is tested to fully water saturation condition. In term of salinity, the more saline water will lead to produce abundant electrolyte ion. When electrical field is applied, the polarization of ion around the grain increases. Thus, it will increase the dielectric constant significantly. Referring to the wettability effect, they claim that the wettability changes, from oil wet to water wet, only affect dielectric constant at the frequency of less than 10 KHz. In this work, they neglect the saturation degree and pore geometry effects on electrical properties. A more recent work by Su et.al [40]

presents the electrical impedance behavior with water saturation for sandstone samples during oil-driving-water test. The measurement is done in two-electrode technique, at the frequency range between 100 Hz and 15 MHz at the time when constant of confining and pore pressure is 10 MPa and 6 MPa respectively. The rock samples are firstly saturated by 10000 ppm brine water and light crude oil is used to drive it. They find that imaginary resistivity correspond linearly with water saturation through interfacial polarization frequency parameter.

2.4.2 Conductivity Properties

Measurement of complex conductivity in low frequency is accomplished by Kulenkampf and Schopper [15]. They observe the real and imaginary conductivity of low water salinity in range of frequency from 10 Hz to 1 MHz to separate volumetric and interlayer conductivity. Volumetric conductivity is dedicated for water volume in the pore space, whereas interlayer is for the interface between solid grain and pore. The result of their experiment exposed that volumetric effect is only characterized by real part and does not depend on the frequency; on the other hand, imaginary conductivity depends on frequency and phase that lead to characterize both volumetric and interfacial. However, they do not take into account how great the pore structure affected the conductivity value. Actually, the specific surface area to volume ratio has close relationship to complex conductivity and nature of fractal as studied by Ruffet [13]. Furthermore, the pore size distribution either rectangular, normal or log normal provide different saturation exponent of *n* during drainage and imbibitions [21]. Hence, the hysteresis evaluation is needed to be accomplished particularly in wet-oil reservoir

2.4.3 Pore Geometry

To investigate the influence of pore geometry on electrical properties, the modeling has been established recently by Toumelin and Verdin [27]. They develop a model of dispersion of dielectric permittivity and electrical conductivity by using effective

medium theory for frequency range from 10 kHz to 1 GHz. The assumption used for their object is clay free porous rocks. The issue of pore scaling and pore connectivity is a major contribution to model electrical properties. Another modeling result initiated by Endres and Bertrand [25] exhibits that pore-size scale model might lead to specific dielectric properties of clean rock and soils. Pore-size types, such as microporosity, mesoporosity and macroporosity, are modeled by using differential effective medium, or DEMA, and an iteratively embedding process is executed to account those pore-size types. The result shows that dielectric to porosity relationship has significantly different responses, dependent on their pore-size scale at high frequencies. Meanwhile Abousrafa et.al [29] investigate pore geometrical model of fully water saturated rock. The model is verified by using finite element model and found that resistivity and formation factor is strongly affected by pore throat radius. On the other hand, porosity is more affected by pore void rather than pore throat radius. Furthermore, cementation factor is controlled by both pore void and pore throat radius.

2.4.4 Theoretical Development

Theoretical evaluation of electrical response of the shaly rock in parallel conductor system approach, such as chemical and volumetric, is done by many researchers. Lima and Sharma [17] introduce a grain conductivity approach for shaly sandstone reservoir. Here, the clay particles are treated as individually or continuously by assuming equivalent volume conductivity. The model result in a similar pattern to volumetric average but it depends on the clay type, distribution and proportion. The generalization of the conductivity dispersion in Maxwell-Wagner polarization range is then been focus to extend the previous result [18]. In this theory, the source of polarization is from surface conductivity in Stern double layer (S-model) and electro-diffusional mechanism (D-model). Both of the models exhibit similar dispersion as introduced by Debye with certain characteristic. To obtain total conductivity of the media, Wagner's mixing model is used and it is found that D-model provides the best fit with the shaly sand experiment. In 2005, Lima et.al [41] analyze the conductivity of shaly media saturated by fresh-water   based on effective volume condition

23

concept. In general, the bulk conductivity is mainly controlled by effective porosity and bound water layer, coated on the grain solid which is associated to electrical double layer. The latter is adopted by them to develop an analytical response of bulk conductivity by using the effective medium and general mixing theory. The plot of bulk conductivity to water conductivity appears to be similar in line with the data obtained for clay gels, shales and shaly sandstone when they are saturated with freshwater to saline water.

CHAPTER 3

EXPERIMENTAL MATERIALS AND METHODS

3.1 Experimental Materials

3.1.1 Core Samples

In order to accommodate the various pore size and distribution, a number of reservoir rock samples having different porosity and permeability are selected. A larger structure is represented by carbonate and a smaller is siliciclastic type of rock. There are nine core samples used in this research, consisting of four carbonates with different pore types and five siliciclastic rocks. Those cores are cut and shaped into cylindrical with 1 inch in diameter. The four carbonate rocks are supplied from CSL (Comparative Sedimentology Laboratory), University of Miami Florida, USA, whereas one sandstone is Berea sand and the rest are sandstones from Malaysian oilfield. The whole core samples are cleaned to remove the remaining oil and salt. Typical properties of these cores and clay mineral are examined using X-ray diffraction (XRD) and the results are listed in Table 3.1 and Table 3.2 respectively.

3.1.2 Brine Sample

The effect of high brine water salinity is believed to reduce the double layer thickness, and therefore, it will lead to increase volumetric conductivity. There are four different classifications of brine sample according to its salinity [42]: fresh water (less than 0.5 ppt), brackish water (0.5-30 ppt), saline water (30-50 ppt) and brine water (more than 50 ppt). Soenarwi [43] reports the most of the formation water salinity at South Asia is about fresh to brackish water. However, in the Middle East and America, the water

salinity is more than 200 to 250 ppt. The synthetic brine established in this work is grouped in brine water category of 80 ppt or 80.000 ppm. The fluid conductivity and TDS are 100.3 mS/cm and 50.2 g/L respectively. Detail of brine composition is listed in Table 3.3.

3.2 Complex Resistivity Apparatus

The schematic diagram of complex resistivity measurement is given in Figure 3.1. The instrument is dedicated to allow both two electrode and four electrode resistivity measurements as a function of frequency, pressure, and temperature. The frequency range used is 0.01 Hz – 200 kHz.

The resistivity core-holder components consist of two silver electrical contacts embedded in the face of each end of cap (Figure 3.2). The end of caps is made of a non-conducting material such as alumina or plastic. One end of the cap is mounted with the pore pressure inlet port contained the contacts for the negative current ($I–$) and negative voltage ($V–$) electrodes. The other end of cap is electrically isolated from the apparatus and contains the contacts for the positive current ($I+$) and positive voltage ($V+$) electrodes.

3.3 Experimental Procedures

3.3.1 Sample Preparation

Sample preparation involves shaping, cutting and core cleaning. This is to make the sample fit with core the holder size.

3.3.1.1 Shaping and Cutting

As the transducer supports for the core samples with 1-inch in diameter, the cores need to be cut according to the core-holder size. After being dried, the samples are weighted. The dimension of core samples is listed in the Table 3.4.

Table 3.1 Core properties.

No	Sample ID	Porosity (%)	Permeability (mD)	Location	Description	Rock Type
1	368	29.15%	5091.025	Marion plateau - ODP Leg194	Dolomitized moldic skeletal packstone-grainstone	Carbonate
2	158	31.94%	648.556	Marion plateau - ODP Leg194	Dolomitized skeletal packstone-grainstone	Carbonate
3	BR-1	17.51%	178.857	USA	Berea clean sandtone	Siliciclastic
4	9056	12.54%	17.523	Maiella outcrop - Italy	Peloidal-sketeal grainstone	Carbonate
5	347	19.66%	2086.069	Marion plateau - ODP Leg194	Red algal/bivavle-skeletal grainstone-packstone	Carbonate
6	P03	21.57%	74.162	Malaysia	Shaly sandstone	Siliciclastic
7	P33	24.92%	467.597	Malaysia	Shaly sandstone	Siliciclastic
8	P45	25.40%	919.552	Malaysia	Shaly sandstone	Siliciclastic
9	P19	23.45%	254.347	Malaysia	Shaly sandstone	Siliciclastic

Table 3.2 Clay mineral of shaly sandstone rock from XRD result.

Sample ID	Clay mineral XRD result (%)		
	ILLITE	EXPD	CHLO
P03	33.9	37.3	28.8
P19	33.1	32.4	34.5
P45	39.8	24.9	35.3

Table 3.3 Synthetic brine compositions.

No	Description	Quantity (ppm)
1	Sodium Chlorite (NaCl)	79280
2	Calcium (Ca)	128
3	Magnesium (Mg)	80
4	Sulphate (SO4)	200
5	Silicon dioxide (SiO2)	200
6	Others	112
	Total	80000
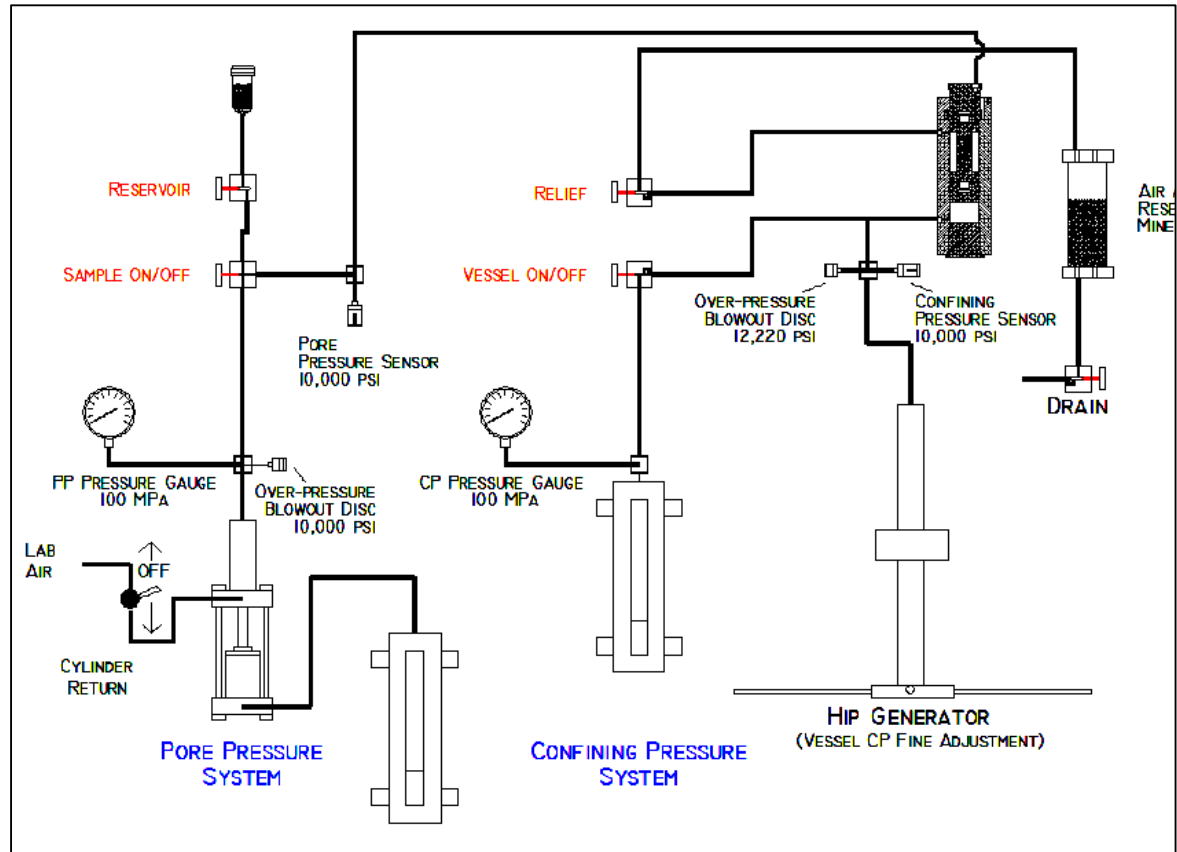
Figure 3.1 Complex resistivity measurement diagram [44].
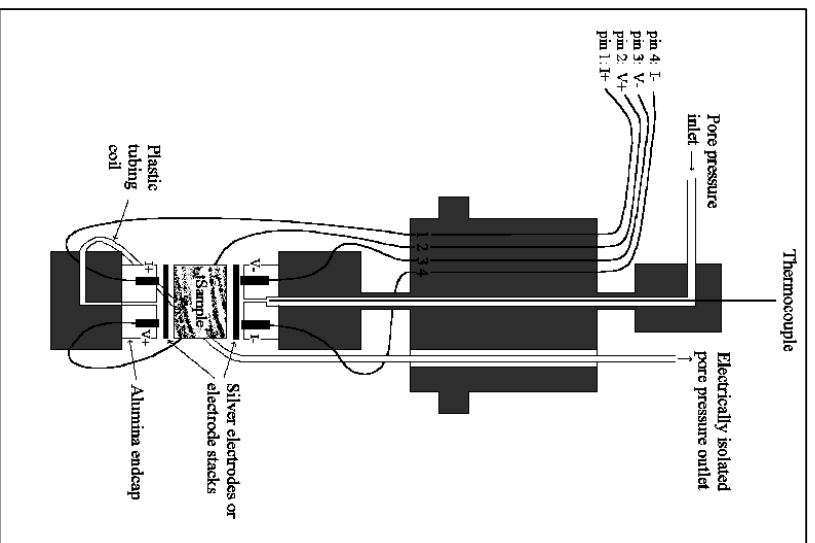
Figure 3.2 Diagram of resistivity core-holder [44].

Table 3.4 Core shaping.

No	Sample ID	Diameter (mm)	Length (mm)
1	368	24.52	20.46
2	158	25.34	25.59
3	BR-1	25.86	34.48
4	9056	24.91	25.89
5	347	25.34	22.55
6	P03	25.35	41.46
7	P33	25.42	38.08
8	P45	25.36	40.77
9	P19	25.38	38.33

3.3.1.2 Core Cleaning

Before testing of the carbonate and sandstone core plugs are carried out, they are cleaned with toluene to remove the oil content. The salt crystal within the rock also has to be removed since the resistivity response to the brine water saturation is very sensitive. The samples are soaked in deionized warm water and its conductivities are measured repetitively until reaching the root mean square (RMS) less than 2%. Table 3.5a-b, and Figure 3.2 show the results of the cleaning.

3.3.2 Measurement of Gas Porosity and Permeability

The cores are dried up first at 80° C for 24 hours and then wrapped with aluminum foil to maintain the moisture. The cores are then inserted into Poro-Perm instrument (Vinci Technology^{TM}) core-holder and confining pressure of 100 psig is applied. Helium gas is then flowed through the cores and the pressure difference between the inlet and the outlet is the main parameter to determine the porosity and permeability.

Table 3.5 Salt cleaning result of: (a). Sandstone (b). Carbonate volume of deionized water is 1600 mL and 1000 mL respectively.

(a)

No	Date	Time	Total Time (hrs)	Water temp (Celcius)	Conductivity (mikr.S/cm)				Remark
					I	II	III	Avg	
1	25/6/2008	12:30	0	25	23.2	23.5	23.8	23.5	Background
2	25/6/2008	14:00	1.5	29.3	598	592	591	593.667	
3	25/6/2008	15:30	3	33	896	892	890	892.667	
4	25/6/2008	16:45	4.5	33.5	1111	1105	1105	1107	
					Conductivity (mS/cm)				
5	26/6/2008	10:00	17	27	2.51	2.5	2.5	2.50333	
6	26/6/2008	12:00	19	28.5	2.65	2.63	2.63	2.63667	
7	26/6/2008	13:30	20.5	29.4	2.72	2.71	2.71	2.71333	
8	26/6/2008	15:00	22	30.5	2.81	2.8	2.79	2.8	
9	26/6/2008	16:30	23.5	31.1	2.88	2.87	2.86	2.87	
10					Conductivity (mS/cm)				
11									
12	27/6/2008	10:00	41	26.1	3.18	3.17	3.16	3.17	
13	27/6/2008	12:30	43.5	26.8	3.26	3.25	3.25	3.25333	
14	27/6/2008	14:30	45.5	29.4	3.29	3.29	3.28	3.28667	
					Conductivity (mS/cm)				
15	30/6/2008	13:00	116	28.1	3.64	3.63	3.62	3.63	
16	30/6/2008	14:30	117.5	28.3	3.67	3.67	3.66	3.66667	

Table 3.5 Salt cleaning result of: (a). Sandstone (b). Carbonate volume of deionized water is 1600 mL and 1000 mL respectively (cont'd).

(b)

No	Date	Time	Total Time (hrs)	Water temp (Celcius)	Conductivity (mikr.S/cm)				Remark
					I	II	III	Avg	
1	8/8/2008	12:00	0	25	27.9	27.9	27.9	27.9	Background
2	8/8/2008	13:00	1	94.4	146.4	148.5	149.1	148	
3	8/8/2008	14:30	2.5	50.7	203	203	201	202.333	
4	8/8/2008	16:00	4	78.3	256	256	253	255	
5	8/8/2008	17:00	5	82.2	295	295	293	294.333	
6	11/8/2008	10:30	70.5	70.5	369	364	365	366	
7	11/8/2008	12:30	72.5	73.8	379	379	376	378	
8	11/8/2008	14:30	74.5	72.5	384	380	378	380.667	
9	11/8/2008	16:30	76.5	74.5	393	391	390	391.333	
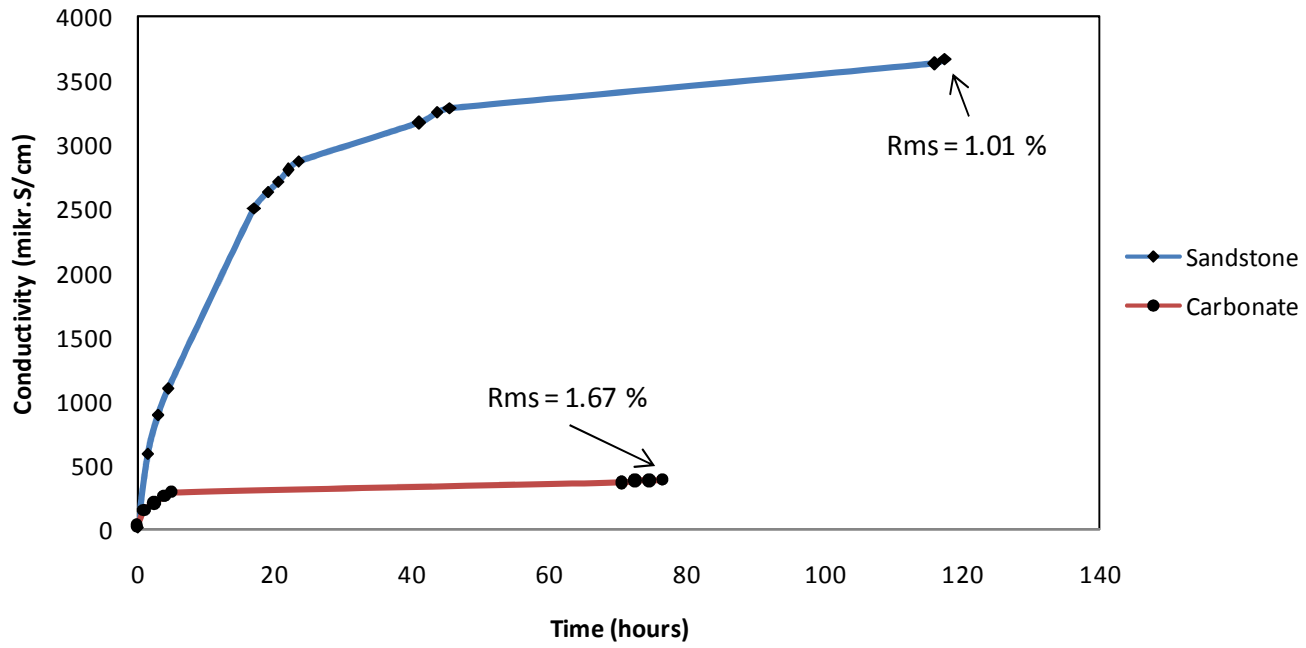
Figure 3.3 Salt cleaning.

3.3.3 Hysteresis test

Since the measurement pressure can go up to 3000-5000 psig, the samples need to be tested subjected to high pressure. Sonic wave is propagated through the sample whilst the confining pressure is increased and decreased. The P-wave and both Sv and Sh waves are recorded in order to determine the impact of the stress. The impact is then analyzed based on the sonic test that the whole samples are safe to be pressurized up to 3000 psig for the brittle samples (BR-1,368,158,347,9056) and for some hard samples are pressurized up to 5000 psig (P33,P19,P03,P45). Figure 3.4 and Figure 3.5 depict the example of velocity against pressure and their arrival time wave picking respectively. Complete result of this test is attached in Appendix A, hysteresis test result. From the hysteresis curve, it is indicated that the samples can sustain the confining pressure without damaging pore structure.

3.3.4 Establishment of Drainage-Imbibitions

Drainage and imbibitions are the process of water saturated and unsaturated during the experiment. The drainage-imbibitions series are determined by weighting the sample saturated brine water repetitively after soaking or heating respectively at a certain period of time. The core samples are wiped to ensure there is no water drop at each step of imbibitions. The degree of saturation is then calculated by

$$S_w = \frac{\theta}{\phi}$$

where θ and ϕ are volumetric water and porosity respectively. The volumetric water is defined as

$$\theta = \frac{\text{Weight in wet - Weight in dry}}{\text{Density of water X Volume of sample}}$$
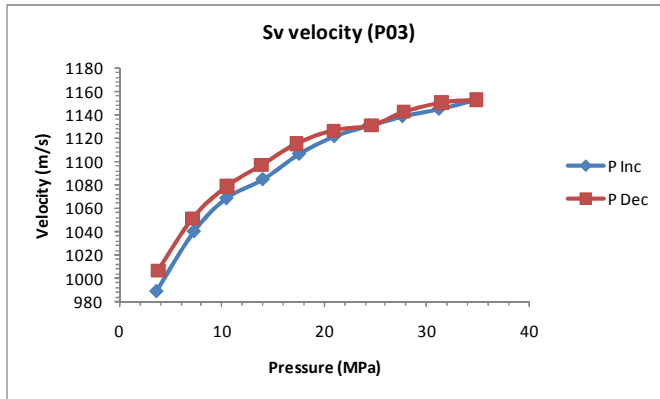
(a)
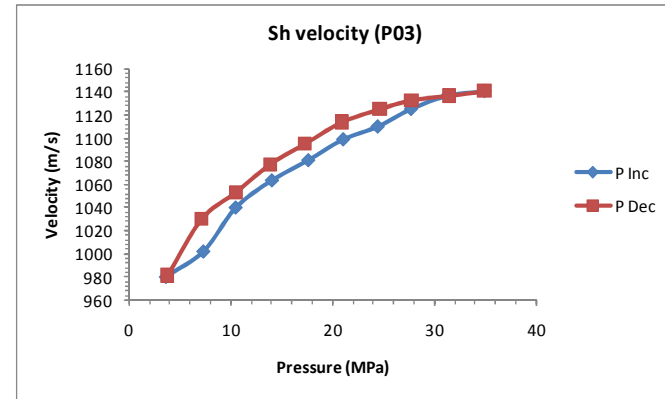
(b)
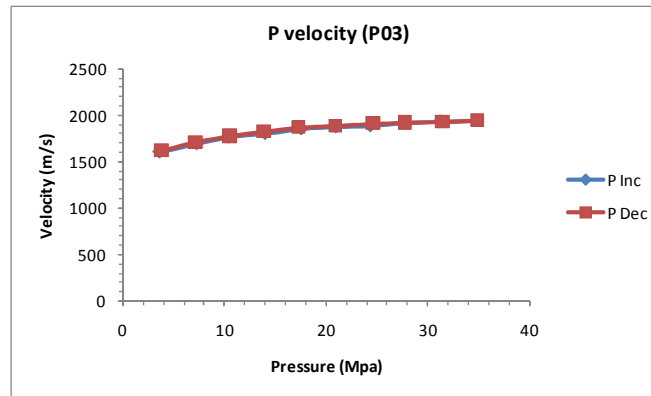
(c)

Figure 3.4 Wave velocity against pressure of sample P03 (sandstone): (a) Sv velocity (b) Sh velocity (c) P velocity.   .

37
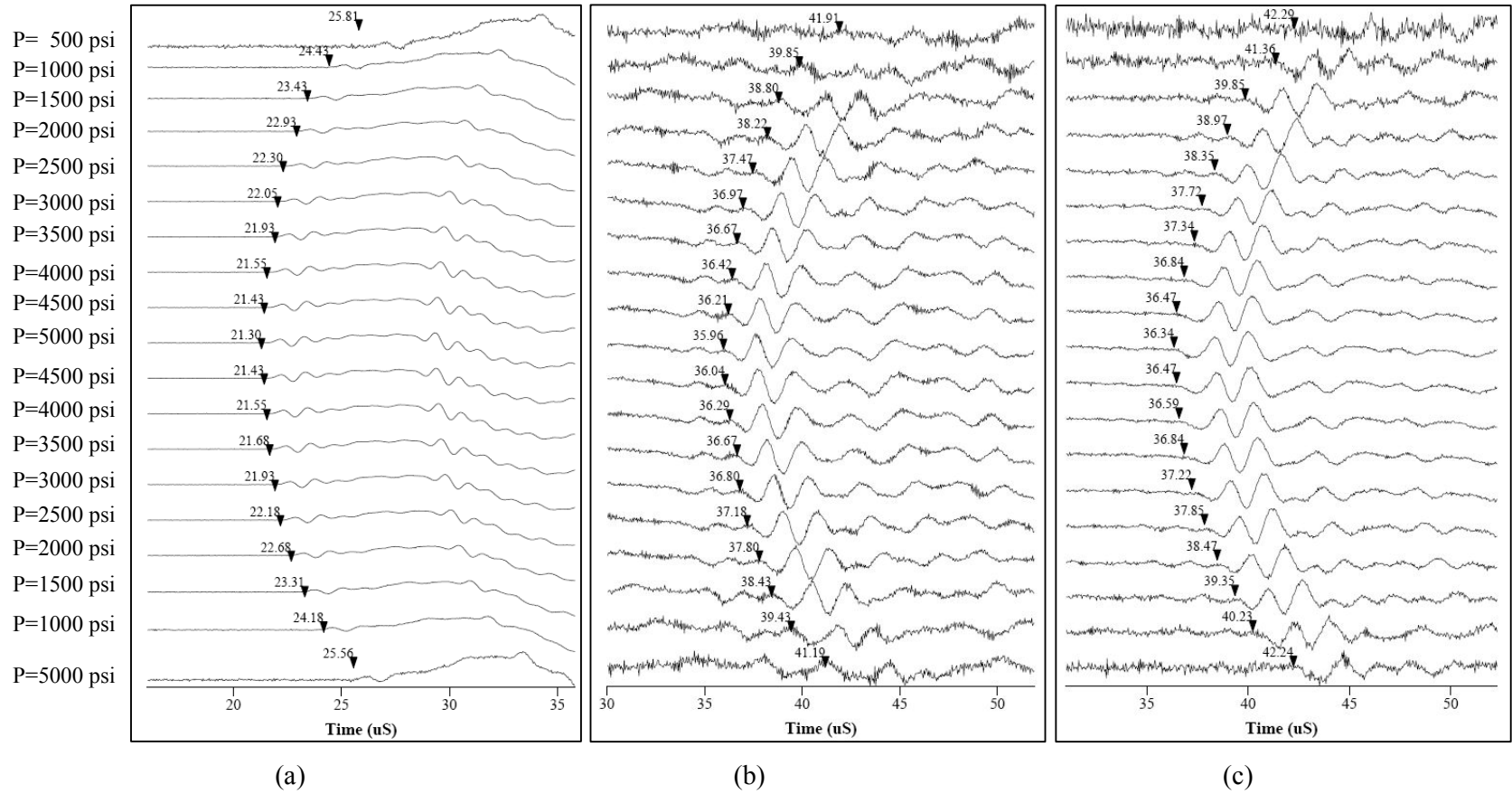
Figure 3.5 Full wave form onset picking of sample P03; (a) P, (b) Sh, (c) Sv wave.

3.3.5 Measurement of Complex Resistivity

Once the core samples are ready to be measured, they are jacketed with rubber slave and installed into the system (Figure 3.6).
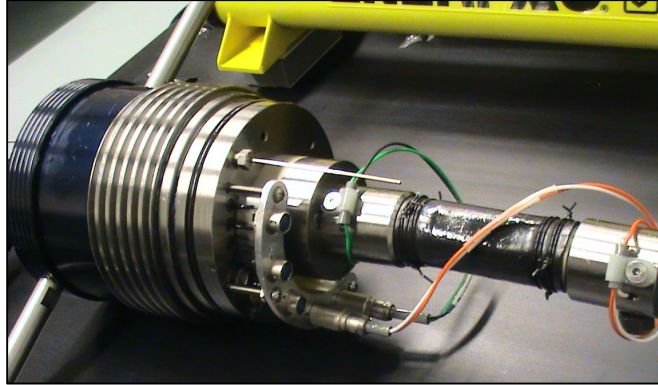
Figure 3.6 Sample is ready to measure.

Confining pressure is applied to the sample from 0 to 3000 psig and the measurement is made at every step of 1000 psig. The range of frequency is set from 0.01 Hz until 0.2 MHz. The samples are weighted before and after the measurement to make sure that there is no significant evaporation.

CHAPTER 4

PETROGRAPHIC IMAGE AND ELECTRICAL DISPERSION ANALYSIS

4.1 Introduction

The total porosity is measured by helium porosimeter or other techniques which traditionally characterizes the pore space of sedimentary rock. The pore space as well as pore geometries, pore shapes and its connectivity have a major impact on physical properties of the rock, such as fluid transport, electricity flow, wave propagation etc. Thus, there is a need to quantify the pore geometry aspect of the reservoir rock. This chapter describes petrographic image and scanning electron microscope analysis of the reservoir rock samples to quantify pores geometry and grain shape using polished thin sections.

The results of analysis includes of this chapter includes the parameters that quantitatively describe pore space and its shape, such as pore radius distribution, circularity, aspect ratio and gamma. This result acts as a basis to correlate electrical dispersion with geometry of the pore.

The method to quantify void or pore space from thin section images is known as petrographic image analysis. The image obtained from thin section is converted to binary in order to distinguish the pore space from solid matrix. Description of matrix includes identification of texture, mineralogy and diagenesis. Method of petrographic analyses starts from rock coring, cutting and grinding with the aim of preparing thin sections with the thickness of 0.03 mm. The samples are impregnated with blue dyed epoxy, and stained with alizarin red and potassium ferricyanide (Table 4.1). Then, the thin section is ready for petrographic analyses using Nikon polarization microscope. Other method to examine grain shape of the rock is by using scanning electron

microscope (SEM). This typical observation does not need thin section if ones prefer to observe three dimensional shapes of the pore and grain. Figure 4.1 presents an example of SEM. The complete pictures of SEM study are given in Appendix B, result of scanning electron microscope.

Table 4.1 Etching and staining characteristics of carbonate minerals.

Mineral	Effect of etching	Stain color with alizarin red S	Stain color with potassium ferricyanide	Combined result
Calcite (non-ferroan)	Considerable (relief reduced)	Pink to red-brown	None	Pink to red-brown
Calcite (ferroan)	Considerable (relief reduced)	Pink to red-brown	Pale to deep blue depending on iron content	Mauve to blue
Dolomite (non-ferroan)	Negligible (relief maintained)	None	None	Colorless
Dolomite (ferroan)	Negligible (relief maintained)	None	Vary pale blue	Vary pale blue (appears turquoise or greenish in thin section)

Historically, SEM is introduced to solve the limitation of TEM (transmission electron microscope). Unless the specimen is made very thin, electrons are strongly scattered within the specimen. This constraint has provided the incentive to develop electron microscopes that are capable of examining relatively thick specimens [45]. Recent development of combining both environmental scanning electron microscope (ESEM) and petrographic image analysis by microphotograph of thin section are initiated by Anselmetti et.al [46]. They provide a very promising result to calculate porosity of the sedimentary rock by joint calculation of micropores and macropores.
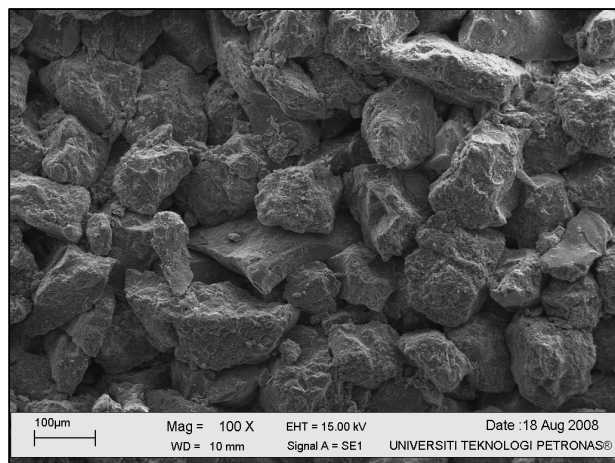
Figure 4.1 Scanning electron microscope for sandstone Sample P33. Porosity and permeability of the rock are 24.92% and 467.6 mD respectively.

To examine pore geometry, pore image analysis has to be handled carefully, particularly for the separation of the initial image into the pore space and solid fraction. This procedure, which belongs to the field of image segmentation, is a crucial step in defining the quality of further analysis. Optical images are usually converted into binary image with the help of an impregnation of the pore space with blue-dyed epoxy [47]. Since the minerals composition of the carbonate and siliciclastic are rarely blue, this impregnation provides a mean of separating rock minerals with pore space by simple color filtering.

Segmentation of pore size based on optical microscopy images has a limitation and is typically insufficient to recognize microporosity. To simplify the case, the borders of micropore and macropore are referred to Anselmetti et.al [46] that is 30 micrometer.

4.2 Image Analysis Workflow

The workflow to analyze pore image is based on Seleznev [23]   as shown in Figure 4.2. The process of image analysis starts from thin section preparation, which includes thin section polishing and impregnation with blue-dyed epoxy. Acquisition of image

is the second stage which can be divided into capturing the image and utilizing the cross-polarized light. The third step is the image classification which separates the pore space from the mineral matrix on the basis of color distinction and produces the binary image. The last step is the feature analysis that is carried out on the binary image to produce quantitative description of the grain and pore space of sedimentary rock.
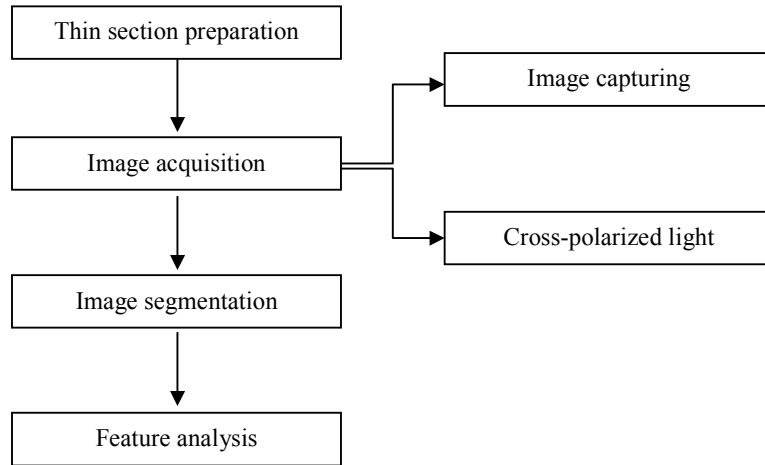
Figure 4.2 Image analysis workflow [23].

4.2.1 Thin Section Preparation

Cutting parts of core sample plug is used to produce the thin section. This material is considered as a representative of the rock without destroying the whole samples. The dimension of thin section is 3.81 cm in length and 2.54 cm in width. Polishing is performed to achieve 30 μm of thin section thickness before it could be utilized for further analysis. The optical microscopy is based on the principle of transmitting light through the thin section, so that the thin section thickness could effectively limit the size of the features that can be examined. Pores and grains having dimension smaller than that of the thin section thickness, are insufficient to be examined by optical microscope due to its interference with other features of thin section. Recognizing the

pore feature and the matrix is conducted by impregnating the thin section with blue-dyed epoxy under vacuum condition and finalized by color filtering.

4.2.2 Image Acquisition

Image capturing includes image acquisition of representative field of view (larger scale) and field of analysis (smaller scale). Larger scale is addressed to observe the main idea of distribution of pore geometry. On the other hand, the smaller scale is focused on pore features analyses. Small scale point of view is located based on the average distribution of pore size. The capture for the larger scale is 1000 μm, and for the smaller scale is 500 μm.

Perfect image is needed to execute further characterization of thin section. Optical distortion that usually persists on the image is resolved by manual focusing, and uniformly light intensity is established throughout the image area. The images are acquired both by plain-polarized light and cross-polarized light.

Separation of images by using one color only is sometimes insufficient. For example, the imperfection of crystal images that may have similar white color may be obtained if the air bubbles are not completely filled with blue-dye epoxy. Therefore, a different technique should be introduced to differentiate these parts.

The light is polarized with respect to the direction of propagation in petrographic microscope when the electric field vectors are restricted to a single plane by filtration. This yields colored micrograph image either in the plain polarized light or in cross-polarized light (XPL). The latter is the term to say that the light has passed to two perpendiculars direction. It strictly requires a careful handling of XPL because the polarizers oriented at 90° to each other do not allow any light to pass through. Otherwise, any mistake that happens in the course of this image acquisition process will completely blacken the image. Figure 4.3 is the example of plain polarized light and cross-polarized light respectively. The complete result of the microphotograph analysis, including texture, porosity type, mineralogy and diagenetic process, is attached in Appendix C, petrographic image analysis.
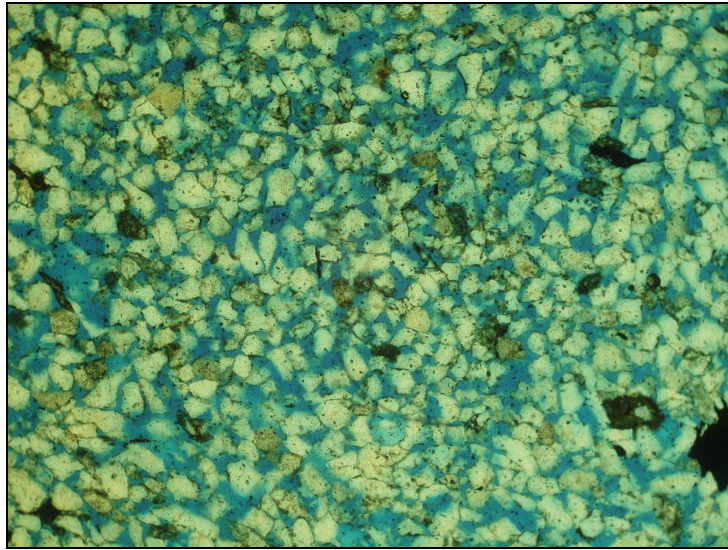
(a)
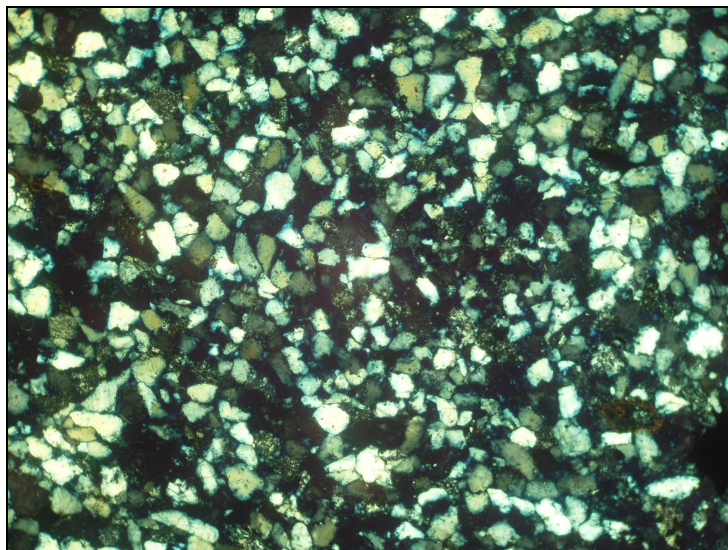
(b)

Figure 4.3 Thin section image of sandstone Sample P45, (a) plain polarized light and (b) cross-polarized light.

4.2.3 Image Segmentation

Image segmentation refers to the task to distinguish the pore space from its matrix on digital images. Traditional segmentation microphotograph is usually preceded by converting the thin image into binary image. This can be facilitated based on the color band in hue-saturation-value (HSV) color space. The technique to classify pore image based on color filtering is used in this step. The weakness of this method exhibits when the image of pore quality saturation is inconsistent or has many impurities such as bubbles or oil artifact. To cope with this particular weakness, it is proposed that the sequences of image processing have to be applied prior to recognizing pore image from the background (Figure 4.4). Image of the sample is firstly adjusted to correct the contrast and its color level. Range of blue color is then determined as a filtering criterion. Multiple pore selection with carefully adjusting pore-matrix boundary is the third step. Next, the pore layer is saturated with white color whereas the other layer is saturated with black. Merging these two layers and threshold are the two last steps of the image converting. Finally, filtering is applied to clean impurities and micro artifact.

4.2.4 Feature Analysis

Binary image, after threshold process, is determined with the help of standard image processing package (Image J version 1.41). In this step image filtering is carried out with the criteria of analyzed object exceeding 100 pixels. Total area, perimeter, gamma, aspect ratio, circularity and orientation of each pore are determined.

The pore radius using Wadell's definition [48] is calculated as follow:

$$r = \sqrt{\frac{A}{\pi}}$$

where A is area of particular pore. This definition has the assumption that pore shape is close to the circular. Since the optical microscope can only be resolved more than
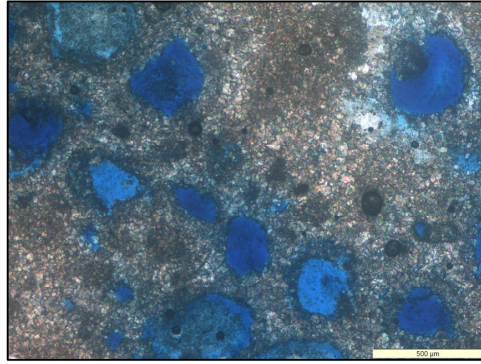
(a)
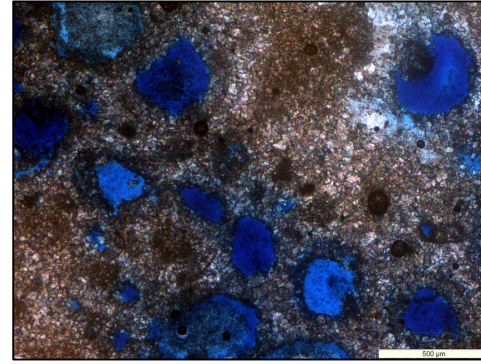
(b)
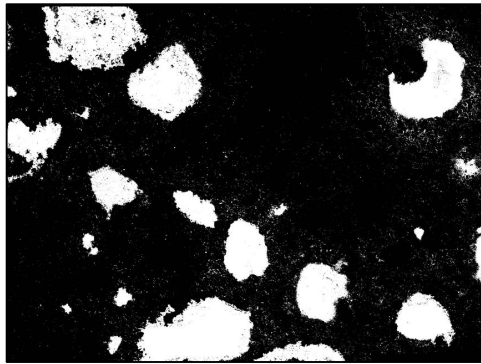
(c)
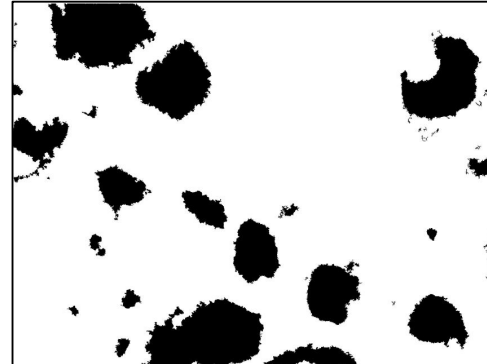
(d)

Figure 4.4 Image segmentation sequences of carbonate Sample 347 (a) original image (b) adjusted image (c) image after tresholding (d) final binary image.

thin section thickness, in this particular analysis the separation of micropore to macropore is assumed as 30 µm [46]. The distributions of the pores are served in histogram with certain bin range. Figure 4.5 exhibits the pore radius distribution in pixel unit prior to converting the micrometer scale.

Gamma parameter is defined as

$$\gamma = \frac{P}{2\sqrt{\pi A}}$$

where P and A are perimeter and area of the pore respectively. Gamma parameter describes how close the shape of the object approaches that of the circle. This parameter is 1 for a perfect circle and is significantly higher for elongated objects such as cracks and fractures.

Aspect ratio is defined as

$$AR = \frac{d_{max}}{d_{min}}$$

where d_{max} and d_{min} are major and minor axes of ellipsoid fitted around the object. These parameters also indicate some aspects of roundness. In contrast to gamma, they clearly distinguish elongated features from star-shaped features, but they produce ambiguities when distinguishing, for example, solid circles from stars.

Circularity is defined as

$$Circ = 4\pi \frac{A}{P} = \frac{1}{\gamma^2}$$

This parameter gives a value of 1.0 for perfect circle. If the value approaches 0, it indicates an increasingly elongated or highly complex region. Figure 4.6 gives the sample histogram results of the rock and Table 4.2 provides the summary of sample geometry. The complete result is available in Appendix D, histograms analysis.
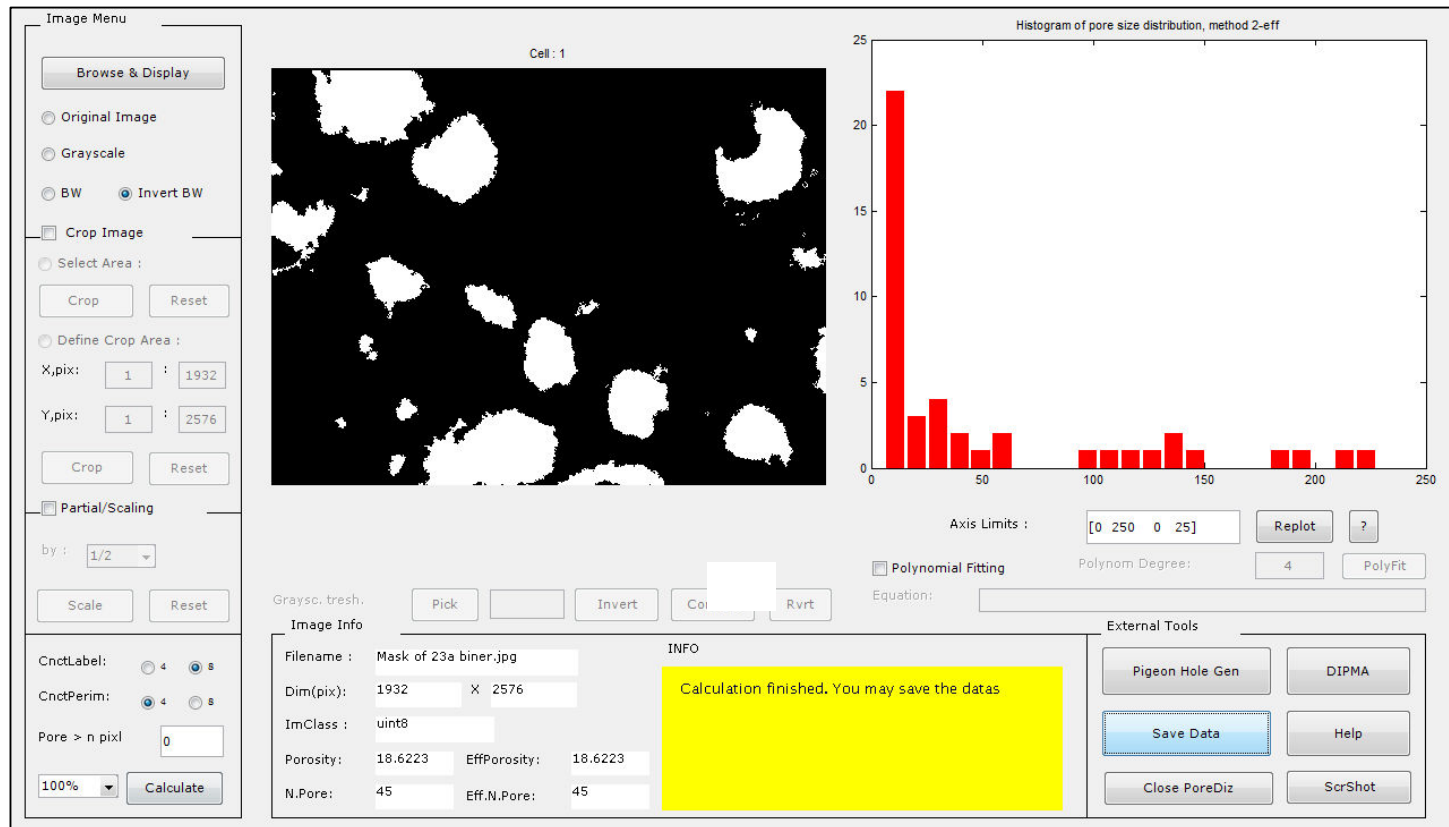
Figure 4.5 Pore radius distribution of carbonate Sample 347, white color is pore while black is matrix.
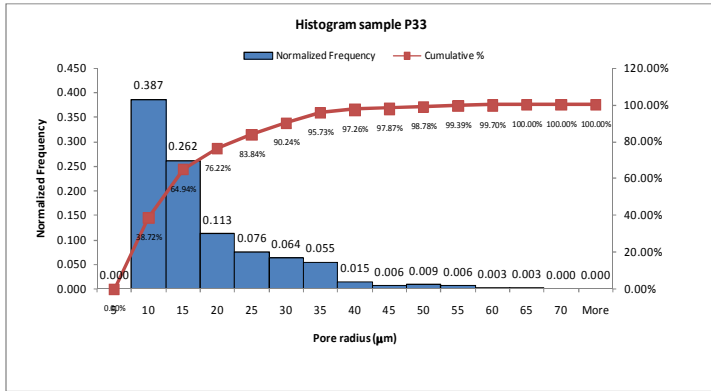
(a)
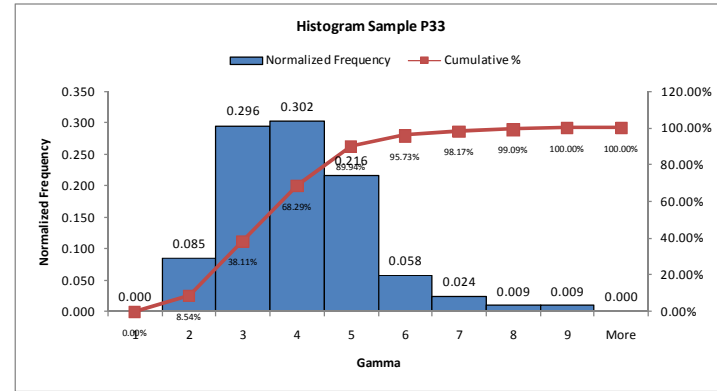
(b)
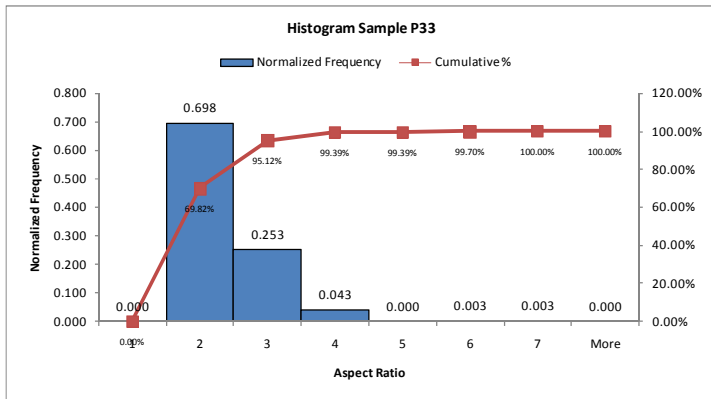
(c)
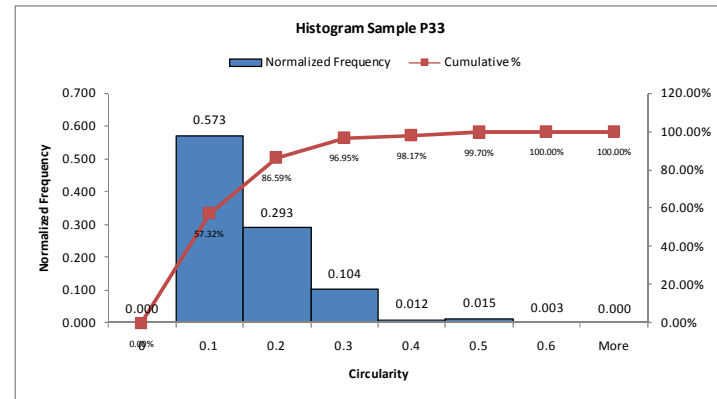
(d)

Figure 4.6 Pore geometry histogram of sample P33 (a) pore radius distribution (b) gamma (c) aspect ratio and (d) circularity.

Table 4.2 Feature analysis of the rock sample.

Sample	Core measurement		Image	Pore radius (µm)			Gamma			Aspect ratio			Circularity			Micropore	Macropore
	φ (%)	κ (mD)	φ (%)	mean	median	mode	mean	median	mode	mean	median	mode	mean	median	mode	(%)	(%)
P33	24.9	467.6	18	15.51	12.18	6.91	3.54	3.38	3.46	1.85	1.71	2	0.12	0.09	0.05	90.24	9.8
P19	23.45	254.35	20	18.92	9.44	4.79	2.86	2.69	3.59	2.64	2.27	2	0.16	0.14	0.07	78.2	21.8
P03	21.57	74.16	20	22.33	10.91	25.24	2.24	2.08	2.50	2.21	1.99	2	0.27	0.24	0.25	76.69	23.31
P45	25.4	919.55	24	26.78	17.27	6.33	3.09	3.01	2.24	2.04	1.82	2	0.14	0.11	0.10	71.92	28.08
BR-1	17.51	178.86	20	15.25	7.46	5.26	2.88	2.74	2.38	2.66	2.20	2	0.15	0.13	0.12	85.71	14.29
368	29.15	5091.03	25	48.11	33.04	#N/A	1.96	1.75	#N/A	2.12	1.87	#N/A	0.33	0.33	#N/A	43.2	56.8
158	31.94	648.56	30	40.15	23.25	#N/A	2.43	2.24	#N/A	2.08	1.85	#N/A	0.21	0.19	0.22	58.82	41.18
347	19.66	2086.07	20	41.69	13.02	5.60	2.84	2.79	#N/A	1.86	1.59	1.86	0.16	0.13	0.11	64.44	35.56
9056	12.54	17.52	25	9.16	7.10	4.82	2.52	2.25	#N/A	1.81	1.71	1.63	0.23	0.20	0.40	97.56	2.44

4.3   Rock Texture

Siliciclastic rock samples (P03, P19, P33, P45 and BR-1) are grouped in sublitharenite to litharenite and compose of grain around 60%. Grains consist of monocrystalline quartz, polycrystalline quartz, lithic fragment, feldspar and mica. Grain size is ranging from silt to fine sand grain except BR-1, medium to coarse grain. In term of grain shape, Sample P33 has angular-subrounded shape, Sample BR-1 subrounded to rounded shape and the others are categorized as subangular-subrounded. Pore radius distribution of Sample P33 is dominantly group as micropore, with the amount of macropore is less than 10%; however in other samples, the amount of macropore could be more (see Table 4.2). Rock grains are cemented clay. Sample P33 contains 10% of clay fraction, but the rest of the samples have less than 5%. Cement of the grain consists of quartz, calcite and iron oxide around 15%. Most of siliciclastic sample grains are well-sorted, point, long and having sutured contacts (the possibilities of diagenesis exist due to the presence of point, long, concavo-convex and sutured contacts). In addition, the possibilities might be caused by mica bending; cementation of quartz, calcite and clay minerals; recrystallization of quartz cement forming secondary overgrowth; dissolution of grains, matrix and cement; and secondary porosity due to dissolution.

Most carbonate rock samples studied have a larger pore size than that of siliciclastic except for Sample 9056. All samples classified as packstone shows a predominantly large structure which is either vug, fracture and intercyrstal (368, 158, 9056) or moldic (347). Carbonate grain consists of red algae, mollusks, larger foraminifera (368, 158, 9056) and ooids (347) (the whole matrix consists of micrite while cement consists of calcite). The possibilities of diagenesis are microbial micritization, dissolution forming vug porosity, dolomitization and forming intercrystal porosity, cementation of calcite and dolomite and compaction forming point, long and sutured contacts. The description of microphotograph can be referred to Appendix C, petrographic image analysis.

4.4 Resistivity Reading

As noted by Schon [4], electrical properties of the rock and mineral depend on the conduction process involved. They are:

a. Metallic conduction such as native metal e.g. gold, copper and graphite

b. Electronic semiconduction such as mineral like ilmenite, magnetite, pyrite and galena.

c. Electrolytic conduction such as solid electrolytes (ionic crystal) and electrolyte water solutions.

Most of rock-forming minerals, such as silicates and carbonate, have a very high resistivity, more than 10^9 Ohm.m and are classified as insulator. Electrical properties of the rock without water content are mainly controlled by matrix properties. This outcomes in three significant observations:

1. Obviously high value resistivity.

2. Increasing temperature leads to exponentially decreasing of resistivity.

3. Increasing pressure will decrease of resistivity non-linearly.

Once the rock sample is saturated by water fluid, the electrical conductivity is mainly controlled by properties of water. The conductivity of its matrix in this case is negligible, however if disseminated ores or graphite are present, they contribute dominantly to the value. The contributions of pore water to the rock conductivity might happen in two ways, either by their intrinsic electrolytic conductivity or by electrochemical interaction at the interface of fluid-solid matrix. In the previous case, rock conductivity is proportional to electrolyte conductivity. But in the latter, geometry of conductive path is controlling internal surface conductivity. For this condition, the interfacing conductivity can be considered to be independent of the electrolytic conductivity. The existence of interface conductivity is firstly detected in shaly sandstone. In clean sandstone, the conductivity is also detected in low water saturation in which the electrical double layer plays dominantly. To study this, the modification of Archie's formula should incorporate conductor and capacitor behavior simultaneously. More detailed discussion of this matter is presented in Chapter 6.

4.5 Result of Resistivity Reading and Pore Geometry

Previously, it is presented that the electrical properties dependencies on textures and minerals are very small when water fluid is introduced to the rock sample. The presence of water fluid behaves as electrical transport because ions can move easier in this medium compared to their propagation throughout the rock matrix and minerals. Although the water fluid is a dominant factor, its distributions and rock transport properties must be considered. Thus, pore geometry, shape, distribution and orientation of the pore are the basis to evaluate electrical properties of the rock. In this case, we deal with resistivity dispersion.

Some features analysis of the rock image will be carried out to search for the geometry effect on resistivity dispersion. These features include pore radius distribution, gamma, pore aspect ratio, circularity of the pore and pore orientation. Each feature is averaged by weighing its individual parameter by the pore size:

$$\bar{x} = \frac{\sum_i (A_i x_i)}{\sum_i x_i}$$

Table 4.3 describes average features, resistivity dispersion and their transport properties. Resistivity dispersion is defined as the difference between resistivity at characteristic frequency (*fc*) and at 200 KHz. Characteristic frequency is a frequency border between the electrode polarization with the sample reading.

It appears that parameter of gamma, circularity, pore aspect ratio and pore orientation do not have a good correlation with resistivity dispersion (Figures 4.7). On the other side, crossplot of resistivity dispersion with pore radius distribution shows a good correlation in positive gradient trendline (Figure 4.8a). It indicates that electrical dispersion is not influenced by the pore shape except the pore size and the electrical polarization occurs at the interface or the boundary between grain and pore fluid. The bigger pore radius causes higher resistivity dispersion. The similar result is shown by Abousrafa et.al [29] who observe the resistivity and formation factor only affected by pore throat radius. The two outliers point (red diamond) occurs due to high initial saturation level in carbonate cores sample of number 347 and 368. Thus,

54

the fluid saturation prefers to fill in large structure rather than small structure because of the difference of their water surface tension and capillary properties. The relationship of saturation level with resistivity dispersion gives an exponential relationship (Figure 4.8b). The higher the water saturation, the lower the resistivity dispersion will be.

Since the electrical dispersion has a good correlation to the pore radius distribution, we can expect the same result in porosity. Figure 4.9a shows a good dependency of porosity on the electrical resistivity dispersion occurring at low water saturation. The three point outlier corresponds to the small pore radius (Sample P33) and to relatively high initial water saturation (Sample 347 and 368). On the other hand, intrinsic electrolyte conductivity does not have a good correlation to electrical resistivity dispersion as can be evaluated on permeability-resistivity dispersion in Figure 4.9b. With these results, it becomes the basis to explore more intensively in exploring the relationship of pore radius with resistivity dispersion as presented in the following chapter.

Table 4.3 Average features of the samples and dispersion parameter.

Sample	Porosity (%)	Perm (mD)	Sw (%)	Avg. rad (mikr.m)	Avg. gamma	Avg. AR	Avg. Cir	Avg. Ang (Deg)	fc (Hz)	ρfc (ohm.m)	ρ200 (ohm.m)	δρ (ρfc-ρ200 KHz)
P03	21.57	74.162	12	101.8	3.54	1.91	0.117	103.89	0.853	1292.55	20.29	1272.26
P19	23.45	254.347	12	76.21	4.09	2.21	0.096	94.95	20.4	951.28	25.08	926.2
P33	24.92	467.597	14	28.95	4.18	1.87	0.088	78	100	32.93	25.68	7.25
P45	25.4	919.552	7	96.47	4.24	1.95	0.079	82.68	4.17	1147	21.02	1125.98
BR	17.51	178.857	10	53.09	3.7	2.18	0.096	86.27	626	294.8	46.11	248.69
158	31.94	648.55	7	144.86	3.49	2.017	0.094	95.83	7.88	1674	35.87	1638.13
347	19.66	2086.069	21	141.1	2.76	1.664	0.141	50.99	100	72.5	48.15	24.35
368	29.15	5091.025	17	165.97	2.49	2.26	0.193	122.2	72.8	52.12	38.77	13.35
9056	12.54	17.523	13	20.77	2.74	2.07	0.177	75.23	130	239.4	60.51	178.89
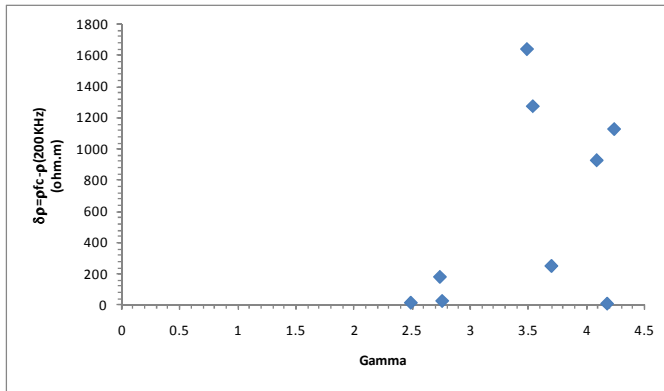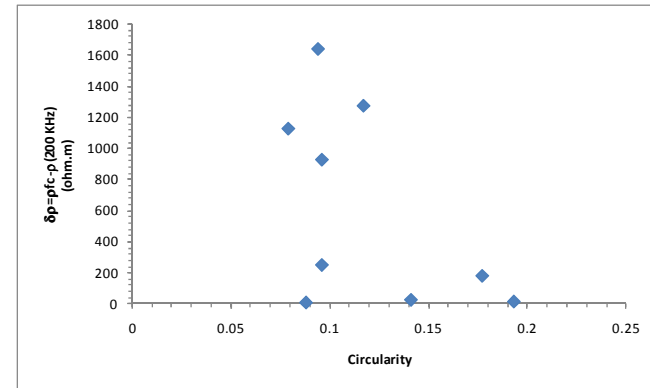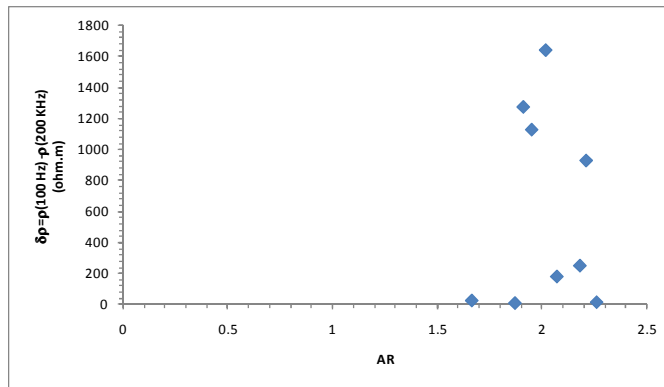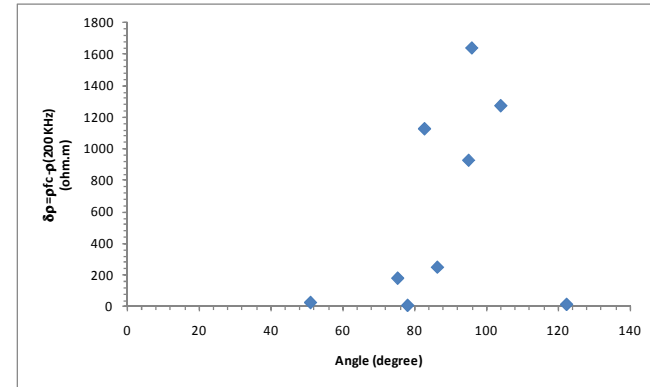
Figure 4.7 Interrelationship of resistivity dispersion with pore geometry properties: (a) gamma (b) circularity (c) aspect ratio (d) pore orientation.
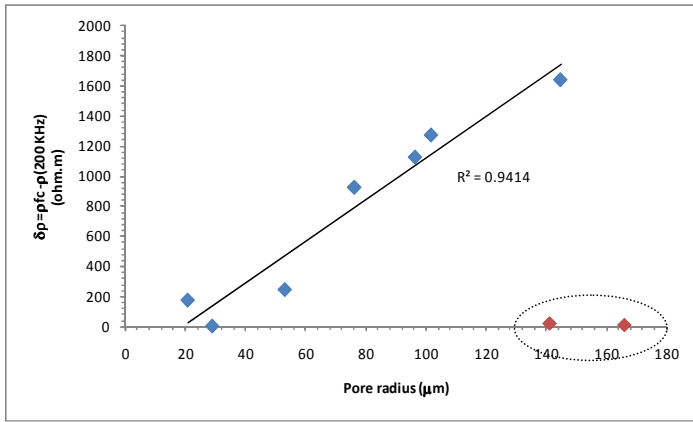
(a)
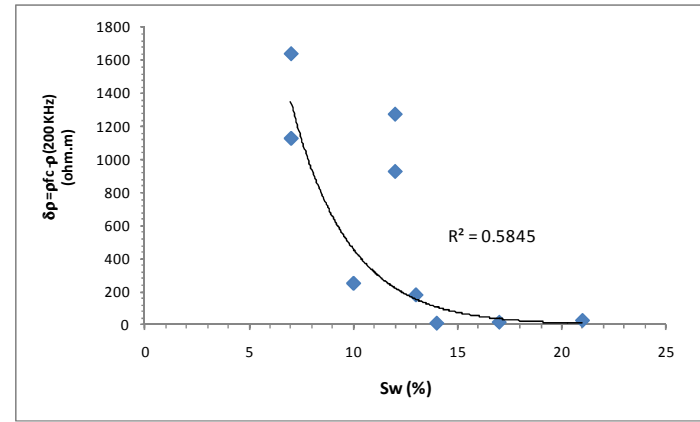
(b)

Figure 4.8 Resistivity dispersion correlations with (a) pore radius and (b) water saturation.
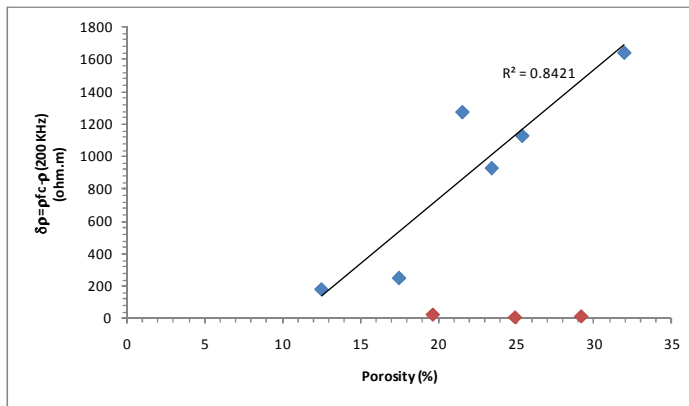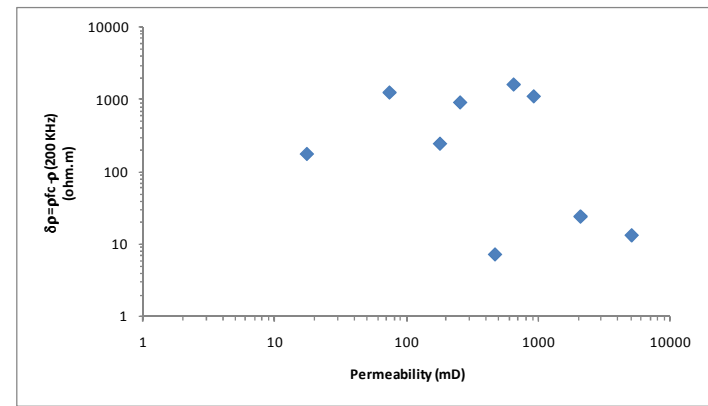
Figure 4.9 Resistivity dispersion relationship on (a) porosity and (b) permeability. Samples are siliclastic and carbonate.

4.6   Summary

Features analyses have been extracted from microphotograph of sedimentary cores samples. They are pore radius distribution, gamma, pore aspect ratio, circularity and pore orientation. In among those samples, 90% of total pore space in sample P33 (sandstone) and 9056 (carbonate) are dominated by micropore size (<30 μm). On the other hand, the rest samples have significantly bigger macropore size, at least twice as big as the thin-slice thickness, although in a small amount.

The presence of water fluid throughout the media insists that the electrical current flows through the water rather than through the solid matrix. Electrical double layer contributes to total rock conductivity from interface of solid-fluid. In this case, solid understanding of electrolytic or volumetric conductivity and surface conductivity should be taken into account. At initial level of water saturation, the surface conductivity contributes more than volumetric. The contribution of surface conductivity can be evaluated by looking at the resistivity dispersion. The dispersion of resistivity depends on the pore size distribution and the water saturation. This is proved by evaluating the dependency of resistivity dispersion on pore radius distribution, porosity and water saturation. Potential application of saturation prediction may come from resistivity dispersion interrelationship, but it should be supported by numerous data.

CHAPTER 5

PORE RADIUS, PRESSURE AND SATURATION EFFECT ON RESISTIVITY

5.1 Introduction

Evaluation of resistivity property in the media needs proper information on several factors. While investigating dynamic of the pore fluid, one has to consider imbibitions and drainage impact on the resistivity. Recovery monitoring for example, requires enough data on the real subsurface condition. In this case, pressure, saturation, and distribution of the pore fluid as well as percolation factor play as the rule of the game. Some deep investigations on the mechanisms that influence or change along with recovery are a key factor to assist the potential application of resistivity for time-lapse reservoir monitoring. Obviously, if the certain reservoir properties changes are relatively large enough when water is injected or produced, the resistivity may be applied to see the fluid distribution. Garrouch and Sharma [39] investigate the electrical properties response to pressure, wettability and clay content on fully brine saturated core samples. They note that for full water saturation the pressure has an insignificant effect on resistivity. On the other hand, brine saturation confidently has a significant effect on the electrical properties of rock [49].

However, the complexities of pore geometry and pore throat as well as inhomogeneous distribution of microporosity may cause non-uniformly oil displacement throughout the rock. Thus, the distributions of fluid before and after it is produced are quite different. In solving pore geometry, careful assessment should be accomplished to see the micropore and macropore effect on resistivity and on water saturation distribution. Cerepi [50] find that micro-structure of the porous system and rock textures have a strong correlation to the transport properties, such as electrical conductivity and permeability. In his study, saturation exponent n depends strongly on

frequency and rock textures. The large pores has high saturation exponent while small pores has low saturation exponent due to surface roughness and their water-wetting. Another result from Ray and Jongmans [28] concludes that particle shape and orientation give contribution to the resistivity regardless its water saturation. Aligned elongated particle and the shape could alter the cementation factor of *m*. However, the detail description of pore geometry, such as pore radius distribution to the resistivity dispersion, is currently unavailable.

This chapter presents the measurement workflow, data editing and experimental result for two types of sedimentary rock, i.e. sandstone and carbonate rock. The discussion on the resistivity is divided into two criteria, firstly to evaluate the effect of pore radius distribution and secondly to observe the effect of pressure and saturation.

5.2 Measurement Workflow

5.2.1 Sample Preparation

The core samples are cut and shaped in accordance with the core-holder size. Saturated-unsaturated (drainage-imbibitions) water fluid is determined by reweighting the sample once the samples immersed and dried up in a certain time. After proper drying and the partial water saturated justification, the samples are installed in the instrument. Prior to installing in the instrument, the samples are jacketed by flexible rubber to avoid mixing of external fluid pressure (simulating overburden) with internal fluid pressure (simulating pore pressure). To measure resistivity, electrode must be carefully aligned on either end of the sample. The voltage electrode touches the insulating pad and the current contacts on the samples. Standard electrode materials consist of porous silver membrane filters manufactured by Osmonics Inc. The measurement of resistivity can be established by means of two or four electrodes configuration.

5.2.2 Measurement Procedures

Methods of resistivity measurement are determined by understanding the core sample characteristics. For highly resistive samples, it is recommended to apply two electrodes while four electrodes are more suitable for less resistive samples. Most of sandstones in this work utilize two electrodes mode and the rest used four electrodes. For two electrodes resistivity measurements, a single electrode (silver filter) is placed between each end of cap and the sample (Figure 5.1). Each electrode has to make contact with both silver contacts on the face of the respective end of cap. The acrylic disk is placed between the end of cap and the electrode stack, with the grooves facing the sample. The disk is required to be oriented properly to allow the silver electrical contacts to touch the silver electrode membranes. The grooves distribute the pore fluid over the face of the sample uniformly. To modify it to become four electrodes, the insulating pad is placed on the voltage to recess the voltage contacts at each end of cap and to mechanically isolate those contacts from the current electrode. This allows the voltage measurement to be made without significant contamination from the electrochemical reactions that are influencing the current electrode. In this work, a polyester felt is used as non-conducting pad.
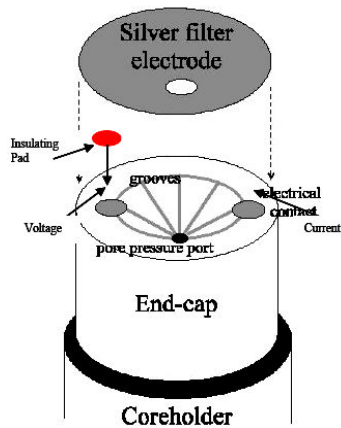
Figure 5.1 Two or four electrodes configuration. Four electrodes was made by attached polyester insulating pad [44].

Resistivity observation is evaluated when overburden pressure increased from 0 to 3000 psig with the interval of every 1000 psig. The frequency is set from 0.01 Hz –

200 KHz in logarithmic sweep. The recording run automatically with 59 points stored for each execution. This mechanism is performed repeatedly until full water brine saturation is achieved. The same process is employed for drainage system. To make sure the evaporation is insignificant, the samples are weighted before and after measurement.

5.2.3 Data Acquisition and Editing

Input files for the system are core length, diameter, density and pore fluid conductivity. The measurement of electrical property of rock in this work is made in a serial mode. The complex impedance Z* is

$$Z^* = R_s - iX_s$$

where R_s is the series resistance and X_s is the reactance. The complex resistivity can be calculated as

$$\rho^* = Z^* \frac{A}{t}$$

where A and t are cross-sectional area and thickness respectively. The complex dielectric permittivity is then formulated

$$\kappa^* = \frac{1}{i\varepsilon_o \omega \rho^*}$$

where ω is angular frequency and ε_o is the vacuum permittivity (8.85 x 10^{-12} F/m).

Quality of the data measurement is adjusted by balancing the Z-meter interface box with the reference resistor. Measurement quality is enhanced by selecting the reference resistor that most closely match the effective (low frequency) resistance of the sample. This effectively balances the voltages measured by the two amplifiers. In addition, correcting for parasitic impedances at high frequencies requires the reference resistor to be equal to or larger than the effective resistance of the sample. The effective resistance of the sample could be estimated by noting the current setting

of the reference resistor switch and comparing the amplitudes of the signals measured on the oscilloscope. Non-linearity due to the presence of strong brine at low frequencies is balanced by reducing sinusoidal signal amplitude.

An electrode polarization that may occur in low frequency is identified by plotting complex resistivity in Argand plot. The semicircle data represent as a response of the sample and the resistivity data below characteristic frequency represent as electrode polarizations [2].

5.3 Result and Discussion

5.3.1 Pore Radius Distribution Effect on Resistivity Reading

The polarizability of the inclusion is a function of the electromagnetic properties of its material as well as the inclusion of geometry. This is taken into account by depolarization factor that explains how the inclusion polarization is diminished in accordance with the particle's shapes. In term of pore space, the polarization occurs on the boundary of the pore wall. This polarization is effectively characterized by its pore radius and water saturation.

Figure 5.2 displays the series scenario of water imbibitions and drainage. The process of water saturation and evaporation can be explained as follow. As the brine water introduces into medium, it begins to make thin layer on the pore wall (Figure 5.2a). This process continues until the water covers the pore wall and makes thick layer (Figure 5.2b-c). Most of the pore throats are now covered by water with the air bubbles trapping inside (Figure 5.2d). Vacuum process is used to suck the air bubbles until the pores completely saturated (Figure 5.2e). Removing the brine water is initiated from the center of pore space whereas it is the weakness part of water molecule bonding (Figure 5.2f). The desaturation continues until both sides of pore walls are separated (Figure 5.2g). The thick water layers now become thinner (Figure 5.2h-i). At the end of drying, the thin layer is slowly discontinuous and makes water-salt film coats the pore wall (Figure 5.2j).

Referring to the previous process it can be concluded that the rate of saturation and desaturation depends on its pore size distribution. The larger the pores radius, the longer the time is needed to saturate. When both sides of pore walls are completely covered by fluid, the volumetric conductivity effect will be more dominant than the surface conductivity (Figure 5.3). Details of water saturation and pressure effects on electrical properties and some aspects on the theoretical electric double layer will be explained in the following chapters.

(a)　　　(b)　　　(c)　　　(d)　　　(e)

(f)　　　(g)　　　(h)　　　(i)　　　(j)
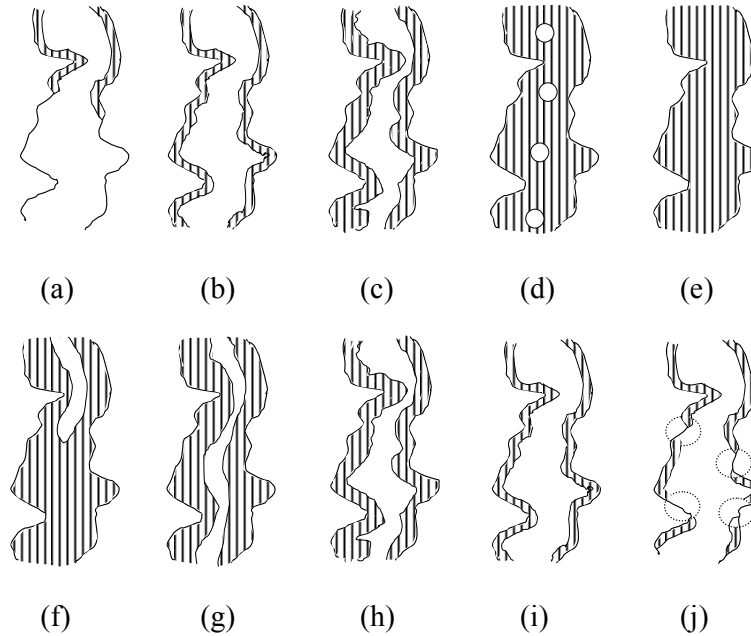
Figure 5.2 Series scenario of water imbibitions (a-e) and drainage (f-j).

Because of the dispersion and the surface conductivity have similar analogy to the capacitor, the smaller the pores radius, the easier the dispersion vanishes. Large structure of pore geometry tends to have more dispersion as well as thin pore-water surface and needs more time to fill the whole pore space. On the other way around, a small structure gives less contribution to the electrical dispersion due to the simple saturation process.
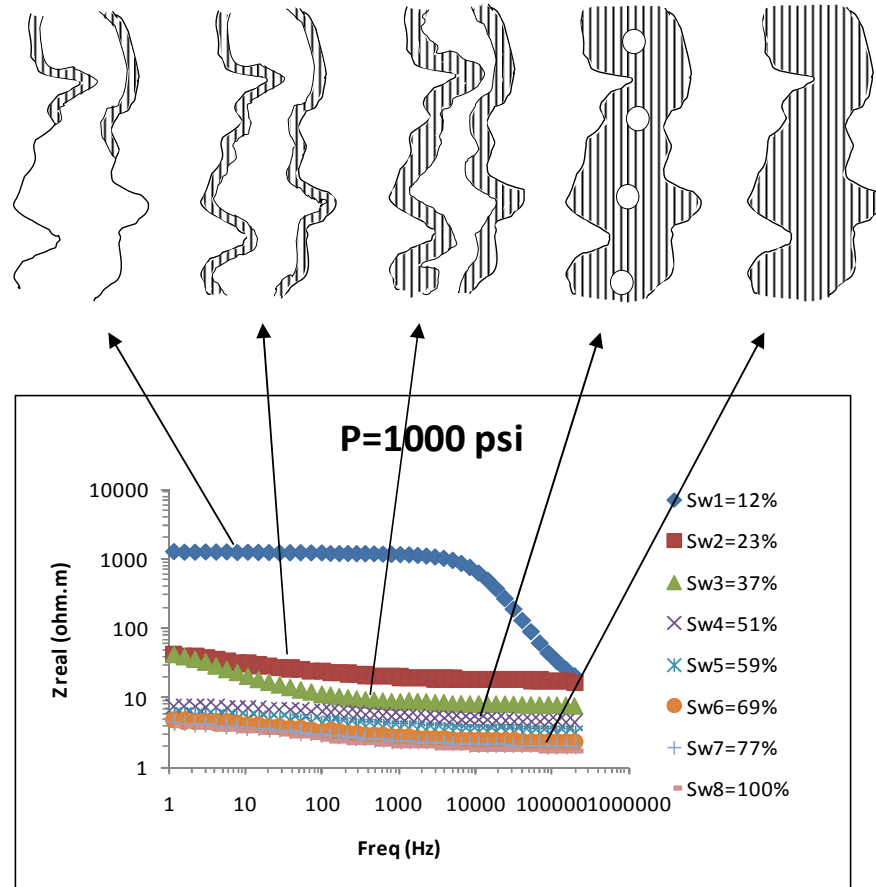
Figure 5.3 Illustration of electrical dispersion curve of different pore wall condition.

The boundary of micropore and macropore is 30 μm which is equal to the thickness of thin section. The pore radius analysis, extracted from microphotograph of thin section, converts the pore space area from pixel into micrometer. The pore radius definition in this work follows the Wadell's [48].

Figure 5.4 presents the pore radius distribution effect on electrical dispersion for sandstone samples. At the time water saturation achieves less than 15%, the dispersion on small pores of Sample P33 will vanish. The pore radius size of Sample P33 is mostly less than 30 μm, whereas small portion of macropore with maximum pore radius is around 65 μm, that does not seem to give significant contribution to the dispersion unless the saturation could be reduced to less than 10%. Although the macropore has a size bigger than 70 μm or approximately twice bigger than micropore very little, it contributes very significant dispersion. This can be observed in Sample P19, P03 and P45. Furthermore, small pore radii may block the anion because the double layers touch each other, while the ion motion is undisturbed for the larger pore radii.   The presence of clay minerals throughout the rock partially blocks ionic solution. Negative charges on clay minerals tend to capture the electrolyte cations and the anion move to the other way. Under the influence of electric field, the cations easily pass the cationic cloud and resulting in the accumulation of ionic charges.

Evaluation on carbonate rock reveals similar trend of resistivity dispersion (Figure 5.5). When the water saturation achieves 13%, the dispersion of Sample 9056 starts to vanish, whereas for other samples it starts moving out when the water saturation reach more than 17%. The small pores on Sample 9056 have one order higher resistivity than the rest. This may occur due to the electrical path is difficult to pass through the medium. The connectivity of the pore-space on Sample 9056 is very low; this is to confirm its low permeability.

(a)
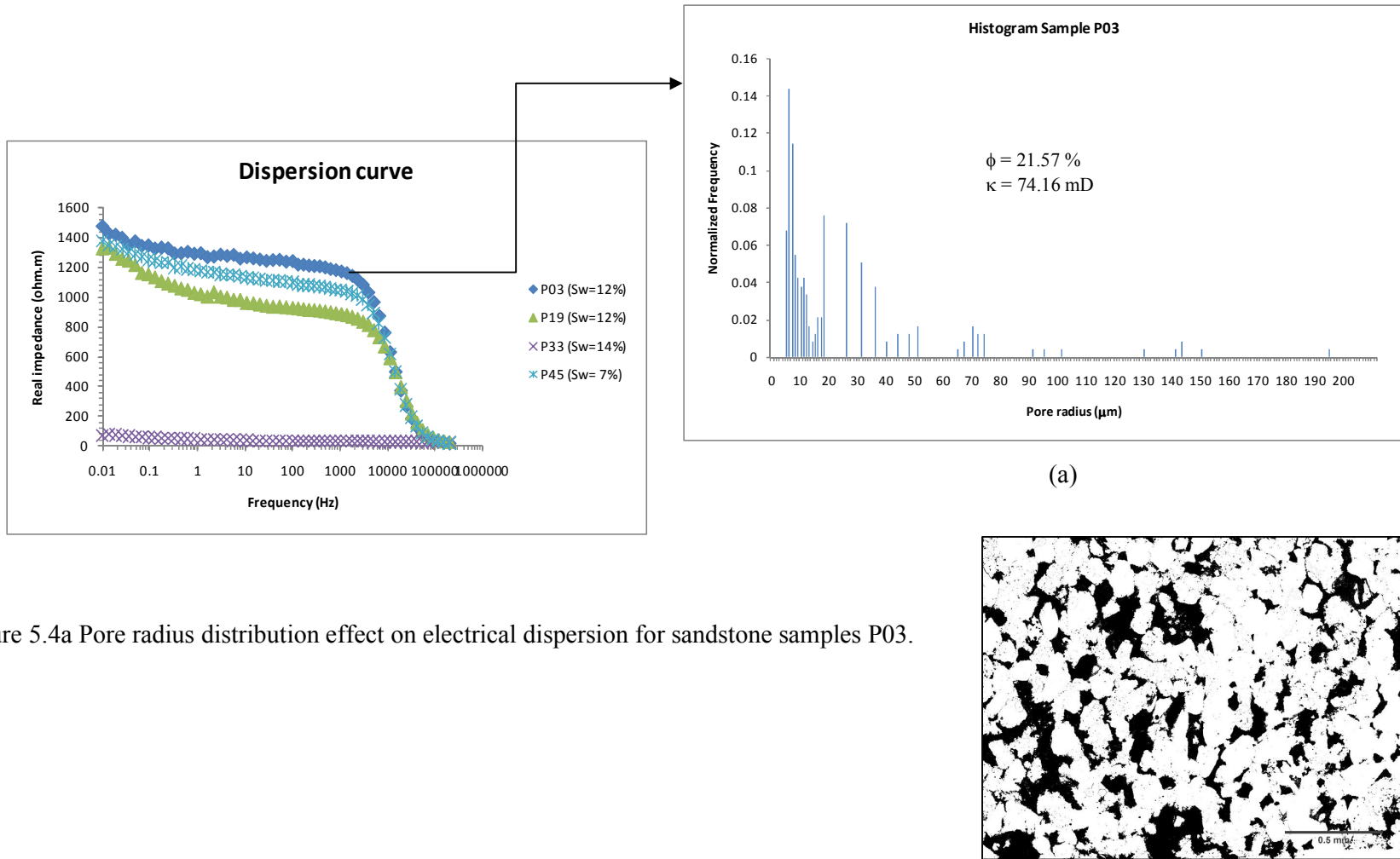
Figure 5.4a Pore radius distribution effect on electrical dispersion for sandstone samples P03.

Dispersion curve

P03 (Sw=12%)
P19 (Sw=12%)
P33 (Sw=14%)
P45 (Sw= 7%)

Histogram Sample P19

$\phi = 23.45\%$
$\kappa = 254.347$ mD

(b)
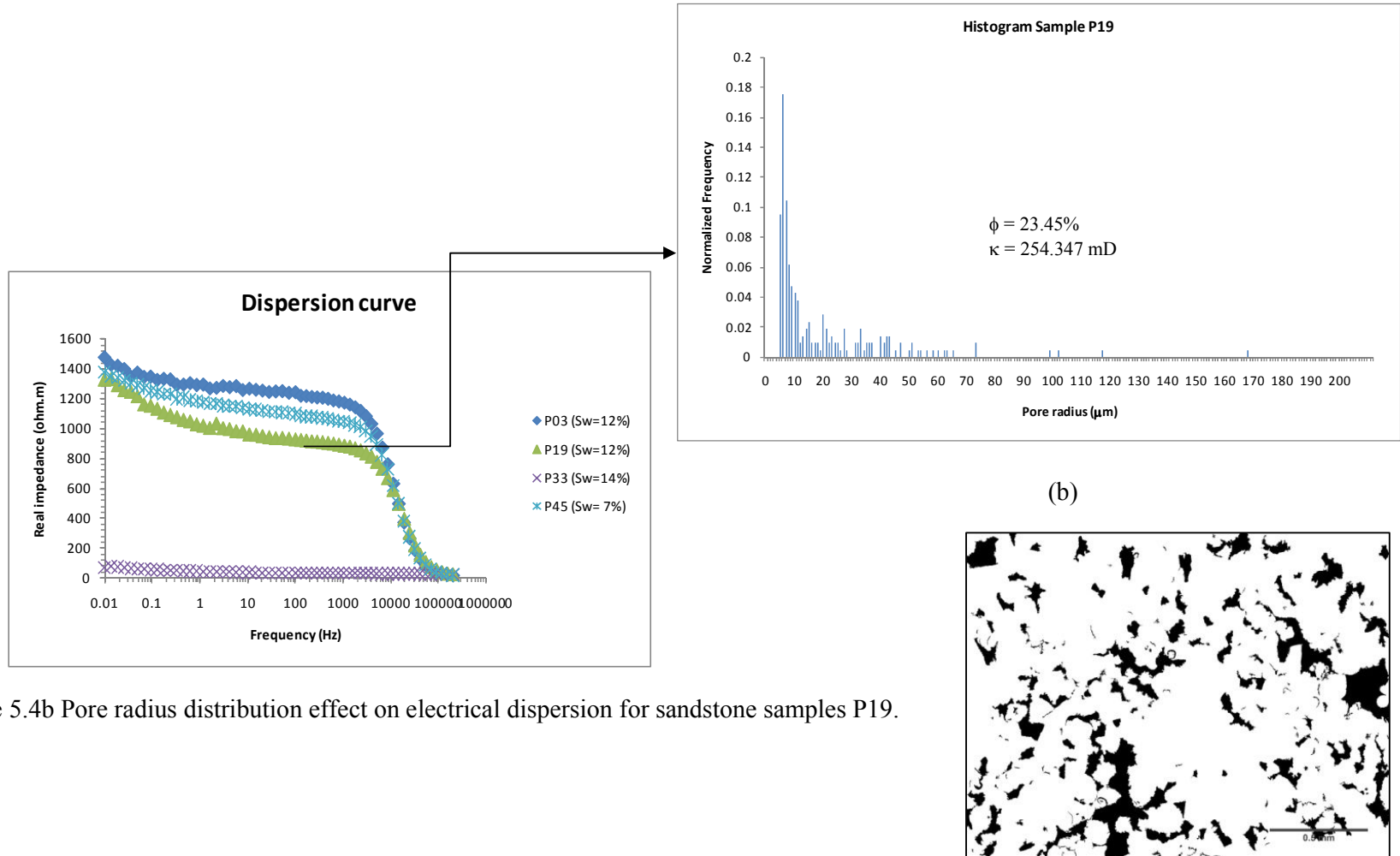
Figure 5.4b Pore radius distribution effect on electrical dispersion for sandstone samples P19.

Figure 5.4c Pore radius distribution effect on electrical dispersion for sandstone samples P45.

Figure 5.4d Pore radius distribution effect on electrical dispersion for sandstone samples P33.

Histogram Sample 9056

$\phi = 12.54\ \%$
$\kappa = 17.523$ mD

Dispersion curve

- 347 (Sw=21%)
- 368 (Sw=17%)
- 9056 (Sw=13%)

(a)

Figure 5.5a Pore radius distribution effect on electrical dispersion for carbonate samples 9056.

Figure 5.5b Pore radius distribution effect on electrical dispersion for carbonate samples 368.

Histogram Sample 347

$\phi = 19.66\,\%$
$\kappa = 2086.1\ \ mD$
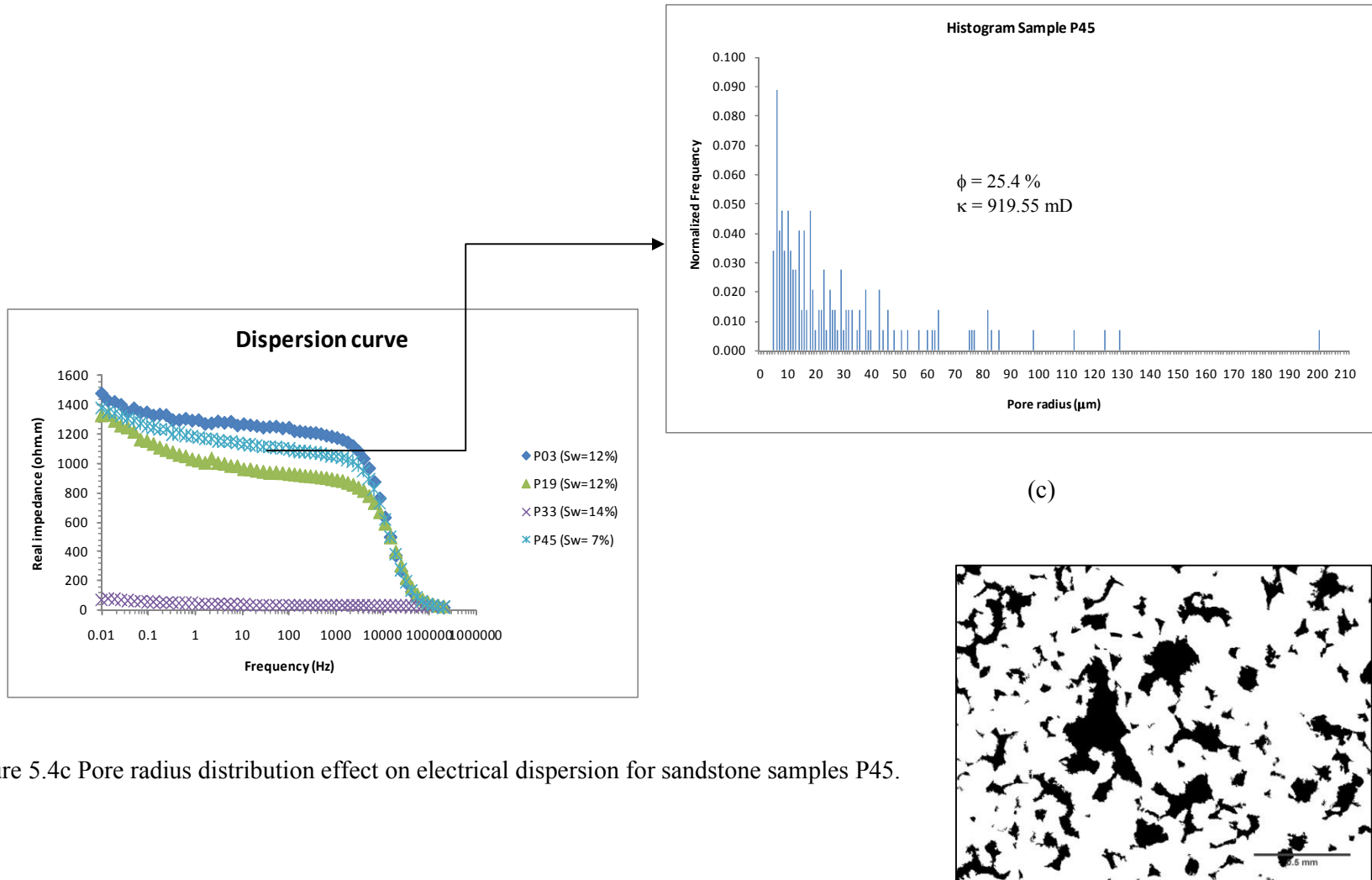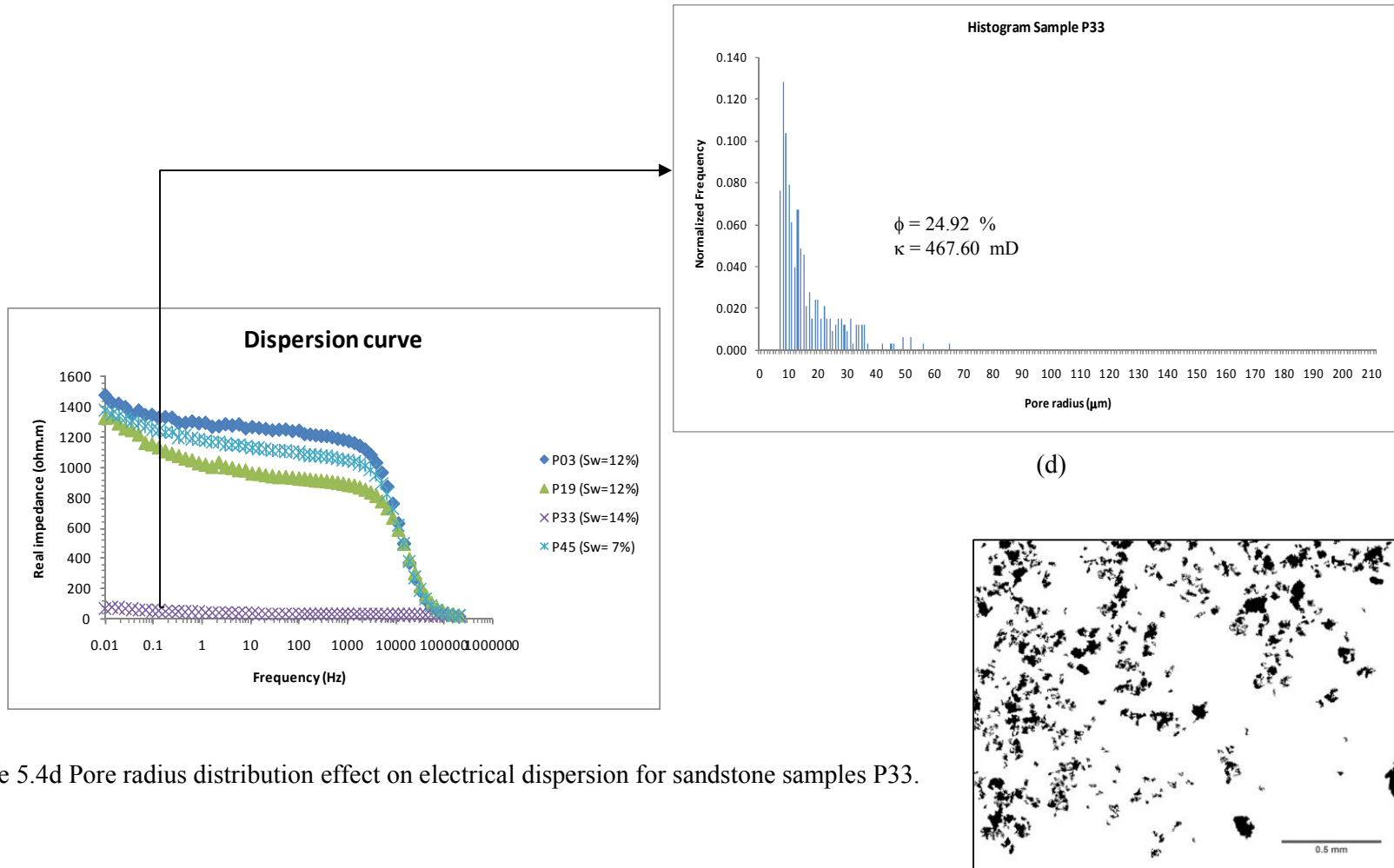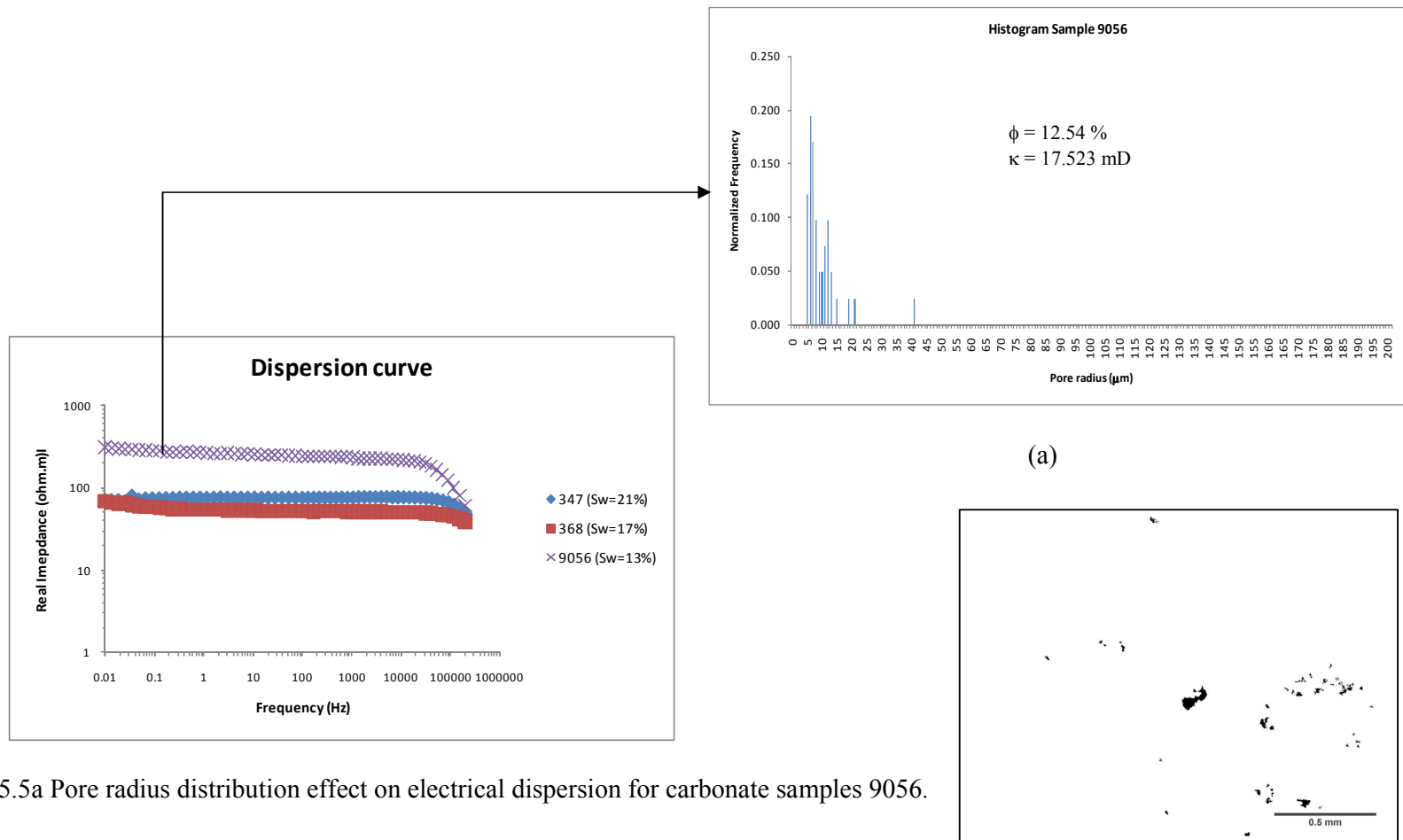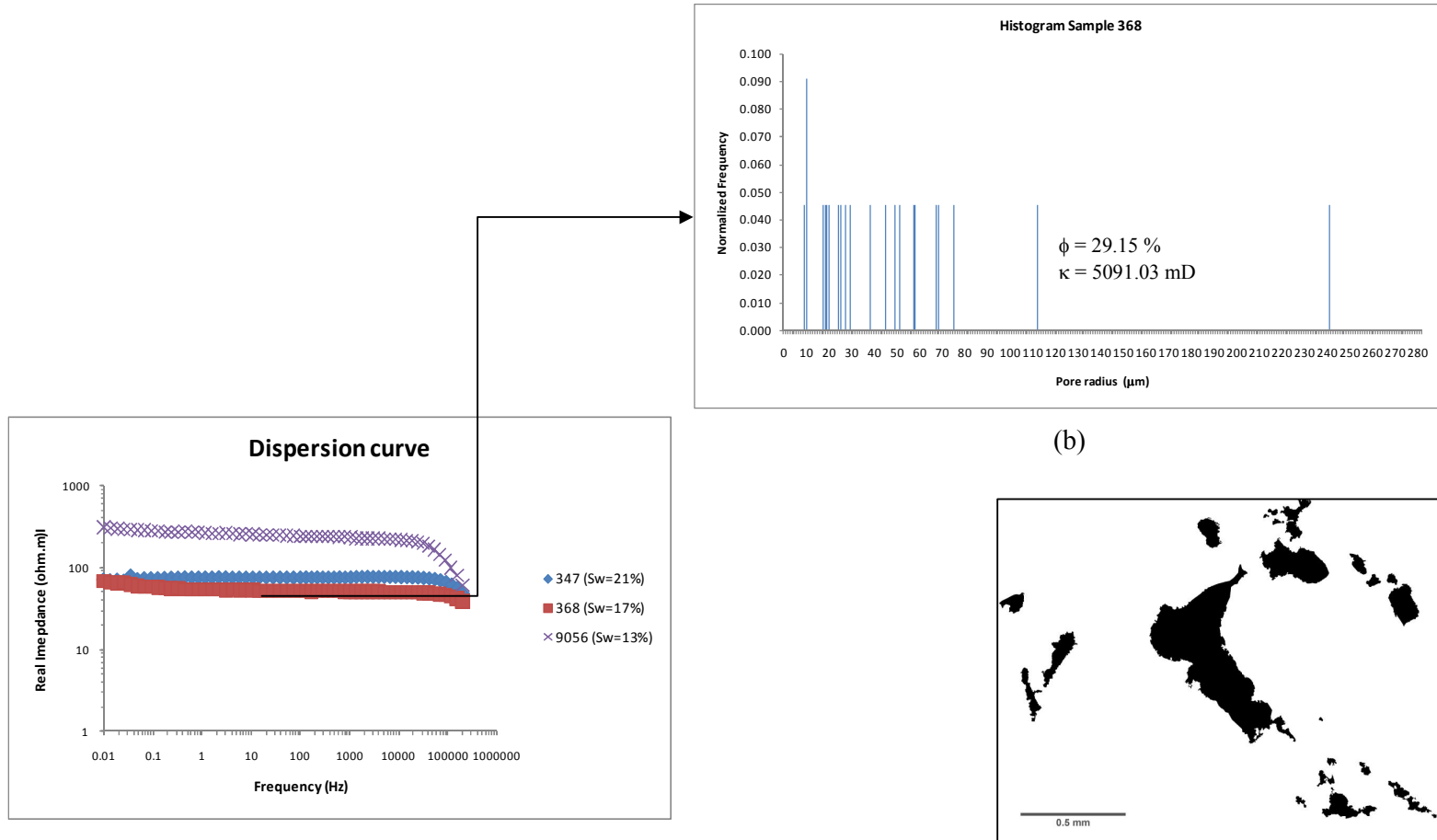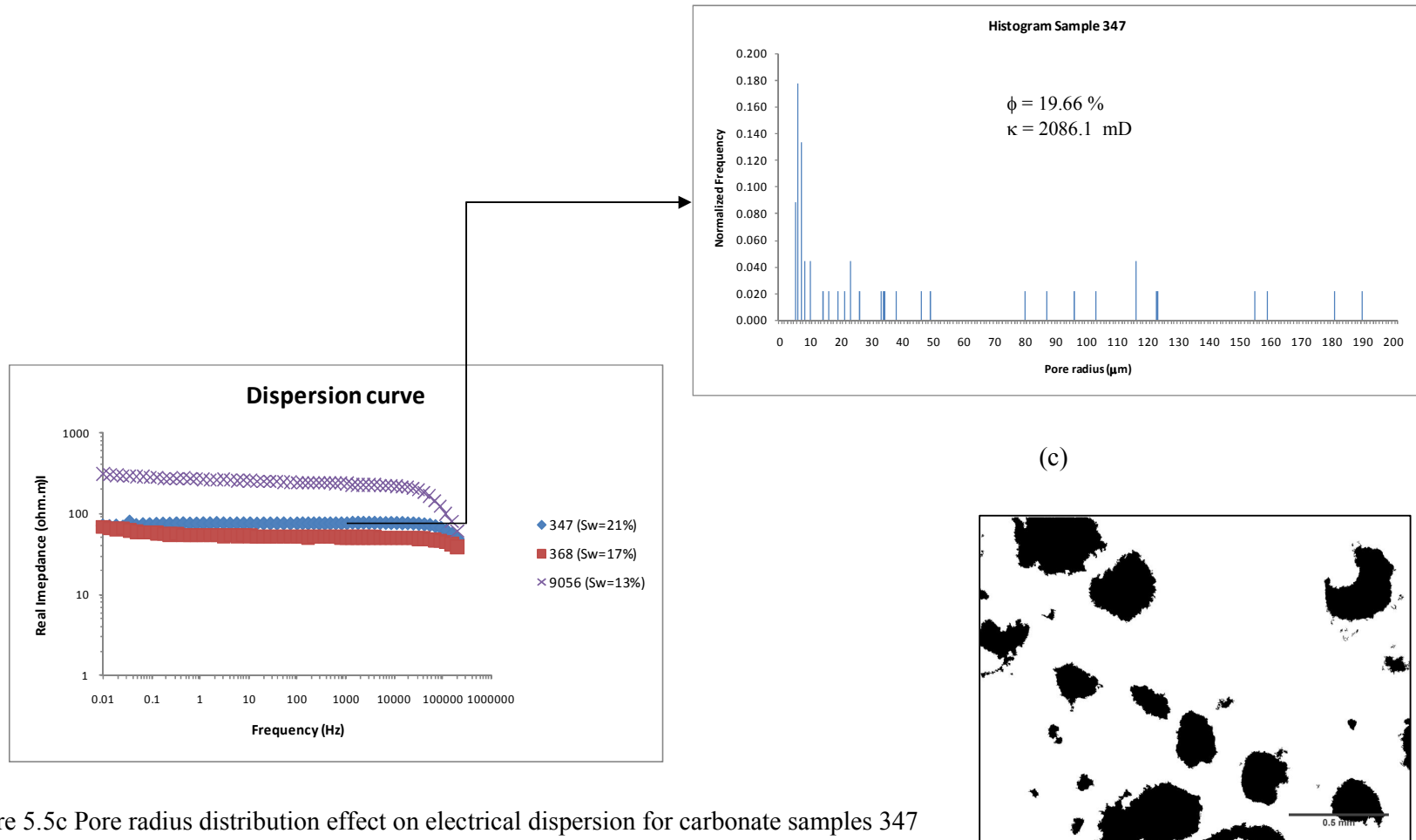
(c)

Dispersion curve

347 (Sw=21%)
368 (Sw=17%)
9056 (Sw=13%)

Figure 5.5c Pore radius distribution effect on electrical dispersion for carbonate samples 347

5.3.2 Pressure and Saturation Effect on Resistivity Reading

Electrical resistivity decreases very slightly when confining pressure is increased from 1000 psi to 3000 psi for all sandstone and carbonate samples. Dispersion curve of electrical resistivity on those types of rocks exhibits insignificant changes in high water saturation (more than 20%) as shown Figure 5.6 and 5.7 from (a)-(i). The frequency of less than 10 KHz produces the dispersion curve (due to Maxwell-Wagner effect) and could easily be observed in low-water saturation only. Whole of those rocks notice that at more than 10 KHz, where the electrical polarization at fluid-solid more intensively vibrates, the separation is difficult to be identified. Due to pressure, the effect of low resistivity changes reflects a small decrease in pore volume.

Based on the observation, it appears that the imaginary resistivity, compared to the real part, has a more sensitive behavior in responding to confining pressure. The result is tabulated in Table 5.1 and Figure 5.8a shows the average imaginary resistivity (at 100 Hz) in responding to confining pressure rapidly changes than real resistivity averagely more than 30%. This means that the imaginary resistivity reading has better characterization to pore geometry changes due to confining pressure at low-water saturation. Figure 5.8b and 5.8c also show the same trend where the real part resistivity cannot recognize the pressure effect on the rock. In contrast, the imaginary resistivity is sufficiently sensitive to differentiate pressure changes supplied on the rock.

The pressure effect on the rock samples may also depress peak loss frequency as confining pressure increases and some of them are shown in Figure 5.9. Referring to the experimental result, we observe that when the saturation achieves more than 20%, the half-circle curve dispersion is missing. However, because of the lack of saturation density data, it is difficult to judge the exact saturation border. Appendix E shows the plot of real and imaginary resistivity in Argand diagram for whole samples as confining pressure increases in low water saturation.
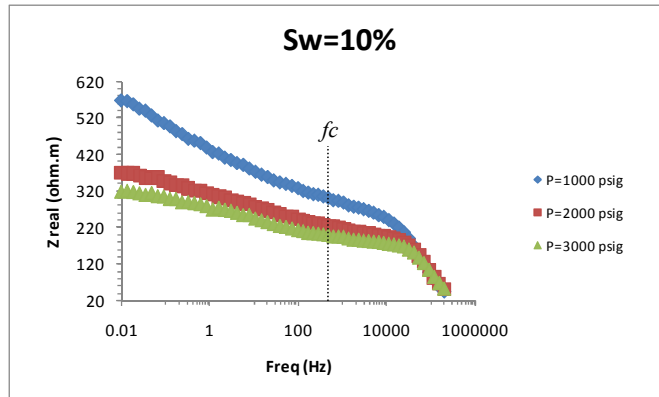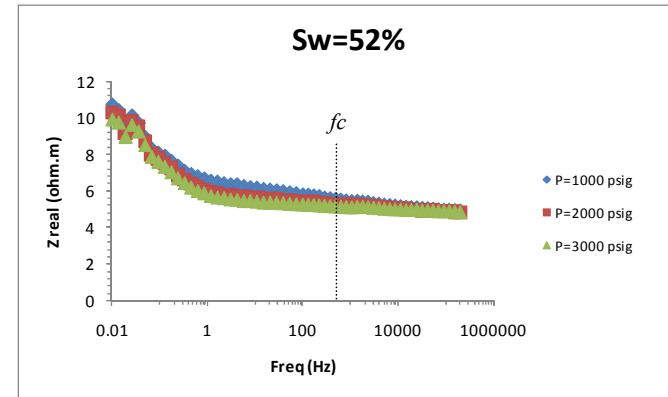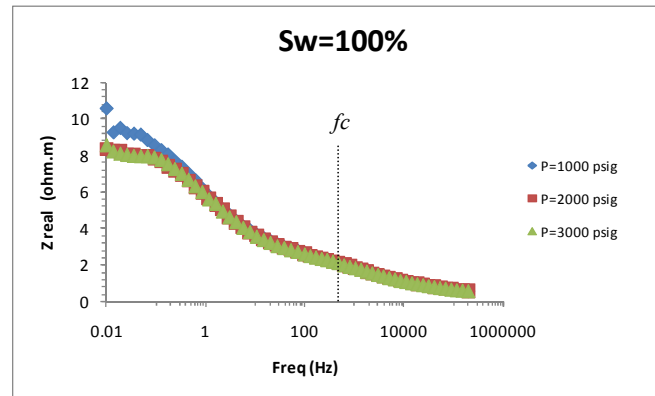
Figure 5.6a-c Dispersion real resistivity curve as a response of confining pressure of clean sandstone (BR-1) with characteristic frequency (*fc*) 626 Hz. The electrode polarization is very obvious for the data lower than characteristic frequency : (a) Sw=10%; (b) Sw=52%; (c) Sw=100%.

Sw=12%

Sw=51%

Sw=100%
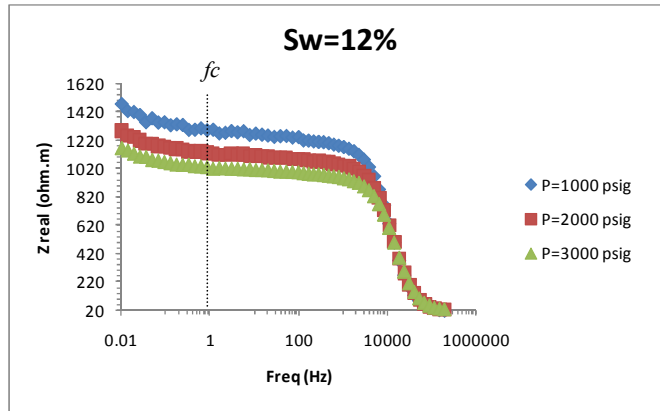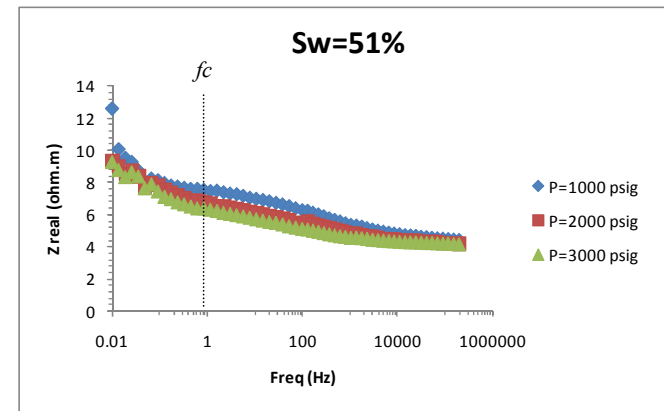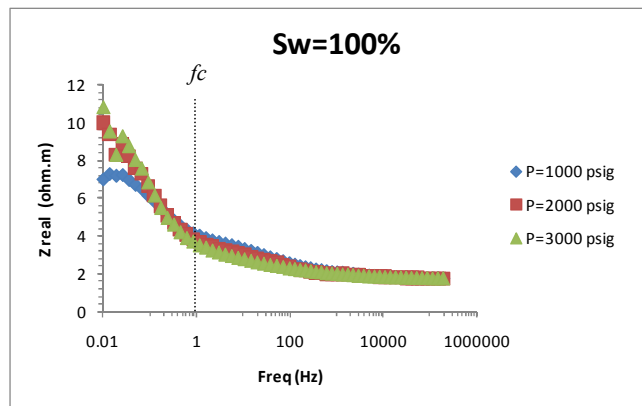
Figure 5.6d-f Dispersion real resistivity curve as a response of confining pressure of shaly sandstone (P03) with characteristic frequency (*fc*) 0.85 Hz. The electrode polarization is very obvious for the data lower than characteristic frequency: (d) Sw=12%; (e) Sw=51%; (f) Sw= 100%
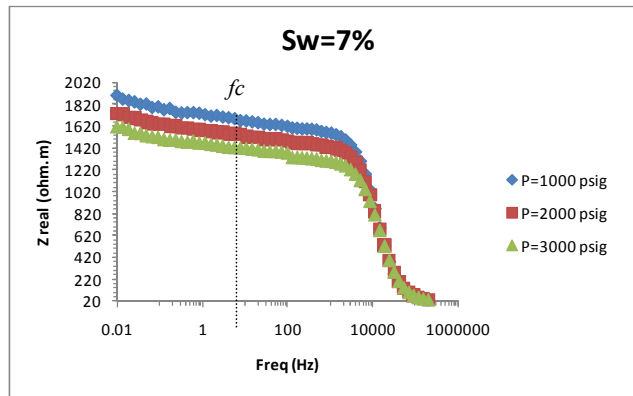
(g)
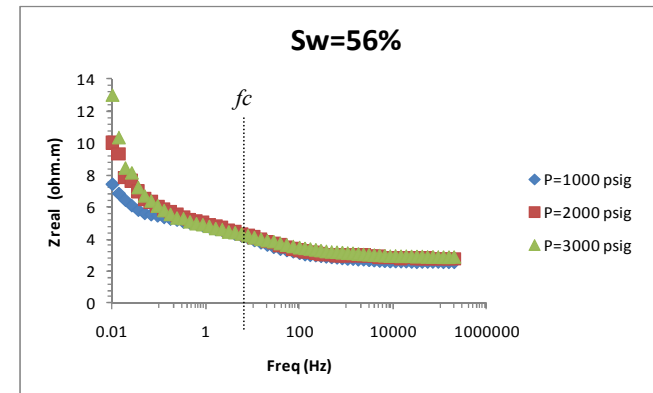
(h)
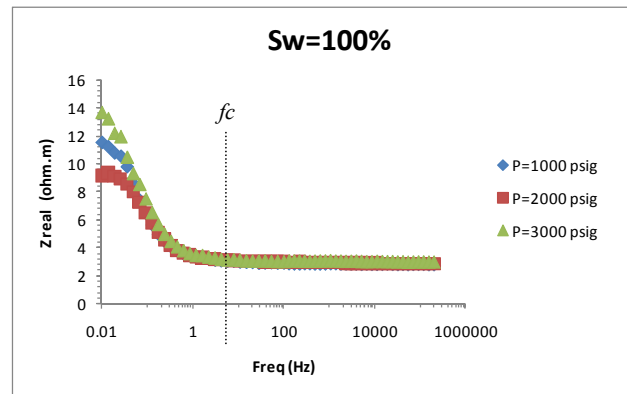
(i)

Figure 5.6g-i Dispersion real resistivity curve as a response of confining pressure of carbonate (158)) with characteristic frequency (*fc*) 7.88 Hz. The electrode polarization is very obvious for the data lower than characteristic frequency: (g) Sw=7%; (b) Sw=56%; (c) Sw=100%.
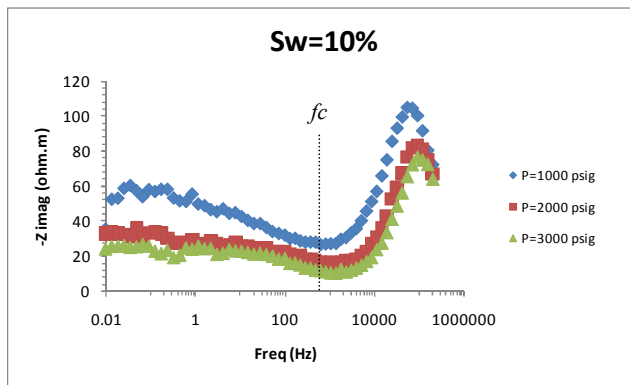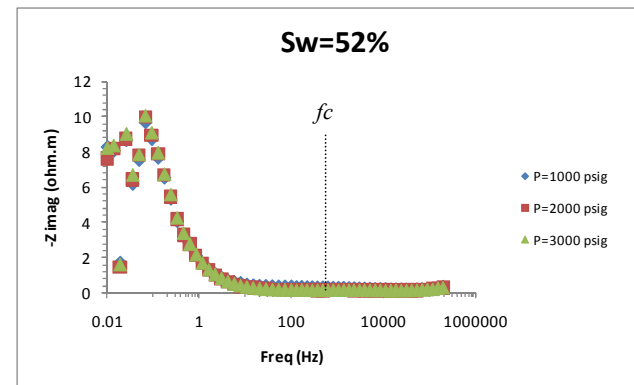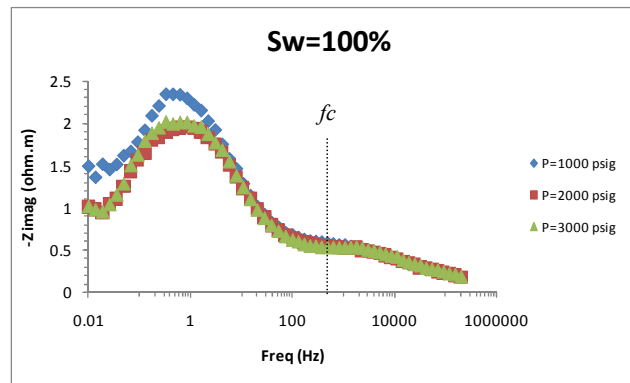
Figure 5.7a-c Dispersion imaginary resistivity curve as a response of confining pressure of clean sandstone (BR-1) with characteristic frequency (*fc*) 626 Hz. The electrode polarization is very obvious for the data lower than characteristic frequency: (a) Sw=10%; (b) Sw=52%; (c) Sw=100%.
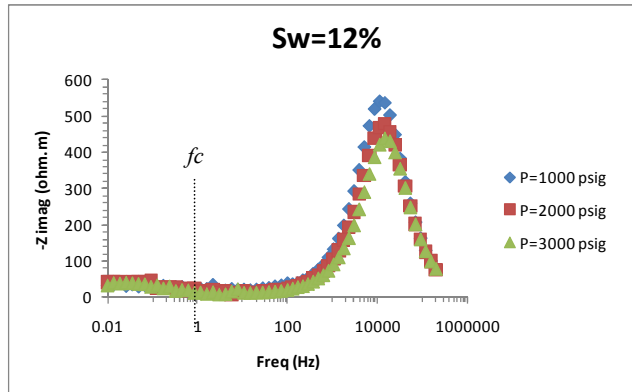
(d)
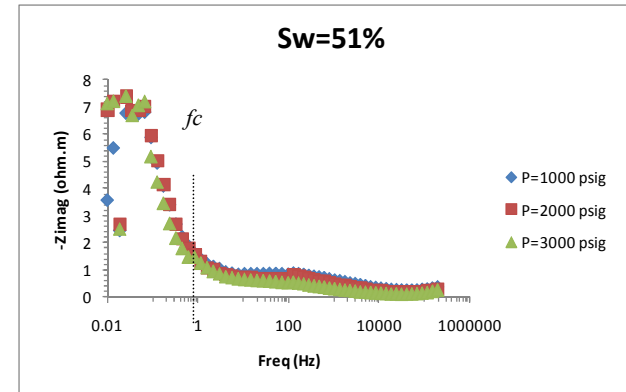
(e)
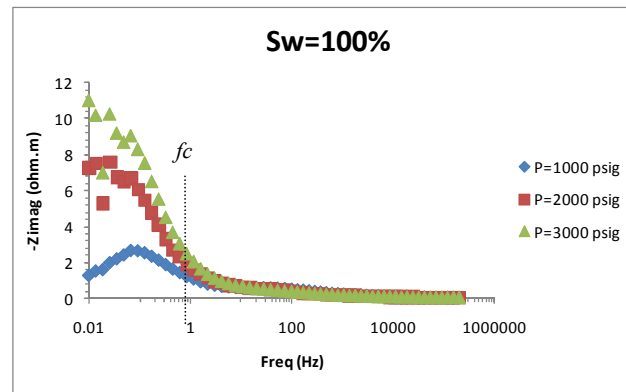
(f)

Figure 5.7d-f Dispersion imaginary resistivity curve as a response of confining pressure of shaly sandstone (P03) with characteristic frequency (*fc*) 0.85 Hz. The electrode polarization is very obvious for the data lower than characteristic frequency: (d) Sw=12%; (e) Sw=51%; (f) Sw= 100%.
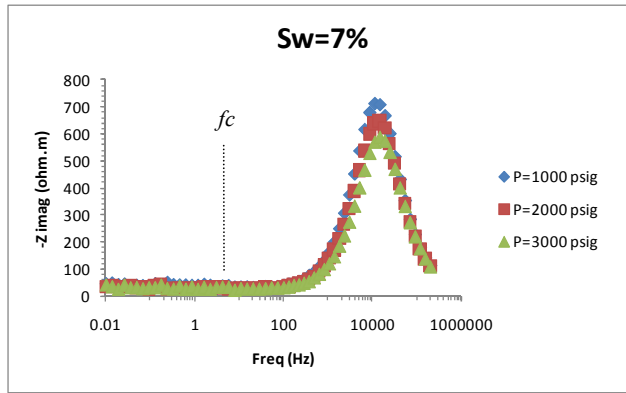
(g)
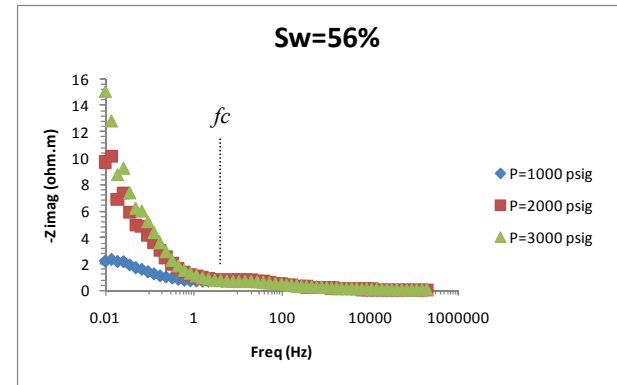
(h)
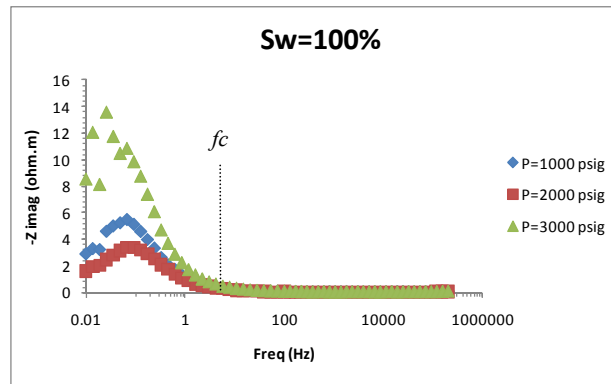
(i)

Figure 5.7g-i Dispersion imaginary resistivity curve as a response of confining pressure of carbonate (158) with characteristic frequency (*fc*) 7.88 Hz. The electrode polarization is very obvious for the data lower than characteristic frequency: (g) Sw=7%; (b) Sw=56%; (c) Sw=100%.

Table 5.1 Resistivity response to confining pressure.

F=100 Hz Sample Number P03	Sw (%)	1000 (psi)		2000 (psi)		3000 (psi)		AVG	
		R (%)	Im (%)	R (%)	Im (%)	R (%)	Im (%)	Re (%)	Im (%)
	12	0	0	-12.36004744	-34.19216318	-19.95819011	-46.02791197	-16.15911878	-40.11003757
	23	0	0	-8.462505237	-11.11663765	-8.630079598	-13.30514797	-8.546292417	-12.21089281
	37	0	0	-11.58558559	-27.04323919	-16.72972973	-41.36465884	-14.15765766	-34.20394901
	51	0	0	-13.29939548	-25.49724419	-18.99459115	-35.32231009	-16.14699332	-30.40977714
	59	0	0	-11.27348643	-36.58923676	-15.44885177	-46.1116722	-13.3611691	-41.35045448
	69	0	0	-6.608328304	-27.98789713	-10.07845504	-38.07866868	-8.343391672	-33.0332829
	77	0	0	-6.504621705	-22.95634586	-9.842519685	-34.04685656	-8.173570695	-28.50160121
	100	0	0	-6.368670886	-16.62861492	-9.533227848	-28.97640791	-7.950949367	-22.80251142
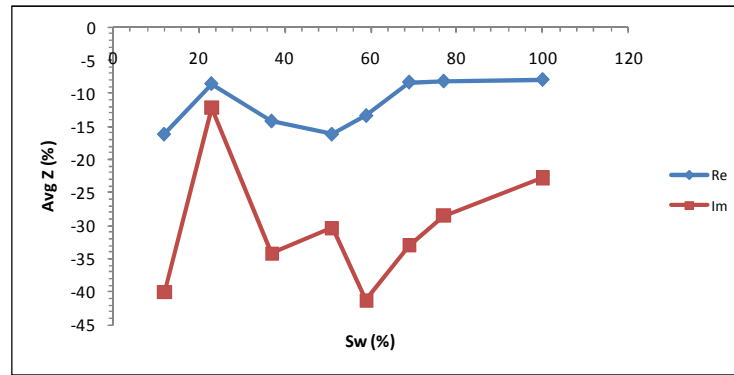
(a)
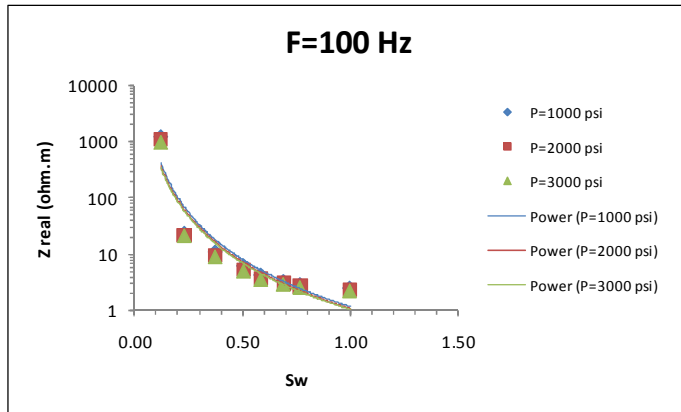
(b)
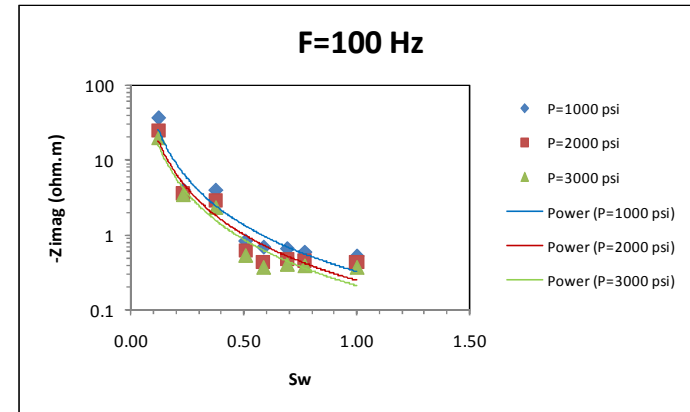
(c)

Figure 5.8 Plot of averagely resistivity response to confining pressure from 1000 psi – 3000 psi in each water saturation sequences; (b) Real resistivity to water saturation response ; (c) Imaginary resistivity to water saturation response.
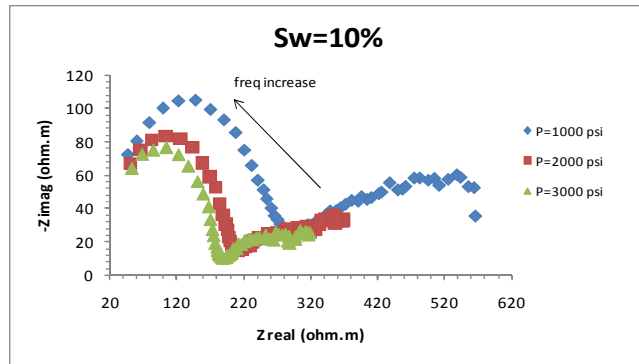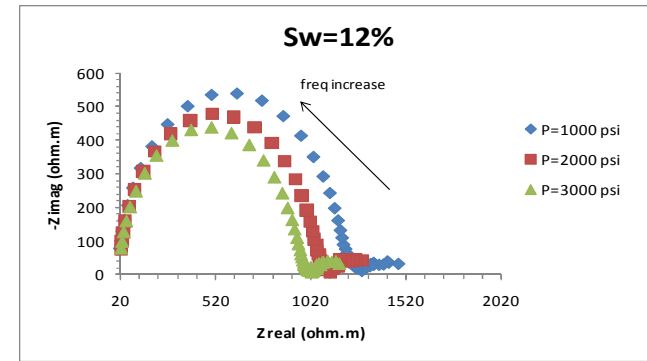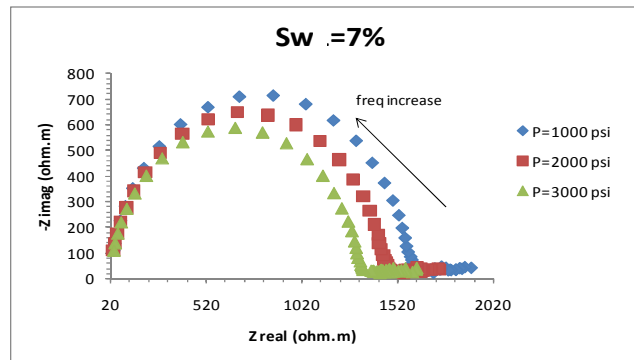
Figure 5.9 Samples of Argand plot for (a) Clean sandstone (BR); (b) Shaly sandstone (P03); (c) Carbonate (158) at low-water saturation.

Figure 5.10 explains more about the characteristic of volumetric conductivity and interlayer by observing the electrical dispersion of real and imaginary resistivity, both in full and partial water saturation. When the water fully fills the pore space, the dispersion effect in low saturation is very small. This reflects that bulk fluid volumetric now controls the path of the electrical current (Figure 5.11). In other word, dispersion curve reflects water-coating grain or an interlayer effect. Because of the higher water salinity will reduce the thickness of electrical double layer, the electrical double layer tends to be less important for water saturation increment.

Another evidence to see the water-coating grain surface can be seen in the plot of dielectric permittivity to water saturation as tested in sample P03 and P19 (Figure 5.12). The relatively low variation in dielectric permittivity after a certain saturation refers to the pore condition fully covered by water. Furthermore, when the saturation sequence increases, the characteristic frequency shifts to the higher frequency (Figure 5.13). However, dispersion relationship to the water saturation might be observed in low water saturation only (refer to Figure 5.11).

To examine a dynamic fluid process, the sample is proceeded to have partially saturated-unsaturated water fluid. Figure 5.14 exhibits a plot of resistivity dispersion in saturation-unsaturated process. As the brine water partially leaves the pore space, the resistivity increases notably. However, unsaturated-resistivity is always lower than the other. The presence of irremovable conductive salt-water film coating the solid-grain acts as an agent of electrical current (the process of saturated-unsaturated has been explained in Figure 5.2). Thus, although the water leaves most of the pore space, the resistivity may become lower than imbibitions.

The water-solid interfacing behavior is more easily analyzed by looking at the imaginary resistivity. Figure 5.15 (a,b) shows the plot of real and imaginary resistivity during the drainage-imbibitions in 100 Hz frequency. Before the whole of solid grain is coated by water film, the electrical resistivity decreases un-smoothly (imbibitions). Reducing the water saturation after imbibitions yields the increase (drainage) of the electrical resistivity monotony at every step of pressure. Both drainage and imbibitions path satisfy the power equation.
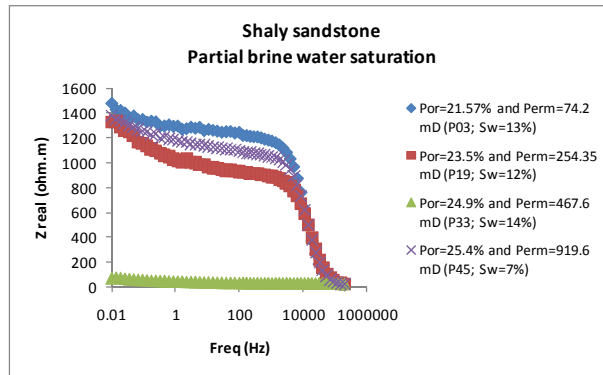
(a)
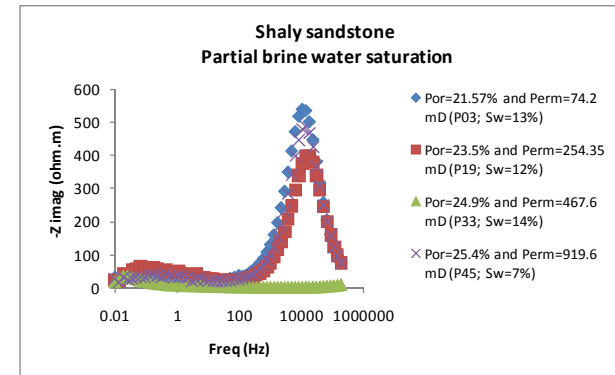
(b)
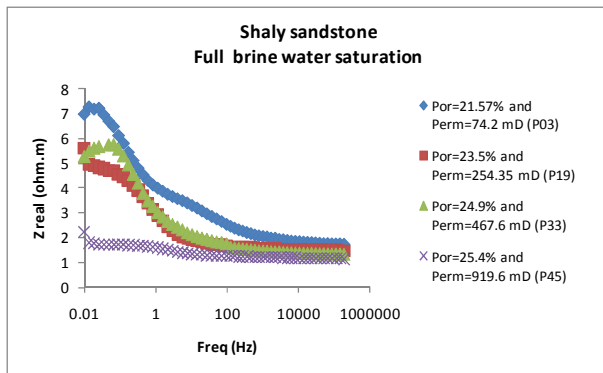
(c)
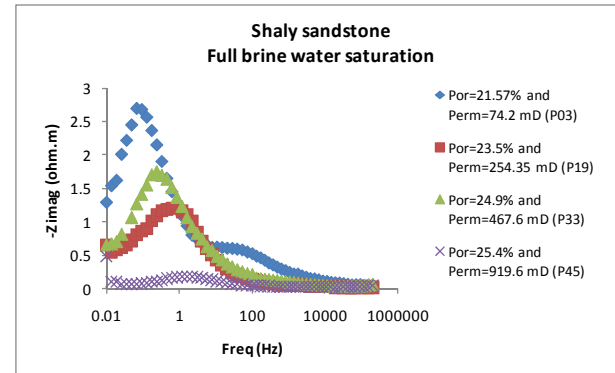
(d)

Figure 5.10 Electrical dispersion in partial water saturation and full water saturation (a,c) real (b,d) imaginary. The flat green line (a,b) indicate small dispersion because of small pore size distribution (see Chapter 5.3.1). If it is removed the electrode polarization effect the dispersion curve of fully water saturation will become insignificant (c,d).
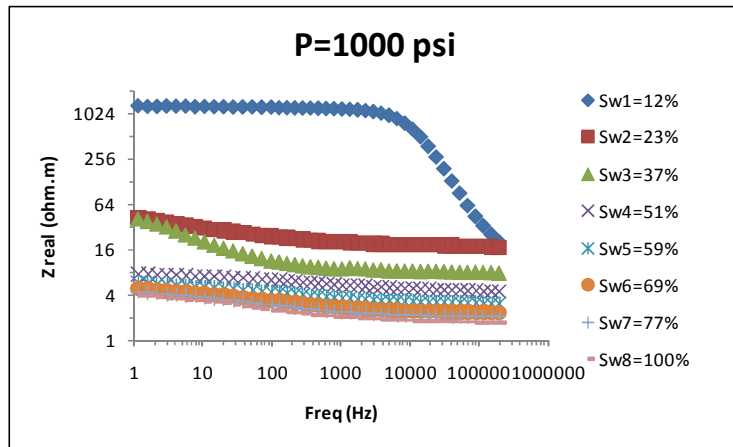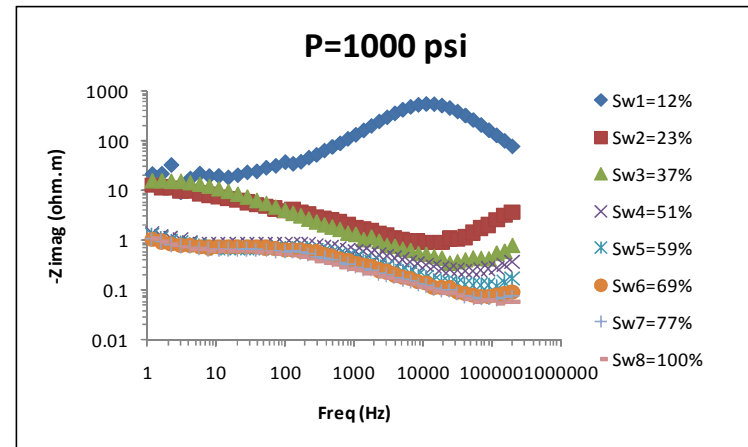
Figure 5.11 Example of dispersion curves in their relationship to the water saturation (a) Real resistivity and (b) Imaginary resistivity. The rock sample is shaly sandstone (P03).
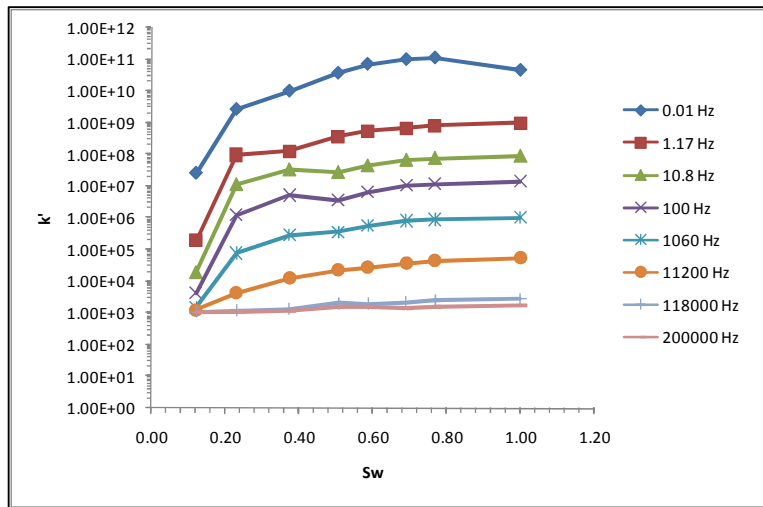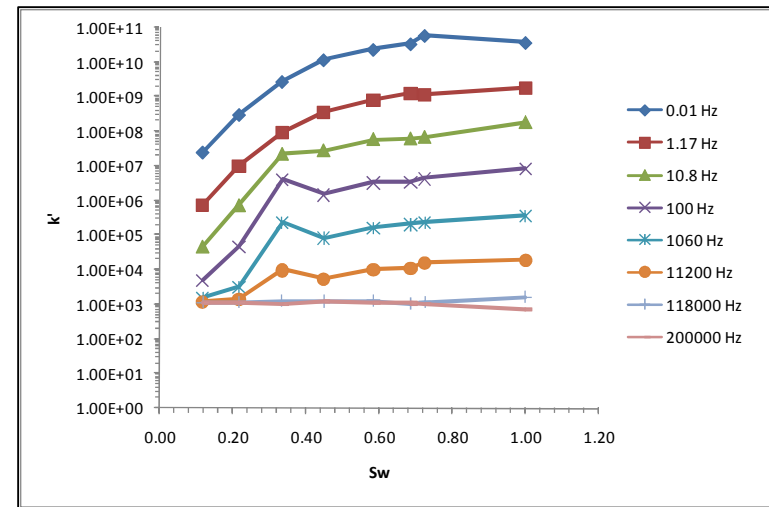
(a)   (b)

Figure 5.12 Water-coating grain surface may be observed in certain saturation degree, (a) is about 20% for sample P03 (b) and is about 30% for sample P19.
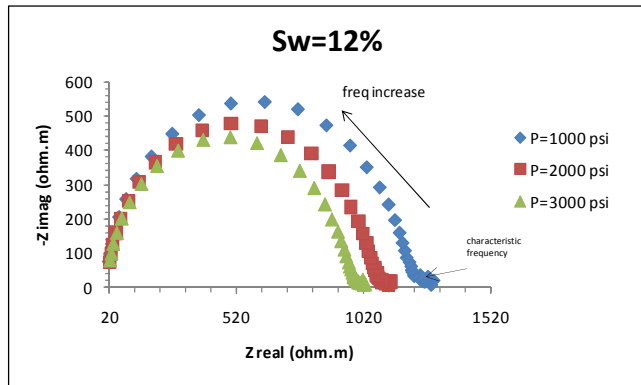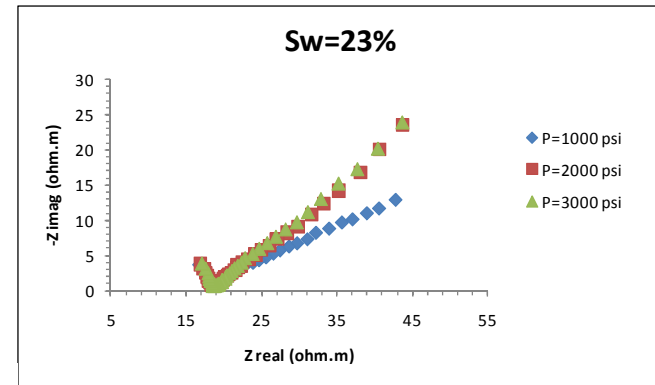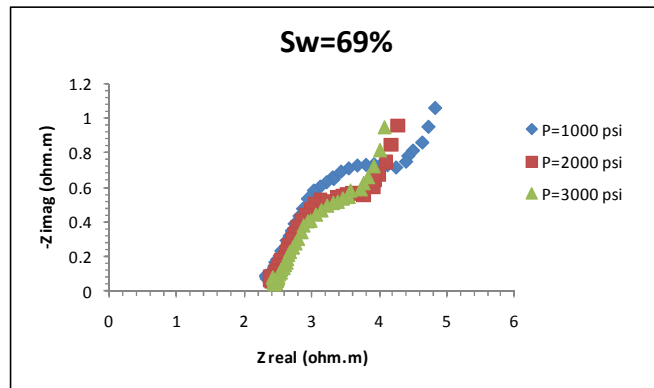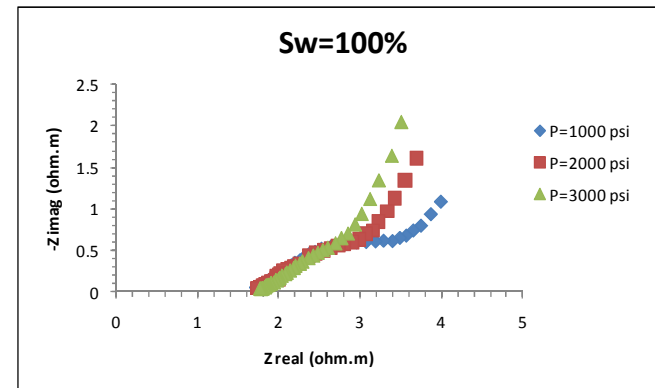
Figure 5.13 Characteristic frequency shifting as water saturation increase on Sample P03, (a) Sw=12%, *fc=0.85* Hz; (b) Sw=23%, *fc*=31900 Hz; (c) Sw=69%, *fc=41500* Hz and (d) Sw=100%, *fc*=53900 Hz.
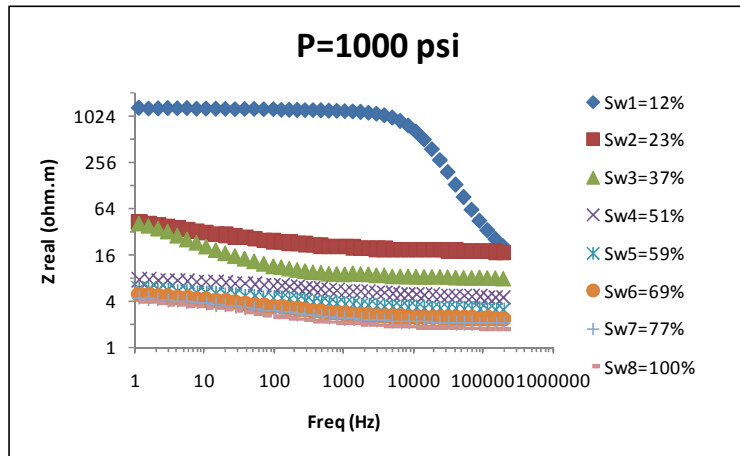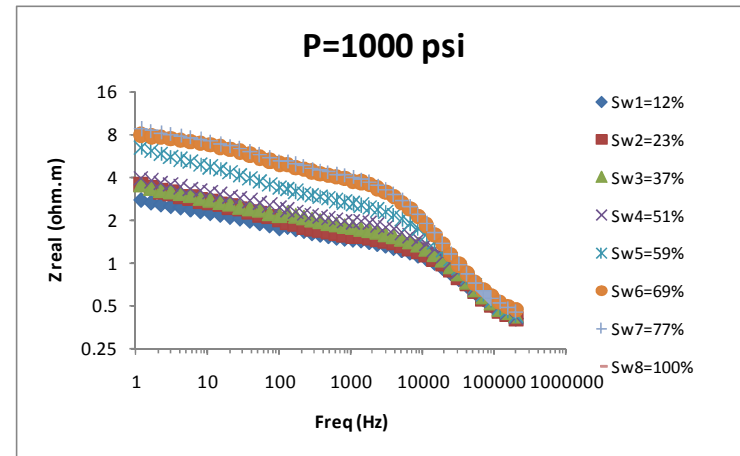
Figure 5.14 Resistivity dispersion on Sample P03 in: (a) saturation process; (b) unsaturated process.
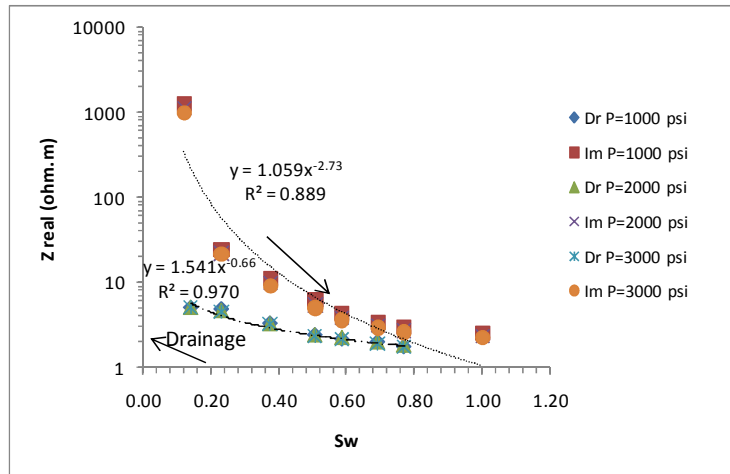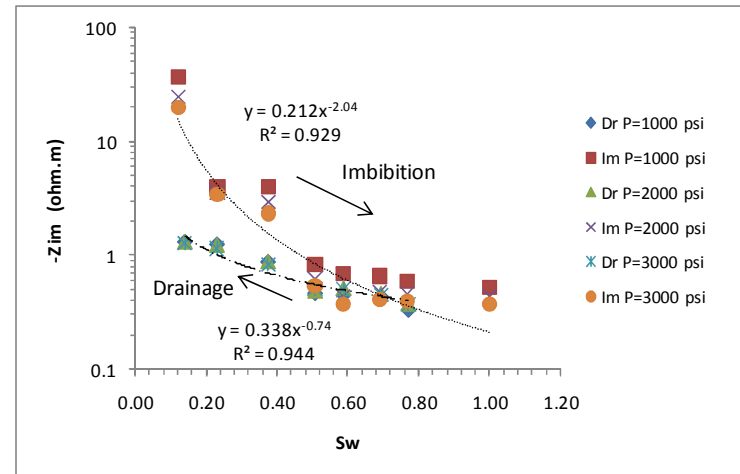
Figure 5.15 Electrical resistivity characteristic during water drainage-imbibitions for shaly sandstone Sample P03 and its respective power equation: (a) real resistivity; (b) imaginary resistivity.

Extending the result at different frequencies will give the same trend. In imbibitions and drainage sequence, the real part resistivity tends to reduce as the water saturation increases. However, for the frequency of more than 10 kHz, the resistivity has a small change as water saturation achieves more than 50% (Figure 5.16).

The theoretical model introduced by Klein-Swift [51] states that the dielectric of brine water slightly changes with its conductivity variation. When the brine water fills the pore space, electrical double layer is present due to the chemical interaction of water-solid grain. The dielectric permittivity increases as macroscopic dipoles reach equilibrium before electrical field orientation changes notably in low frequency. This yields polarization build-up. When the orientation of macroscopic dipoles cannot follow the applied field (in high frequency), because of the viscosity of the fluid, the energy dissipation then takes over. Analysis on dielectric permittivity exposes that anomalous gigantism may occur at low frequency for any type of the rock (Figure 5.17). The dielectric dispersion relationship, either real or imaginary one, with water saturation gives the power-law formula at any level of saturation as follow:

$$\kappa' = \kappa'' = \frac{C}{\omega^q} \qquad\qquad 5.1$$
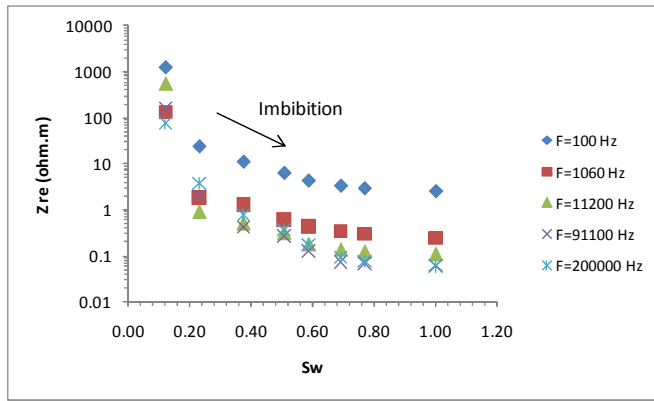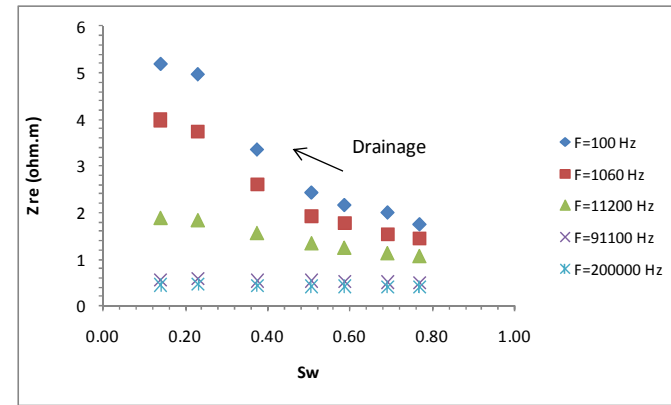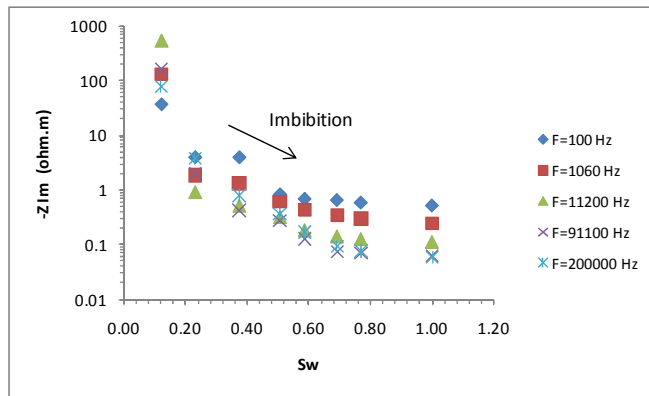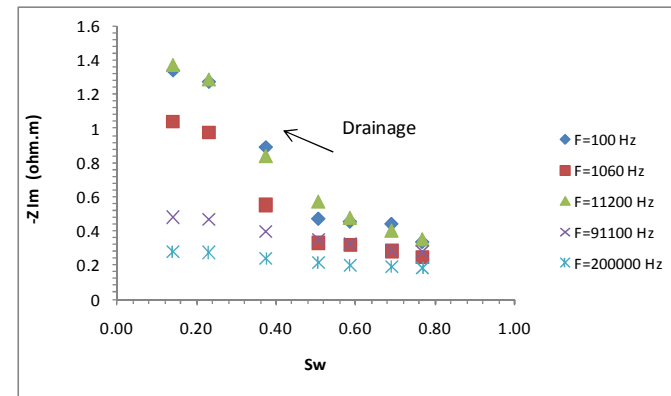
Figure 5.16 Real and imaginary resistivity impedance to water saturation at different frequencies for sample P03: (a and c) Imbibitions; (b and d) Drainage.
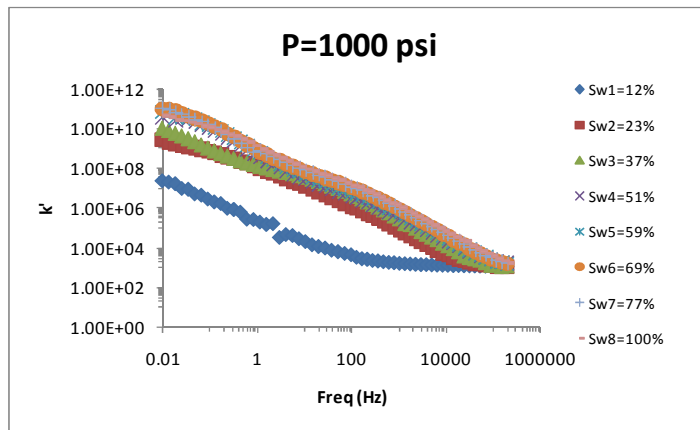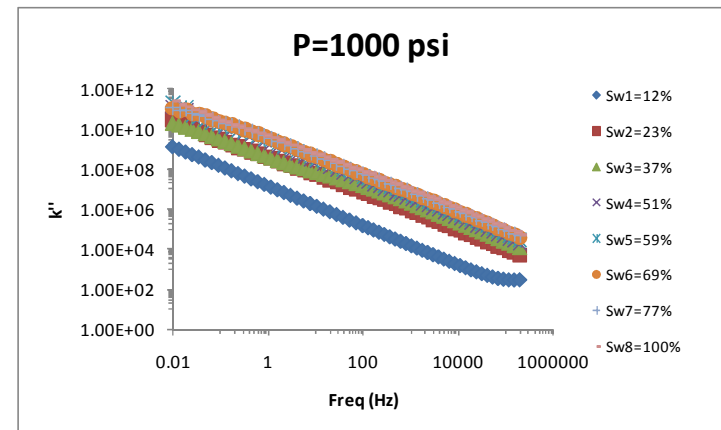
(a)   (b)

Figure 5.17 Dielectric dispersion of Sample P03: (a) real (b) imaginary.

5.4 Summary

The large pore geometry structure appears to give more contribution than the small one although in small numbers of large pore distributions. The fluid supplied during saturation needs more time to make thin water layer fully-fill pore volume in large structure. Conversely, it occurs in the small structure due to its simple saturation process. From the observation, it shows that pore radius of more than 70 μm has a significant effect on electrical dispersion. Microstructure of the pore behaves like capillary pore tube. Ion selective membrane system occurs when electric field is applied to the small pore radii.

Confining pressure applied on rock sample only accommodates small effect in pore geometry changes and contributes insignificant complex resistivity dispersion at high water saturation. This indicates that bulk volumetric is more dominant compared to interfacial. On the other way around, surface conductivity occurs at low water saturation. The imaginary resistivity is more sensitive to geometry changes due to the pore pressure compared to the real resistivity. Thus it has been proven that imaginary resistivity should be taken into the account to observe interfacial and geometry changes.

The presence of salt-water film coating the pore wall will act as an agent for electric current to flow. Although the water leaves most of the pore space in dynamic saturation process, the resistivity of its drainage may go lower than imbibitions. In the beginning of saturation or at the end of drainage, the electrical double layers still dominate the electrical properties. When the volumetric fluid covers most of the pore space, the electrical double layer vanishes. It occurs at the time when saturation achieves more than 20% in average.

CHAPTER 6

DIELECTRIC AND CONDUCTIVITY MODEL DEVELOPMENT

6.1 Introduction

Various series of processes are involved when the rocks are formed on the surface. The nature of electrical properties in the rock is very heterogeneous and unique in each place. Siliciclastic and carbonate rocks having various matrices provide different pores-system interconnection. Thus, it may give unique electrical responses for each rock as its pores are filled with different fluid and gas or the interface of matrix-air is also presented by them.

When the time varying electric field is applied through dielectric substance, electric polarization may occur, depending on its frequencies. Electrical polarization refers to a phenomenon of relative displacement of the atoms or molecules. The mechanisms of polarization are divided into several ranges of frequencies (Figure 6.1) that are electronic, atomic, dipolar, Maxwell-Wagner and membrane polarization [3, 48-50]. Electronic polarization occurs in a range of ultraviolet frequencies ($7.5.10^{14}$ Hz – 3.10^{16} Hz). This type of polarization causes relative displacement of outer electron clouds with respect to the inner positive atomic cores. Atomic or ionic polarization is observed in a range of infrared frequencies (3.10^{12} Hz – 4.10^{14} Hz). The phenomenon in this polarization is that the atoms or ions displace relatively to each other. Dipolar polarization exists when the frequencies of external electric field are in range of 10^8 Hz – 10^{11} Hz. The electric field causes the molecule orientation to change following external field orientation. In the range of frequencies of 10^3 Hz – 10^6 Hz there is Maxwell-Wagner effect which corresponds to charge build-up at the interface between two different conductivity medias [3, 27, 52]. At the lowest frequencies range below 1 Hz, the membrane or interfacial polarization may occur.

This type of polarization corresponds to mobile and trapped charges injected from electrical contact [53].

Membrane polarization is related to the presence of clay minerals throughout the rock. This occurs when clay surface partially blocks ionic solution. Negative charges on clay minerals tend to capture the electrolyte cations and move to the other way to anions.
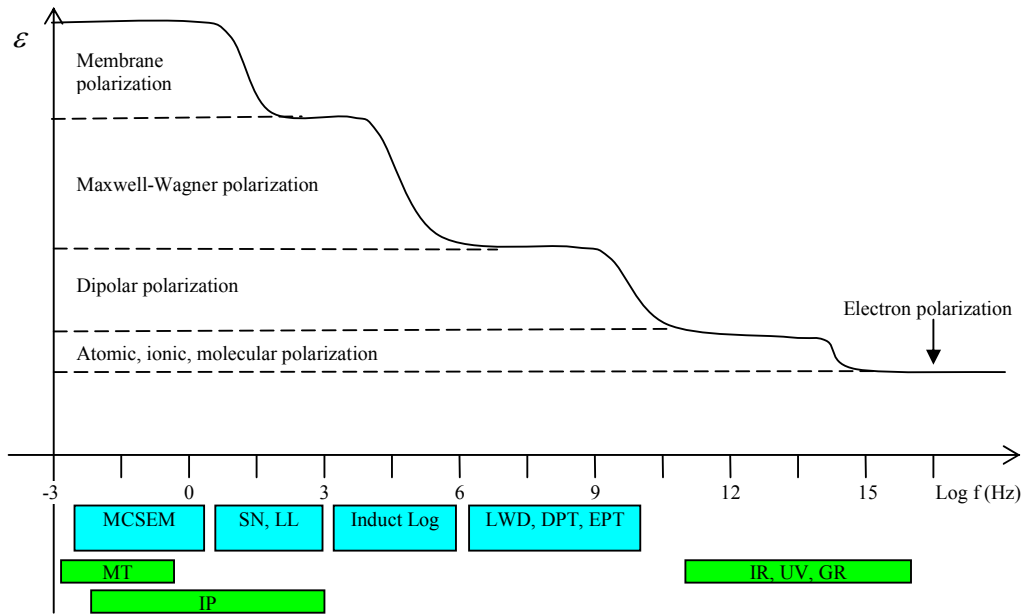
Figure 6.1 Dielectric polarization and geophysical and petrophysical measuring systems. MT-magnetotelluric; IP-induced polarization; MCSEM-marine controlled source EM; SN, LL-short normal and laterolgs; Induct-induction logs; LWD-logging while drilling; DPT-dielectric tool; EPT-electromagnetic propagation tool .

Under the influence of electric field, the cations easily pass the cationic cloud but ionic charges accumulate. This makes ion-selective membrane system (Figure 6.2). The magnitude of the potential is the greatest near the pore wall and decreases with respect to the distance from the wall scaled by Debye length [4].

Atomic displacement mentioned above has certain polarization-depolarization time called as relaxation time. The electronic and atomic polarization time is generally very short, less than 10^{-12} second. The phenomenon is also referred as

98

resonance process because it involves vibration modes that are close to the natural frequency of the substance. The other polarization type has quite long time relaxation, depending on dielectric systems.
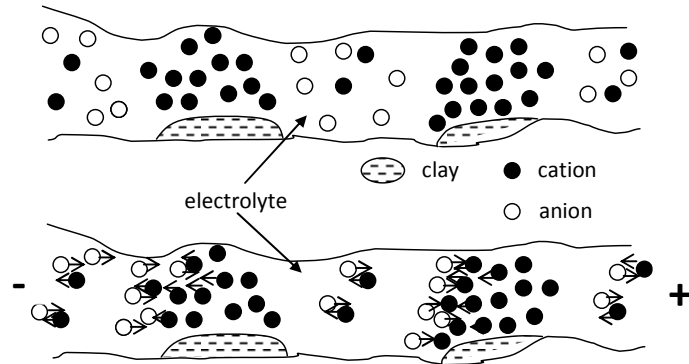
Figure 6.2 Membrane polarization mechanism (after Schon, 1998).

The existence of absorption and dispersion in the system may cause dielectric losses. Therefore, there is no dielectric material independence from frequency either real or imaginary part. The model developed to evaluate dispersion and absorption is split into two folds: one relaxation model and many relaxation models. The following sub-chapter discusses the complex dielectric permittivity derived from Maxwell equation and its relationship to conductivity and resistivity. The measurement workflow to obtain dielectric properties of reservoir rock is also presented and followed with the dielectric and relaxation model in more detail. To observe relaxation time, the dispersion model, such as basic Debye and Cole-Cole model, should be analyzed.

This chapter presents the electrical double layer phenomena, existing model of electrical properties of rock, and proposes a new dielectric permittivity dispersion and conductivity model and computational fitting technique to achieve the best fitness to the experimental data.

6.2 Complex Dielectric Permittivity of Rock

When the external electric field is employed into dielectric in a certain long time, the average atoms or molecules polarization will follow it and the dielectric coefficient of the substance is equal to static dielectric (ε_o). Conversely, when the polarization is measured soon after the electric field is employed, only small amount of dipole is displaced (ε_∞). The time characteristic measured from its polarized position until it is back to initial position after the electric field is removed is very difficult to be directly measured. One of the ways to estimate time characteristic is by modeling the inversion of Cole-Cole model [54]. This parameter corresponds to specific surface area, pore size as well as permeability which is very important properties for oil and gas exploration and production [55].

Evaluating Maxwell equation is as follow:

$$\nabla x \vec{H}(r,t) = \vec{j}(r,t) + \frac{\partial \vec{D}(r,t)}{\partial t} \qquad\qquad 6.1$$

$$\nabla x \vec{E}(r,t) = -\frac{\partial \vec{B}(r,t)}{\partial t} \qquad\qquad 6.2$$

$$\nabla . \vec{D}(r,t) = \rho(r,t) \qquad\qquad 6.3$$

$$\nabla . \vec{B}(r,t) = 0 \qquad\qquad 6.4$$

where is

$$\vec{D} = \varepsilon \vec{E} \qquad\qquad 6.5$$

$$\vec{B} = \mu \vec{H} \qquad\qquad 6.6$$

Electric density is formulated as $\vec{j}(t) = \sigma \vec{E}(t)$ \qquad\qquad 6.7

Substituting Equation 6.5, 6.6 and 6.7 into Maxwell formula Equations 6.1 to 6.4 yields

$$\nabla x H(t) = \sigma E(t) + \varepsilon \dot{E}(t)$$
$$\nabla x H(t) = j' + ij''$$
$$\nabla x H(t) = j^*$$

6.8

Solution for electric field is $E(t) = E_o e^{i\omega t}$

Equation 6.8 can be manipulated in term of frequency $E(\omega)$ and its differential as

$$j^*(\omega) = (\sigma(\omega) + i\omega\varepsilon_o\varepsilon(\omega)) \cdot E(\omega)$$
$$j^*(\omega) = \sigma^* \cdot E(\omega)$$

6.9

and

$$j^*(\omega) = \left(\frac{\sigma(\omega)}{i\omega} + \varepsilon_o\varepsilon(\omega) \right) \cdot \dot{E}(\omega)$$
$$j^*(\omega) = \varepsilon^* \cdot \dot{E}(\omega)\varepsilon_o$$

6.10

Following are the simpler form of Equation 6.9 and 6.10

$$j^*(\omega) = \begin{cases} \varepsilon^*(\omega)\dot{E}(\omega)\varepsilon_o \\ \sigma^*(\omega)E(\omega) \end{cases}$$

Then the relationship of ε^* and σ^* can be expressed as

$$\varepsilon^* = \frac{\sigma^*}{i\omega\varepsilon_o}$$

6.11

The last Equation 6.11 shows the similarity of dielectric permittivity and conductivity. The real part of dielectric permittivity (ε') is equal to imaginary part of conductivity (σ'') and the imaginary part of dielectric permittivity (ε'') is equal to real part of conductivity (σ'').

In term of complex notation, conductivity and resistivity can be written as

$$\sigma^*(\omega) = \sigma'(\omega) + i\sigma''(\omega)$$

$$\rho^*(\omega) = \frac{1}{\sigma^*(\omega)} = \rho'(\omega) + i\rho''(\omega)$$

The general relationship of dielectric permittivity to conductivity and resistivity is then evaluated as [13]

$$\varepsilon^*(\omega) = -\frac{i\sigma^*(\omega)}{\omega} = -\frac{i}{\omega\rho^*(\omega)} = \varepsilon'(\omega) - i\varepsilon''(\omega) \qquad 6.12$$

and dielectric constant or relative dielectric permittivity is defined as

$$\kappa^*(\omega) = \frac{\varepsilon^*(\omega)}{\varepsilon_o} = \kappa'(\omega) - i\kappa''(\omega)$$

An alternating electric field propagating through the sample gives the effect to the polarity of the atoms or molecule following the oscillation in full circulation. The inner process yields the dissipation energy because of the molecules friction. The first term in the right side of Equation 6.12 is addressed as the capacity energy of substance, whereas the imaginary part is more emphasized on loss of energy in material in term of heat [56].

Dielectric constant of the rock depends on various parameters, such as mineral content, porosity, pore-fluid, temperature and fracture. Silicate and carbonate minerals have very low relative dielectric permittivity in range of $4-9$ [4]. Table 6.1 shows the values of relative dielectric carbonate and silica minerals. The evaluated mineral dielectric compilations published by Olhoeft [57] and Schon [4] are listed in this study.

Gas, oil and water have different relative dielectric values. Gas and oil are grouped as nonconductor fluids whereas water is ionic conductors. The type, concentration, temperature, volume fraction and its distribution [4] mainly control the electric behavior of pore water. The relative dielectric value of fresh water is $\kappa = 81$

and oil $\kappa < 3$. Since those two types of fluids have obviously different relative dielectric values, the fluid differentiation by using this parameter is considered applicable.

Table 6.1 Relative dielectric permittivity [4] ; D-[58]; P-[59]; O-[57]; K-[60].

Mineral	κ
Carbonates	
calcite	6.35 (O); 7.5 - 8.7 (D,P)
dolomite	7.46 (O); 6.3 - 8.2 (P); 6.8 - 8 (K)
aragonite	8.67 (O); 7.4 (P)
siderite	9.3 (O); 5.2 - 7.4 (P)
Silicates	
quartz	4.5 (O); 4.19 - 5 (K)
sillimanites	11 (O)
augite	9.3 (O); 6.9 - 10.3 (K)
amphiboles	8.0 (O); 4.9 (D); 6.5 (P)
muscovite	7.6 (O); 6.2 - 8.0 (K,P)
biotite	6.3 (O); 6.2 - 9.3 (K)
chlorite	9.0 (O)
kaolinite	11.8 (O); 9.1 (P)

The hysteresis must be taken into account when evaluating the electrical resistivity or dielectric well logs. The wettability has dominant influence on the resistivity and the water saturation interrelationship. The resistivity characteristic of water-wet and oil-wet condition may provide different results due to the presence of thin film and water distribution. Thus the cycles of drainage-imbibitions observation have to be considered during the evaluation.

6.3 Electrical Double Layer

Electrical double layer (EDL) is formed on the interface of pore water and solid grain. The presence of EDL may contribute to electrical properties of rock, depending on pore fluid, pore geometry, and saturation. The high salinity is mainly influenced by bulk volume of conduction process while the low salinity is influenced by interlayer or fluid-grain surface conductivity [4, 13, 15, 16]. The previous one is usually compensated by Archie's law and well known as a tool to determine water saturation.

Employing Archie's law on the shaly sandstone is insufficient due to ignoring surface conductivity effect on the shale mineral. Complete expression of effective conductivity is therefore

$$\sigma_o = \frac{\sigma_w}{F} + \sigma_q \qquad\qquad 6.13$$

where σ_q is surface conductivity. The effect of EDL on electrical properties of rock also depends on ratio of interface surface thickness to pore radius [4]. If the pore radii are small, the double layer can touch each other and may barriers the anion. While for the larger pore radii, the ion motion is undisturbed (Figure 6.3).

Khairy, H et.al [31] carry out the laboratory measurement on shaly sandstone and find that the partial saturation has a significant effect on the resistivity curve dispersion due to EDL and produced small changes with confining pressure. Our study shows that the electrical double layer (EDL) is also present in high water salinity especially in low water saturation degree. Thus, there is a need to develop a new electrical dispersion model that can cover from the relatively low frequency to the high frequency. The more saturated the brine fluid, the lesser the dispersion appears (Figure 6.4). Klien-Swift [47] notes, if these measurements want to be compared to the dispersion model developed by them, that water fluid only does not contribute to the permittivity dispersion in great effect (Table 6.2 and Figure 6.5). These results agree with the experiment showing that EDL should be playing a major contribution to the electrical properties of rock.
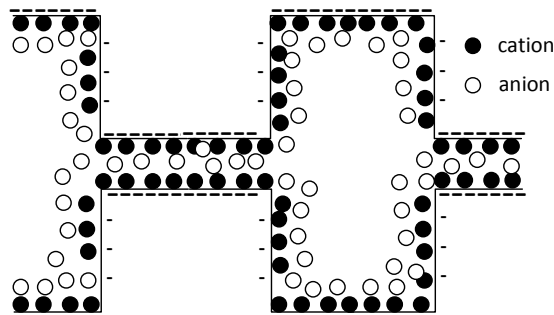
Figure 6.3 Mechanism of the anion barriers due to change of pore radius (after Schon, 1998).

The presence of clay minerals throughout the rock either dispersed or coated may cause membrane polarization as discussed in Section 6.1. The effective conductivity model then must be modified to take into account interlayer conductivity although in high salinity as noted in Equation 6.18. Therefore, in low water saturation, interfacing conductivity still exists, but disappearing when saturation is increased.

Basically, most of the models are established based on parallel conductor systems that are *electrolytic* and *clay* components. Archie's relationship takes place the electrolytic part meanwhile clay components can be evaluated either by considering various clay types and distributions or by understanding physical and chemical phenomena at the border of grain and fluid. The simplest model to calculate the effective conductivity/permittivity is based on clay distributions, mixing composite model. This is developed by assuming quasi-static approximation in which the electromagnetic wavelength is much larger than the characteristic size of rock constituents, pores and grains.

Table 6.2 Water conductivity and dielectric constant calculated by Klein-Swift formula at temperature 23° Celcius.

No	Salinity (ppm)	σw (S/m)	κ
1	1.2	2.10E-04	78.9
2	10	1.75E-03	78.9
3	100	0.018	78.9
4	1000	0.174	78.6
5	3000	0.513	78.2
6	7000	1.164	77.2
7	10000	1.631	76.6
8	40000	5.7	70.5
9	80000	10.3	57
10	100000	11.312	44.9
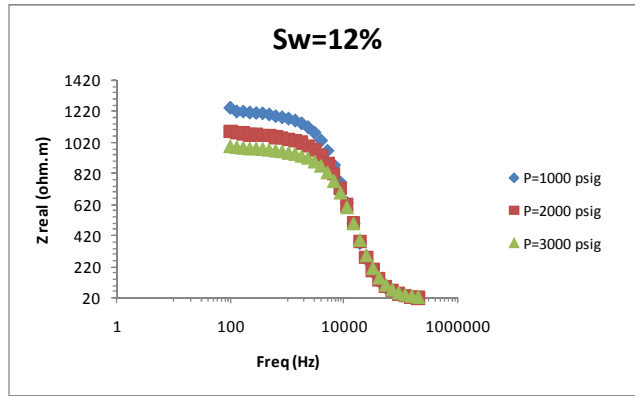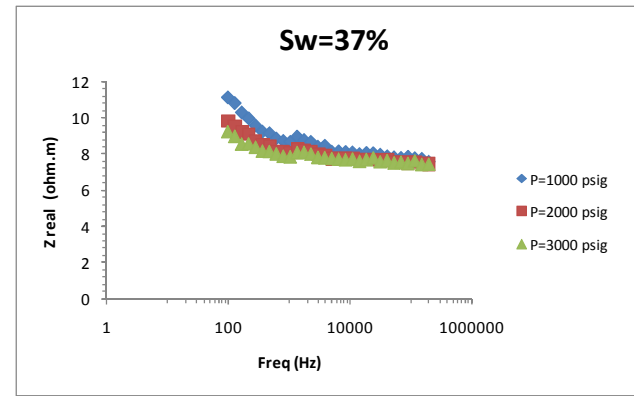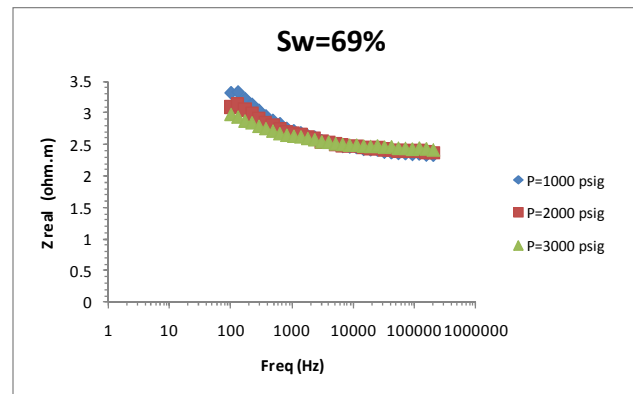
Figure 6.4 Resistivity dispersion with partial saturation and confining pressure in shaly sandstone: (a) Sw=12%; (b) Sw=37%; (c) Sw=69% [31].
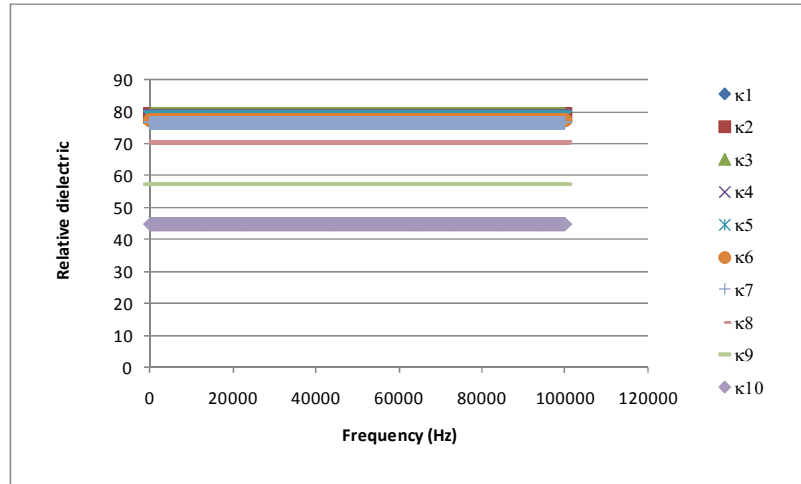
Figure 6.5 Relative dielectric permittivity of water fluid with different conductivity generated by Klein-Swift model.

In 1997, Revil and Glover [16] present the surface conductivity model based on surface chemical reactions description and electrical diffuse layer processes. This model is dedicated for the condition of diffuse layer thickness smaller than local radius of mineral surface and its pore size. The model is also considered an amphoteric mineral surface and derives the fractional occupancies of positive, negative, and neutral sites on the surface, and the fractional ionic diffuses layer densities, as a function of the salinity and the pH. Result of the model is that the electrical surface conduction has a dependency on electrolyte concentration and pH. Lima and Sharma [17, 18] study the grain conductivity by considering self-similar mixtures of conductive grain. Later, they generalize the result to evaluate Maxwell-Wagner theory for membrane polarization in shaly sandstones. There are two possibilities of polarization mechanisms that occur, i.e. bound layer and diffusive layer polarization. At the following sub-chapters, the mechanism and theoretical model will be presented in detail.

6.4 Model Consideration

Either a static or time dependent electromagnetic model is presented to explain electrical properties of reservoir rock. It is developed when Archie [1] published his fundamental empirical work and continuously improves to cover the recent problems. The electrical static model can be applied to the time dependent electromagnetic model if certain conditions are satisfied. In case of rocks, the static model is considered if the electromagnetic wavelength is much larger than the rock constituent, such as pores and grain size.

As shown in Figure 6.6, the permittivity of medium is kept constant at 80 and it is found that for frequency of less than 1 MHz, the wavelength is significantly larger than the typical pore size of more than 1 m. This condition is sufficiently valid when compared to the pore size diameter in order of 0.0001 m. The evaluation on skin depth penetration also gives the larger result than pore diameter (Figure 6.7). It means the electromagnetic field intensity does not change significantly. With those results, the mixing law can be utilized to evaluate electrical properties in certain frequency.

6.4.1 Mixing Model

Numerous mixing models are now available. Basically the model is built based on two or three components. Two component models refer to the rock with only one conductive. Meanwhile three components are considered more than one and in the present work are pore water fluid and clay.

6.4.1.1 Two Components Mixing Model

The two-component mixing model is usually classified into three:

a. Sheet models

Sheet models are presented as parallel (harmonic) or series (arithmetic) electrical resistivity.

$$\frac{1}{\rho_{eff}} = (1-\phi)\frac{1}{\rho_m} + \phi\frac{1}{\rho_w} \qquad \text{(parallel)}$$

$$\rho_{eff} = (1-\phi)\rho_m + \phi\rho_w \qquad \text{(series)}$$

In terms of conductivity

$$\sigma_{eff} = (1-\phi)\sigma_m + \phi\sigma_w \qquad \text{(parallel)}$$

$$\frac{1}{\sigma_{eff}} = \frac{(1-\phi)}{\sigma_m} + \frac{\phi}{\sigma_w} \qquad \text{(series)}$$

The resistivities described by parallel and series models are two extreme cases where the lowest possible resistivity and the highest possible resistivity may be present (Figure 6.8). Visualization of the model may refer to Figures 6.9.

b. Pore channel models

In the pore channel models, the tube as depicted in Figure 6-10, is analyzed. This model is preferred as an idealization of electrical conductivity of water saturated clean porous rock.

The effective resistivity is calculated by

$$\rho_{eff} = \rho_w \frac{T^2}{\phi}$$

where T is tortuosity, defined as $T = \frac{l}{L}$. The longer the path of the pore throat, the higher the effective resistivity will be (Figure 6.11).
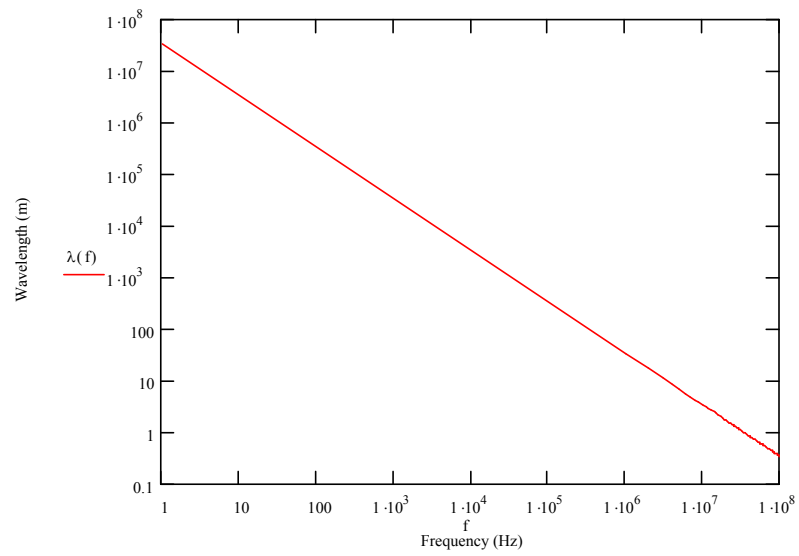
Figure 6.6 Dependency of EM wavelengths on frequency.
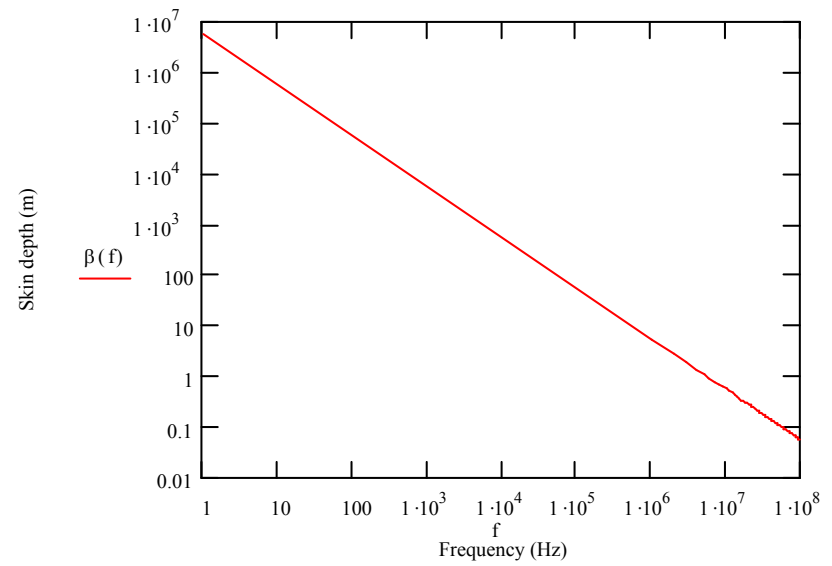
Figure 6.7 Skin depth analyses on frequency. The medium permittivity is 80.

c. Inclusion models

Various models exist to evaluate electrical properties of composite substance. The inclusion models are derived by assuming the spherical inclusion dispersed in the rock. Maxwell-Garnet [61], for example, may assume the grain as a background and the fluid as an inclusion, and vice versa. Equation 6.14 expresses that the background is matrix and water is included while Equation 6.15 is reversed.
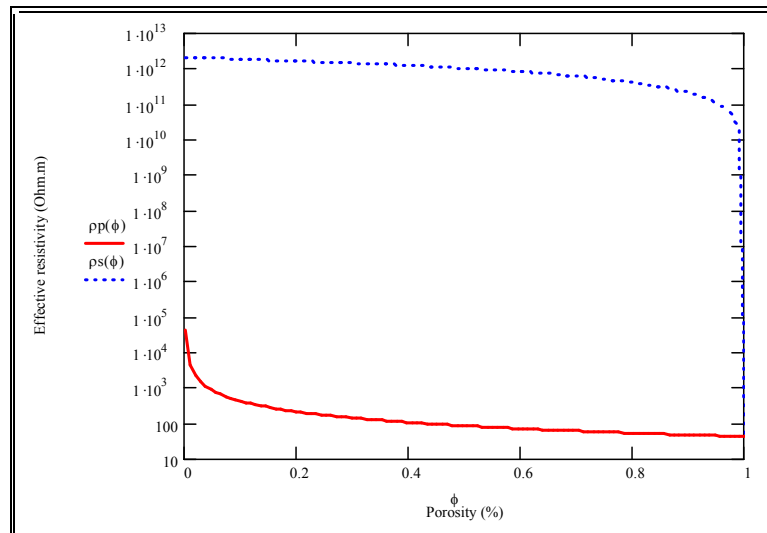
Figure 6.8 Boundary of resistivity based on parallel (red) and series (dot blue) models. Resistivity of silicates matrix and water are 2.10^{12} Ohm.m and 41.7 Ohm.m respectively.
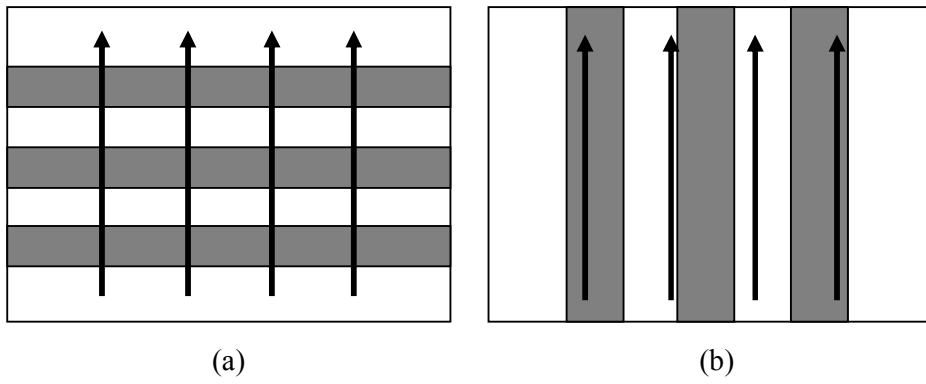
Figure 6.9 Effective medium model (a) series model (b) parallel model.
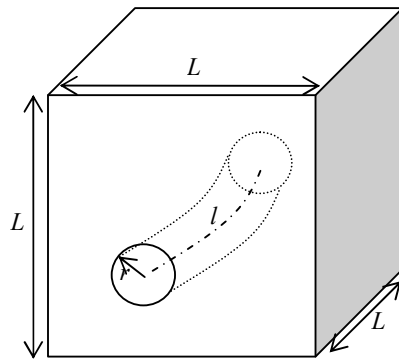
Figure 6.10 Pore tube model whereas *r, l* and *L* are tube radius, length of capillary and cube length respectively.
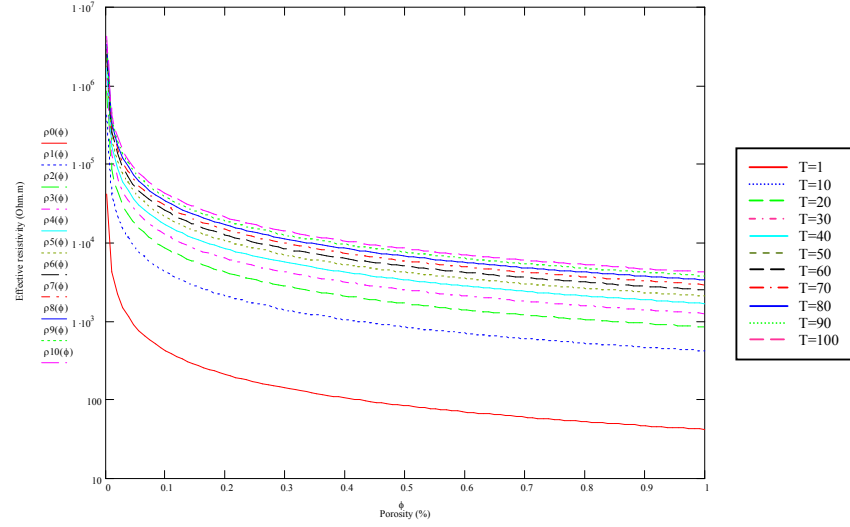
Figure 6.11 Plot of effective resistivity with porosity water resistivity is 41.7 Ohm.m
The tortuosity *(T)* is increased from 1 until 100.

$$\sigma_{eff} = \sigma_m + 3\sigma_m \left(\frac{\phi \dfrac{[\sigma_w - \sigma_m]}{\sigma_w + 2\sigma_m}}{1 - \phi \dfrac{[\sigma_w - \sigma_m]}{\sigma_w + 2\sigma_m}} \right) \qquad\qquad 6.14$$

$$\sigma_{eff} = \sigma_w + 3\sigma_w \left(\frac{\dfrac{[1-\phi][\sigma_m - \sigma_w]}{\sigma_m + 2\sigma_w}}{1 - \dfrac{[1-\phi][\sigma_m - \sigma_w]}{\sigma_m + 2\sigma_w}} \right) \qquad\qquad 6.15$$

Other models ignoring the host and inclusion terms are Hanai-Bruggeman and Wagner models [62]. They derive the general relationship for the calculation of the heterogeneous mixtures by considering individual fraction components and properties. The models are:

113

(Hanai-Bruggemen)

$$\frac{\sigma_{eff} - \sigma_m}{\sigma_w - \sigma_m}\left(\frac{\sigma_w}{\sigma_{eff}}\right)^{\psi} = \phi$$
6.16

where ψ is depolarization factor

(Wagner)

$$\sigma_{eff} = \sigma_w\left(\frac{2\sigma_w + \sigma_m - 2\phi[\sigma_w - \sigma_m]}{2\sigma_w + \sigma_m + \phi[\sigma_w - \sigma_m]}\right)$$
6.17

If depolarization factor ψ in Hanai-Bruggemen model is set to 0 or 1, the geometry changes into serial and parallel respectively (Figure 6.12).
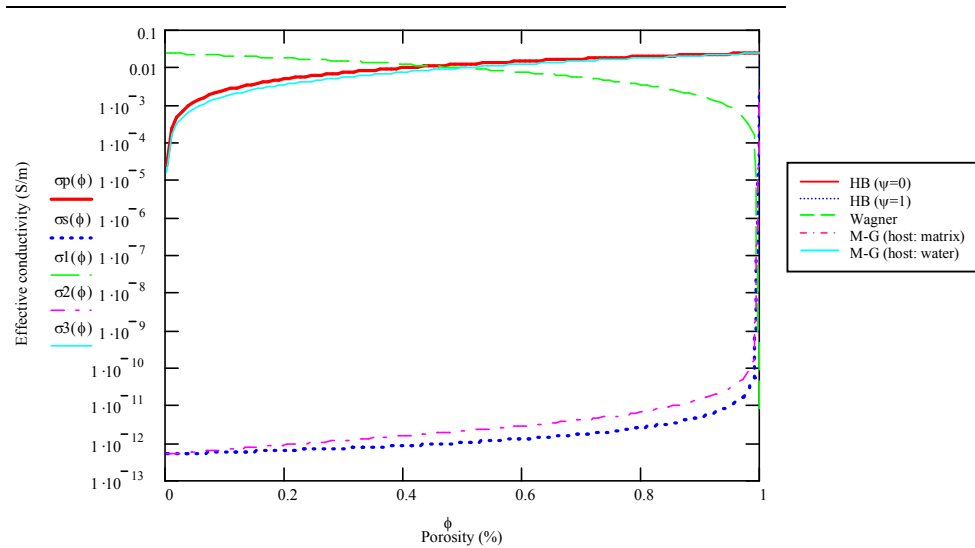
Figure 6.12 Plot of conductivity model. Conductivity of water and silica are 0.024 S/m and 2×10^{-12} respectively.

6.4.1.2 Three Components Mixing Model

The previous model is known as a clean rock model that is built based on two components: conducting (water) and non-conducting (solid matrix). The three components consider one more conducting component, i.e. clay. Laminated shale and dispersed shale are the two most evaluated models.

a. Laminated shale model

Series of shale-sand lamination is used for this model. The shale and sand behave as two parallel conductors electrically. The effective conductivity of the rock is formulated as

$$\sigma_{eff} = (1 - V_{sh})\frac{\sigma_w}{F_{sd}} + V_{sh}\sigma_{sh}$$

where F_{sd}, V_{sh} are formation factors related to sand layer and volume shale respectively. Formation factor of sand layer can be calculated by

$$F_{sd} = \frac{a}{\phi_{sd}^m}$$

where

$$\phi_{sd} = \frac{\phi}{1 - V_{sh}}$$

Model of laminated shale and plot of effective conductivity as a response of volume shale are depicted on Figure 6.13.

(a)   (b)
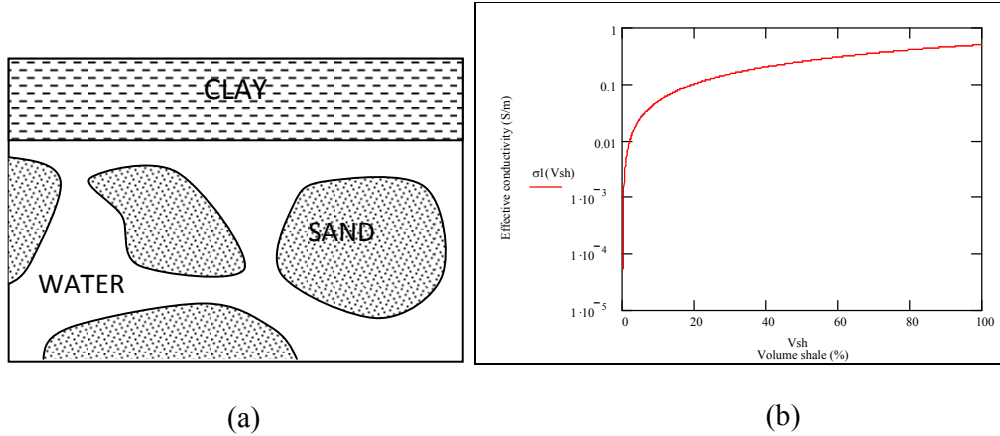
Figure 6.13 (a) Laminated shale-sand model (b) Plot of effective conductivity with volume shale. Shale conductivity is $\sigma_{sh} = 5 \times 10^{-3}$ S/m.

b. Dispersed shale model

A dispersed model following the behavior of electrical current flows through the mixture of pore water and dispersed clay. Maxman and Smith [63] propose the model of this dispersed clay as

$$\sigma_{eff} = \frac{1}{F}\left(\sigma_w + BQ_v\right)$$

where F is formation factor analogy with Archie's equation, and B and Q_v represent the average mobility of the counterions near the grain surface and concentration of clay exchange cations respectively.

Lima and Sharma [17] formulated another dispersed clay model as

$$\sigma_{eff} = \frac{1}{F}\left[\sigma_w + \frac{3p}{2}(F-1)\sigma_{sh}\right]$$

where p is volume fraction of clay in solid portion. Figure 6.14 is the model of dispersed clay and plot of its effective conductivity.

116

(a)   (b)
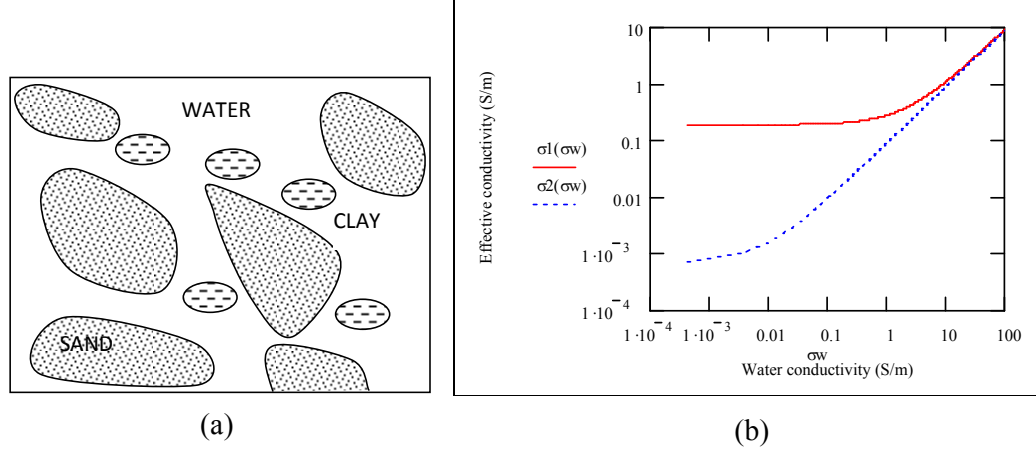
Figure 6.14 (a) Conductivity dispersed shale model; (b) Plot of effective conductivity as a function of water fluid conductivity for Maxman-Smith (Red) and Lima-Sharma (dot blue). Medium is water fluid with σ_w=0.024 S/m, σ_{sh} = 5 x 10^{-3} S/m, p=0.1 B=0.689 m^2/V.s, kaolinite cation exchange Qv=3 meq/100g.

6.4.2 Dispersion Model

Classical approach to figure out electrical dispersion is introduced by Debye [64]. He analytically derive the dielectric relaxation model dependent on frequency as

$$\varepsilon^*(\omega) = \varepsilon_\infty + \frac{(\varepsilon_o - \varepsilon_\infty)}{1 + i\omega\tau} \qquad\qquad 6.18$$

where $\varepsilon_o, \varepsilon_\infty, \omega, \tau$ are static dielectric coefficient (DC mode), dynamic dielectric coefficient (AC mode), frequency and relaxation time respectively. This model is established based on a certain assumption for simplicity as follow [53]:

1. The local field is the same as the external field

2. The conductivity of the materials is negligible

3. The dipoles only have single relaxation time

117

As reservoir rock comprises of multi-minerals and various pore fluid types, it is insufficient to use Debye model to describe multi-relaxation inside the rock. To consider many relaxation processes, Cole-Cole [65] proposes revision for previous model as

$$\varepsilon^*(\omega) = \varepsilon_\infty + \frac{(\varepsilon_o - \varepsilon_\infty)}{1 + (i\omega\tau)^{1-\alpha}}$$

$(1-\alpha)$ represents the relaxation distribution parameter. If the DC conductivity is taken into account, the Cole-Cole model above then becomes:

$$\varepsilon^*(\omega) = \varepsilon_\infty + \frac{(\varepsilon_o - \varepsilon_\infty)}{1 + (i\omega\tau)^{1-\alpha}} - i\frac{\sigma}{\omega\varepsilon_o}$$

The mathematical representation of Debye and Cole-Cole models in argand plot shows a semi-circle form (Figure 6.15) as expressed in the Appendix F, derivation of semi circle of Debye and Cole-Cole model.

Mathematically dispersion model introduced by Debye and Cole-Cole does not consider the effect of thin double layer and charged clay. The presence of shaly material consequently adds the surface conductivity (see Section 6.3) and should be calculated while evaluating the electrical conductivity in low salinity regime. Later, Lima and Sharma [18] release the model of shaly material for the membrane polarization. The membrane polarization is defined through two mechanisms; they are bound layer (S-model) and diffusive polarization (D-model).

$$\sigma_c^* = \sigma_{c,\infty} - \frac{\sigma_{c,0}}{1 - i\omega\tau} \quad \text{(S-model)} \qquad\qquad 6.19$$
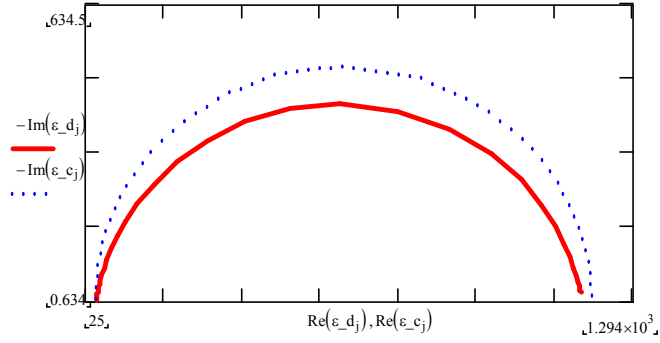
(a)
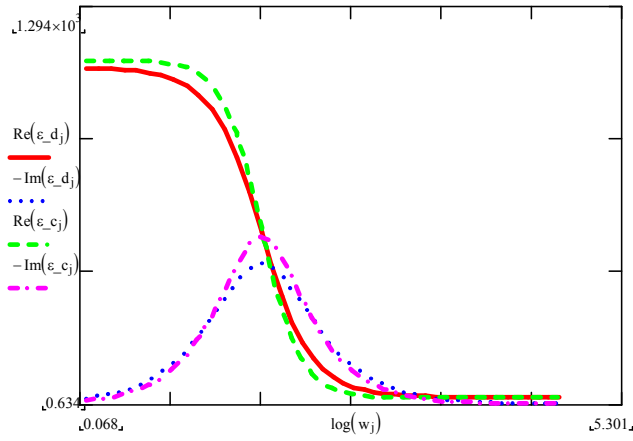
(b)

Figure 6.15 (a) Plot of dielectric model of Debye (red) and Cole-Cole (dot blue); (b) Real and imaginary dispersion of Debye model (red and dot blue) and Cole-Cole (green and magenta).

where

$$\sigma_{c,0} = 2\frac{\lambda_0}{a}$$

$$\sigma_{c,\infty} = 2\frac{(\lambda + \lambda_0)}{a}$$

Equation 6.19 conceptually has similarity to the Debye's equation as in Equation 6.18. Symbols of λ, λ_0, a, ω, τ refer to surface conductivity of diffusive layer, surface conductivity of fix thin layer, particle radius, angular frequency and relaxation time

119

respectively. Because counterions are not tightly bound to solid parts, some of them diffuse close to particles as depicted in Figure 6.16. Another model, called the D-model which is analogously similar to Cole-Cole formula, is developed. The D-model is formulated as

$$\sigma_c^* = \sigma_{c,\infty} + \frac{\sigma_{c,0} - \sigma_{c,\infty}}{1 + f(\omega,\tau)i^{-(1-\alpha)}} \quad \text{(D-model)}$$

where

$$\sigma_{c,\infty} = \delta_1 \sigma_w$$

$$\sigma_{c,0} = \frac{2\delta_1 \sigma_w}{2 + \delta_1}$$

$$f(\omega,\tau) = \frac{2\omega\tau}{\left(2+\delta_1\right)\left[\left(1+\sqrt{\omega\tau}\right)^2 + \omega\tau\right]}$$

$$\delta_1 = \frac{\beta_1}{aC_1}$$

In this notation, β_1 refers to surface counterion density required to balance immobile charges on the particle having radius a; and C_1 is the cationic concentration in the electrolyte.
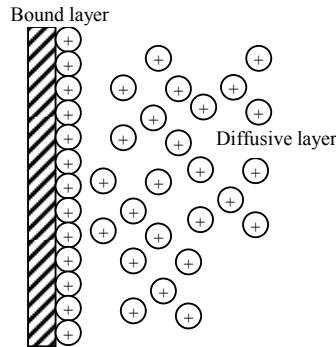
Figure 6.16 Illustration of bound layer and diffusive layer.

In order to extend those single particles into shaly material, Wagner's model is used and the form of effective conductivity is rearranged as

$$\sigma_o^* = \sigma_{o,0} - \frac{i\omega\tau_m\left[\sigma_{o,\infty} - \sigma_{o,0}\right]}{1 - i\omega\tau_m} - i\omega\varepsilon_{o,\infty}$$

where

$$\sigma_{o,0} = \sigma_w\left[\frac{2\sigma_w + \sigma_{c,0} - 2p\left(\sigma_w - \sigma_{c,0}\right)}{2\sigma_w + \sigma_{c,0} + p\left(\sigma_w - \sigma_{c,0}\right)}\right]$$

$$\sigma_{o,\infty} = \varepsilon_{o,\infty}\frac{\sigma_w}{\varepsilon_w} - \frac{9p\left[\sigma_w\varepsilon_{c,\infty} - \varepsilon_w\sigma_{c,\infty}\right]}{\left[2\varepsilon_w + \varepsilon_{c,\infty} + p\left(\varepsilon_w - \varepsilon_{c,\infty}\right)\right]^2}$$

$$\varepsilon_{o,\infty} = \varepsilon_w\left[\frac{2\varepsilon_w + \varepsilon_{c,\infty} - 2p\left(\varepsilon_w - \varepsilon_{c,\infty}\right)}{2\varepsilon_w + \varepsilon_{c,\infty} + p\left(\varepsilon_w - \varepsilon_{c,\infty}\right)}\right]$$

$$\tau_m = \frac{2\varepsilon_w + \varepsilon_{c,ef} + p\left(\varepsilon_w - \varepsilon_{c,ef}\right)}{2\sigma_w + \sigma_{c,ef} + p\left(\sigma_w - \sigma_{c,ef}\right)}$$

$$\varepsilon_{c,0} = \frac{2\delta_1}{2 + \delta_1}\left(\varepsilon_w + \frac{\delta_1\tau\sigma_w}{2 + \delta_1}\right)$$

$$\varepsilon_{c,\infty} = \delta_1\varepsilon_w$$

The plot of effective conductivity for shaly material shows a circular arcs with spurs at very high frequency is given in Figure 6.17. The parameters used in the model are the same as Lima-Sharma's [18] i.e. $a=9\times10^{-7}$ m; $\beta_l=1.2\times10^{18}/\text{m}^2$; $\sigma_w=0.024$ S/m; $\varepsilon_w=6.9\times10^{-10}$ F/m; $D_l=2\times10^{-9}$ m^2/s; p=0.39; $\tau_m=2\times10^{-4}$ s

121
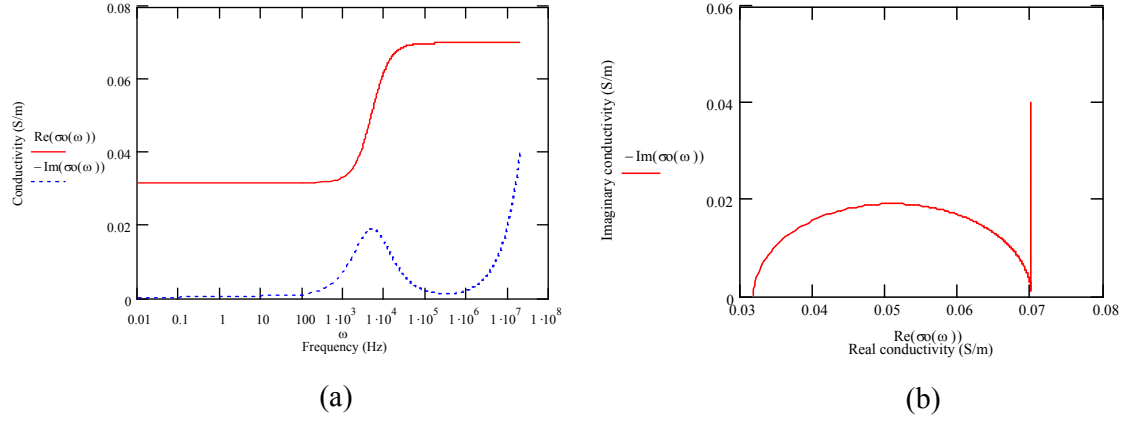
Figure 6.17 (a) plot of shaly material conductivity by using D-Model (red) and Wagner composite model (dot blue); (b) plot of real versus imaginary resistivity.

An electrical dispersion properties model of spherical sand grain coated by an aggregate of clay is made by introducing coating clay as directed by Lima and Sharma [17] as

$$\sigma_m^* = \sigma_c^* \left[\frac{2p\sigma_c^* + (3 - 2p)\sigma_a^*}{(3 - p)\sigma_c^* + p\sigma_a^*} \right] \qquad 6.20$$

into Hanai-Brugemen (Equation 6.16) and Wagner formula (Equation 6.17). Result of the coated clay-sand model with approximation is made for $\varepsilon_{cs} \gg \varepsilon_w$ and $\sigma_w \gg \sigma_{cs}$ is

a. Wagner model

$$\sigma_o^* = \sigma_w \left[\frac{2(1-\phi)(2+\phi)\sigma_w^2 + \omega^2 \varepsilon_{cs}^2 (2\phi+1)(1-\phi) - i\omega\varepsilon_{cs}\sigma_w \left[(2\phi+1)(2+\phi) - 2(1-\phi)^2 \right]}{(2+\phi)^2 \sigma_w^2 + \omega^2 \varepsilon_{cs}^2 (1-\phi)} \right] \quad 6.21$$

where

$$\varepsilon_{cs} = \frac{2p\varepsilon_{cef}}{3 - p} \qquad\qquad \varepsilon_{cef} = \frac{\delta_1(1 + \delta_1 A)\varepsilon_w + \delta_1^2 B \dfrac{\sigma_w}{\omega}}{(1 + \delta_1 A)^2 + \delta_1^2 B^2}$$

122

b. Hanai-Bruggemen

$$\sigma_o^* = \phi\sigma_w + i\omega\varepsilon_{cs}(\phi-1) \qquad\qquad (\psi=0) \qquad 6.22$$

$$\sigma_o^* = \frac{\sigma_w\omega\varepsilon_{cs}}{\left[\dfrac{\phi(q+r)}{2}+i\sigma_w\left(\dfrac{-\phi(q+r)}{2\omega\varepsilon_{cs}}+1\right)\right]} \qquad\qquad (\psi=1/2) \qquad 6.23$$

$$\sigma_o^* = \frac{\phi\omega^2\varepsilon_{cs}^2\sigma_w + i\omega\varepsilon_{cs}\sigma_w^2(\phi-1)}{\sigma_w^2(\phi-1)^2+(\phi\omega\varepsilon_{cs})^2} \qquad\qquad (\psi=1) \qquad 6.24$$

where

$$q = \phi(\omega\varepsilon_{cs}-i\sigma_w) \quad\text{and}\quad r = \left[\phi^2\left(\omega^2\varepsilon_{cs}^2-\sigma_w^2\right)+i2\omega\varepsilon_{cs}\sigma_w\left(2-\phi^2\right)\right]^{\frac{1}{2}}$$

Figure 6.18 displays the dispersion of conductivity and dielectric permittivity from Wagner's and Hanai-Bruggemen models (Equation 6.21 to 6.24).

In term of salinity, the conductivity and dielectric permittivity dispersion cause significant changes when a salinity of pore fluid is increased. Figure 6.19 shows that both conductivity and dielectric permittivity dispersion generated by Wagner's model are higher as salinity is added.

In spite of Lima-Sharma's model successfully explains the dispersion for shaly material in range of frequency of 100 Hz to 1 MHz, this model is still incomplete because it does not account the saturation effect. Some results noted by [4, 13, 15] say that the surface conductivity has to be taken into account in low salinity regime, whereas the bulk volume conductivity (Archie's model) is more dominant and replaces the relationship in high salinity regime (see Equation 6.13). However, the experimental result in high water salinity by Khairy and Zuhar [66] shows that electrical dispersion effect remains in existence in initial low saturation degree and vanishes when saturation increases.
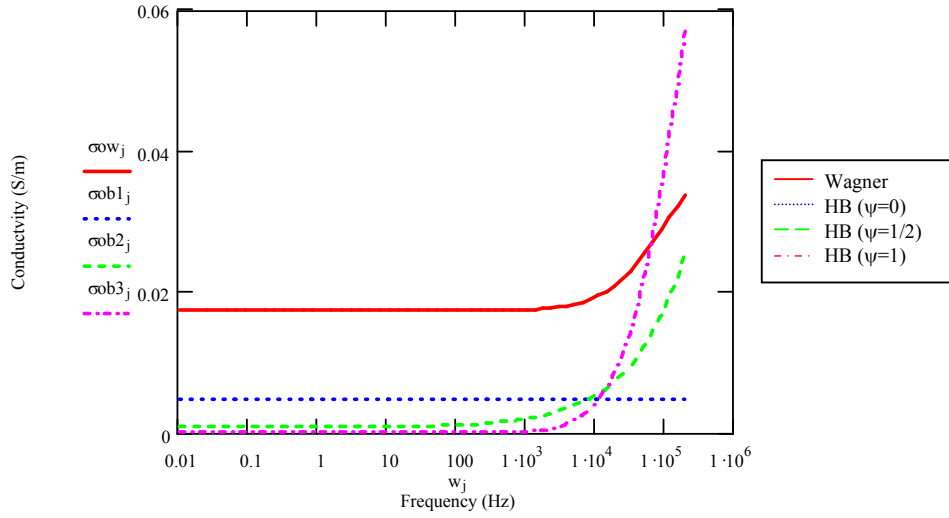
(a)
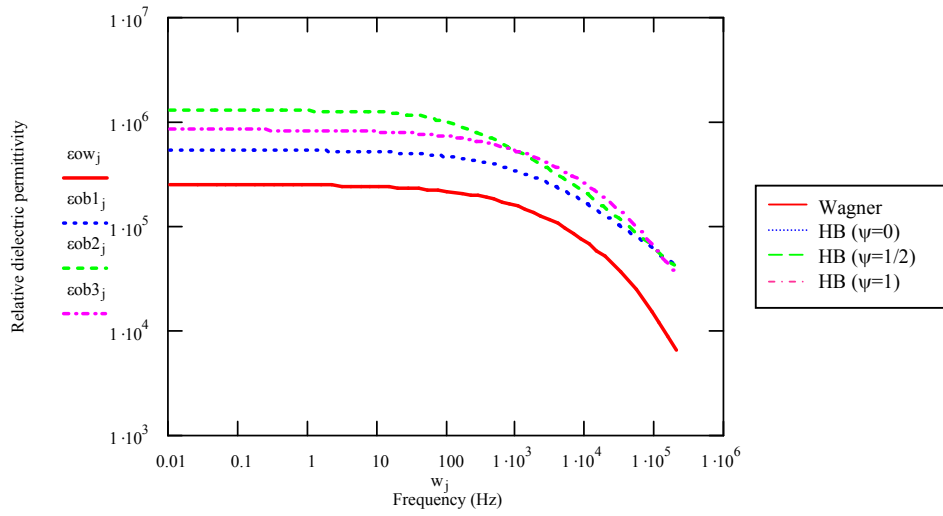
(b)

Figure 6.18 Display of conductivity (a) and dielectric permittivity (b) for sand-clay system based on Wagner and Hanai-Bruggemen model. Input parameter are the same with Figure 6-17.
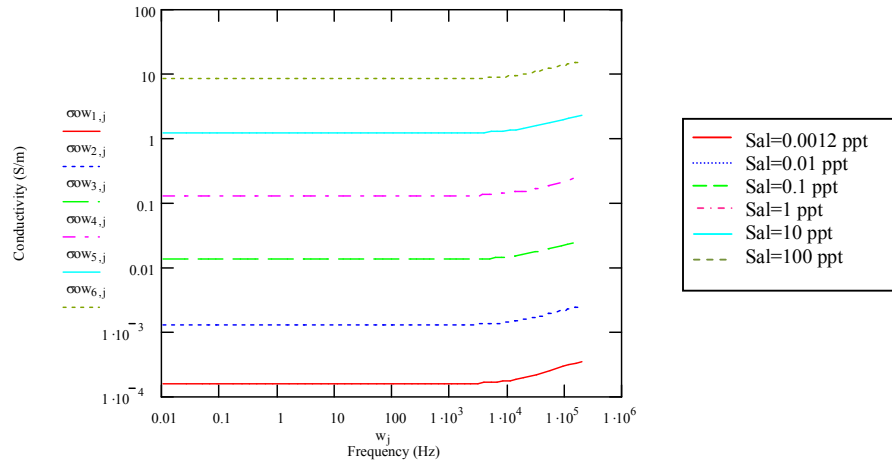
(a)
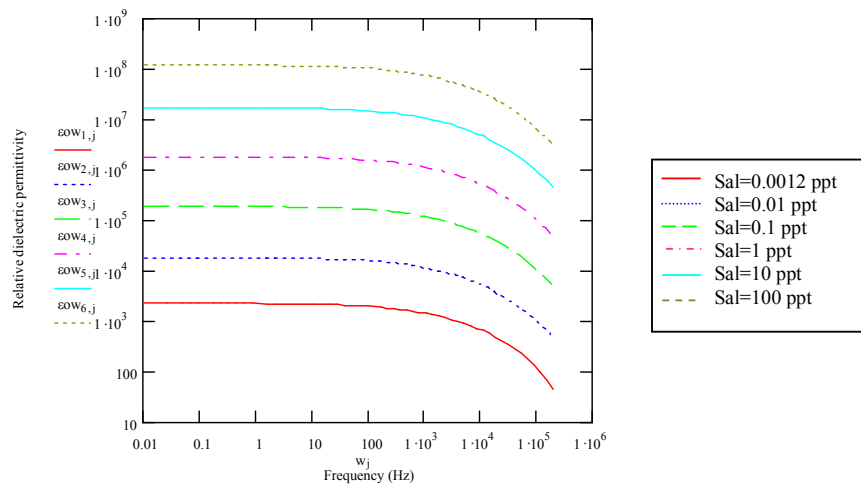
(b)

Figure 6.19 Salinity effect on conductivity (a) and dielectric permittivity
(b) dispersion based on Wagner's model.

The effect of double layer should not be ignored if the medium is in low water saturation condition; unless it is in high water saturation level where the bulk volume factor is introduced (an illustration saturated-desaturated shown in Figure 6.20). In other word, the surface conductivity must be accounted, even in high water salinity. To make this result agree to the model, the improvement should be introduced to account partial saturation.
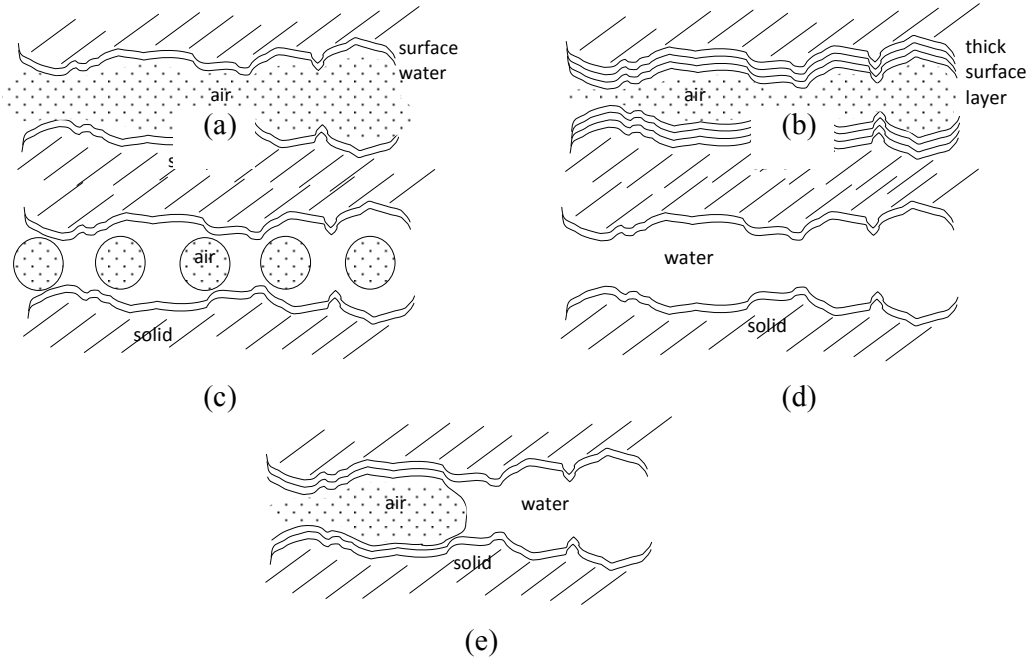
Figure 6.20 Illustration of saturated-unsaturated process in rock media. (a) surface water coating the grain solid in low partial saturation; (b) during saturation thick surface water layer developed; (c) while increasing water saturation, fluid reorganize to make more stable; (d) fully water saturation are achieved; (e) beginning of unsaturated process, thin layer still exist while pore space fluid removed.

6.4.3 Development New Dispersion Model

Dispersion model developed previously by Lima-Sharma [18] is dedicated for low salinity fluid. Electrical double layer may be exist as long as the solid grain makes a contact with the pore-fluid. Therefore, this new model developed should take into the account the partial saturation. Electrical double layer plays a role in low water saturation and bulk volume conductivity; more dominantly in high water saturation.

By evaluating Maxwell equations and their constitutive relationship with subjected time dependence of harmonic sinusoidal field $\left(e^{-i\omega t}\right)$ it can be obtained that:

$$J^{*}\left(\omega\right)=\left(\sigma\left(\omega\right)-i\omega\varepsilon\left(\omega\right)\right)E\left(\omega\right)\equiv\sigma^{*}\left(\omega\right)E\left(\omega\right) \qquad 6.25$$

The electrical properties of composite conductive minerals having dispersed spherical particles deduced from Wagner's theory can be written as (see Equation 6.17)

$$\sigma_o^* = \sigma_w^* \left[\frac{2\sigma_w^* + \sigma_c^* - 2\phi\left(\sigma_w^* - \sigma_c^*\right)}{2\sigma_w^* + \sigma_c^* + \phi\left(\sigma_w^* - \sigma_c^*\right)} \right]$$

whereas ϕ, σ_o^*, σ_w^*, σ_c^* are porosity, total electrical conductivity, fluid and solid grain respectively. Each of conductivities is a complex function as shown by Equation 6.25 as follow:

$$\sigma_o^* = \sigma_o - i\omega\varepsilon_o$$

$$\sigma_w^* = \sigma_w - i\omega\varepsilon_w$$

$$\sigma_c^* = \sigma_c - i\omega\varepsilon_c$$

The presence of clay-coated sand grain will replace σ_c^* with Equation 6.20

$$\sigma_m^* = \sigma_c^* \left[\frac{2p\sigma_c^* + (3-2p)\sigma_a^*}{(3-p)\sigma_c^* + p\sigma_a^*} \right]$$

In this case σ_c^* and σ_a^* are refer to solid clay and non-conducting mineral. For most sandstone detrital minerals $\sigma_a^* = 0$ [17]. The parameter p refers to volume fraction of clay and normally equal to $1 - \left(\frac{a}{b}\right)^3$ $\left[p = 1 - \left(\frac{a}{b}\right)^3 \right]$ with a and b are the radius of core and the radius of composite sphere. The parameter σ_m^* refers to an effective complex conductivity of grain and it is associated with double layer effect. This complex conductivity depends on particle dimension, salinity and surface charge density. The complex conductivity of solid clay σ_c^* is given by

$$\sigma_c^* = \frac{\delta_1 \sigma_w^*}{1 - \delta_1 Y} \qquad\qquad 6.26$$

where Y is the complex number given by

$$Y = -\frac{1+(1-i)\sqrt{\omega\tau}}{2+2(1-i)\sqrt{\omega\tau}-2i\omega\tau} \qquad 6.27$$

Variable τ represents relaxation time for the double layer around the charged particle. Relaxation time explains period of polarization before electrical field direction changes notably. By referring to Equation 6.25, conductivity of solid clay has a complex function as

$$\sigma_c^* = \sigma_{cef} - i\omega\varepsilon_{cef} \qquad 6.28$$

By evaluating Equation (6.26) and (6.27) it is obtained

$$\sigma_{cef} = \frac{\delta_1\left(1+\delta_1 A\right)\sigma_w - \omega\delta_1^2 B\varepsilon_w}{\left(1+\delta_1 A\right)^2 + \delta_1^2 B^2}$$

$$\varepsilon_{cef} = \frac{\delta_1\left(1+\delta_1 A\right)\varepsilon_w - \delta_1^2 B\dfrac{\sigma_w}{\omega}}{\left(1+\delta_1 A\right)^2 + \delta_1^2 B^2} \qquad 6.29$$

where

$$A = \frac{\left(1-y^3\right)}{2\left(1-y^4\right)} \qquad\qquad y = \sqrt{\omega\tau}$$

$$B = \frac{y^2\left(1-y\right)}{2\left(1-y^4\right)}$$

The experimental result from Chapter 5 indicates that dielectric properties depend on frequency in power-law (see Equation 5.1) at all levels of saturation and this is in line with other experimental results [2, 13]. To accommodate saturation effect, modification of Equation 6.28 should be made to incorporate power-law frequency as follows [67]

$$\varepsilon_{cef\_mod} = \frac{\delta_1 \left(1 + \delta_1 A\right) \dfrac{C\varepsilon_w}{\omega^q} - \delta_1^2 B \dfrac{C\sigma_w}{\omega^{1+q}}}{\left(1 + \delta_1 A\right)^2 + \delta_1^2 B^2}$$

where q is the constant that depends on the level of saturation. Substituting Equation 6.28 into Equation 6.20 gives

$$\sigma_m^* = \frac{2p}{3-p}\left(\sigma_{cef} - i\omega\varepsilon_{cef}\right)$$

$$\sigma_m^* = \sigma_m - i\omega\varepsilon_m \tag{6.30}$$

Then if Wagner's composite model is applied by substituting Equation 6.30, the following result is obtained:

$$\sigma_o^* = \sigma_w \left[\frac{2\left(\sigma_w - i\omega\varepsilon_w\right) + \left(\sigma_m - i\omega\varepsilon_m\right) - 2\phi\left[\left(\sigma_w - i\omega\varepsilon_w\right) - \left(\sigma_m - i\omega\varepsilon_m\right)\right]}{2\left(\sigma_w - i\omega\varepsilon_w\right) + \left(\sigma_m - i\omega\varepsilon_m\right) + \phi\left[\left(\sigma_w - i\omega\varepsilon_w\right) - \left(\sigma_m - i\omega\varepsilon_m\right)\right]} \right] \tag{6.31}$$

As noted from Garrrouch [68], approximation can be made to simplify Equation (6.31) by assuming that clay-sand grain permittivity ε_m is much greater than the water fluid permittivity ε_w and fluid conductivity σ_w is much greater than clay-sand grain conductivity σ_m. Using those two approximations the composite clay-sand grain conductivity can be simplified as

$$\sigma_o^* = \sigma_w \left[\frac{2\left(1-\phi\right)\sigma_w - i\omega\varepsilon_m\left(2\phi+1\right)}{\left(2+\phi\right)\sigma_f - i\omega\varepsilon_m\left(1-\phi\right)} \right]$$

Separating imaginary and real conductivity by multiplying their denominators with complex conjugate results in:

$$\mathrm{Re}\ \sigma_o^* = \sigma_w \left[\frac{2\left(1-\phi\right)\left(2+\phi\right)\sigma_w^2 + \omega^2\varepsilon_m^2\left(2\phi+1\right)\left(1-\phi\right)}{\left(2+\phi\right)^2\sigma_w^2 + \omega^2\varepsilon_m^2\left(1-\phi\right)^2} \right] \tag{6.32}$$

$$\text{Im } \sigma_o^* = \sigma_w \left[\frac{9\varepsilon_m \sigma_w \phi}{\left(2+\phi\right)^2 \sigma_w^2 + \omega^2 \varepsilon_m^2 \left(1-\phi\right)^2} \right] \qquad 6.33$$

Approximation for low and high frequencies yield

$$\text{Re } \sigma_{o(\omega\to\infty)} = \sigma_w \frac{\left(2\phi+1\right)}{\left(1-\phi\right)}$$

$$\text{Re } \sigma_{o(\omega\to0)} = \sigma_w \frac{\left(1-\phi\right)}{\left(2+\phi\right)}$$

$$\text{Im } \varepsilon_{o(\omega\to\infty)} = \frac{9\sigma_w^2 \phi}{\omega^2 \varepsilon_m \left(1-\phi\right)^2}$$

$$\text{Im } \varepsilon_{o(\omega\to0)} = \frac{9\varepsilon_m \phi}{\left(2+\phi\right)^2}$$

The presence of clay coated sand-grain in partial saturation produces an electrical double layer (EDL) when it contacts with small amount of water. The model that will be developed must be in agreement, in which in the low level water saturation interface conductivity, it has a significant contribution, but in high level saturation, it turns into bulk volume conductivity. Equation 6.13 then may be introduced by saturation factor and interfacing conductivity as follows:

$$\sigma_o = S_w^n \sigma_w \phi^m + \left(1-S_w\right)\left(1-\phi\right) N \sigma_q \qquad 6.34$$

where S_w, m, n, N, σ_q are water saturation, cementation factor, saturation exponent, water-coated volume factor, and spherical grain clay-sand conductivity (Equation 6.32) respectively. The coated-water volume factor represents the amount of water-film coating the grain. This intuitively has the similar analogy with irreducible water saturation, but with $N \ll S_w$. Figures 6.21a and 6.21b exhibit a comparativeness of relative dielectric permittivity calculated by the modified D-model (Equation 6.33) and its initial model and effective conductivity calculated from Equation 6.34. It is shown that the more saturation added, the less conductivity dispersion resulted. If the

full saturation is achieved, the model turns back to previous Archie's model (Figure 6.21b).

Modified D-model communicates with initial D-model throughout q parameter. Figure 6.22 presents relative dielectric permittivity with variation of q from 0 to 1.5. The increasing of q will lead to the gradient increase. If the q equals to 0, the modified D-model turns into initial one.

(a)

(b)
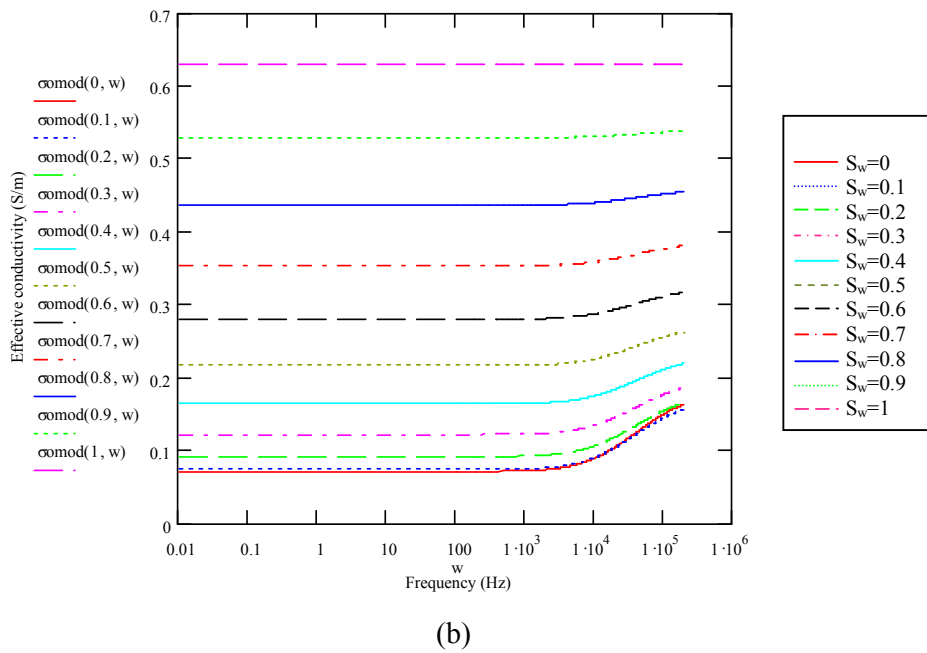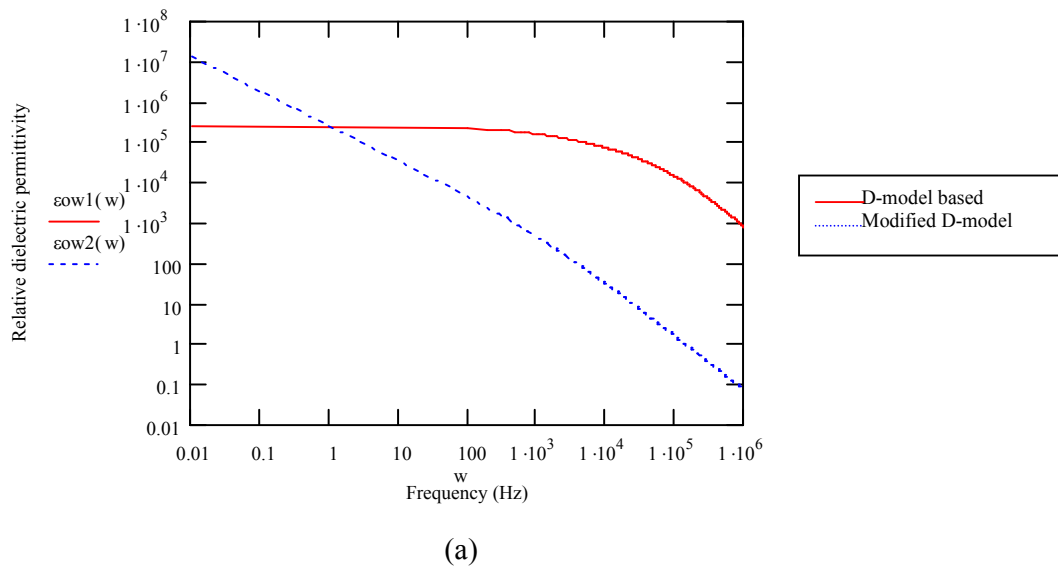
Figure 6.21 (a) Result of modified D-model with input as same as Lima-Sharma and
q=0.85 (b) Effective conductivity model, N=0.01.

132
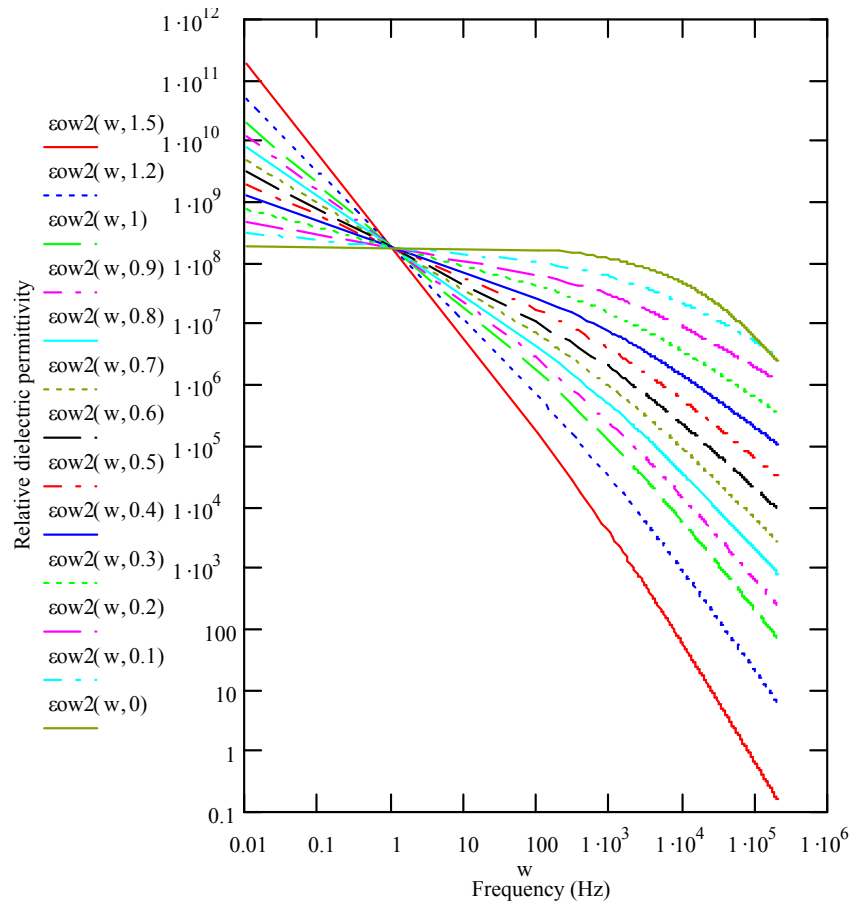
Figure 6.22 Relative dielectric permittivity with various *q* parameter.

6.5 Computational Fitting

Dispersion curve fitting is performed by calculating the misfit of experimental data and dielectric modified-D model iteratively. Saturation level constants, q and C as in Equation 6.69, are the model parameters to be estimated during the iteration. The method formulated by Taylor is a series expansion of the model where q and C are the unknown variables.

Column vectors O and T are defined as:

O = column vector of dielectric as reference data

T = column vector of dielectric as model

The unknown parameter can be approximated by following equations:

$$T\left(m^{n+1}\right) = T\left(m^{n}\right) + \left(\frac{\partial T}{\partial q}\right)\Delta q + \left(\frac{\partial T}{\partial C}\right)\Delta C$$

$$\left[\varepsilon\left(m^{n+1}\right)\right] = \left[\varepsilon\left(m^{n}\right)\right] + \left[\partial\varepsilon\left(m^{n}\right)/\partial q\right]\Delta q + \left[\partial\varepsilon\left(m^{n}\right)/\partial C\right]\Delta C$$

$$\left[\varepsilon\left(m^{n+1}\right)\right] = \left[\varepsilon\left(m^{n}\right)\right] + \left[\partial\varepsilon\left(m^{n}\right)/\partial q \quad \partial\varepsilon\left(m^{n}\right)/\partial C\right]x\begin{bmatrix}\Delta q \\ \Delta C\end{bmatrix}$$

$$T\left(m^{n+1}\right) = T\left(m^{n}\right) + G\Delta m \qquad\qquad 6.35$$

The Equation 6.35 is solved iteratively until meet the minimum misfit criteria. Misfit or error function of model and perturbation is formulated as

$$E = \sqrt{\frac{\sum_{i=1}^{N}\left(\left(O_{i} - T_{i}\right)/O_{i}\right)^{2}}{2N}} \quad \text{or}$$

$$E = \sqrt{\frac{\sum_{i=1}^{N}\left(\frac{\varepsilon_{data} - \varepsilon}{\varepsilon_{data}}\right)^{2}}{2N}}$$

The objective or cost functions of dielectric is written as

$$\varepsilon_o = \sigma_w \left[\frac{9\varepsilon_m \sigma_w \phi}{\left(2+\phi\right)^2 \sigma_w^2 + \omega^2 \varepsilon_m^2 \left(1-\phi\right)^2} \right]$$

Jacobian matrix (G) consists of derivation of objective equation to model parameter. The component of Jacobian matrix is derived as:

$$U = 9\varepsilon_m \sigma_f^2 \phi$$

$$V = \left(2+\phi\right)^2 \sigma_w^2 + \omega^2 \varepsilon_m^2 \left(1-\phi\right)^2$$

$$\frac{\partial \varepsilon_o}{\partial q} = \frac{9\sigma_f^2 \phi V - 2\omega^2 \varepsilon_{cs} \left(1-\phi\right) U}{V^2} \frac{-2p}{3-p} \frac{\delta_1 \left(1+\delta_1 A\right)\varepsilon_w - \delta_1^2 B \frac{\sigma_w}{\omega}}{\left(1+\delta_1 A\right)^2 + \delta_1^2 B^2} \frac{Cq}{\omega^{q+1}}$$

$$\frac{\partial \varepsilon_o}{\partial C} = \frac{9\sigma_f^2 \phi V - 2\omega^2 \varepsilon_{cs} \left(1-\phi\right) U}{V^2} \frac{2p}{3-p} \frac{\delta_1 \left(1+\delta_1 A\right)\varepsilon_w - \delta_1^2 B \frac{\sigma_w}{\omega}}{\left(1+\delta_1 A\right)^2 + \delta_1^2 B^2} \frac{1}{\omega^q}$$

6.5.1 Levenberg-Marquardt and Singular Value Decomposition Optimization

Levenberg-Marquardt (LM) optimization is known as a hybrid method as a combination result of gradien method and quasi-Newton. At the beginning iteration, when the peturbation is far from solution, we apply gradient method. As the error goes down then the rest of the process is handled by quasi-Newton. The least square iteration equation for LM optimization is formulated as

$$m_{n+1} = m_n + \left(G_n^T G_n + \varepsilon^2 I\right)^{-1} G_n^T \left(d - g\left(m_n\right)\right) \tag{6.36}$$

When the perturbation is far from the solution, the weight factor (ε^2) is set high. Thus, the diagonal matrix (I) becomes dominant. If the process tends to converge the weight factor is to be low so that the Jacobian matrix (G) more controls the process. Even the LM algorithm makes the computing time better than the classical Newton or quasi-Newton but the non-unique solution is still present.

To avoid singularity problem on matrix optimization in Equation 6.36 we solve the optimization matrix by transforming it into the following form

$$p = A^{-1}b \qquad\qquad 6.37$$

whereas $A = \left(G_n^T G_n + \varepsilon^2 I\right)$, $b = G_n^T \left(d - g(m)\right)$. Decomposing of matrix A becomes the product of three matrices, $A = USV^T$. U and V are the ortonormal matrices and S is a diagonal matrix. The solution of Equation 6.37 is

$$m_{n+1} = m_n + VS^{-1}U^T b$$

The diagonal component of matrix S is then added with a small number of w=0.00001 to prohibit the optimization matrix to become infinity.

The optimization steps are described in the following flow chart (Figure 6.23):

6.6 Result and Discussion

Modified D-model is applied to the two shaly sandstone samples, i.e. P03 and P45. The experimental data measurement of relative dielectric permittivity for these samples is shown in Figure 6.24. The parameter used to fit the model with experimental data is similar to that of Lima-Sharma's [18]. Figure 6.25a gives the results of original Lima-Sharma's, modified model and experimental data. Predicted and its dielectric permittivity data are depicted in Figure 6.25b. Exponent of q and C are the two constants dependent on water saturation level and must be estimated by data fitting. In Figure 6.26, variations of constant C only multiply the model and yield the similar trend, whereas q variations may change the gradient. If q=0, the model turns back to Lima-Sharma's model.
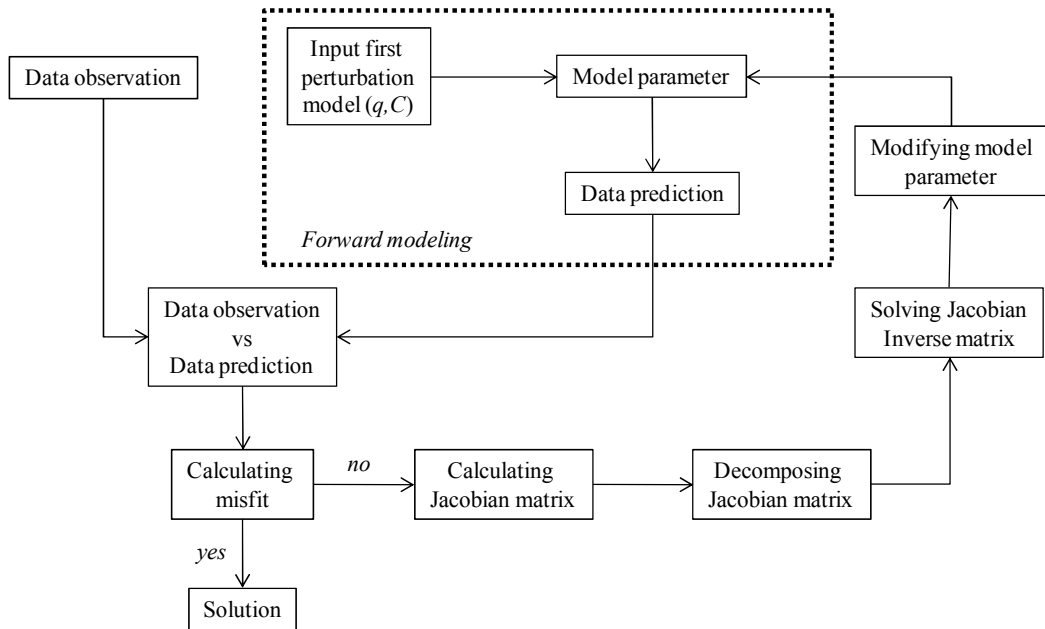
Figure 6.23 Optimization process.

Although the constant resulted from the experiment depends on water saturation level, and this also agrees to other experiments [2], it is obviously difficult to recognize the border of saturation having no contribution to dielectric permittivity. Once the threshold of saturation is achieved, the addition of saturation has small influence to dielectric permittivity. This coincides with the conductivity as described in Figure 6.27. The increase of saturation only contributes small variation of conductivity when it averagely achieves more than 50%.

To find the fittest parameters of q and C, the curve fitting optimization based on inverse problem should be accomplished. The solution of inverse problem modeling is non-unique. It means that one model may have several solutions. When dealing with a non-unique optimization solution, it may be diminished by considering the following constraints: a. physical constraints such as velocities are positive, causality; b. Non-informative priors such as Bayesians inference; c. result from lab experiments; c. common sense (earth model from geologist).

Set of experimental data, that is relative dielectric permittivity, is measured to test the optimization process. The goal of the result is to find the fittest saturation exponents of q and C. The strategy to cope with local minima is by reducing the perturbation model or by setting the input model parameter to be close enough to the solution. A Forward modeling process is then applied to get the initial model. Figure 6.28 and Table 6.3 give the optimization result of sample P03.
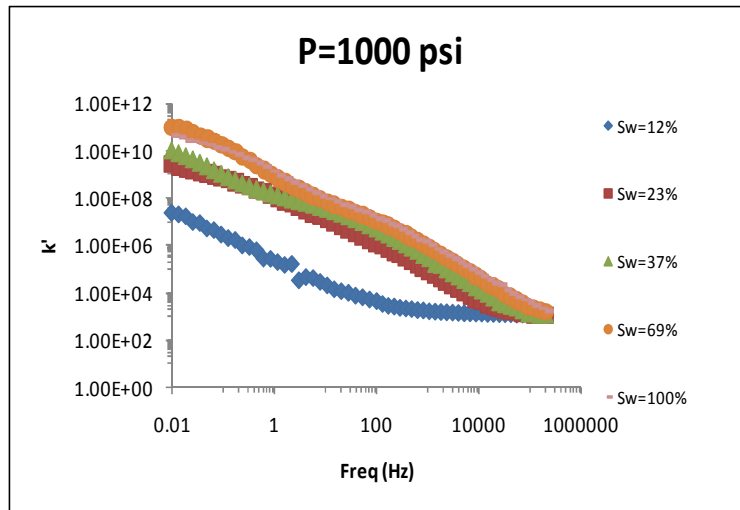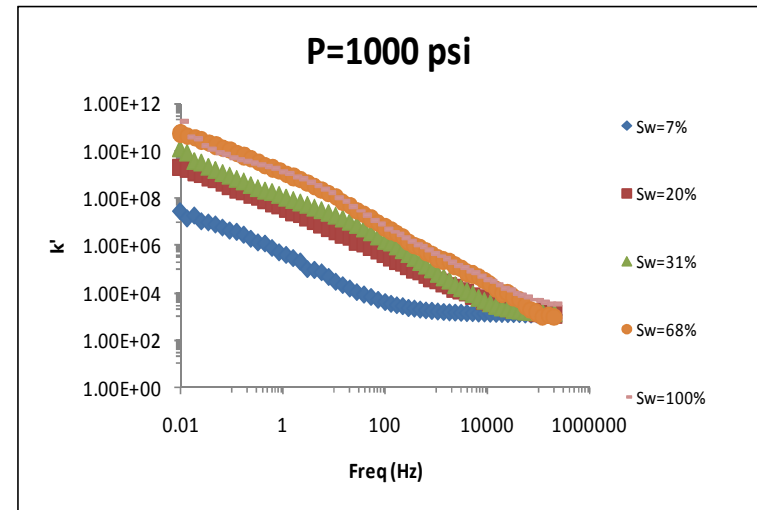
Figure 6.24 Relative dielectric permittivity of shaly sandstone variation with water saturation of sample (a) P03 (b) P45.

(a)

(b)
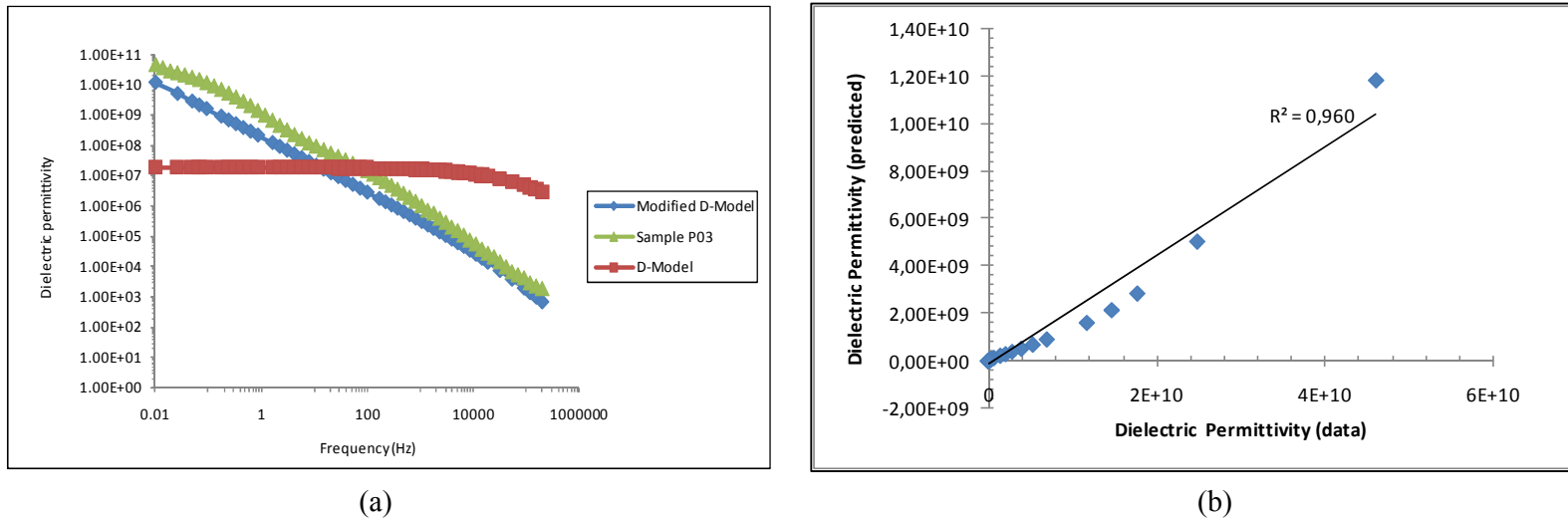
Figure 6.25 Relative dielectric permittivity of shaly sandstone (P03): (a) Comparison of modified D-model, D-model and experimental data. Para meter used are: Sw=100%, p=0.94, δ_1=1.2x10^{18}/m^2, σ_w=10.03 S/m, ε_w=6.78x10^{-10} F/m, D_1=0.315x10^{-8} m^2/s, τ_m=2.315x10^{-5} s, ϕ=0.216, C=10.1, q=0.83. (b) Predicted data from modified D-model and experimental data with correlation coefficient equal to 0.96.
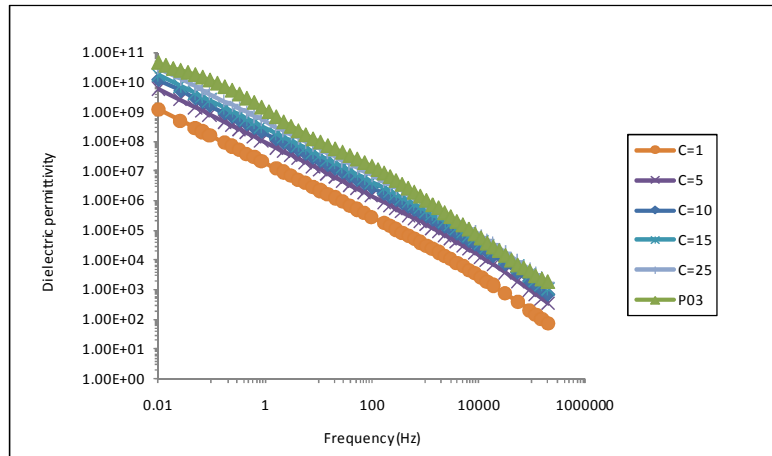
(a)
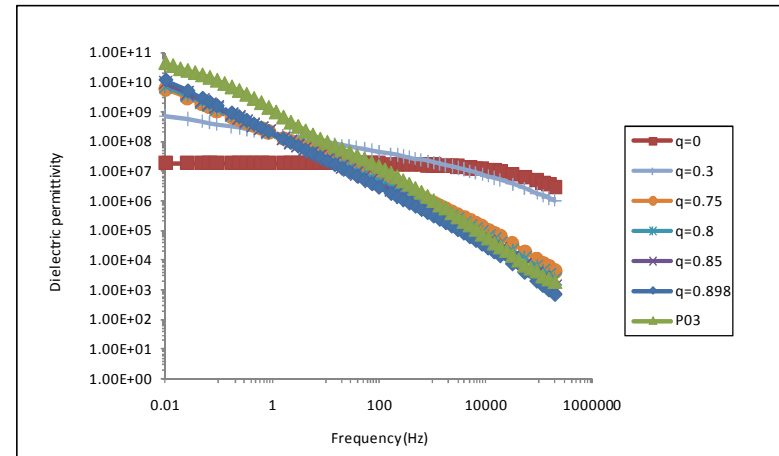
(b)

Figure 6.26 Variation of: (a) C and (b) q constant of sample P03 based on modified D-model.
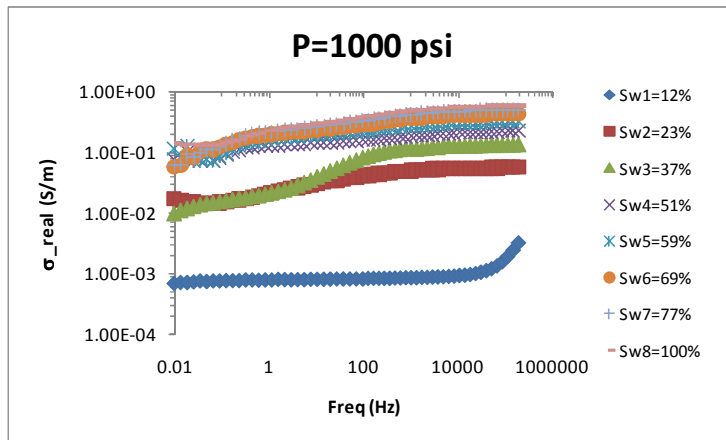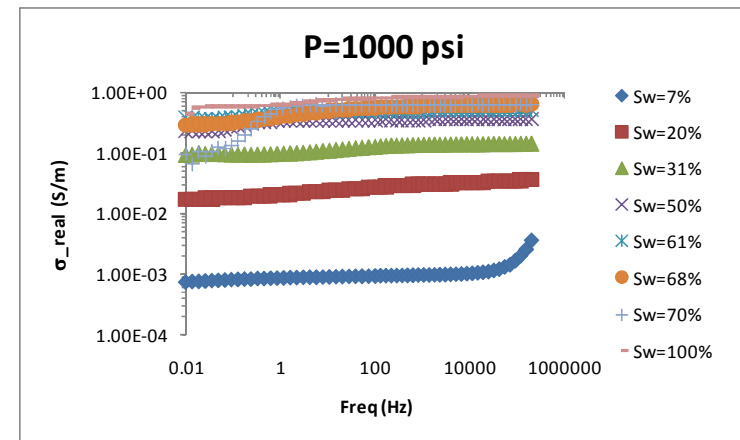
Figure 6.27 Conductivity variation with water saturation level (a) P03 (b) P45.
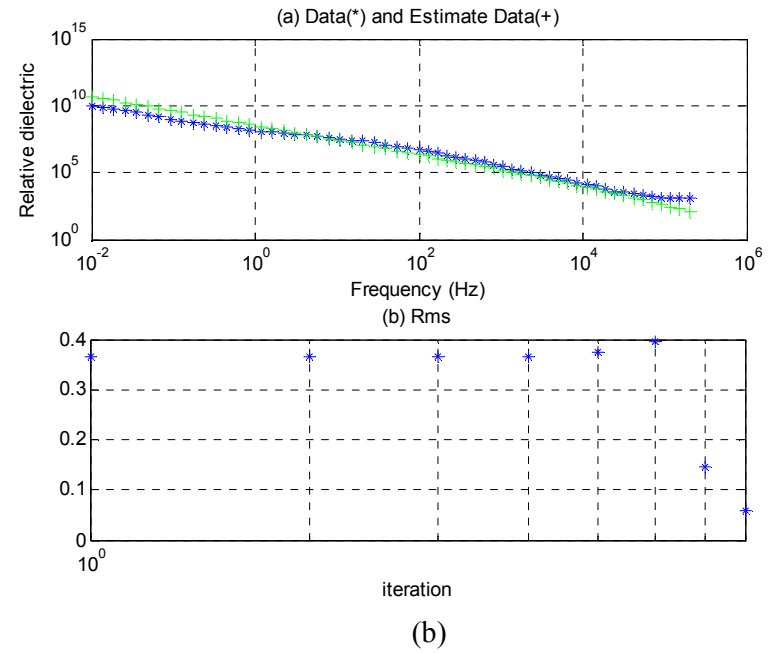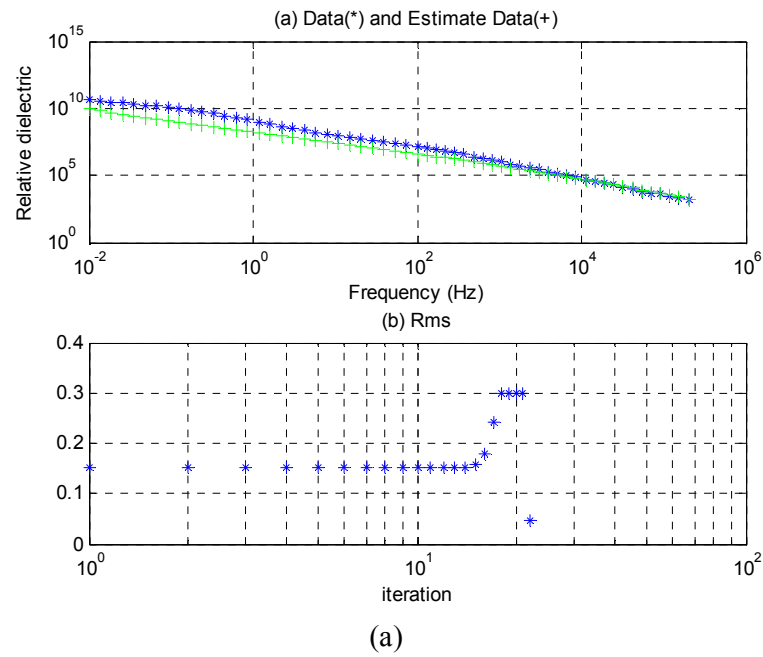
Figure 6.28a-b Curve fitting of dielectric permittivity by using Lavenberg-Marquardt: (a) Sw=100% with RMS=0.045; (b) Sw=37% with RMS=0.059
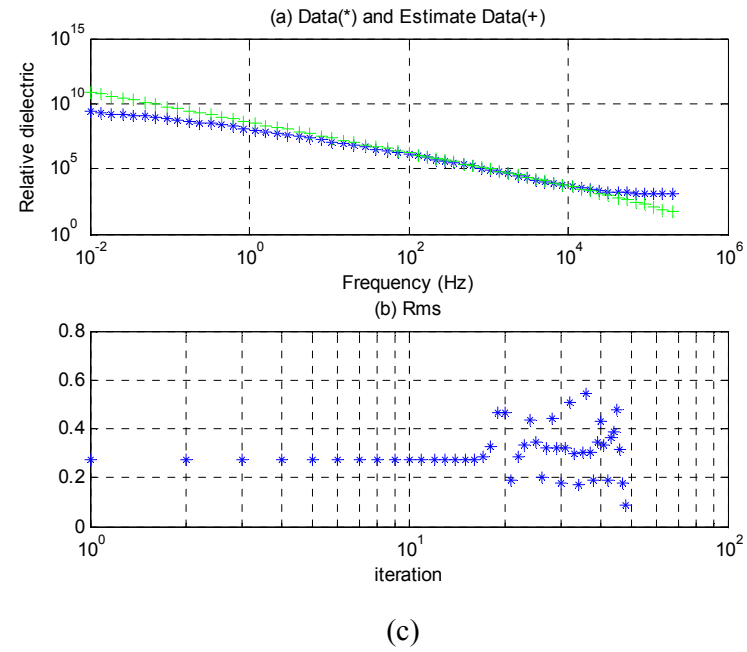
Figure 6.28c Curve fitting of dielectric permittivity by using Lavenberg-Marquardt Sw=23% with RMS=0.085

Table 6.3 Optimization result of parameter q and C

Sw (%)	Initial input		Result		RMS
	q	C	q	C	
100	0.5	10	0.8278	10.1448	0.0453
37	0.2	10	1.3471	8.0127	0.0591
23	0.5	10	1.5889	12.9534	0.0851

Plotting modified EDL conductivity to frequency with water saturation variation based on Equation 6.78 results in similar trend to the experimental data (Figure 6.29). Fitting should be made for coating volume factor parameter (N) in order to fit with the data. The input parameters are p=0.94, δ_i=1.2x10^{18}/m^2, σ_w=10.03 S/m, ε_w=6.78x10^{-10} F/m, D_l=0.315x10^{-8} m^2/s, τ_m=2.315x10^{-5} s, ϕ=0.254, N=0.0001. Cementation factor (m) is 1.887 for sample containing 10% shale [69] and saturation exponent (n) is 1.8 for wet shaly sandstone [70].
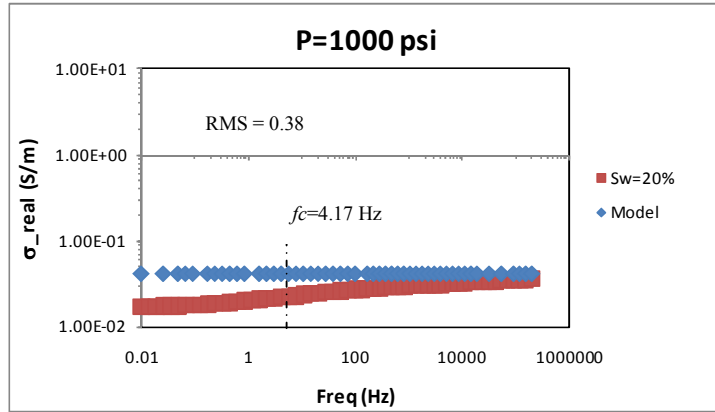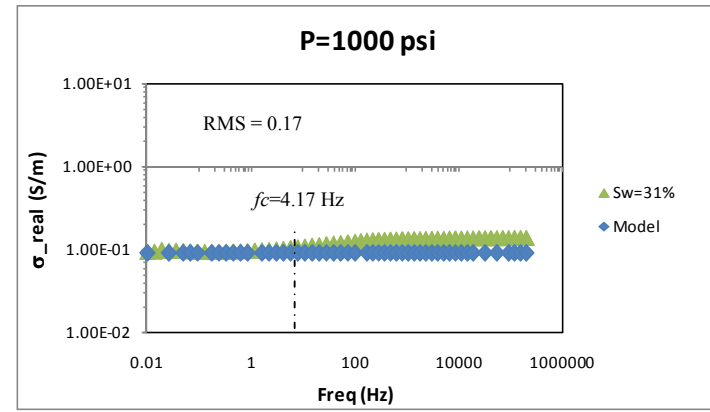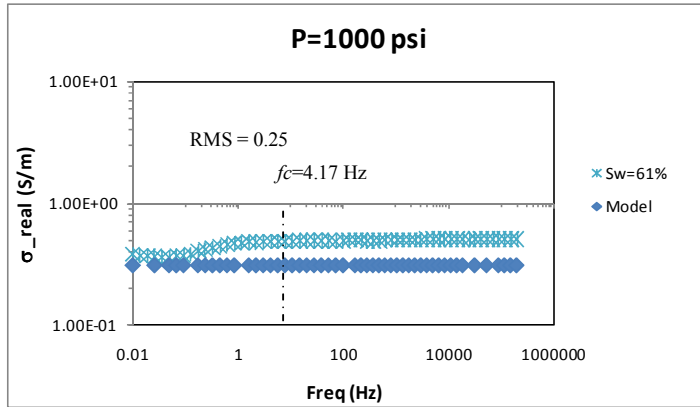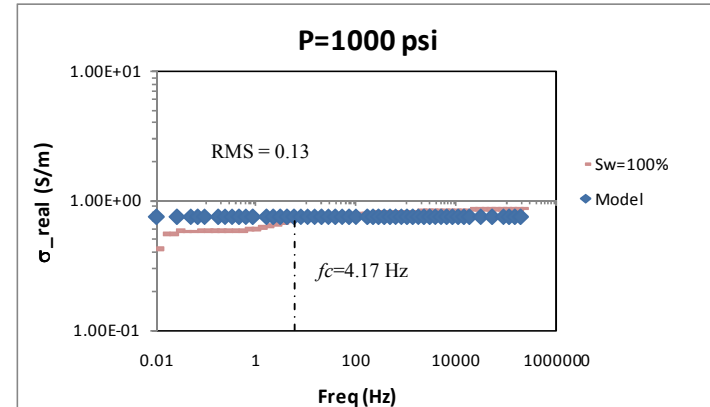
Figure 6.29 Conductivity dispersion with different water saturation level at sample P45: (a) Sw=20% (b) Sw=31% (c) Sw=61% (d) Sw=100%. The deviation in the beginning due to electrode polarization, the characteristic frequency *(fc)* is 4.17 Hz.

6.7 Summary

A new dielectric permittivity dispersion model and an effective conductivity have been established. The conductivity model adapts the effect of electric double layer in low water saturation and bulk volumetric in high water saturation. This model extends the Archie's formula which only accommodates bulk volumetric conductivity.

The modified electro diffusion mechanism (D-model) is also presented and the dielectric permittivity model resulted here agrees to the experimental data in a wide range of frequencies. An integration of empirical relationship into diffusion mechanism should be considered. The previous model communicates to the latter through the water saturation level constant of q. This dielectric permittivity model is addressed for a wide range of water salinities. It is concluded that the model shows good agreement to shaly sandstone measurement.

CHAPTER 7

GENERAL DISCUSSION AND CONCLUSION

7.1 Reservoir Rock Characterization

Electrical evaluation of reservoir rock needs to consider several factors that really describe subsurface condition. As confining pressure can collapse pore space of the rock that makes rock properties also change, it needs to see the detail of how much the effect of the pore geometry alteration when pressurized to electrical properties. Moreover, determination of particular pore geometry changes might help petrophysicists for further interpretation of the most categories that contribute more to the electrical properties.

The presence of shale particle might complicate electrical properties. Not only water film effect during saturation and un-saturation but also electrical double layer play a role to add bulk electrical conductivity. The low salinity of the water gives impact on swelling clay and thus increases diffusive layer length. In contrast, high salinity might significantly reduce that thickness. The behavior of the electrical properties in high salinity water during imbibitions-drainage and pressure variation in this work are intensively studied. The modification of conductivity and dielectric dispersion model is proposed upon answering the electrical dispersion dependency on water saturation. In many cases, sea water is still commonly used, and it might have very different salinity from formation water. A proper evaluation on salinity effect to formation damage still needs to be investigated.

7.2 Rock Geometry, Textures and Electrical Dispersion

Photomicrograph has been used to extract geometry of the rock. This includes image data acquisition, image segmentation and feature analysis. The method starts from rock coring, cutting, grinding until preparing thin sections with the thickness of 0.03 mm. Prior to pore analysis, the samples are impregnated with blue dyed epoxy to produce clear image separation between the matrix and pore space. To provide minerals recognition, the samples are stained with alizarin red and potassium ferricyanide. Pore space separation from the matrix is accomplished in the image segmentation process by converting the thin image into binary. Description of the matrix, e.g. texture, mineralogy and its diagenesis, is also provided.

To cope with the inconsistency of color saturation during pore recognition due to many impurities, a multiple pore selection with carefully adjusting pore-solid matrix boundary is manually applied. The image of the sample is firstly adjusted to correct the contrast and its color level. Range of blue color is then determined as a filtering criterion. After multiple pore selection, the pore layer is saturated with white color then merged with the black background.

Features analyses to be provided for pore space interrelationship with resistivity dispersion are: pore radius distribution, circularity, gamma, aspect ratio and pore angle. The pore radius definition follows Wadell's formula.

Texture of siliciclastic rock samples consists of sublitharenite to litharenite with grain around 60%. The grain consists of monocrystalline quartz, polycrystalline quartz, lithic fragment, feldspar and mica. The grain size is from medium silt to coarse sand grain. The grain shapes of the sample are angular to subrounded, well sorted, point, long and have sutured contacts. In term of pore radius, only sample P33 has dominant micropore (less than 30 μm), whereas the rest have macropore although in small number.

Carbonate rock samples averagely have a larger pore size than that of siliciclastic. All of the packstone shows a predominantly large structure which is either vug, fracture, intercyrstal or moldic. The carbonate grain consists of red algae, mollusks,

larger foraminifera and ooids. Whole matrix consists of micrite while cement consists of calcite.

Dependency of electrical properties of rock is less sensitive to the rock mineral while the medium is saturated by water fluid. The contributions of pore water to the rock conductivity are in two ways either by their intrinsic electrolytic conductivity or by electrochemical interaction at the interface of fluid-solid matrix. For the previous one, rock conductivity is proportional to electrolyte conductivity. The latter, the geometry of conductive path is controlling internal surface conductivity. In this case, interface conductivity can be considered to be independent from the electrolytic conductivity. Surface conductivity plays more in shaly sandstone and reveals significant contribution to the effective rock conductivity in low partial water saturation.

The output of the work reflects that resistivity dispersion occurs in low water saturation. This is the condition where the thin water layer starts to cover the grain surface. List of rock geometry features has been tested for its interrelationship with resistivity dispersion. Referring to the observation it is concluded that only pore radius distribution contributes to the resistivity dispersion. The result shows good agreement if the resistivity dispersion is linked to porosity interrelationship. This indicates that resistivity dispersion can be applied to extract porosity of the rock. The relationship of this dispersion to initial water saturation gives good outcomes. It is concluded also that resistivity dispersion is a function of pore size distribution and water saturation.

7.3 Pore Radius Distribution, Pressure and Partial Saturation Effect on Electrical Properties

Potential application of electrical methods can be applied for waterflood monitoring, salt water intrusion movement in hydrogeology, formation evaluation, etc. To fit with objectives, the impact of different pore radius, subsurface pressure and partial water saturation to the electrical properties of the rock need to be answered. Thus, an

analysis of pore radius distribution, pressure variation and dynamic of the fluid movement should be carried out to obtain a comprehensive understanding of subsurface electrical properties of the rock. Surely, if those properties changes are relatively large enough during evaluation, the resistivity may be applied to see fluid distribution.

Preparation measurement of electrical properties consists of sample preparation, measurement procedure, data acquisition and data editing.

After the core samples are cut and shaped according to core-holder size, the samples are saturated by synthetic brine repetitively until full saturation is achieved. The resistivity measurement performed in each of their series. Either four- or two-electrode method is applied, depending on characteristics of the core samples. For most resistive samples, two electrodes are employed. Meanwhile the four-electrode mode is preferred to be applied in less resistive samples. Parasitic impedance that is always present in higher frequency can be covered by balancing its reference resistor to be equal to or larger than the effective resistance of the sample. On the other hand, non-linearity due to strong brine is usually present at low frequencies, balanced by reducing sinusoidal signal amplitude. To deal with electrode polarization, it is separated with intrinsic electrical resistivity by plotting them in Argand plot between their real and imaginary parts. The analysis is then made by purely intrinsic resistivity of the sample. The variation of overburden pressure increases from 1000 psi until 3000 psi and the measurement is conducted at every step of 1000 psi.

Geometry of the pore rock is one of the causing polarizability factors that take into account in depolarization factor. Polarization-depolarization occurs in the water fluid because of its molecule orientation. The effect of polarization may cause electrical resistivity dispersion and occurs on the boundary of pore water to solid matrix. The experiment leads the resistivity dispersion effectively characterized by its pore radius and water saturation. The rate of saturation and desaturation depends on its pore size distribution. The larger the pores radius, the longer the time is needed to saturate. While both sides of the pore walls have been completely covered by fluid, the volumetric conductivity effect is now more dominant than the surface conductivity.

Electrical resistivity dispersion behaves like a capacitor; the smaller the pores radius is, the easier the dispersion vanishes. Here, a large structure of pore geometry tends to have more dispersion as well as thin pore-water surface and needs more time to fill the whole pore space. On the other way around, the small structure gives less contribution to the electrical dispersion due to the simplicity of saturation process. Furthermore, small pore radii may barrier the anion because the double layer touches each other. While pore radii are large, the ion motion is undisturbed. The presence of clay minerals throughout the rock partially blocks ionic solution. Negative charges on clay minerals tend to capture the electrolyte cations and move to the other way to anions. Under the influence of electric field, the cations easily pass the cationic cloud but ionic charges accumulate.

Variation of resistivity only gives small changes under confining pressure, particularly in high water saturation of more than 20%. Meanwhile, if initial low water saturation is less than 20%, the resistivity can be noticed for the frequency of less than 10 KHz. This correlates to the Maxwell-Wagner polarization where the charge builds-up at the interface between the two medias with different conductivities. The low-resistivity changes the effect due to pressure that reflects a small decrease in pore volume. To characterize pore rock changes due to pressure, it is shown that imaginary resistivity is better than real resistivity.

In term of saturation, when pore-filled fluid occupies most of the rock space and the thin-water interfacing already covers almost of the grain surface, the dispersion leaves. This reflects that bulk fluid volumetric is now controlling the path of the electrical current. In other word, the real resistivity is more responsible to the bulk volumetric fluid while imaginary resistivity is to water-solid interfacing. Therefore, the electrical double layer tends to be unimportant with the increase of water saturation. To examine dynamic fluid process, the sample is proceeded to have partially saturated-unsaturated water fluid. As water brine partially leaves the pore space, the resistivity increases notably. However, unsaturated-resistivity is always lower than the other. The presence of irremovable conductive salt-water film coating the solid-grain acts as an agent of electrical current that allows this result. Thus, although the water leaves most of the pore space, the resistivity may go lower than the

imbibitions. In summary, at the beginning of fluid water movement, the dynamic of the fluid may be observed easily by imaginary resistivity.

7.4 A New Electrical Dispersion Model for Shaly Sandstone

Nature of the rock is very complex and composes of degree of process to be formed. When electric field passes through the rock medium, series of polarization occurs, depending on its frequency. The presence of clay material may complicate the electrical properties. This is due to the response of effective conductivity, not only from volumetric water but also from interface water-grain. Furthermore, the clay may initiate membrane polarization when it partially blocks ionic solution and atches its electrolyte cation.

The model usually used to describe effective conductivity in shaly sandstone is a parallel conductor system. Within this model, the conductor is divided into two components, i.e. electrolytic and clay component. The electrolytic or volumetric is attached to the Archie's model while the clay component may be considered by evaluating clay distribution, clay types or chemical reaction.

The mixing law is used to develop a new electrical dispersion model. Since wavelength of electrical field applied is much larger than the pore size of rock, it is then valid to use the static model for time dependent electromagnetic field. Debye and Cole-Cole are the firsts to develop a dispersion model for one and multiple relaxation time respectively. Their models do not account the effect of thin double layer and charged clay. Later, Lima and Sharma release the model of shaly material for the membrane polarization. The membrane polarization is defined through two mechanisms: bound layer (S-model) and diffusive polarization (D-model). This model answers the dispersion in range of 100 Hz to 1 MHz for low water fluid salinity. The application of D-model in high water salinity leads deviation of dielectric permittivity lower in low frequency (less than 100 Hz) and produces higher dielectric permittivity in higher frequency (more than 100 Hz). The evaluation of D-model with Hanai-Brugemann and Wagner models result in the similar trend of dielectric permittivity and conductivity with frequency.

153

Even though Lima-Sharma's model successfully explains the dispersion for shaly material in range of frequency of 100 Hz to 1 MHz, this model is still incomplete because it does not account the saturation effect. Furthermore, the application of the model is still limited for low water salinity. Many results note volumetric conductivity more contribute for high water salinity rather than low salinity; however our experiment shows that electric double layer (EDL) is also present in high salinity, particularly in low water saturation degree. The effect of double layer may not be ignored while the medium is in low saturation level, unless it is in high water saturation level where the bulk volume factor is introduced. Thus, there is a need to develop a new electrical dispersion model that can cover from relatively low frequency to high frequency. This model must be in accordance with the observation that EDL is present in low water saturation and vanishes when water saturation increases.

Modified D-model is then introduced and inserted into Wagner model to obtain both dielectric permittivity and conductivity. The new model of dielectric permittivity can fit the data from the frequency of 0.1 Hz until 0.2 MHz and can communicate with the prior model if parameter q is equal to zero. This parameter is strongly dependent on water saturation and surface area to volume ratio. To deal with electrical double layer, the former Archie's model is modified by adding surface conductivity. The surface conductivity depends on water saturation and the parameter of water-coated volume factor which indicates thin water film coating solid grain. In the beginning when water saturation is introduced, the surface conductivity contributes more; but it goes to the other way if water saturation increases. The volumetric conductivity becomes to completely govern the effective conductivity of the rock when all surface of the pore-rock is already covered by water fluid. When water saturation is full, the model turns into classic Archie's model. Curve fitting by using hybrid inversion and SVD is accomplished to obtain the best parameter of q.

7.5 Future Study

It is identified that several potential studies for further investigation are as follows:

1. Water flood recovery monitoring by complex dielectric and complex resistivity because both of two methods are very good to see fluid distribution and to separate fluid to solid rock matrix.
2. Extracting cementation factor of Archie (*m*) by evaluating pore distribution, compactness and pore shape.
3. Water saturation estimation study by further analysis of spectral IP, electrical dispersion and time constant.
4. Porosity and permeability reduction due to pressurization and their interrelationship with electrical properties.
5. Join inversion of sonic and electrical properties of rock to monitor fluid distribution, pressure prediction and anisotropy study.

REFERENCES

1.   Archie, G.E., *The electrical resistivity log as an aid in determining some reservoir characteristics.* Trans. Americ. Inst. Mineral. Met, 1942. **146**: p. 54-62.

2.   Knight, R.J., Nur, A., *The dielectric constant of sandstones, 60 kHz to 4 MHz.* Geophysics, 1987. **5**: p. 644-654.

3.   Alvarez, R., *Complex dielectric permittivity in rocks: A method for its measurement and analysis.* Geophysics, 1973. **38**: p. 920-940.

4.   Schon, J.H., *Physical properties of rocks: Fundamentals and principles of petrophysics*. 1998, Netherland: Pergamon.

5.   Chang, D., Myers, M.T. , *Estimation of producible and remaining oil using high frequency dielectric log in carbonate reservoir.* SPE, 1995(30586): p. 587-596.

6.   Meador, R.A., Cox, P.T., *Dielectric constant logging, a salinity independent estimation of formation water volume.* SPE, 1975. **5504**.

7.   Butler, D.B., Knight, R.J., *The effect of steam quality on the electrical behavior of steam-flooded sands: A laboratory study.* Geophysics, 1995. **60**(4): p. 998-1006.

8.   Wilt, M., Zhan, P., Morea, M., Julander, D., Mock, P. *Using Crosswell Electromagnetics to Map Water Saturation and Formation Structure at Lost Hills*. in *SPE*. 2001.

9.   Gomez, C.T., Dvorkin J. , *Feasibility of reserve estimate from combined elastic and resistivity data*, in *SEG/San Antonio Annual Meeting*. 2007: USA. p. 1475-1479.

10.   Onishi, K., Yoshihiko, I., Yasuhiro, Y., Toshifumi, M, *Measuring electric resistivity of rock specimens injected with gas, liquid and supercritical CO2*, in *SEG/New Orleans annual meeting*. 2006: USA. p. 1480-1484.

11.   Sava, D.C., Hardage, Bob A., *Gas-hydrate concentration and uncertainty estimation from electrical resistivity log: examples from Green Canyon, Gulf of Mexico*, in *SEG/San Antonio Annual Meeting*. 2007: USA. p. 1579-1583.

12. Hubbard, S.S., Peterson Jr, J. E., Majer, E. L., Zawislanski, P. T., Williams, K. H., Roberts, J and Wobber, F. , *Estimation of permeable pathways and water content using tomographic radar data*, in *The Leading Edge*. 1997. p. 1623-1628.

13. Ruffet, C., Guenguen, Y., Darot, M. , *Complex conductivity measurements and fractal nature of porosity.* Geophysics, 1991. **56**: p. 758-768.

14. Krohn, C.E., *Sandstone fractal and Euclidean pore volume distribution.* J.Geophys.Res, 1988. **93**: p. 3286-3296.

15. Kulenkampff, J., Schopper, J.R. , *Low Frequency Complex Conductivity-A means for Separating Volume and Interlayer Conductivity*, in *11th Europe formation evaluation symp.* 1988: Oslo.

16. Revil, A., Glover, P.W.J. , *Theory of ionic-surface electrical conduction in porous media.* Physical Review B, 1997. **55**(3): p. 1757-1773.

17. Lima, d.O.A.L., Sharma, M.M. , *A grain conductivity approach to shaly sandstones.* Geophysics, 1990. **55**(10): p. 431-446.

18. Lima, d.O.A.L., Sharma, M.M. , *A generalized Maxwell-Wagner theory for membrane polarization in shaly sands.* Geophysics, 1992. **57**(3): p. F1-F10.

19. Knight, R.J., Abad, A. , *Rock/water interaction in dielectric properties: Experiments with hydrophobic sandstones.* Geophysics, 1995. **60**: p. 431-436.

20. Nguyen, B.-L., Bruining, J., Slob, E.C. . *Effects of Wettability on Dielectric Properties of Porous Media*. in *SPE*. 1999a.

21. Suman, J.R., Knight, R.J. , *Effects of pore structure and wettability on the electrical resistivity of partially saturated rocks-A network study.* Geophysics, 1997. **62**: p. 1151-1162.

22. Nguyen, B.-L., Bruining, J., Slob, E.C. . *Hysteresis in dielectric properties of fluid-saturated porous media*. in *SPE*. 1999b.

23. Seleznev, V.N., *Theoretical and laboratory investigation of dielectric properties of partially saturated carbonate rocks*. 2005, Delft University: Netherland.

24. Szerbiak, R.B., McMechan, G.A., Forster, Craig and Stephen, H., *Electrical and petrophysical modeling of Ferron Sandstone data.* Geophysics, 2006. **71**: p. G197-G210.

25. Endres, A.L., Bertrand, E.A. , *A pore-size scale model for the   dielectric properties of water-saturated clean rocks and soils.* Geophysics, 2006. **71**: p. F185-F193.

157

26.   Sengwa, R.J., Soni A, *Low-frequency dielectric dispersion and microwave dielectric properties of dry and water-saturated limestones of the Jodhpur region.* Geophysics, 2006. **71**(G269-G277).

27.   Toumelin, E., Verdin, C.T., *2D pore-scale simulation of wide-band electromagnetic dispersion of saturated rocks.* Geophysics, 2007. **72**: p. F97-F110.

28.   Rey, E., Jongmans, D. , *A 2D numerical study of the effect of particle shape and orientation on resistivity in shallow formations.* Geophysics, 2007. **72**: p. F9-F17.

29.   Abousrafa, E.M., Somerville, J.M., Hamilton, S.A., Olden, P.W.H., Smart, B.D.G., Ford, J. , *Pore geometrical model for the resistivity of brine saturated rocks.* Journal of Petroleum Science and Engineering, 2009. **65**: p. 113-122.

30.   Gueguen, Y., Palciauskas, V., *Introduction to the physics of rocks.* 1994, USA: Princeton University Press.

31.   Khairy, H., Zahir, Z.Th., Fauzi, U., *Pressure and Partial Saturation Effect on the Complex Resistivity of Reservoir Rock*, in *SEG-Beijing Conference*. 2009: Beijing.

32.   Stow, D.A.V., *Sedimentary rocks in the field: A color guide.* 2005, London: Manson Publishing Ltd.

33.   *Carbonate   Advisor.*   2008   [cited;   Available   from: https://www.slb.com/~/media/Files/evaluation/brochures/wireline_open_hole/petrophysics/carbonate_advisor_br.ashx.

34.   *Choquette and Pray classification.*   1999   [cited;   Available   from: http://www.encyclopedia.com/doc/1O13-ChoquetteandPrayclassfctn.html.

35.   *Galleries of Carbonate Porosity.*   2009   [cited;   Available   from: http://sepmstrata.org/carbporositygallery/carbporositygallery.html.

36.   *Black Gold Beneath the Bayous.*   1999   [cited;   Available   from: http://dnr.louisiana.gov/sec/execdiv/techasmt/educational_resources/BGBB/4/.

37.   Glover, P., *What is the cementation exponent? A new interpretation*, in *The leading edge*. 2009, SEG.

38.   Zach, J., Frenkel, M.A., Riyard, D., Hincapie, J., Dubois, B and Morten, J.P. , *Marine CSEM time-lapse repeatability for hydrocarbon field monitoring*, in *SEG Houston 2009 International Exposition and Annual Meeting.* 2009, SEG: USA. p. 820.

39.   Garrouch, A.A., Sharma, M.M. , *The influence of clay content, salinity, stress, and wettability on dielectric properties of brine-saturated rocks: 10 Hz – 10 MHz.* Geophysics, 1994. **59**: p. 900-917.

40.   Su, Q., Qining, Feng and Shang, Zuoyuan. , *Electrical impedance variation with water saturation in rock.* Geophysics, 2000. **65**: p. 68-75.

41.   Lima, d.O.A.L., Clennell, M.B., Nery, G.G., Niwas, S., *A volumetric approach for the resistivity response of freshwater shaly sandstones.* Geophysics, 2005. **70**: p. F1-F10.

42.   *Salinity*. 2010 [cited; Available from: http://en.wikipedia.org/wiki/Salinity.

43.   Soenarwi, S., *Personal Communication*. 2010.

44.   *Autolab-500 manual book*. 2007, New England Research Inc: USA.

45.   Egerton, R.F., *Physical principles of electron microscopy*. 2007, USA: Springer science.

46.   Anselmetti, F.S., Luthi, S.M., Eberli, G.P. , *Quantitative characterization of carbonate pore systems by digital image analysis.* AAPG bulletin, 1998. **82**(10): p. 1815-1836.

47.   Crabtree, S.J., Ehrlich, R and Prince, C., *Evaluation of strategies for segmentation of blue-dyed pores in thin section of reservoir rocks.* Computer Vision, Graphic and Image Processing, 1984. **28**: p. 1-18.

48.   Wadell, H., *Volume, shape and roundness of quartz particles.* J. Geology, 1935. **43**(250–280).

49.   Ewing, R.P., Hunt, A.G. , *Dependence of the Electrical Conductivity on Saturation in Real Porous Media.* Vadose Zone Journal, 2006. **5**: p. 731-741.

50.   Cerepi, A., *Geological control of electrical behavior and prediction key of transport   properties in sedimentary porous systems.* Physicochem. Eng. Aspects, 2004. **241**: p. 281-298.

51.   Klein, L.A., Swift, C.T. , *An improved model for the dielectric constant of sea water at microwave frequencies.* IEEE Transactions on antennas and propagation, 1977. **ap-25**(1).

52.   Olhoeft, G.R., *Low frequency electrical properties.* Geophysics, 1985. **50**: p. 2492-2503.

53.   Kao, K.C., *Dielectric phenomena in solids: with emphasis on physical concepts of electronic processes*. 2004, London: Elsevier Academic Press.

54.   Khairy, H., *Penentuan waktu relaksasi batuan melalui inversi model Cole-Cole menggunakan metoda SVD*, in *Department of physics*. 1999, Institut Teknologi Bandung: Bandung.

55. Slater, L., Dimitrios, N., DeBonne, W, *On the relationship induced polarization and surface area in metal-sand and clay-sand mixtures.* Geophysics, 2006. **71**(2): p. A1-A5.

56. William, D., Callister, Jr., *Material science and engineering: An introduction.* 1985, USA: John Wiley and Sons Inc.

57. Olhoeft, G.R., *Electrical properties of rock*, in *Physical Properties of Rocks and Minerals*, Y.S. Touloukain, W.R Judd., R.F Roy, Editor. 1981, McGraw Hill: New York.

58. Dortman, N.B., *Fiziceskie svoistva gornich porod i polesnich iskopamych.* 1976, Moskva: Izdat.

59. Parchomenko, E.J., *Elektriceskie svoistva gornich porod.* 1965, Nauka, Moskva: Izad.

60. Keller, G.V., *Electrical properties*, in *Practical handbook of Physical Properties of Rock and Minerals.* 1989, CRC Press: Boca Raton, USA.

61. Maxwell-Garnett, J.C., *Colors in metal glasses and in metal films.* Transaction of the Royal Society, 1904. **CCIII**: p. 385-420.

62. Hanai, T., *Electrical properties of emulsions*, in *Emulsion science*, P. Sherman, Editor. 1968, Academic Press Inc: New York.

63. Maxman, M.H., Smits, L.J.M, *Electrical conductivities in oil-bearing shaly sand.* SPE, 1968. **8**: p. 107-122.

64. Debye, P.J.W., *Polar molecules.* 1929: Chemical Catalog Co.

65. Cole, K.S., Cole, R.H. , *Dispersion and Absorption in Solid.* J. of chemical physics, 1941: p. 341-351.

66. Khairy, H., Zahir, Z.Th., *Complex resistivity of shaly sandstone: study on pressure and saturation effect.* International Journal of Engineering and Sciences, 2010. **3**: p. 36-44.

67. Khairy, H., Zahir, Z.Th., *Pore geometry, pressure and saturation impact on electrical properties: model and laboratory study on sandstone and carbonate rock.* Journal of Petroleum Science and Engineering (under review), 2010.

68. Garrouch, A.A., *A novel analysis of the electrical transport mechanisms in porous media.* Transport in porous media, 2001. **44**: p. 559-575.

69. Cagatay, M.N., Al Fossail Khalid., Saner Salih. , *Shalliness Effect On The Log-derived Archie Cementation Factor: Study Of A Saudi Arabian Sandstone Reservoir.* The log analyst, 1994. **35**(6).
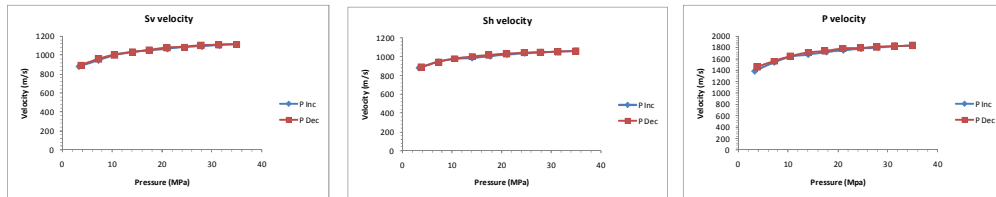
70.   Abdassah, D., Permadi,P., Sumantri,Y and Sumantri,R, *Saturation exponent at various wetting condition: fractal modeling of thin-sections.* Journal of Petroleum Science and Engineering, 1998. **20**: p. 147-154.
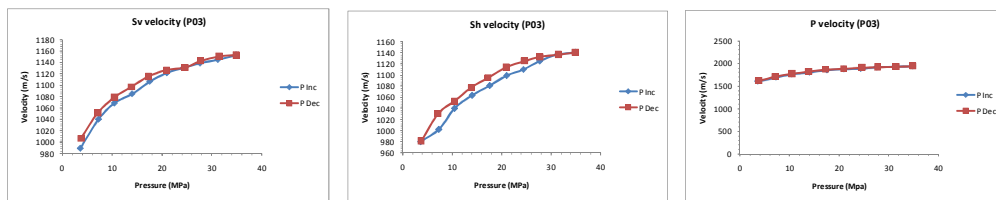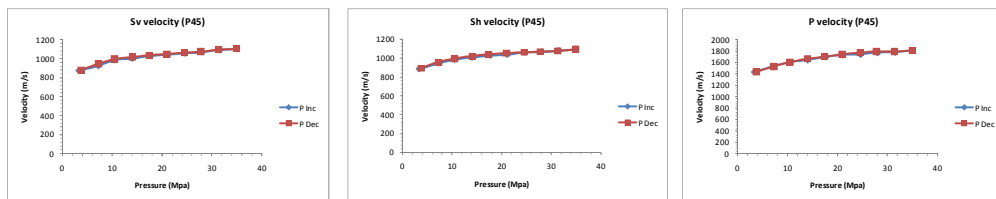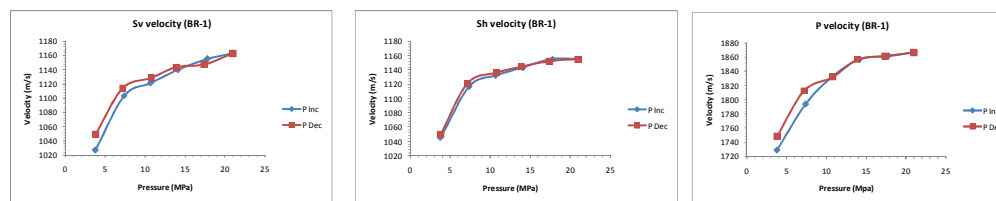
APPENDIX A

HYSTERESIS TEST RESULT

a.   Sample P33
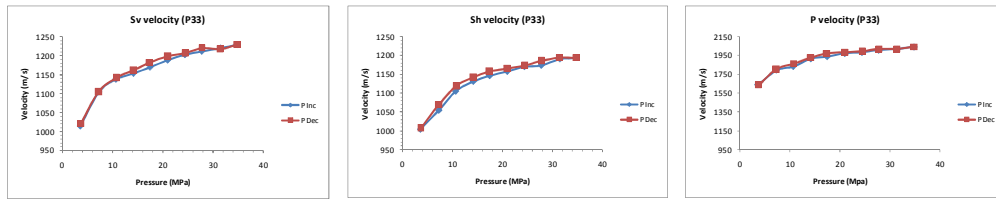
b.   Sample P19

c.   Sample P03

d.   Sample P45

e.   Sample BR-1

f.   Sample 368
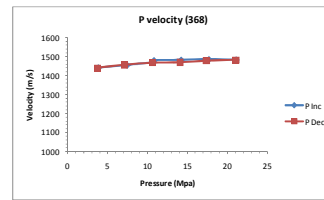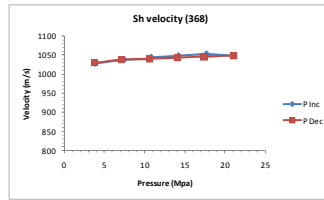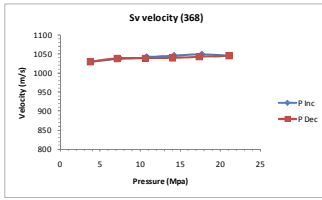
g.   Sample 158
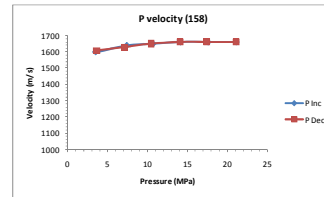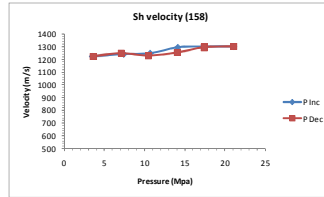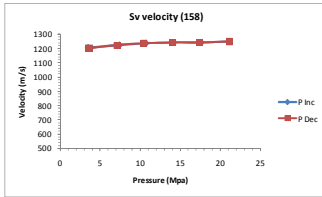
h.   Sample 347
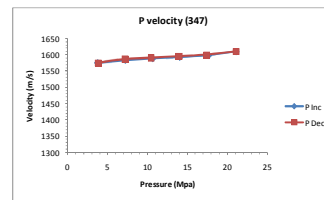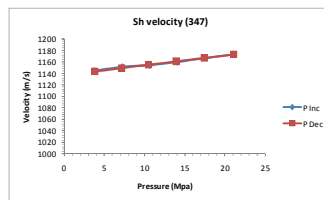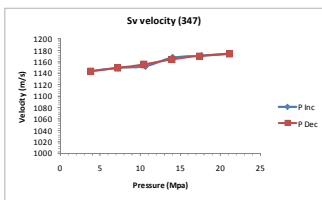
i.   Sample 9056
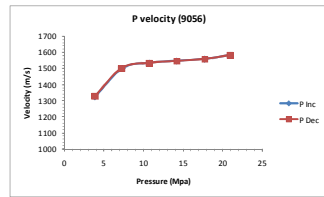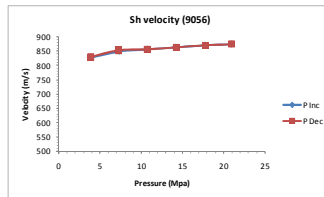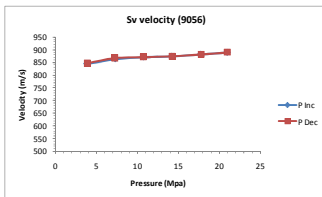
APPENDIX B

RESULT OF SCANNING ELECTRON MICROSCOPE

Sample P33	Sample P19
$\phi = 24.92\%$	$\phi = 23.45\%$
$\kappa = 467.6$ mD	$\kappa = 254.4$ mD
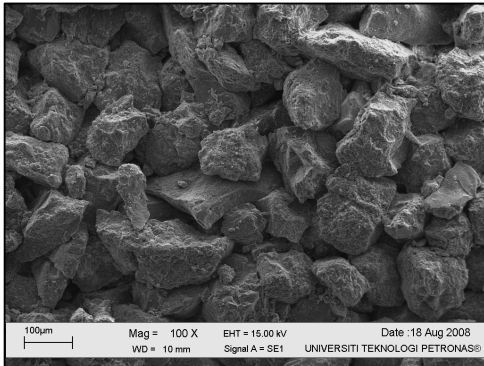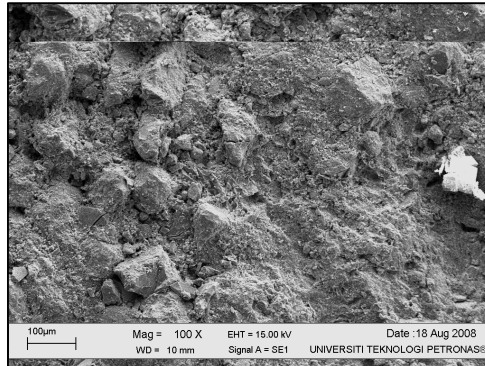
Sample P03	Sample P45
$\phi = 21.57\%$	$\phi = 25.40\%$
$\kappa = 74.2$ mD	$\kappa = 919.6$ mD

Sample BR-1	Sample 368
$\phi = 17.51\%$	$\phi = 29.15\%$
$\kappa = 178.9$ mD	$\kappa = 5091.0$ mD

166
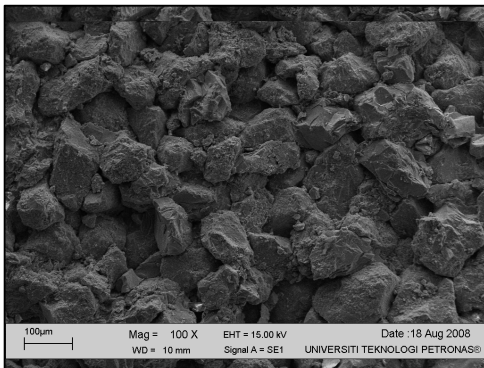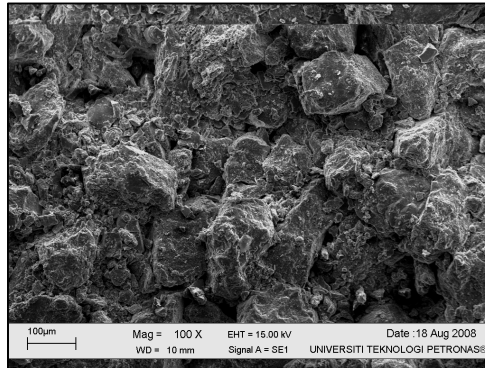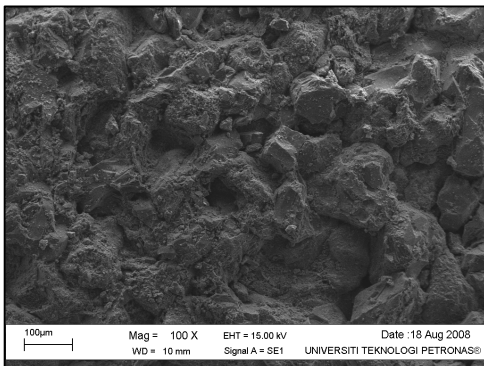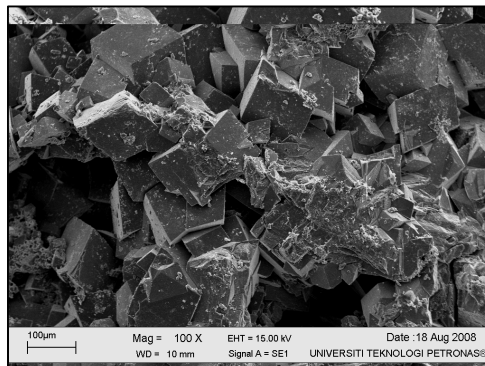
Sample 158
$\phi = 31.94\%$
$\kappa = 648.6$ mD
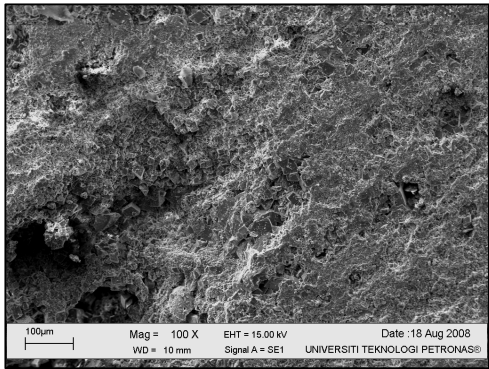
Sample 347
$\phi = 19.66\%$
$\kappa = 2086.1$ mD
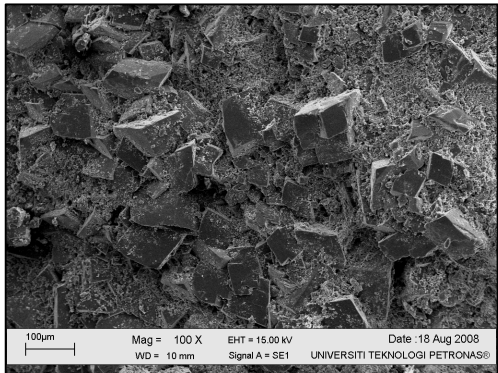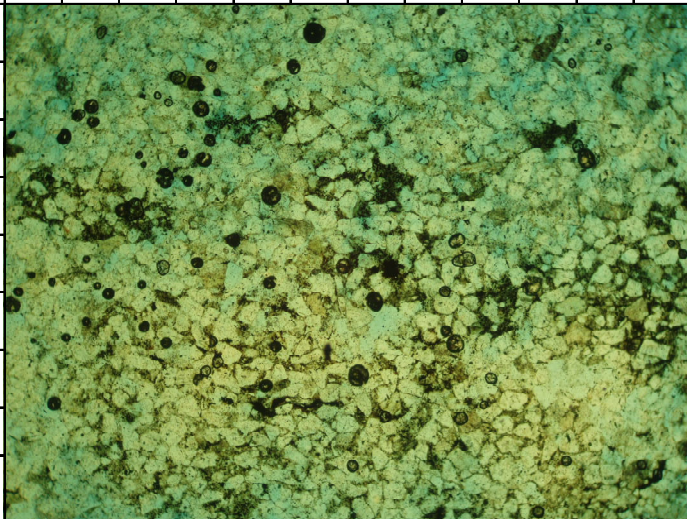
Sample 9056
$\phi = 12.54\%$
$\kappa = 17.5$ mD

167
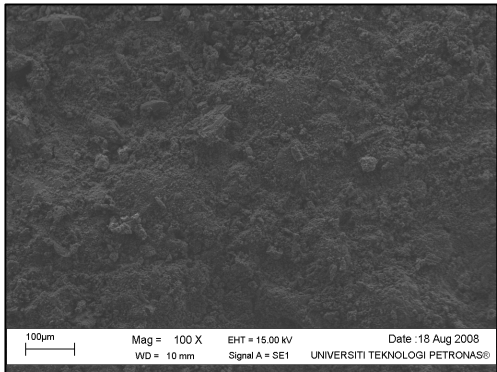
APPENDIX C

PETROGRAPHIC IMAGE ANALYSIS

Sample No. : 1/P33

▲ // nicol   1 mm   X nicol ▼

Photomicrograph of Sublitharenite showing monocrystalline quartz (I5, L3), polycrystalline quartz (H5), lithic fragment (A1), feldspar (L6), mica, and heavy minerals bounded by matrix of detrital clay (G4, L6), cement consists of clay minerals (I5), iron oxide (G5), quartz and hydrocarbon (E8). Porosity type is dissolution (A2, D2, I2) and intergranular (G2, H1).

PETROGRAPHIC ANALYSIS - 1
(SILICICLASTIC ROCKS)

SAMPLE / WELL NO.	1/P33	LITHOLOGY	Sandstone
DEPTH (ft)		ROCK NAME	Sublitharenite
FORMATION		CLASSIFICATION	Pettijohn (1987)

GRAIN SIZE (mm)	
Minimum	0.04 (Coarse Silt)
Mode	0.13 (Fine Sand)
Maximum	0.23 (Fine Sand)

TEXTURE	
Sorting	Well
Roundness	Angular – subrounded
Grain contacts	Point, long and sutured contacts
Structure	-

GRAIN COMPOSITION	%
Quartz	
Monocrystalline quartz	38
Polycrystalline quartz	4
Feldspar	5
Lithic fragments :	
Igneous rocks	
Volcanic rocks	
Sedimentary rocks	7
Metamorphic rocks	
Other :	
Heavy minerals	1
Glauconite	
Mica	3
Opaque minerals	
Fossil	
Carbon	

MATRIX	%
Detrital clay	10
Carbonate ooze	
Carbonaceous	
Others	

POROSITY	%
Intergranular	6
Dissolution	12
Fracture	
Microporosity	

CEMENTS	%
Clay minerals	5
Pyrite	
Carbonate :	
Calcite (non-ferroan)	
Calcite (ferroan)	
Dolomite (non-ferroan)	
Dolomite (ferroan)	
Siderite	
Glauconite	
Hematite	
Quartz	2
Iron Oxide	5
Hydrocarbon	2

SUMMARY :

Sublitharenite composed of grain 58%, grains consist of monocrystalline quartz, polycrystalline quartz, lithic fragment, feldspar, mica, and heavy minerals, grain size is from coarse silt to fine sand grained (0.04-0,23), with its mode of 0.13 mm, well sorted, point, long and sutured contacts, angular-subrounded in grain shape. The grains are bounded by matrix 10% and cement 14%. Matrix consist of detrital clay. Cement consists of clay minerals, iron oxide, quartz and hydrocarbon filling the pore spaces of the rock. Rock porosity of dissolution and intergranular type is 18%.

DIAGENESIS :

The diagenesis stage which can be analyzed in the thin section is :
- Compaction which was identified by point, long and sutured contacts.
- Cementation of clay minerals, iron oxideand quartz.
- Recrystallizaton of quartz cement forming secondary overgrowth
- Dissolution of grains, matrix and cement.
- Secondary porosity due to dissolution.

170

	A	B	C	D	E	F	G	H	I	J	K	L	
1													1
2													2
3													3
4													4
5													5
6													6
7													7
8													8
9													9

▲ // nicol   1 mm   X nicol ▼

	A	B	C	D	E	F	G	H	I	J	K	L	
1													1
2													2
3													3
4													4
5													5
6													6
7													7
8													8
9													9

	A	B	C	D	E	F	G	H	I	J	K	L	

Photomicrograph of Sublitharenite showing monocrystalline quartz (H7), polycrystalline quartz (H4), lithic fragment (E2, G7), feldspar (C8, D8), mica (J1), and heavy minerals (J2) bounded by matrix of detrital clay, cement consists of calcite (J2), quartz (H6), clay minerals (B9), and hydrocarbon (H2). Porosity type is dissolution (C6, E1) and intergranular (F6).

171

PETROGRAPHIC ANALYSIS - 2
(SILICICLASTIC ROCKS)

SAMPLE / WELL NO.	7/P19	LITHOLOGY	Sandstone
DEPTH (ft)		ROCK NAME	Sublitharenite
FORMATION		CLASSIFICATION	Pettijohn (1987)

GRAIN SIZE (mm)	
Minimum	0.03 (Medium Silt)
Mode	0.20 (Fine Sand)
Maximum	0.45 (Medium Sand)

TEXTURE	
Sorting	Well
Roundness	Subangular – subrounded
Grain contacts	Point, long, concavo-convex and sutured contacts
Structure	-

GRAIN COMPOSITION	%
Quartz	
Monocrystalline quartz	37
Polycrystalline quartz	6
Feldspar	5
Lithic fragments :	
Igneous rocks	
Volcanic rocks	
Sedimentary rocks	8
Metamorphic rocks	
Other :	
Heavy minerals	2
Glauconite	
Mica	2
Opaque minerals	
Fossil	
Carbon	

MATRIX	%
Detrital clay	5
Carbonate ooze	
Carbonaceous	
Others	

POROSITY	%
Intergranular	6
Dissolution	14
Fracture	
Microporosity	

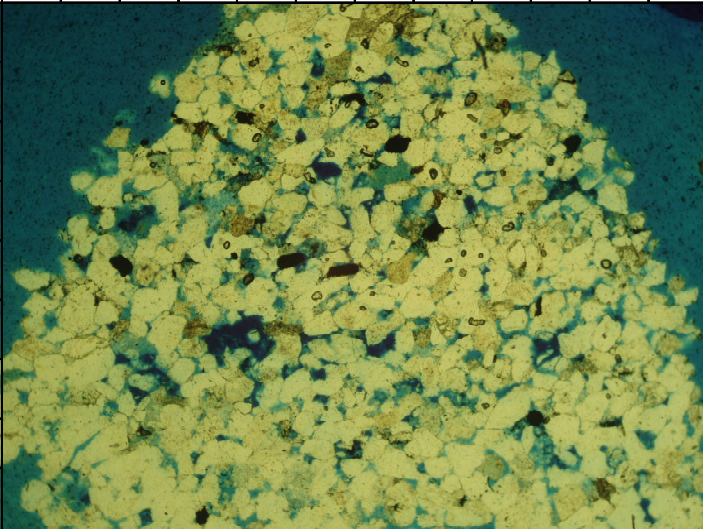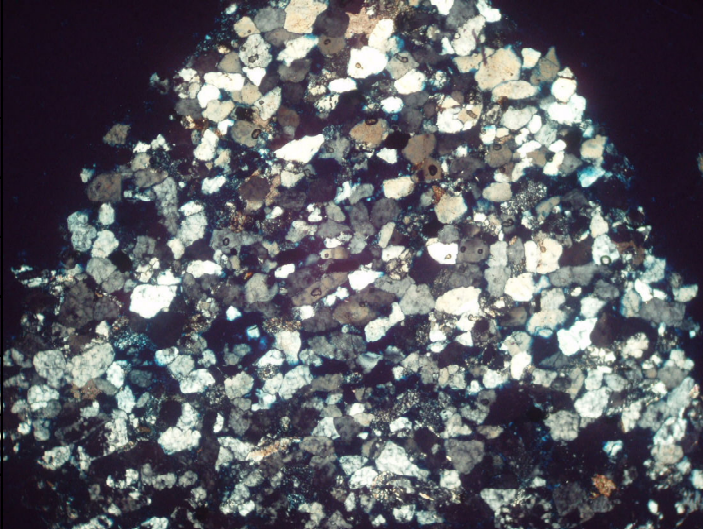| CEMENTS	%
Clay minerals	2
Pyrite	
Carbonate :	
Calcite (non-ferroan)	5
Calcite (ferroan)	
Dolomite (non-ferroan)	
Dolomite (ferroan)	
Siderite	
Glauconite	1
Hematite	
Quartz	4
Iron Oxide	
Hydrocarbon	3

SUMMARY :

Sublitharenite composed of grain 60%, grains consist of monocrystalline quartz, polycrystalline quartz, feldspar, lithic fragment, mica, and heavy minerals, grain size is from medium silt to medium sand grained (0.03-0.45), with its mode of 0.20 mm, well sorted, point, long, concavo-convex and sutured contacts, subangular-subrounded in grain shape. The grains are bounded by matrix 5% and cement 15%. Matrix consist of detrital clay. Cement consists of calcite, quartz, clay minerals and hydrocarbon filling the pore spaces of the rock. Rock porosity of dissolution and intergranular type is 20%.

DIAGENESIS :

The diagenesis stage which can be analyzed in the thin section is :
• Compaction which was identified by point, long, concavo-convex and sutured contacts.
• Cementation of calcite, quartz, clay minerals and hydrocarbon.
• Recrystallizaton of quartz cement forming secondary overgrowth
• Replacement of grains by calcite.
• Dissolution of grains, matrix and cement.
• Secondary porosity due to dissolution.

	A	B	C	D	E	F	G	H	I	J	K	L	
1													1
2													2
3													3
4													4
5													5
6													6
7													7
8													8
9													9

▲ // nicol   1 mm   X nicol ▼

Photomicrograph of Sublitharenite showing monocrystalline quartz (H6), polycrystalline quartz (H3, J3), feldspar (F6), lithic fragment (I4), mica (E8), and heavy minerals bounded by matrix of detrital clay, cement consists of quartz (G5), calcite (G1), clay minerals (D4), iron oxide and hydrocarbon (G3). Porosity type is dissolution (E6) and intergranular (J6).

PETROGRAPHIC ANALYSIS - 3
(SILICICLASTIC ROCKS)

SAMPLE / WELL NO.	15/P3	LITHOLOGY	Sandstone
DEPTH (ft)		ROCK NAME	Sublitharenite
FORMATION		CLASSIFICATION	Pettijohn (1987)

GRAIN SIZE (mm)		TEXTURE	
Minimum	0.03 (Medium Silt)	Sorting	Well
Mode	0.20 (Fine Sand)	Roundness	Subangular – subrounded
Maximum	0.35 (Medium Sand)	Grain contacts	Point, long, concavo-convex and sutured contacts
		Structure	-

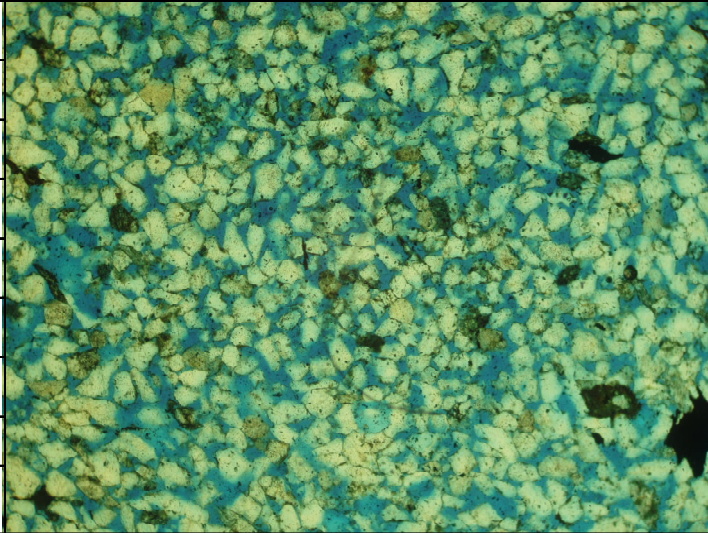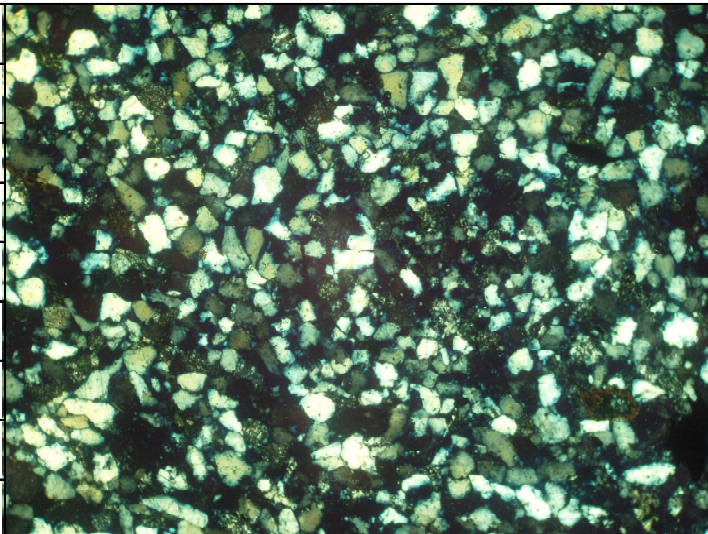| GRAIN COMPOSITION	%	MATRIX	%	CEMENTS	%
Quartz		Detrital clay	5	Clay minerals	3
Monocrystalline quartz	37	Carbonate ooze		Pyrite	
Polycrystalline quartz	5	Carbonaceous		Carbonate :	
Feldspar	5	Others		Calcite (non-ferroan)	3
Lithic fragments :				Calcite (ferroan)	
Igneous rocks				Dolomite (non-ferroan)	
Volcanic rocks				Dolomite (ferroan)	
Sedimentary rocks	8			Siderite	
Metamorphic rocks				Glauconite	
Other :		POROSITY	%	Hematite	
Heavy minerals	2	Intergranular	6	Quartz	4
Glauconite		Dissolution	12	Iron Oxide	3
Mica	3	Fracture		Hydrocarbon	4
Opaque minerals		Microporosity			
Fossil					
Carbon					

SUMMARY :

Sublitharenite composed of grain 60%, grains consist of monocrystalline quartz, polycrystalline quartz, feldspar, lithic fragment, mica, and heavy minerals, grain size is from medium silt to medium sand grained (0.03-0.35), with its mode of 0.20 mm, well sorted, point, long, concavo-convex and sutured contacts, subangular-subrounded in grain shape. The grains are bounded by matrix 5% and cement 17%. Matrix consist of detrital clay. Cement consists of quartz, calcite, clay minerals, iron oxide and hydrocarbon filling the pore spaces of the rock. Rock porosity of dissolution and intergranular type is 18%.

DIAGENESIS :

The diagenesis stage which can be analyzed in the thin section is :
- Compaction which was identified by point, long, concavo-convex and sutured contacts, also mica bending.
- Cementation of quartz, calcite, clay minerals, iron oxide and hydrocarbon.
- Recrystallizaton of quartz cement forming secondary overgrowth
- Replacement of grains by calcite.
- Dissolution of grains, matrix and cement.
- Secondary porosity due to dissolution.

174

	A	B	C	D	E	F	G	H	I	J	K	L	
1													1
2													2
3													3
4													4
5													5
6													6
7													7
8													8
9													9

▲ // nicol   1 mm   X nicol ▼

Photomicrograph of Sublitharenite showing monocrystalline quartz (B7, E3, J9), polycrystalline quartz (J6), lithic fragment (L7), feldspar, and mica bounded by matrix of detrital clay, cement consists of quartz (J2), calcite (K7), clay minerals, and hydrocarbon (L8). Porosity type is dissolution (B5) and intergranular (A2).

PETROGRAPHIC ANALYSIS - 4
(SILICICLASTIC ROCKS)

SAMPLE / WELL NO.	16/P45	LITHOLOGY	Sandstone
DEPTH (ft)		ROCK NAME	Sublitharenite
FORMATION		CLASSIFICATION	Pettijohn (1987)

GRAIN SIZE (mm)	
Minimum	0.03 (Medium Silt)
Mode	0.17 (Fine Sand)
Maximum	0.37 (Medium Sand)

TEXTURE	
Sorting	Well
Roundness	Subangular – subrounded
Grain contacts	Point, long, concavo-convex and sutured contacts
Structure	-

GRAIN COMPOSITION	%
Quartz	
Monocrystalline quartz	40
Polycrystalline quartz	5
Feldspar	5
Lithic fragments :	
Igneous rocks	
Volcanic rocks	
Sedimentary rocks	8
Metamorphic rocks	
Other :	
Heavy minerals	
Glauconite	
Mica	2
Opaque minerals	
Fossil	
Carbon	

MATRIX	%
Detrital clay	3
Carbonate ooze	
Carbonaceous	
Others	

POROSITY	%
Intergranular	6
Dissolution	18
Fracture	
Microporosity	

CEMENTS	%
Clay minerals	2
Pyrite	
Carbonate :	
Calcite (non-ferroan)	2
Calcite (ferroan)	
Dolomite (non-ferroan)	
Dolomite (ferroan)	
Siderite	
Glauconite	
Hematite	
Quartz	4
Iron Oxide	
Hydrocarbon	5

SUMMARY :

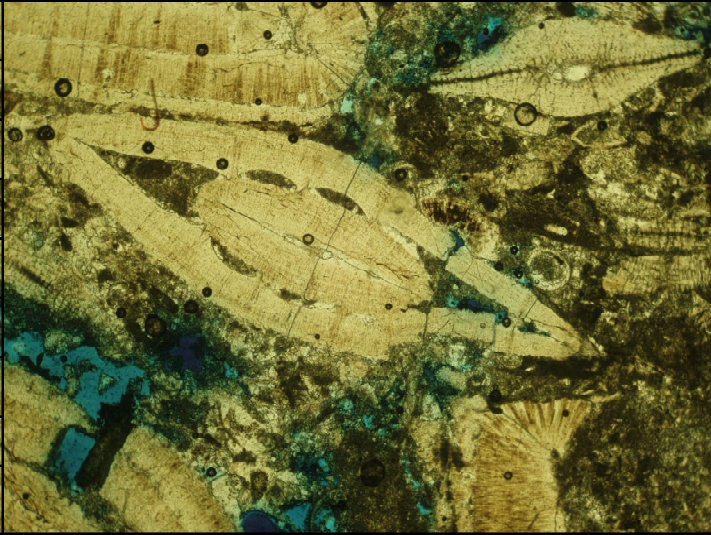Sublitharenite composed of grain 60%, grains consist of monocrystalline quartz, polycrystalline quartz, lithic fragment, feldspar, and mica, grain size is from medium silt to medium sand grained (0.03-0.37), with its mode of 0.17 mm, well sorted, point, long, concavo-convex and sutured contacts, subangular-subrounded in grain shape. The grains are bounded by matrix 3% and cement 13%. Matrix consist of detrital clay. Cement consists of quartz, calcite, clay minerals, and hydrocarbon filling the pore spaces of the rock. Rock porosity of dissolution and intergranular type is 24%.

DIAGENESIS :

The diagenesis stage which can be analyzed in the thin section is :
- Compaction which was identified by point, long, concavo-convex and sutured contacts, also mica bending.
- Cementation of quartz, calcite, clay minerals, and hydrocarbon.
- Recrystallizaton of quartz cement forming secondary overgrowth
- Replacement of grains by calcite.
- Dissolution of grains, matrix and cement.
- Secondary porosity due to dissolution.

Sample No. : 10/BR-1

▲ // nicol   1 mm   X nicol ▼

Photomicrograph of Sublitharenite showing monocrystalline quartz (F3, K6), polycrystalline quartz (F4), lithic fragment (B3, F2, H3), feldspar (), heavy mineral (B5, C6) and mica (K9) bounded by matrix of detrital clay, cement consists of quartz (K2), calcite (B2), clay minerals (C3), and hydrocarbon (A6). Porosity type is dissolution (H3, I3) and intergranular (H4).

PETROGRAPHIC ANALYSIS - 5
(SILICICLASTIC ROCKS)

SAMPLE / WELL NO.	10/BR-1	LITHOLOGY	Sandstone
DEPTH (ft)		ROCK NAME	Litharenite
FORMATION		CLASSIFICATION	Pettijohn (1987)

GRAIN SIZE (mm)	
Minimum	0.04 (Coarse Silt)
Mode	0.22 (Fine Sand)
Maximum	0.51 (Coarse Sand)

TEXTURE	
Sorting	Well
Roundness	Subrounded-Rounded
Grain contacts	Point, long, concavo-convex and sutured contacts
Structure	Orientation of grains

GRAIN COMPOSITION	%
Quartz	
Monocrystalline quartz	36
Polycrystalline quartz	7
Feldspar	7
Lithic fragments :	
Igneous rocks	
Volcanic rocks	
Sedimentary rocks	10
Metamorphic rocks	
Other :	
Heavy minerals	2
Glauconite	
Mica	2
Opaque minerals	
Fossil	

MATRIX	%
Detrital clay	3
Carbonate ooze	
Carbonaceous	
Others	

POROSITY	%
Intergranular	6
Dissolution	14
Fracture	
Microporosity	

CEMENTS	%
Clay minerals	2
Pyrite	
Carbonate :	
Calcite (non-ferroan)	4
Calcite (ferroan)	
Dolomite (non-ferroan)	
Dolomite (ferroan)	
Siderite	
Glauconite	
Hematite	
Quartz	3
Iron Oxide	
Hydrocarbon	4

SUMMARY :
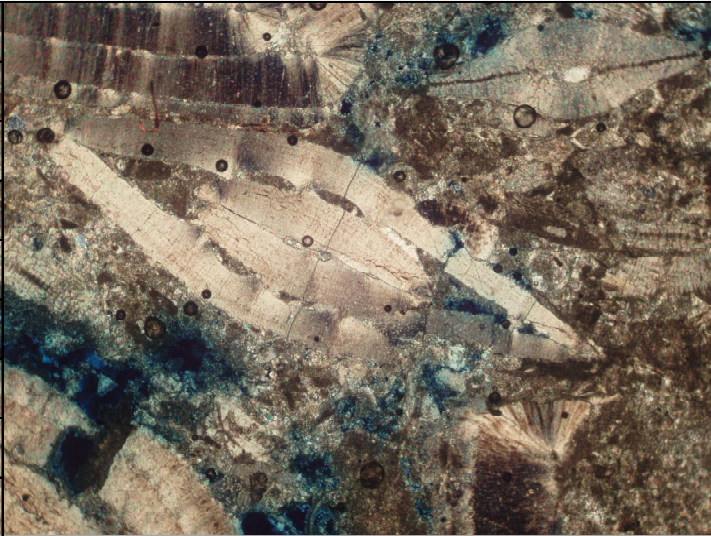
Litharenite composed of grain 60%, grains consist of monocrystalline quartz, polycrystalline quartz, lithic fragment, feldspar, heavy mineral and mica, grain size is from coarse silt to coarse sand grained (0.04-0.51), with its mode of 0.22 mm, well sorted, point, long, concavo-convex and sutured contacts, subrounded-rounded in grain shape. The grains are bounded by matrix 3% and cement 13%. Matrix consist of detrital clay. Cement consists of quartz, calcite, clay minerals, and hydrocarbon filling the pore spaces of the rock. Rock porosity of dissolution and intergranular type is 20%.

DIAGENESIS :

The diagenesis stage which can be analyzed in the thin section is :
- Compaction which was identified by point, long, concavo-convex and sutured contacts, also mica bending.
- Cementation of quartz, calcite, clay minerals, and hydrocarbon.
- Recrystallizaton of quartz cement forming secondary overgrowth
- Replacement of grains by calcite.
- Dissolution of grains, matrix and cement.
- Secondary porosity due to dissolution.

Sample No. : 3/368

	A	B	C	D	E	F	G	H	I	J	K	L	
1													1
2													2
3													3
4													4
5													5
6													6
7													7
8													8
9													9

▲ // nicol   1 mm   X nicol ▼

Photomicrograph of Larger Foraminifera Packstone showing larger foraminifera (A9, C1, F5, J2), echinoderms, corals, red algae, planktonic foraminifera (J5), and benthonic foraminifera bounded by matrix of micrite (H2), cement consists of calcite (E8, J2), and dolomite (H1). Porosity type is vug (B7, E9), fracture (H5) and intercystal (H1, H7).

179

PETROGRAPHIC ANALYSIS - 6
(CARBONATE ROCKS)

SAMPLE / WELL NO.	3/368	LITHOLOGY	Limestone
DEPTH (ft)		ROCK NAME	Larger Foraminifera Packstone
FORMATION		CLASSIFICATION	Dunham, 1962

TEXTURE			
Grain size mode	2.4 mm	Abrasion	Abraded > unabraded
Grain size range	0.16– 7.65mm	Fabric	Mud-grain supported
Sorting	Poorly	Grain contact	Point, long and sutured contacts
Roundness	Angular - Subrounded	Structure	Fracture

GRAIN COMPOSITION	%
Quartz	
Monocrystalline quartz	
Polycrystalline quartz	
Feldspar	
Lithic fragments :	
Igneous rocks	
Volcanic rocks	
Sedimentary rocks	
Metamorphic rocks	
Other :	
Heavy minerals	
Glauconite	
Mica	
Opaque minerals	

POROSITY	%
Interparticle	
Intraparticle	
Intercrystal	3
Moldic	
Fenestral	
Shelter	
Growth Framework	
Fracture	2
Channel	
Vug	20

GRAIN COMPOSITION	%
Carbonate Grains :	
Clastic lime, Bio, Pyhsico Ch.	
Intraclasts	
Extraclasts	
Peloids	
Ooids	
Pisoids	
Oncoids	
Skeletal Grains	
Red Algae	4
Green Algae	
Blue-Green Algae	
Planktonic Foraminifera	3
Benthonic Foraminifera	2
Large Foraminifera	33
Trilobites	
Brachiopods	
Corals	4
Bryozoans	
Echinoderms	7
Molluscs	
Ostracods	
Indeterminate bioclasts	

MATRIX	%
Micrite (Lime mud)	10
Clay minerals	
Carbonaceous	
Others	

CEMENTS	
Clay minerals	
Pyrite	
Carbonate :	
Calcite (non-ferroan)	8
Calcite (ferroan)	
Dolomite (non-ferroan)	4
Dolomite (ferroan)	
Siderite	
Glauconite	
Hematite	
Quartz	
Iron Oxide	
Hydrocarbon	

TYPE OF CEMENTS							
Needle (fine acicular)		Pendant		Meniscus		Acicular (fibrous)	v
Pelodial		Micritic	v	Columnar		Equant (blocky)	
Overgrowth		Poikilotopic		Baroque (saddle)		Syntaxial	v
Circumgranular isopachus acicular		Sparry		Circumgranular equant		Epitaxial	

SUMMARY :

Larger Foraminifera Packstone consist of carbonate grain 53%, mud-grain supported, poorly sorted, point, long and sutured contacts, angular-subrounded in grain shape. The grains are bounded by matrix 10% and cement 12%. Rock porosity of vug, fracture and intercystal type is 25%. Carbonate grain consist of larger foraminifera, echinoderms, corals, red algae, planktonic foraminifera and benthonic foraminifera. Matrix consist of micrite. Carbonate cement consist of calcite, and dolomite. Type of cement consist of acicular, and syntaxial.

DIAGENESIS :

The diagenesis stage which can be analyzed in the thin section is :
- Microbial micritization.
- Dissolution forming vug porosity.
- Dolomitization and forming intercrystal porosity.
- Cementation of calcite and dolomite, with cements type of syntaxial overgrowth in echinoderms, and acicular.
- Neomorphism micrite to microspar
- Compaction forming point, long and sutured contacts, and fracture porosity.

Photomicrograph of Dolomitized Red Algae Packstone showing red algae (K3), larger foraminifera (K6), molluscs, and indeterminate bioclast, bounded by matrix of micrite (G5), mostly of micrite neomorphised to microspar than mostly had been dolomitized (B3, C4, F3, G8) and to form intercrystal porosity (A1, E3), dissolution to form vug (F9, H1) and moldic (J7) porosity.
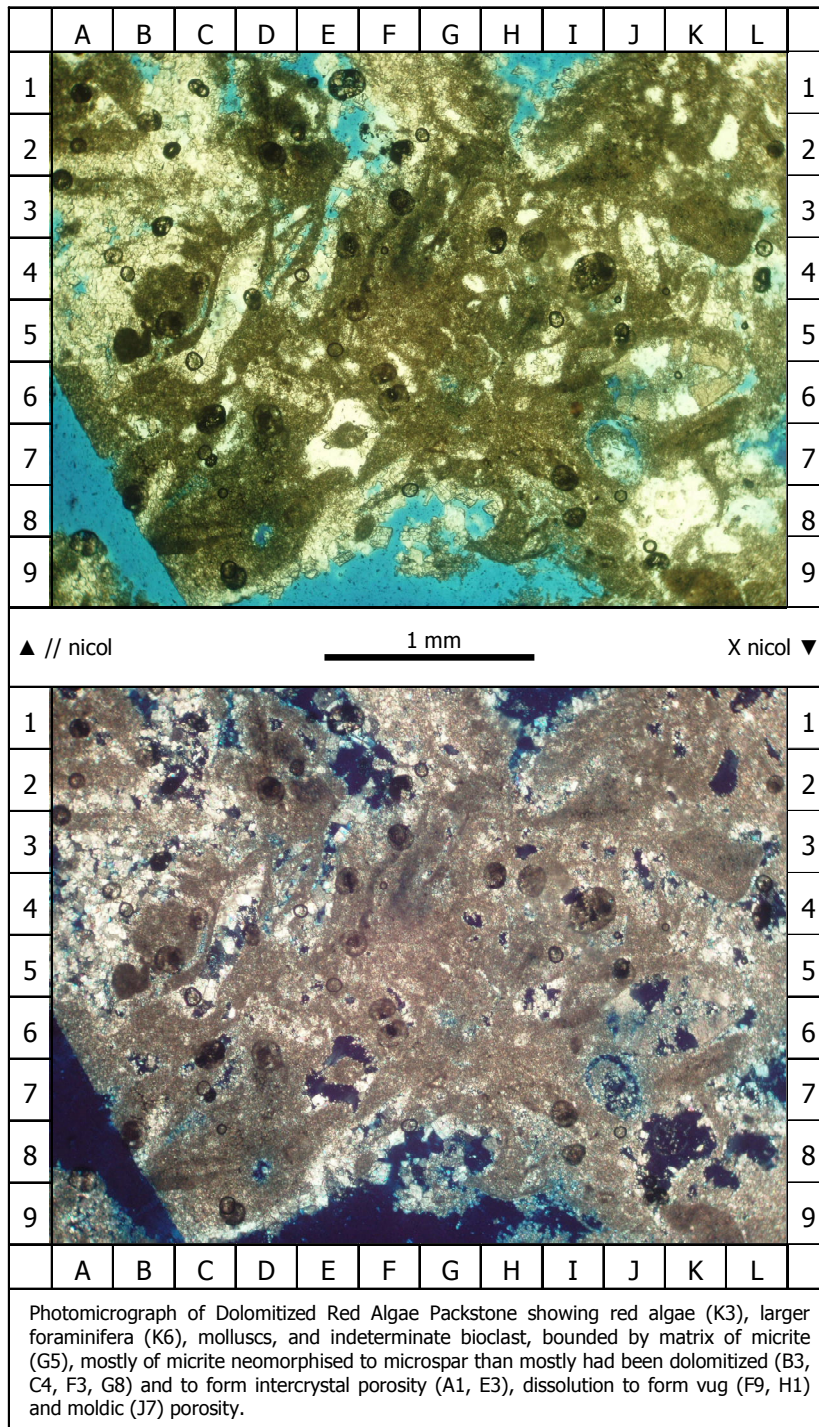
PETROGRAPHIC ANALYSIS - 7
(CARBONATE ROCKS)

SAMPLE / WELL NO.	12/158	LITHOLOGY	Limestone
DEPTH (ft)		ROCK NAME	Dolomitized Red Algae Packstone
FORMATION		CLASSIFICATION	Dunham, 1962

TEXTURE			
Grain size mode	1.4 mm	Abrasion	Abraded > unabraded
Grain size range	0.40–4.15 mm	Fabric	Mud-grain supported
Sorting	Poorly	Grain contact	Point and long contacts
Roundness	Angular - subrounded	Structure	

GRAIN COMPOSITION	%
Quartz	
Monocrystalline quartz	
Polycrystalline quartz	
Feldspar	
Lithic fragments :	
Igneous rocks	
Volcanic rocks	
Sedimentary rocks	
Metamorphic rocks	
Other :	
Heavy minerals	
Glauconite	
Mica	
Opaque minerals	

POROSITY	%
Interparticle	
Intraparticle	
Intercrystal	15
Moldic	5
Fenestral	
Shelter	
Growth Framework	
Fracture	
Channel	
Vug	10

GRAIN COMPOSITION	%
Carbonate Grains :	
Clastic lime, Bio, Pyhsico Ch.	
Intraclasts	
Extraclasts	
Peloids	
Ooids	
Pisoids	
Oncoids	
Skeletal Grains	
Red Algae	27
Green Algae	
Blue-Green Algae	
Planktonic Foraminifera	
Benthonic Foraminifera	
Large Foraminifera	2
Trilobites	
Brachiopods	
Corals	
Bryozoans	
Echinoderms	
Molluscs	1
Ostracods	
Indeterminate bioclasts	5

MATRIX	%
Micrite (Lime mud)	10
Clay minerals	
Carbonaceous	
Others	

CEMENTS	
Clay minerals	
Pyrite	
Carbonate :	
Calcite (non-ferroan)	10
Calcite (ferroan)	
Dolomite (non-ferroan)	15
Dolomite (ferroan)	
Siderite	
Glauconite	
Hematite	
Quartz	
Iron Oxide	
Hydrocarbon	

TYPE OF CEMENTS							
Needle (fine acicular)		Pendant		Meniscus		Acicular (fibrous)	
Pelodial		Micritic		Columnar		Equant (blocky)	v
Overgrowth		Poikilotopic		Baroque (saddle)		Syntaxial	
Circumgranular isopachus acicular		Sparry		Circumgranular equant		Epitaxial	

SUMMARY :

Dolomitized Red Algae Packstone consist of carbonate grain 35%, mud-grain supported, poorly sorted, point and long contacts, angular-subrounded in grain shape. The grains are bounded by matrix 10% and cement 25%. Rock porosity of intercrystal, vug, and moldic type is 30%. Carbonate grain consist of red algae, larger foraminifera, molluscs, and indeterminate bioclast. Matrix consist of micrite. Carbonate cement consist of calcite and dolomite. Type of cement consist of equant.
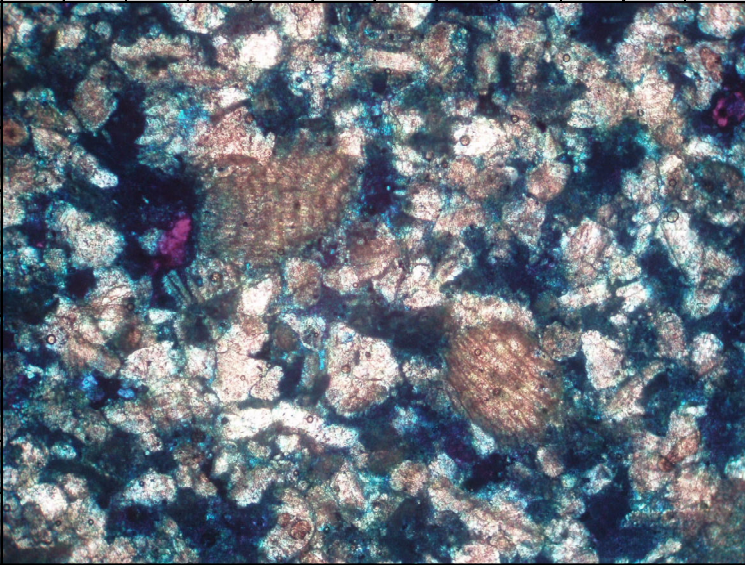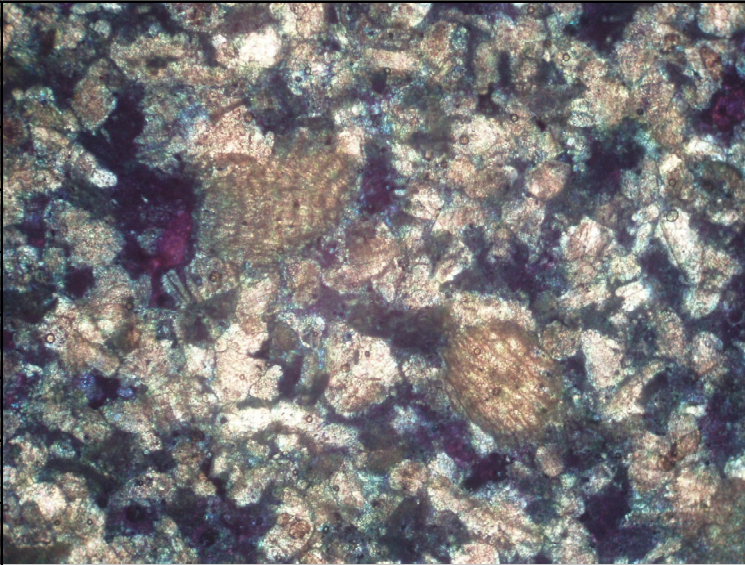
DIAGENESIS :

The diagenesis stage which can be analyzed in the thin section is :
- Dissolution forming vug and moldic porosity.
- Dolomitization and forming intercrystal porosity.
- Cementation of calcite and dolomite, with cements type of equant.
- Neomorphism micrite to microspar
- Compaction forming point and long contacts.

182

Sample No. : 2/347

Photomicrograph of Silicified-Dedolomitized Ooids Packstone showing ooids (E6), bounded by matrix of micrite (K4), mostly of micrite had been dolomitized, dolomite partially had been dedolomitized to form calcite. Cement consists of dolomite (L7), quartz (C5, D9, J5) and calcite. Porosity type is moldic (K3), vug (C8), and intercystal (J1, J9).

PETROGRAPHIC ANALYSIS -8 (CARBONATE ROCKS)			

SAMPLE / WELL NO.	2/347	LITHOLOGY	Limestone
DEPTH (ft)		ROCK NAME	Silicified-Dedolomitized Ooids Packstone
FORMATION		CLASSIFICATION	Dunham, 1962

TEXTURE			
Grain size mode	0.58 mm	Abrasion	Abraded < unabraded
Grain size range	0.10–0.92 mm	Fabric	Mud-grain supported
Sorting	Poorly	Grain contact	Point and long contact
Roundness	Subrounded - rounded	Structure	

GRAIN COMPOSITION	%
Quartz	
Monocrystalline quartz	
Polycrystalline quartz	
Feldspar	
Lithic fragments :	
Igneous rocks	
Volcanic rocks	
Sedimentary rocks	
Metamorphic rocks	
Other :	
Heavy minerals	
Glauconite	
Mica	
Opaque minerals	

POROSITY	%
Interparticle	
Intraparticle	
Intercrystal	5
Moldic	10
Fenestral	
Shelter	
Growth Framework	
Fracture	
Channel	
Vug	5

GRAIN COMPOSITION	%
Carbonate Grains :	
Clastic lime, Bio, Pyhsico Ch.	
Intraclasts	
Extraclasts	
Peloids	
Ooids	30
Pisoids	
Oncoids	
Skeletal Grains	
Red Algae	
Green Algae	
Blue-Green Algae	
Planktonic Foraminifera	
Benthonic Foraminifera	
Large Foraminifera	
Trilobites	
Brachiopods	
Corals	
Bryozoans	
Echinoderms	
Molluscs	
Ostracods	
Indeterminate bioclasts	

MATRIX	%
Micrite (Lime mud)	10
Clay minerals	
Carbonaceous	
Others	

CEMENTS	
Clay minerals	
Pyrite	
Carbonate :	
Calcite (non-ferroan)	5
Calcite (ferroan)	
Dolomite (non-ferroan)	25
Dolomite (ferroan)	
Siderite	
Glauconite	
Hematite	
Quartz	10
Iron Oxide	
Hydrocarbon	

TYPE OF CEMENTS							
Needle (fine acicular)		Pendant		Meniscus		Acicular (fibrous)	
Pelodial		Micritic	v	Columnar		Equant (blocky)	v
Overgrowth		Poikilotopic		Baroque (saddle)		Syntaxial	
Circumgranular isopachus acicular		Sparry		Circumgranular equant		Epitaxial	

SUMMARY :

Silicified-Dedolomitized Ooids Packstone consist of carbonate grain 30%, mud-grain supported, poorly sorted, point and long contact, subrounded-rounded in grain shape. The grains are bounded by matrix 10% and cement 40%. Rock porosity of moldic, vug, and intercrystal type is 20%.

Carbonate grain consist of ooids. Matrix consist of micrite. Carbonate cement consist of dolomite, quartz and calcite. Type of cement consist of micritic and equant.

DIAGENESIS :

The diagenesis stage which can be analyzed in the thin section is :

- Microbial micritization.
- Dissolution forming vug and moldic porosity.
- Dolomitization and forming intercrystal porosity.
- Development of authigenic quartz.
- Cementation of dolomite, quartz and calcite, with cements type of micritic and equant.
- Neomorphism micrite to microspar.
- Compaction forming point and long contacts.

	A	B	C	D	E	F	G	H	I	J	K	L	
1													1
2													2
3													3
4													4
5													5
6													6
7													7
8													8
9													9

▲ // nicol   1 mm   X nicol ▼

Photomicrograph of Bioclastic Packstone showing echinoderms, larger foraminifera (E4, H6), molluscs, benthonic foraminifera, planktonic foraminifera and indeterminate bioclasts bounded by matrix of micrite, cement consists of calcite, and dolomite (C6). Porosity type is vug (C4, L2), moldic and intercystal (D2, G2).

PETROGRAPHIC ANALYSIS - 9
(CARBONATE ROCKS)

SAMPLE / WELL NO.	14/9056	LITHOLOGY	Limestone
DEPTH (ft)		ROCK NAME	Bioclastic Packstone
FORMATION		CLASSIFICATION	Dunham, 1962

TEXTURE			
Grain size mode	0.80 mm	Abrasion	Abraded > unabraded
Grain size range	0.08–3.25 mm	Fabric	Mud-grain supported
Sorting	Moderately	Grain contact	Point, long and sutured contacts
Roundness	Subangular - subrounded	Structure	

GRAIN COMPOSITION	%
Quartz	
Monocrystalline quartz	
Polycrystalline quartz	
Feldspar	
Lithic fragments :	
Igneous rocks	
Volcanic rocks	
Sedimentary rocks	
Metamorphic rocks	
Other :	
Heavy minerals	
Glauconite	
Mica	
Opaque minerals	

POROSITY	%
Interparticle	
Intraparticle	
Intercrystal	7
Moldic	
Fenestral	
Shelter	
Growth Framework	
Fracture	
Channel	
Vug	18

GRAIN COMPOSITION	%
Carbonate Grains :	
Clastic lime, Bio, Pyhsico Ch.	
Intraclasts	
Extraclasts	
Peloids	
Ooids	
Pisoids	
Oncoids	
Skeletal Grains	
Red Algae	
Green Algae	
Blue-Green Algae	
Planktonic Foraminifera	2
Benthonic Foraminifera	5
Large Foraminifera	10
Trilobites	
Brachiopods	
Corals	
Bryozoans	
Echinoderms	12
Molluscs	8
Ostracods	
Indeterminate bioclasts	5

MATRIX	%
Micrite (Lime mud)	15
Clay minerals	
Carbonaceous	
Others	

CEMENTS	
Clay minerals	
Pyrite	
Carbonate :	
Calcite (non-ferroan)	18
Calcite (ferroan)	
Dolomite (non-ferroan)	
Dolomite (ferroan)	
Siderite	
Glauconite	
Hematite	
Quartz	
Iron Oxide	
Hydrocarbon	

TYPE OF CEMENTS							
Needle (fine acicular)		Pendant		Meniscus		Acicular (fibrous)	
Pelodial		Micritic	v	Columnar		Equant (blocky)	
Overgrowth		Poikilotopic		Baroque (saddle)		Syntaxial	v
Circumgranular isopachus acicular		Sparry		Circumgranular equant		Epitaxial	

SUMMARY :

Bioclastic Packstone consist of carbonate grain 42%, mud-grain supported, moderately sorted, point, long and sutured contacts, subangular-subrounded in grain shape. The grains are bounded by matrix 15% and cement 18%. Rock porosity of vug, and intercrystal type is 25%.
Carbonate grain consist of echinoderms, larger foraminifera, molluscs, benthonic foraminifera, planktonic foraminifera and indeterminate bioclasts. Matrix consist of micrite. Carbonate cement consist of calcite. Type of cement consist of syntaxial, and micritic.

DIAGENESIS :

The diagenesis stage which can be analyzed in the thin section is :
- Microbial micritization.
- Dissolution forming vug porosity.
- Dolomitization and forming intercrystal porosity, then dedolomitization.
- Cementation of calcite, with cements type of syntaxial overgrowth in echinoderms, and micritic.
- Neomorphism micrite to microspar.
- Compaction forming point, long and sutured contacts.

APPENDIX D

HISTOGRAM OF PORE GEOMETRY

Lithology	Porosity (%)	Permeability (mD)
Sandstone	24.9	467.6
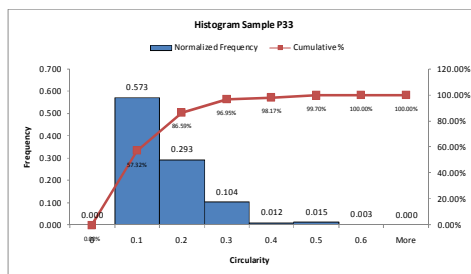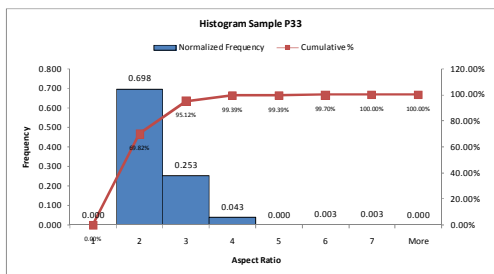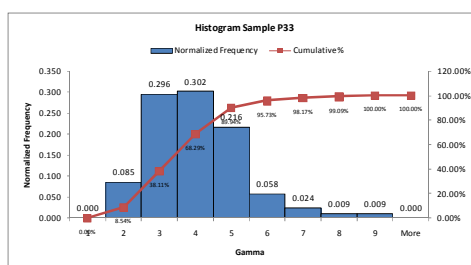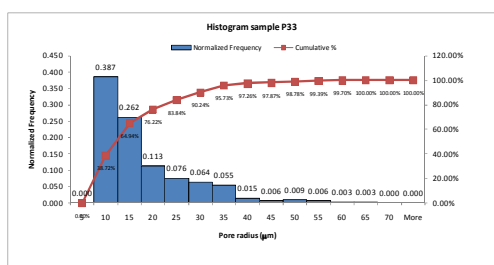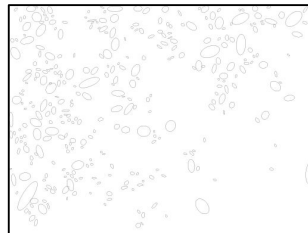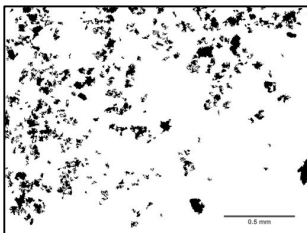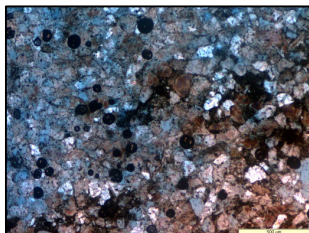
Pore size distribution of sample P33: micropore size is around 90.24% and macropore is 9.8%.

Lithology	Porosity (%)	Permeability (mD)
Sandstone	23.45%	254.347
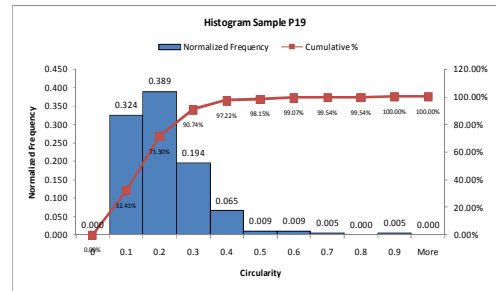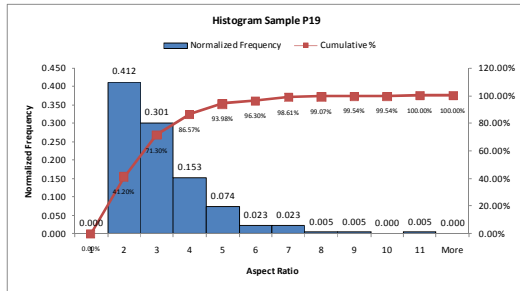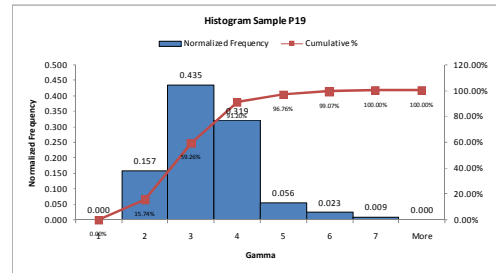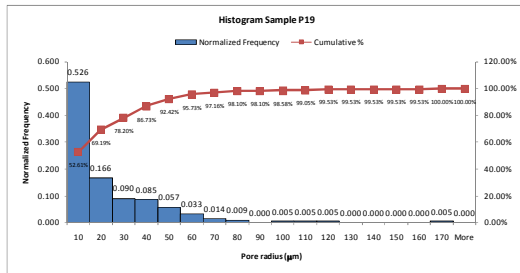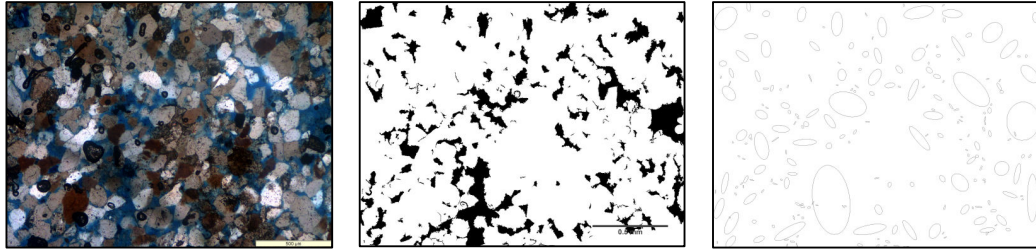
Pore size distribution of sample P19: micropore size is around 78.20 % and macropore is 21.8 %.

Sample Number : P03

Lithology	Porosity (%)	Permeability (mD)
Sandstone	21.57%	74.162
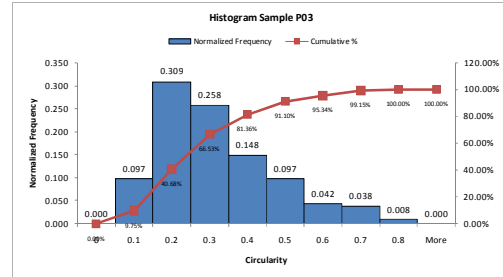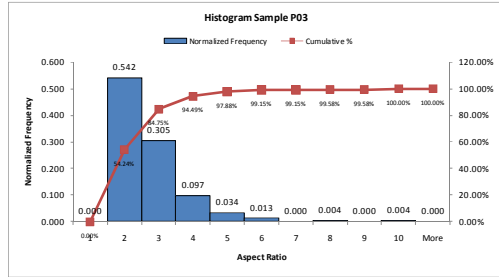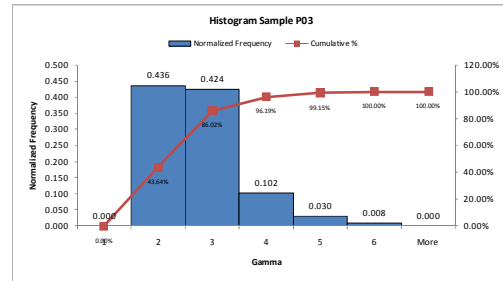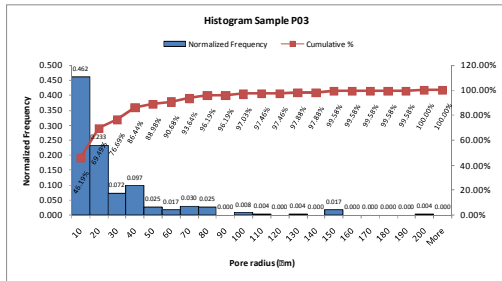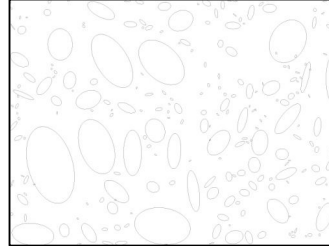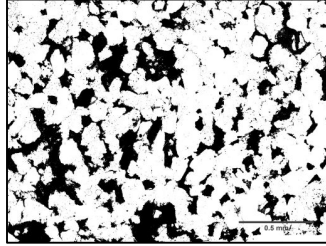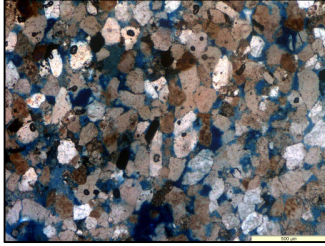
Pore size distribution of sample P03: micropore size is around 76.69 % and macropore is 23.31 %.

Lithology	Porosity (%)	Permeability (mD)
Sandstone	25.40%	919.552
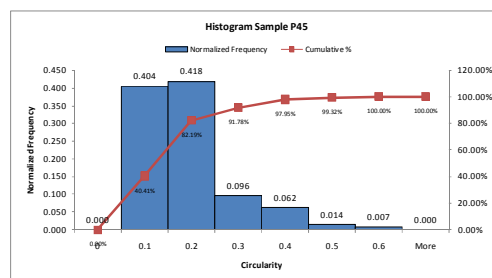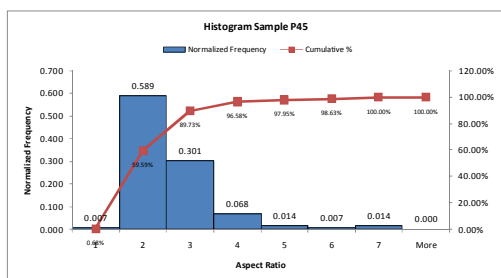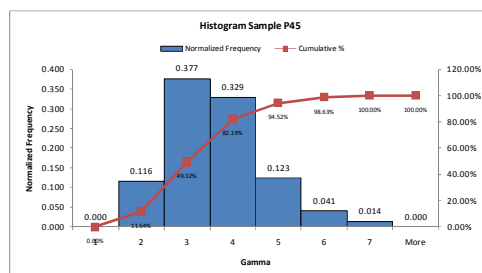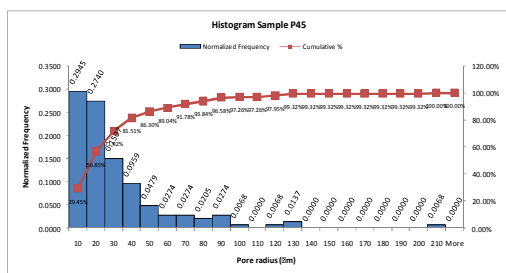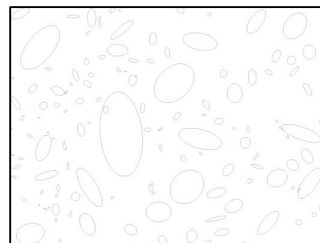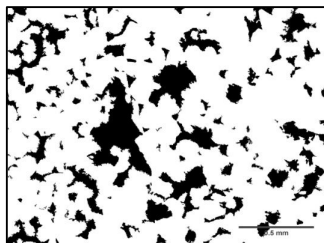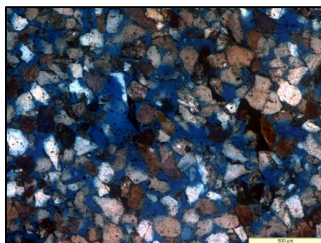
Pore size distribution of sample P45: micropore size is around 71.92 % and macropore is 28.08 %.

Sample Number : BR-1

Lithology	Porosity (%)	Permeability (mD)
Sandstone	17.51%	178.857
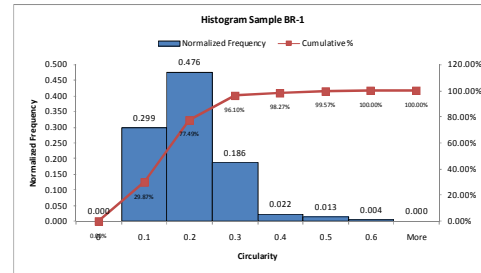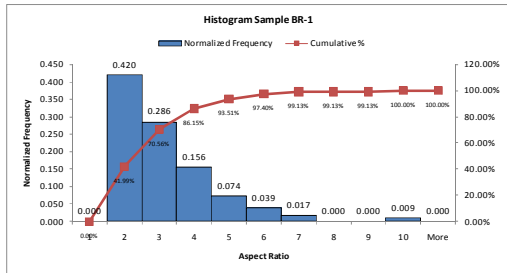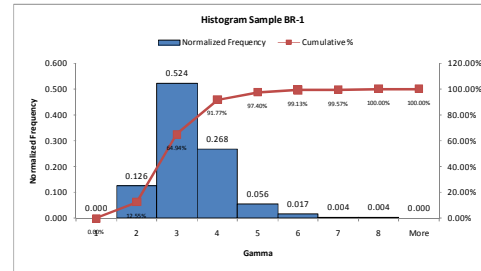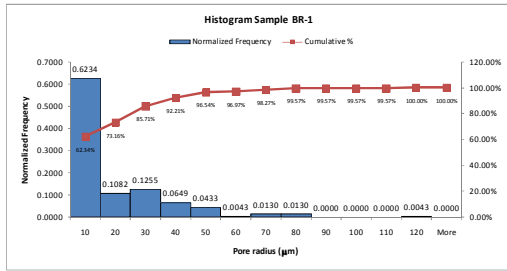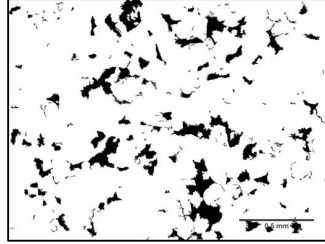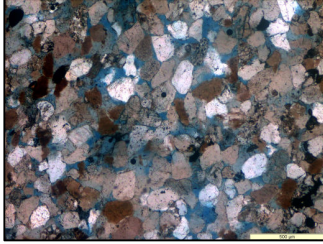
Pore size distribution of sample BR-1: micropore size is around 85.71 % and macropore is 14.29 %.

Lithology	Porosity (%)	Permeability (mD)
Carbonate	29.15%	5091.025
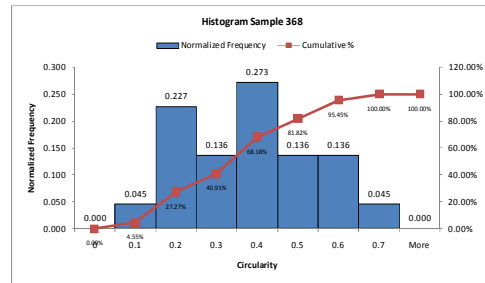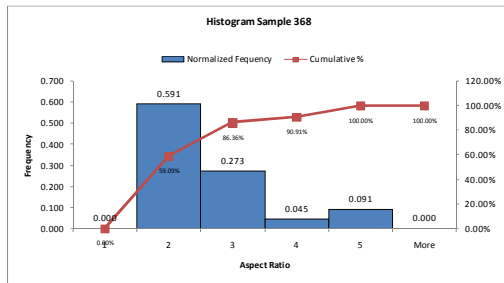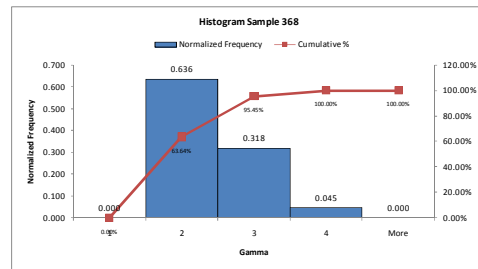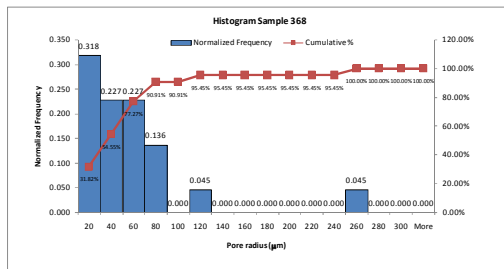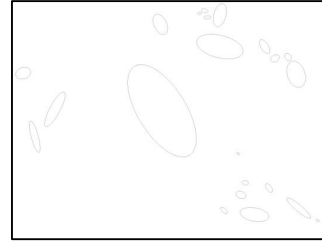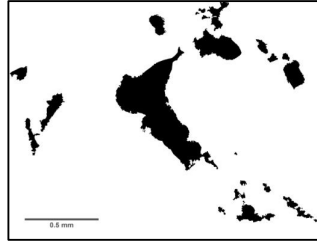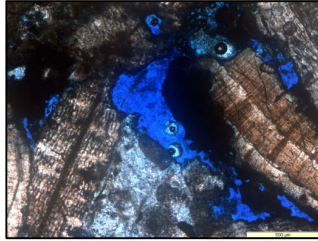
Pore size distribution of sample 368: micropore size is around 43.2 %   and macropore is 56.8 %.

Sample Number : 158

Lithology	Porosity (%)	Permeability (mD)
Carbonate	31.94%	648.556
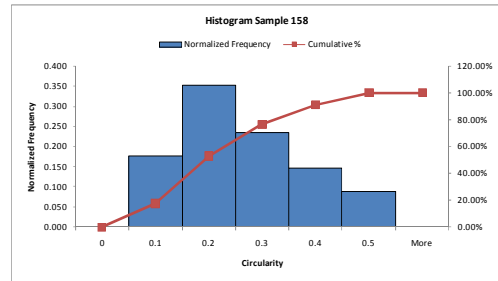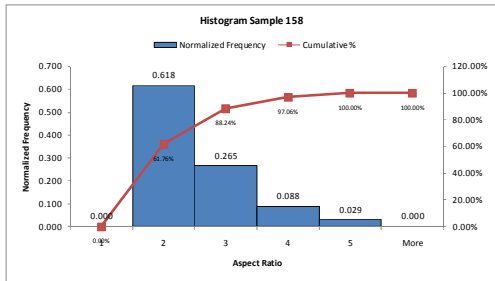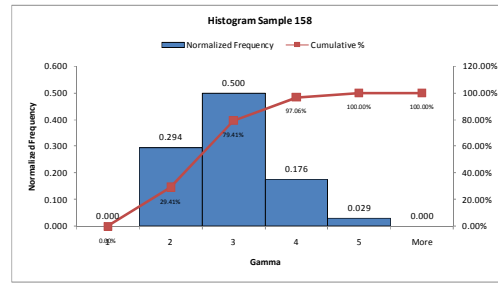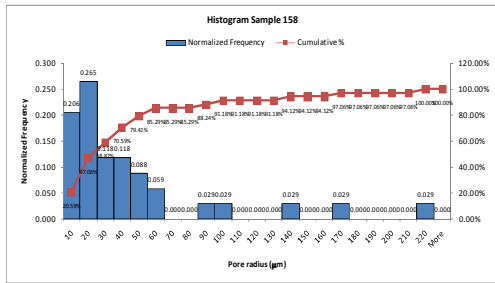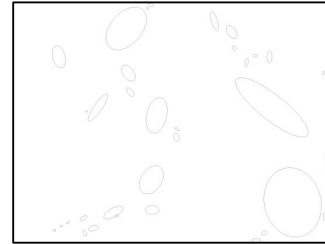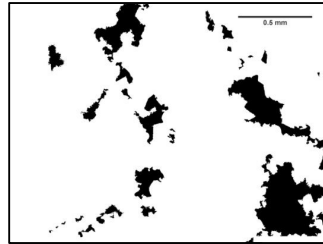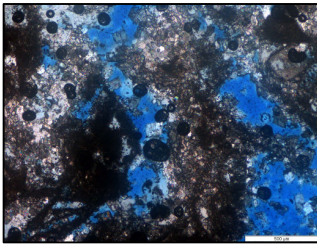
Pore size distribution of sample 158: micropore size is around 58.82 % and macropore is 41.18 %.

Sample Number : 347

Lithology	Porosity (%)	Permeability (mD)
Carbonate	19.66%	2086.069
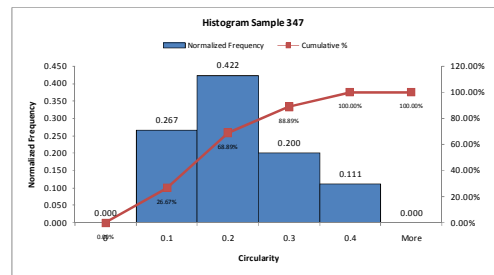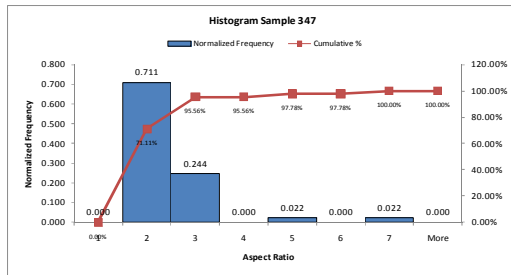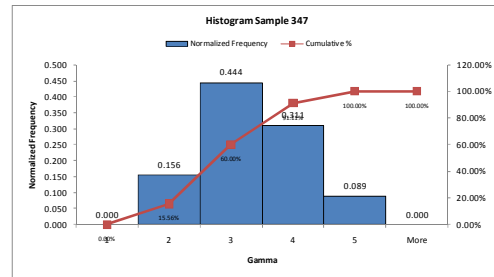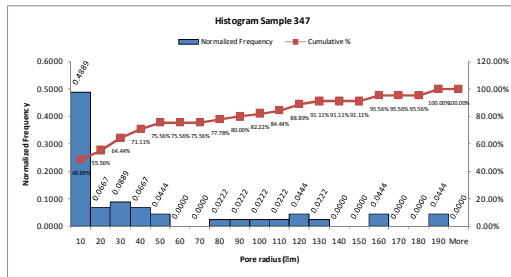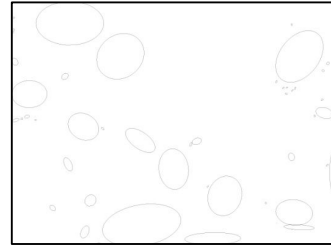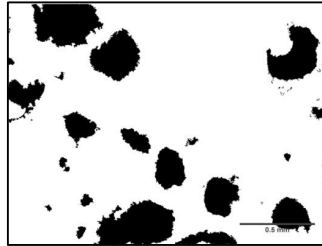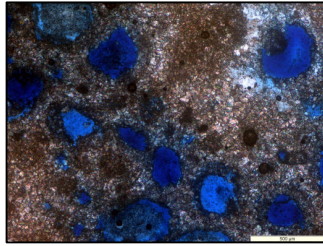
Pore size distribution of sample 347: micropore size is around 64.44 % and macropore is 35.56 %.

Sample Number : 9056
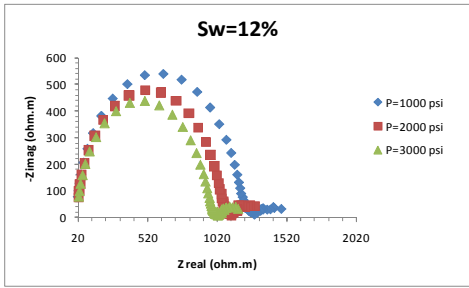
Lithology	Porosity (%)	Permeability (mD)
Carbonate	12.54%	17.523
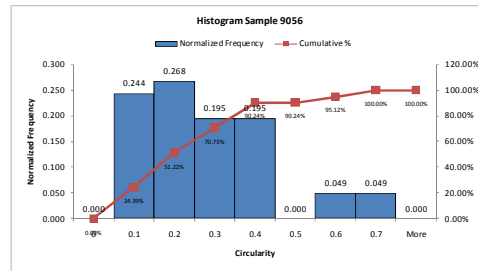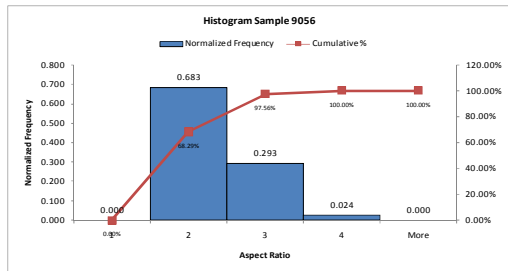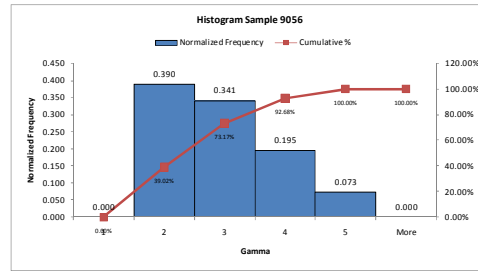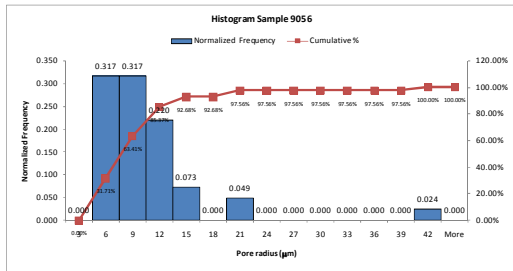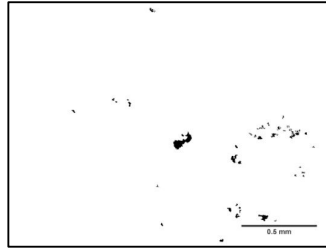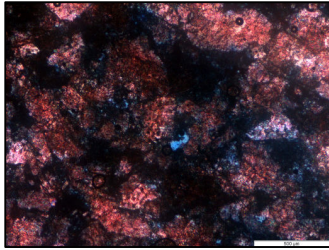
Pore size distribution of sample 9056: micropore size is around 97.56 % and macropore is 2.44 %.
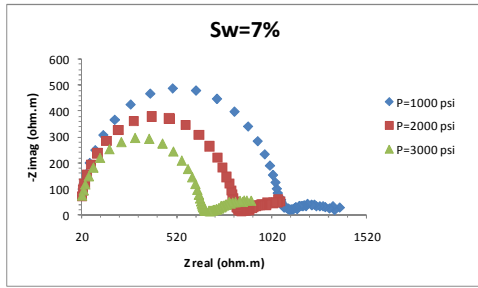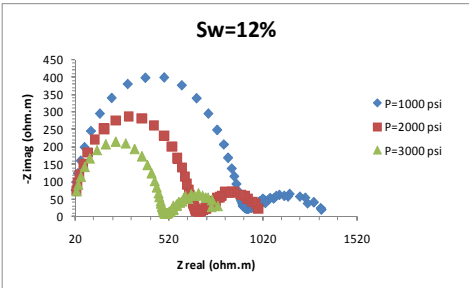
APPENDIX E

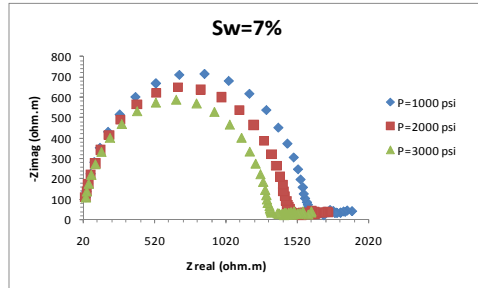PLOT OF REAL AND IMAGINARY RESISTIVITY
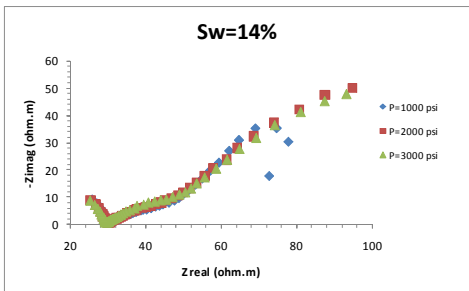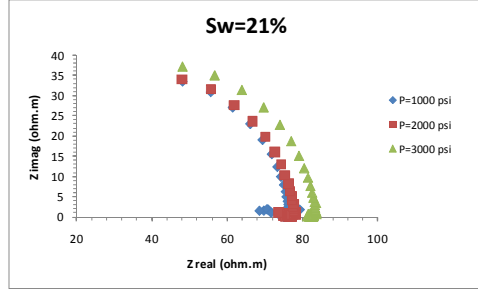
Sample P03

Sample P45

Sample P19

Sample 158

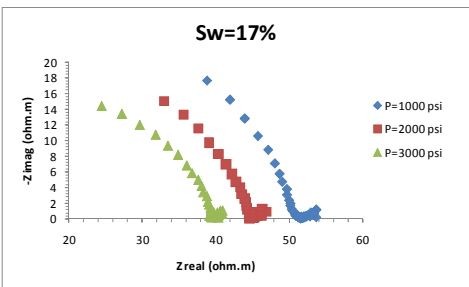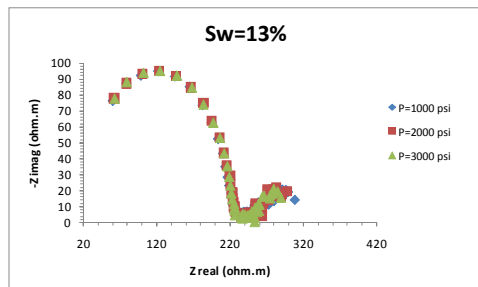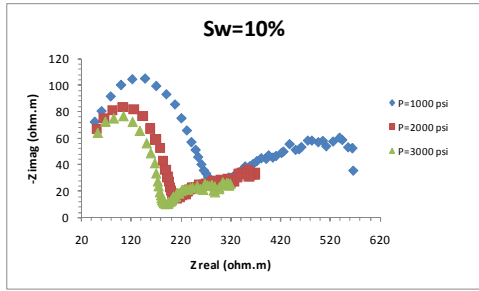
Sample P 33

Sample347

Sample 368

Sample 9056

198

Sample BR-1

APPENDIX F

DERIVATION OF SEMI CIRCLE OF DEBYE AND COLE-COLE MODEL

A. Debye Model

$$\varepsilon^*(\omega) = \varepsilon_\infty + \frac{\varepsilon_o - \varepsilon_\infty}{1 + i\omega\tau} \tag{A.1}$$

$$\varepsilon^*(\omega) = \varepsilon_\infty + \frac{\varepsilon_o - \varepsilon_\infty}{1 + \omega^2\tau^2} - i\frac{(\varepsilon_o - \varepsilon_\infty)\omega\tau}{1 + \omega^2\tau^2} \tag{A.2}$$

$$\varepsilon^*(\omega) = \varepsilon' - i\varepsilon'' \tag{A.3}$$

where is

$$\varepsilon' = \varepsilon_\infty + \frac{\varepsilon_o - \varepsilon_\infty}{1 + \omega^2\tau^2} \tag{A.4}$$

$$\varepsilon'' = \frac{(\varepsilon_o - \varepsilon_\infty)\omega\tau}{1 + \omega^2\tau^2} \tag{A.5}$$

Shifting $\omega^2\tau^2$ in equation (A.4) to the left side yields

$$\omega^2\tau^2 = \frac{(\varepsilon_o - \varepsilon_\infty)}{(\varepsilon' - \varepsilon_\infty)} - 1 \tag{A.6}$$

If equation (A.6) is substituted into equation (A.5), the result is:

$$\varepsilon''^2 = (\varepsilon_o - \varepsilon_\infty)^2 \frac{1}{(1 + i\omega^2\tau^2)^2} \omega^2\tau^2 \tag{A.7}$$

$$\varepsilon''^2 = -\left(\varepsilon' - \frac{\varepsilon_o + \varepsilon_\infty}{2}\right)^2 + \left(\frac{\varepsilon_o - \varepsilon_\infty}{2}\right)^2 \tag{A.8}$$

201

The last equation represents a circle equation

$$\left(\varepsilon' - \frac{\varepsilon_o + \varepsilon_\infty}{2}\right)^2 + \varepsilon''^2 = \left(\frac{\varepsilon_o - \varepsilon_\infty}{2}\right)^2 \qquad (A.9)$$

Where the central coordinate of the circle is $\left(\frac{\varepsilon_o + \varepsilon_\infty}{2}, 0\right)$ and the radius is

$$r = \left(\frac{\varepsilon_o - \varepsilon_\infty}{2}\right)$$

B. Cole-Cole Model

$$\varepsilon^*(\omega) = \varepsilon_\infty + \frac{(\varepsilon_o - \varepsilon_\infty)}{1 + (i\omega\tau)^\beta} \quad \text{with} \quad \beta = 1 - \alpha$$

Defined $i^\beta = \left(e^{i\frac{\pi}{2}}\right)^\beta = \cos\left(\frac{\beta\pi}{2}\right) + i\sin\left(\frac{\beta\pi}{2}\right)$ and if it substituted into Cole-Cole equation, the result is:

$$\varepsilon^* = \varepsilon_\infty + \frac{(\varepsilon_o - \varepsilon_\infty)\left\{\left[1 + (\omega\tau)^\beta \cos\left(\frac{\beta\pi}{2}\right)\right] - i(\omega\tau)^\beta \sin\left(\frac{\beta\pi}{2}\right)\right\}}{\left[1 + (\omega\tau)^\beta \cos\left(\frac{\beta\pi}{2}\right)\right]^2 + (\omega\tau)^{2\beta} \sin^2\left(\frac{\beta\pi}{2}\right)} \qquad (B.1)$$

Assume

$$\Delta\varepsilon = \varepsilon_o - \varepsilon_\infty$$

$$a = 1 + (\omega\tau)^\beta \cos\left(\frac{\beta\pi}{2}\right)$$

$$b = (\omega\tau)^\beta \sin\left(\frac{\beta\pi}{2}\right)$$

202

Then the equation (B.1) can be expressed as

$$\varepsilon^* = \varepsilon' + i\varepsilon''$$ (B.2)

where is

$$\varepsilon' = \varepsilon_\infty + \frac{\Delta\varepsilon a}{a^2 + b^2}$$ (B.3)

$$\varepsilon'' = \frac{\Delta\varepsilon b}{a^2 + b^2}$$ (B.4)

Mathematical manipulation of the equation (B.3) and (B.4)

$$\left(\varepsilon' - \varepsilon_\infty\right)^2 + \varepsilon''^2 = \frac{\Delta\varepsilon^2 a^2}{\left(a^2 + b^2\right)^2} + \frac{\Delta\varepsilon^2 b^2}{\left(a^2 + b^2\right)^2}$$ (B.5)

$$\left(\varepsilon' - \varepsilon_\infty\right)^2 + \varepsilon''^2 = \frac{\Delta\varepsilon^2}{\left(a^2 + b^2\right)}$$ (B.6)

The followings are the re-evaluation of equation (B.4) and (B.3)

$$\frac{\Delta\varepsilon\left(\omega\tau\right)^\beta}{a^2 + b^2} = \frac{\varepsilon''}{\sin\left(\dfrac{\beta\pi}{2}\right)}$$ (B.7)

$$\frac{\Delta\varepsilon}{\left(a^2 + b^2\right)} = \left(\varepsilon' - \varepsilon_\infty\right) - \frac{\varepsilon''}{\sin\left(\dfrac{\beta\pi}{2}\right)}\cos\left(\dfrac{\beta\pi}{2}\right)$$ (B.8)

If the equation (B.8) is substituted into equation (B.6) yield the circle equation as expressed by

$$\left(\varepsilon' - \frac{\left(\varepsilon_o + \varepsilon_\infty\right)}{2}\right)^2 + \left(\varepsilon'' + \frac{\left(\varepsilon_o + \varepsilon_\infty\right)\cot\left(\frac{\beta\pi}{2}\right)}{2}\right)^2 = \left(\frac{\varepsilon_o - \varepsilon_\infty}{2}\right)^2 + \left(\frac{\varepsilon_o - \varepsilon_\infty}{2}\right)^2 \cot^2\left(\frac{\beta\pi}{2}\right) \qquad \text{(B.9)}$$

The central coordinate of the circle is $\left(\left(\dfrac{\varepsilon_o + \varepsilon_\infty}{2}\right), -\dfrac{\left(\varepsilon_o - \varepsilon_\infty\right)\cot\left(\dfrac{\beta\pi}{2}\right)}{2}\right)$ and the

radius is $r = \left(\left(\dfrac{\varepsilon_o - \varepsilon_\infty}{2}\right)^2 + \dfrac{\left(\varepsilon_o - \varepsilon_\infty\right)^2 \cot\left(\dfrac{\beta\pi}{2}\right)}{2}\right)^{\frac{1}{2}}$